CORRELATION OF MICROSTRUCTURE AND THERMO-MECHANICAL

PROPERTIES OF A NOVEL HYDROGEN TRANSPORT MEMBRANE

By

Yongjun Zhang

RECOMMENDED: _____

_____

_____

_____
Advisory Committee Chair

_____
Chair, Department of Mining & Geological
Engineering

APPROVED: _____
Dean, College of Engineering and Mines

_____
Dean of the Graduate School

_____
Date

CORRELATION OF MICROSTRUCTURE AND THERMO-MECHANICAL

PROPERTIES OF A NOVEL HYDROGEN TRANSPORT MEMBRANE

A

THESIS

Presented to the Faculty

of the University of Alaska Fairbanks

in Partial Fulfillment of the Requirements

for the Degree of

DOCTOR OF PHILOSOPHY

By

Yongjun Zhang, B.Eng., M.Eng.

Fairbanks, Alaska

May 2014

ABSTRACT

A key part of the FutureGen concept is to support the production of hydrogen to fuel a "hydrogen economy," with the use of clean burning hydrogen in power-producing fuel cells, as well as for use as a transportation fuel. One of the key technical barriers to FutureGen deployment is reliable and efficient hydrogen separation technology. Most Hydrogen Transport Membrane (HTM) research currently focuses on separation technology and hydrogen flux characterization. No significant work has been performed on thermo-mechanical properties of HTMs. The objective of the thesis is to understand the structure-property correlation of HTM and to characterize (1) thermo mechanical properties under different reducing environments and thermal cycles (thermal shock), and (2) evaluate the stability of the novel HTM material.

A novel HTM cermet bulk sample was characterized for its physical and mechanical properties at both room temperature and at elevated temperature up to 1000°C. Micro-structural properties and residual stresses were evaluated in order to understand the changing mechanism of the microstructure and its effects on the mechanical properties of materials. A correlation of the microstructural and thermo mechanical properties of the HTM system was established for both HTM and the substrate material.

Mechanical properties of both selected structural ceramics and the novel HTM cermet bulk sample are affected mainly by porosity and microstructural features, such as grain size and pore size-distribution. The Young's Modulus (E-value) is positively correlated to the flexural strength for materials with similar crystallographic structure. However, for different crystallographic materials, physical properties are independent of mechanical properties. Microstructural properties, particularly, grain size and crystallographic structure, and thermodynamic properties are the main factors affecting the mechanical properties at both room and high temperatures. The HTM cermet behaves more like an elastic material at room temperature and as a ductile material at temperature above 850°C.

The oxidation and the plasticity of Pd phase mainly affected the mechanical properties of HTM cermet at high temperature, also as a result of thermal cycling. Residual stress induced in the HTM by thermo cycles also plays a very critical role in defining the thermo-mechanical properties.

TABLE OF CONTENTS

xii

LIST OF FIGURES

Page

LIST OF TABLES

xxviii

ACKNOWLEDGEMENT

Last but not least, my eternal gratitude to my Dad Qiang Zhang, my Mom Fengqin Hu and my sister Yongmei Zhang, my husband John Netzel, and my three lovely daughters, Danyi Wang, Ziye Wang and Rebecca Netzel for their sacrifices, love and encouragements, which have always been invaluable asset for me.

CHAPTER I: INTRODUCTION

1.1   Background

A key part of the FutureGen concept is to support the production of hydrogen to fuel a "hydrogen economy," with the use of clean burning hydrogen in power-producing fuel cells, as well as for use as a transportation fuel. One of the key technical barriers to FutureGen deployment is reliable and efficient hydrogen separation technology. Hydrogen can be purified through several techniques. Today the most commonly used method for hydrogen separation is a process known as pressure swing adsorption (PSA).This technology is based on an adsorbent bed that captures impurities in the syngas stream at higher pressure and then releases them at low pressure. Multiple beds are utilized simultaneously so that a continuous stream of hydrogen may be produced. This technology can produce hydrogen with a purity greater than 99.9% [1]. Temperature swing adsorption is a variation of PSA; it is, however, not widely used due to the relatively long time required to heat and cool sorbents. Electrical swing adsorption, currently in the development stage, has been proposed as well. Existing cryogenic processes to purify hydrogen require extremely low temperatures, making them very expensive and energy-intensive [2, 3].

Advances in gas separation technologies [4-8], such as improved separation membranes, resulting from the need to recover pure hydrogen from a mixed gas stream, have the potential to improve efficiency and recovery while decreasing the costs of hydrogen production. Membrane-related hydrogen separation processes are considered attractive alternative to PSA and other energy-driven processes depending upon purity and scale of production. A variety of hydrogen transport membranes have been proposed for several energy applications that involves the production of essentially pure hydrogen by separation of hydrogen from a hydrogen containing feed through hydrogen ion transport through such membrane. In such membranes, the transport of hydrogen ion principally

occurs within a dense layer that allows both hydrogen ions and electronic transport at elevated temperatures. The key to accounting for both these characteristics is the catalytic splitting of molecular hydrogen. The resulting hydrogen atoms are adsorbed on the membrane surface, rapidly absorbed into the metallic lattice and diffused to the opposite surface where they recombine to form molecular hydrogen which is released to the permeate stream.

The hydrogen from a hydrogen containing feed ionizes on one surface of the membrane and the resultant hydrogen ions are transported through the dense layer and emerge on the opposite side thereof to recombine into elemental hydrogen. In the recombination, electrons are liberated and are transported back through the membrane to ionize the hydrogen. There are no interconnect pores, thus, a molecule cannot swim through from one side to the other side. Such membranes can employ two phases, an ionic phase to conduct the hydrogen ions and an electronic phase to conduct the electrons. In order to minimize the resistance of the membrane to the ionic transport, such membranes are made as thin as possible and are on porous support (substrate) layers. The resulting composite hydrogen transport membrane can be fabricated as a planar element or as a tube in which the dense layer is situated either on the inside or the outside of the tube.

The problem that exists with all composite hydrogen transport membranes is one of strength and durability. This problem arises in part due to the high temperatures when such membranes are subjected to process conditions and in reactors. Since the dense layer is very thin it must be supported. As a result, there must be a close match between the thermal expansion of the dense layer, its porous support and any intermediate active porous layer. Additionally, the hydrogen transport membranes are particularly susceptible to material creep, in which the material will fail under prolonged thermal and mechanical stress.

Most research in hydrogen membrane industry is focused on the areas of separation

technologies and characterizations of hydrogen fluxes. No significant work has been performed to determine the effect of the intrinsic factors (such as grain size and phase distribution) and extrinsic factors (such as temperature and atmosphere) on the macro-structural and thermo mechanical properties of HTM. It is recognized that none of these membranes will be used without a porous support. Therefore, a good porous support is essential on which a functional membrane can be deposited. An understanding of the correlation between the microstructural and the thermo-mechanical properties of a porous substrate is, therefore, required to define the complete HTM system, which consists of a functional HTM membrane and a porous substrate.

In the followings, a comprehensive literature review of hydrogen transport membranes (HTMs) and the development of HTM technologies are presented.

1.2   Principles of Hydrogen Separation Membranes

Most hydrogen separation membranes operate on the principle that only hydrogen can permeate the membrane because of the material's inherent properties. Each type of membrane has advantages and disadvantages, and many research and industrial organizations are trying to develop better membranes. Figure 1 illustrates the basic operating principles of hydrogen separation membranes for use in coal-derived syngas [9]. This particular figure shows a tubular membrane, but plate and frame-style membranes have also been developed. In Figure 1, the "syngas in" stream refers to the feeding of mixed gases into the membrane module. The permeate stream (mostly hydrogen in this case) has permeated the membrane wall. The raffinate is the left-over feed stream once the permeate hydrogen is separated. N_2/Ar sweep gas is used in the lab experiments to sweep away the permeated H_2 from membrane surface to GC/Mass Spectrometer for analysis. In industrial application there won't be any sweep gas. If sweep gas is used then H_2 has to be separated from a mixture of H_2/N_2 or H_2/Ar mixture. In "real-world", the feed side will be at high pressures and sweep side will be at or near atmospheric pressure.

4

Hydrogen separation can be broadly attributed to the following four mechanisms:

>   Knudsen Diffusion – as illustrated in Figure 2 (a), Knudsen diffusion occurs
     when the pore diameter of the barrier (d) is smaller than the mean free path of
     the hydrogen (λ).
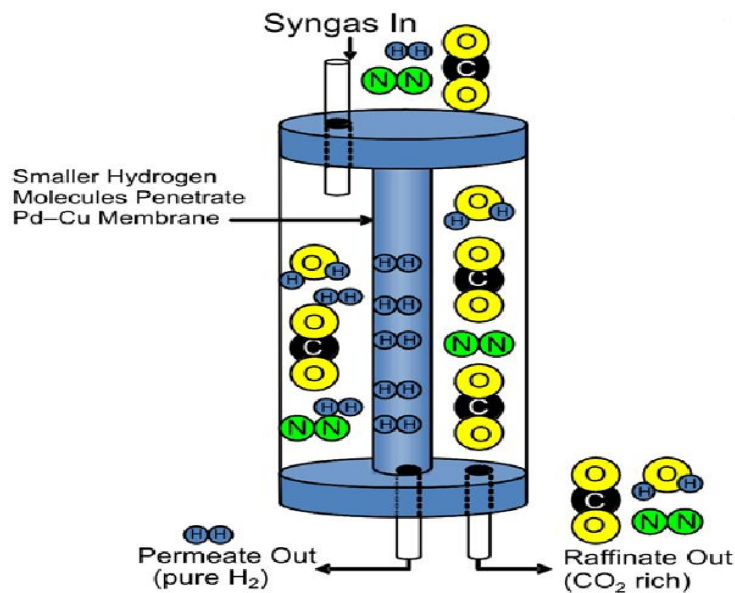
Figure 1:   Operation Principleof Hydrogen Separation Membrane [9]

>   Molecular (Fickian) Diffusion – as illustrated in Figure 2 (b), molecular
     diffusion occurs when pore diameter of the barrier (d) is greater than the
     mean free path of the hydrogen (λ).

>   Solution Diffusion – this mechanism is based on the solubility and mobility
     of H_2 through a barrier, such as a Pd-based dense membrane.

>   Surface Diffusion – this process involves the motion of atom, molecule, and
     atomic clusters (ad particles) at solid material surfaces. This mechanism is
     normally parallel with Knudsen diffusion.

Knudsen diffusion occurs when the Knudsen number (K_n) is large. Knudsen number is

defined:

$$K_n = \frac{\lambda}{d}$$

<div align="right">Equation 1</div>

where,

K_n = Knudsen number

λ = free path of the hydrogen

d = pore diameter
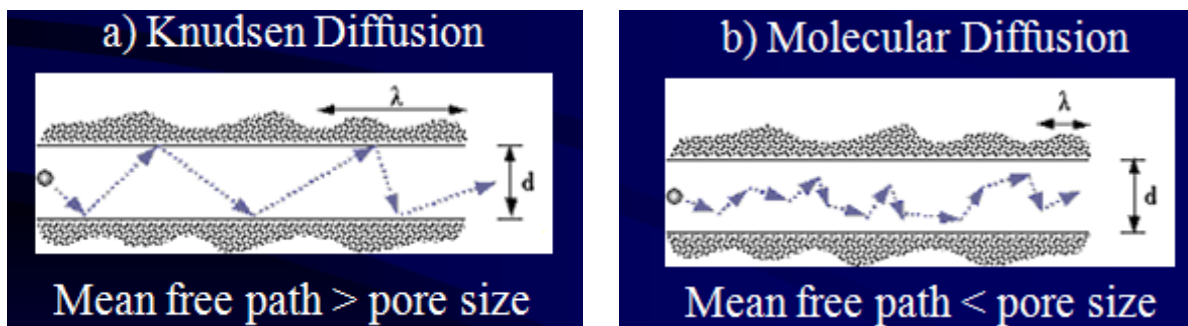
Figure 2:   Mechanisms of Hydrogen Diffusion Though HTMs [3, 10, 11]

At Knudsen numbers greater than 10, Knudsen diffusion becomes significant. Surface diffusion refers to gas molecules that are absorbed by the pore wall and migrate along the surface to the other side. Surface and Knudsen diffusion can occur simultaneously. Capillary condensation occurs if a partially condensed phase fills the pores and does not let other molecules penetrate. Molecular sieving occurs when the pores are so small that only the smaller molecules can fit through. Selectivity toward hydrogen is greatest with molecular sieving and is least with the Knudsen diffusion mechanism. Although relatively straightforward in nature, the solution/diffusion mechanism is somewhat more complex than the diffusion mechanisms. Ockwig [12] presented a seven-step mechanism in which (1) the hydrogen mixture moves to the surface of the membrane, (2) the H_2 molecules dissociate into H^+ ions and electrons, (3) the ions adsorb into the membrane bulk, (4) the H^+ ions diffuse through the membrane, (5) the H^+ ions desorb from the membrane, (6) the H^+ ions and electrons recombine back to H_2 molecules, and (7) the H_2

diffuses from the surface of the membrane. With metal membranes, only hydrogen undergoes the solution/diffusion mechanism; therefore the membranes are considered 100% selective to hydrogen.

The performance of each membrane is gauged by two important parameters: hydrogen selectivity and hydrogen flux. The selectivity of hydrogen can be defined as [10]:

$$\alpha_{A/B} = \frac{Y_A/Y_B}{X_A/X_B} \qquad\qquad Equation\ 2$$

where,

α = selectivity factor of component A over component B in the mixture

$Y_A\ and\ Y_B$ = fractions of those components in the permeate

$X_A\ and\ X_B$ = the fractions of those components in the feed

Components A and B are usually defined so that a higher selectivity factor refers to better membrane performance. A selectivity factor of 1 means there is no component separation.

Hydrogen flux is a performance measurement of a membrane and can be expressed as mass or mole per unit time per unit area. It is generally calculated as [3, 10]:

$$J_x = \frac{P(p_{x,feed}^n - p_{x,permeate}^n)}{t} \qquad\qquad Equation\ 3$$

where,

J_x = represents the flux of species x

P = represents the permeability of species x

$p_{x,feed}$ = partial pressures of species x in the feed

$p_{x,permeate}$ = partial pressures of species x in the permeate streams

t = thickness of membrane

n = the partial pressure exponent, $0.5 < n < 2$

Like the value of P, the value of n is normally attributed to the transport mechanism assumed. When n = 1, the equation is called Fick's law. For hydrogen transport through a metal membrane, the value of n is usually 0.5, and the equation reduces to what is

referred to as Sievert's law [3]. Sievert's law is a useful way of measuring membrane performance because it takes into account membrane thickness and the partial pressure of hydrogen on each side of the membrane.

Since most membranes operate on a partial pressure differential, some hydrogen will always be left behind in the raffinate stream. Therefore, an additional measurement of performance is the recovery or yield as calculated by the following equation:

$$S = \frac{q_p}{q_f}$$
<div align="right">*Equation 4*</div>

where,

S = the yield of the chosen system

q_p = permeate flow

q_f = feed flow

There are numerous other ways to quantify the yield, including calculating the volume reduction in the raffinate or the percentage of hydrogen recovery from the feed.

1.3 Types of Hydrogen Transport Membranes

Hydrogen transport membranes (HTMs) can be broadly categorized into two types: organic and inorganic. An organic membrane is the same as a polymer membrane, which is an existing technology [13]. Inorganic membranes can be classified based on their raw materials (metal, ceramic, cermet, etc.) and their microstructure (porous or dense). Typically, there are six popular types of membrane: polymer, metal, silica, zeolite, carbon, and cermet. A brief description of each is summarized below for ready reference.

1.3.1 Organic Membranes for H_2 Purification

Polymeric membranes for hydrogen separation were first introduced as "hydrogen-selective" membranes, allowing hydrogen to pass through based on its small size. In contrast, "hydrogen-rejective" membranes favor the passage of high-solubility molecules

such as CO_2 while blocking the less-soluble H_2 molecules. Glassy polymers are often used for the separation of H_2 and CO_2 due to their ability to sieve penetrant gases on the basis of molecular size, specifically the molecular kinetic diameter [14]. In the past decade, polymeric membranes such as the Polysep system (UOP) and the PRISM system (Monsanto Air Products and Chemicals Inc.) are the accepted technology to separate hydrogen from industrial refinery synthesis gas mixtures. However, their limited mechanical strength, relatively high sensitivity to swelling and compaction, and susceptibility to certain chemicals such as hydrochloric acid (HCl), sulfur oxides (SO_x), and CO_2 make polymeric membranes less attractive.

1.3.2 Inorganic Membranes for H_2 Purification

The limitations of polymeric membranes rallied more effort to the synthesis of inorganic membranes because of their good thermal stability and chemical inertness for many industrial applications. For the fabrication of hydrogen separation membranes, many techniques are available: phase inversion, rolling, electroless-plating, chemical vapor deposition (CVD), sputtering, spray pyrolysis, coating, metal deposition, and sol-gel.

> ➢ *Alloys and Metals.* The physical mechanism of H_2 permeation through metallic membranes is a functioning process of absorbing and dissociating gaseous H_2 on the metal surface exposed to the feed stream and subsequent diffusion of atomic H through interstitial sites in the metal. Recombination of atomic H into H_2 on the downstream membrane side completes the transport of H_2 across the membrane [15]. Figure 3 presents hydrogen permeability for selected metals based on data previously presented [3]. Of all metals in the metallic membranes, palladium (Pd) and its alloys remain most attractive for H_2 separation applications [16-19], even with their mechanical limitations such as embrittlement, cracks, pinhole film defects, delamination, and sulfur sensitivity.

➢ *Silicas and Zeolites*. Recently, porous ceramic membranes including silica, silicalites, and zeolites have also been widely investigated for hydrogen separation because of their high H_2 fluxes and good selectivity with respect to other synthesis gases [20-22]. Moreover, these materials eliminate the need for scarce precious metals, and they are less expensive with higher hydrogen permeance. An extension of silica membrane researches is the development of hybrid metal-coated silica system, such as the Al-coated SiO_2 [23] and Ti-silicate umbite membranes [24], which has a much enhanced permeance of hydrogen (H_2) over the other compositions in the syngases such as CO_2, N_2, CO, and CH_4.

➢ *Carbon-Based Membranes*. With respect to hydrogen permeability and selectivity, carbon membranes and carbon nanotubes (CNTs) have been shown to achieve excellent performance in the separation of hydrogen from light hydrocarbons such as methane in Alaska.

➢ *Ceramic-Metal (Cermet) Membranes*. Cermets for hydrogen separation were developed by dispersing metals of high hydrogen permeability in a thermodynamically and mechanically stable ceramic matrix such as alumina (Al_2O_3) or zirconia (ZrO_2). The major advantages of these membranes are that hydrogen separation does not require electrodes or an external power supply, and hydrogen separated from the mixed gas stream is of high purity, so post-separation purification steps are unnecessary.

The mechanism of hydrogen transport differs depending upon the inherent nature of each membrane type, as shown in Table 1 [3, 10, 12]. The seven basic types of membranes given in the table have inherent advantages and disadvantages, depending on desired operating conditions and necessary product specifications. With data presented by Kluiters [10] and modified with Adhikari [3] and Ockwig [12], Table 1 summarizes the relative operational performance of the seven types of functional membrane. Typical
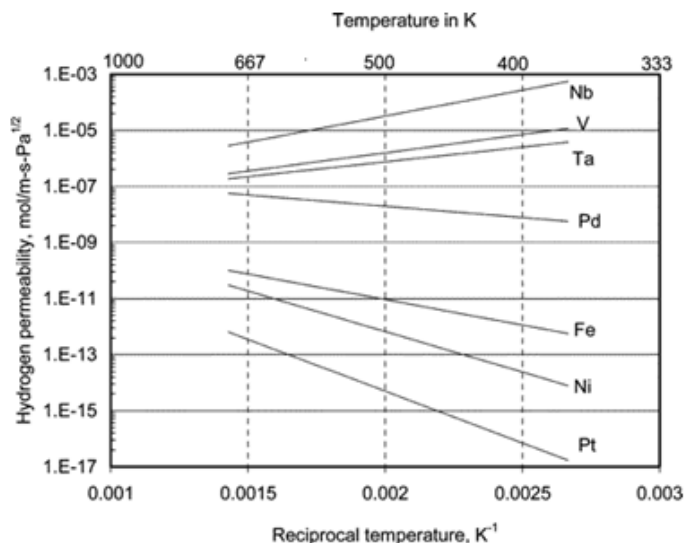
Figure 3:   Hydrogen Permeability for Selected Metals [3]

Table 1:   Performance Comparison of Different HTMs [3, 6, 10, 12, 25]

Properties	Membrane Type					
	Dense Polymer	Micro porous	Dense Ceramic	Porous Carbon	Dense Metallic	Dense Cermet
Temperature Range	<100°C	200-600°C	600-900°C	500-900°C	300-600°C	300-900°C
H_2 Selectivity	Low	Moderate	Very High	Low	Very High	Very High
H_2 Flux	Low	High	Moderate	Moderate	High	High
Stability Issues	Swelling, compaction	Stability in H_2O	Stability in CO_2	Brittle	Phase Transition	Phase Transition
Poisoning Issue	HCl, SOx, CO_2	/	H_2S	Adsorbing Vapor	H_2S, HCL, CO	H_2S
Example Material	Polymer	Silica, Alumina,	$SrCeO_{3-\delta}$ $BaCeO_{3-\delta}$	Carbon	Palladium Alloys,	ANL-3e Dense

operational temperature will vary by specific membrane type. In general, the dense

polymer membranes are only applicable at low temperature, while dense ceramic and dense metallic membranes have the highest hydrogen selectivity, and hydrogen flux is highest for dense metallic or microporous ceramic membranes. Although dense metallic membranes seem to give the best performance relative to hydrogen, they are also very susceptible to poisoning from many compounds found in syngas, and palladium alloys are very expensive. Dense ceramic membranes are less susceptible to poisoning, and they can be much less expensive, providing high potential for commercial applications. More development work is under way with each of these membrane types to increase their resistance to poisoning and to reduce cost.

1.4   Review of ANL-3e Dense Membranes

Under DOE/NETL sponsorship, Argonne National Laboratory (ANL) developed dense cermet membranes to separate hydrogen at commercially significant fluxes from gas mixtures such as the product streams from coal gasification, methane partial oxidation, and water-gas shift reactions. The status of the ANL-3e membrane presented in Figure 4 was provided by Balachandran [25]. The laboratory's efforts focused primarily on ANL-3e membranes (composed of Pd and Y_2O_3-stabilized ZrO_2), because they gave the highest hydrogen flux ($\approx$26 and $\approx$50 cm^3/min-cm^2 at 400 and 900°C, respectively) using 90% H_2/balance Helium (He) at ambient pressure as the feed gas (Figure 4). To judge their performance at high pressures at temperature up to 900°C, the ANL-3e membranes were tested at DOE/NETL with feed pressure up to $\approx$350 psig and at Argonne with feed pressure up to $\approx$300 psig.

Figure 5 shows the hydrogen flux for ANL-3e membranes at various temperatures versus $\Delta pH_2^{1/2}$, which is defined in terms of the partial pressures of hydrogen on the feed and sweep sides of the membrane:

$$\Delta pH_2^{1/2} \equiv \sqrt{pH_2(feed)} - \sqrt{pH_2(sweep)}$$

Equation 5
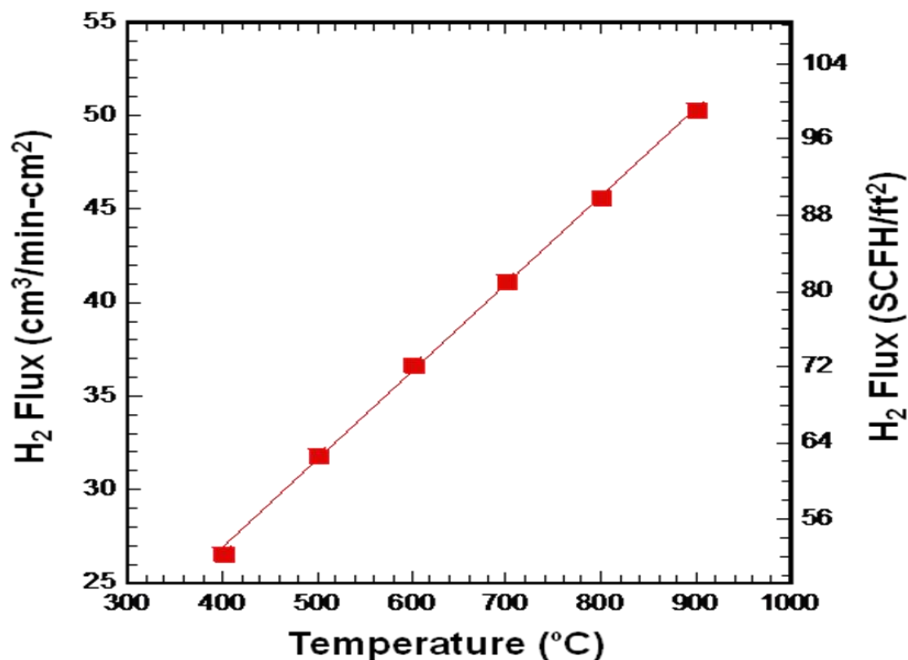
Figure 4: **Hydrogen Flux of ANL-3e (Thickness ≈20 μm) Measured at Argonne Using 90% H$_2$/Balance He at Ambient Pressure as Feed Gas**

The data were collected at NETL and Argonne with high-pressure feed gas; the value measured at 400°C according to DOE/NETL test protocol was measured at Argonne. NETL test protocol calls for a feed gas composed of 50.3% H$_2$, 1.0% CO, 30.2% CO$_2$, and 18.5% H$_2$O with a total pressure of ≈200 psig. To compare flux values for membranes with different thicknesses, all values were normalized for a thickness of 20 μm. Flux was measured at $\Delta pH_2^{1/2}$ <1 atm$^{1/2}$ by varying the feed composition while fixing the total pressure at 1 atm. Flux was measured at $\Delta pH_2^{1/2}$ >1 atm$^{1/2}$ by fixing the feed composition at 90% H$_2$/balance He while varying the total pressure. The point in red at $\Delta pH_2^{1/2}$ ≈2.4 atm$^{1/2}$ was measured according to NETL test protocol, and the red point at $\Delta pH_2^{1/2}$ ≈1 atm$^{1/2}$ was measured using feed gas of ≈90% H$_2$/balance He (pressure ≈3–7 psig) after completion of the protocol test. The results show that ANL-3e membranes have potential to achieve DOE flux targets if membrane thickness is reduced to ≈10 μm. Low He leakage and high purities (>99%) during the high-pressure tests show that Argonne's reactor can be used to make measurements according to the established

protocol.
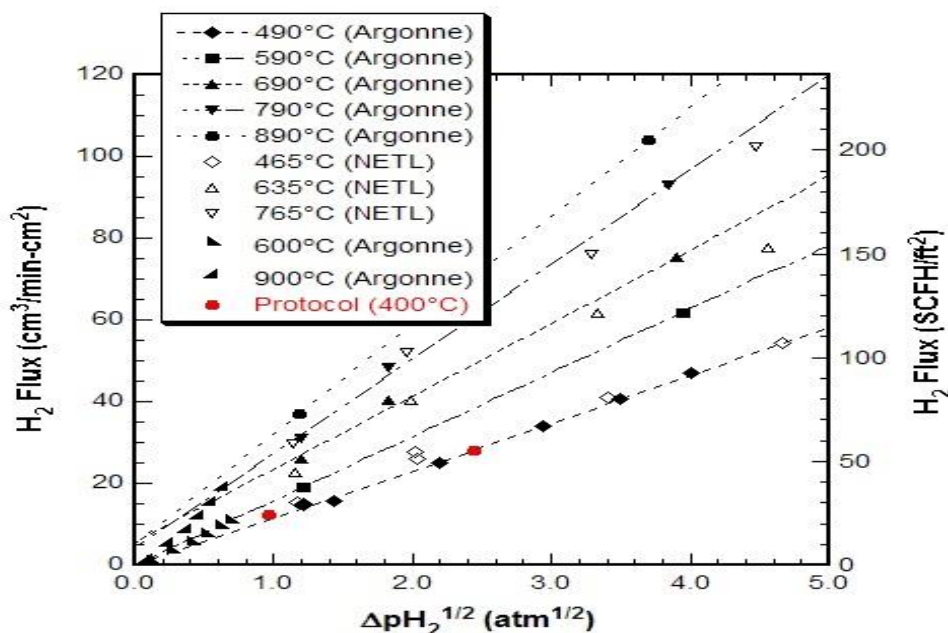
Figure 5: **Hydrogen Flux at Various Temperatures vs. $\Delta pH_2^{1/2}$ (Defined in Text) for ANL-3e Membranes Tested at Argonne and NETL. Red Symbol at 400°C Gives Value Measured at Argonne According to NETL Test Protocol. All Values are Normalized for a Membrane Thickness of 20 micron meters**

Good chemical stability is a critical requirement for membranes separating hydrogen from the product streams of coal gasification and/or methane reforming. Because the membranes will encounter hydrogen sulfide (H_2S), which can degrade Pd-containing membranes by forming palladium sulfide (Pd_4S), ANL-3e membranes were tested to determine the conditions under which Pd_4S forms. Figure 6 shows the Pd/Pd_4S phase boundary determined at Argonne by experiment and by calculation using thermodynamic parameters derived from the experimental data. The lines were calculated for feed with 73% H_2 and 10% H_2 to show the effect of hydrogen concentration (through the $H_2/S_2/H_2S$ equilibrium) and give temperatures at which Pd and Pd_4S are in equilibrium for given H_2 and H_2S concentrations.

For a given H_2S concentration (Figure 6), Pd is stable and Pd_4S does not form at temperatures above the phase boundary. At temperatures below the phase boundary,

14

formation of Pd₄S impedes hydrogen permeation of the membrane.
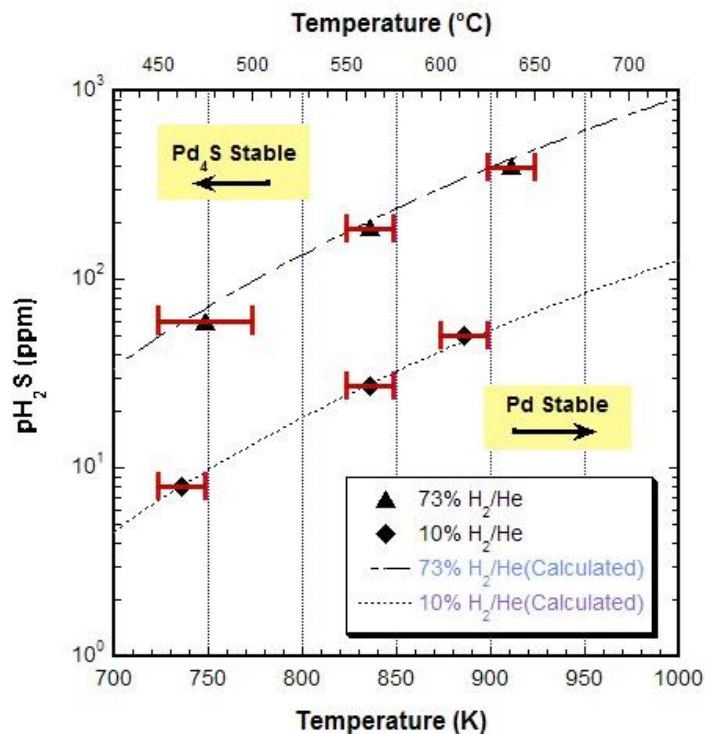
Figure 6: **Partial Pressure of H₂S vs. Temperature Showing Pd/Pd₄S Phase Boundary Determined at Argonne Using Pd Foil and ANL-3e Samples. Curves Calculated Using Thermodynamic Parameters Derived from Experimental Data**

It does not necessarily destroy the membrane, as ANL-3e membranes can be regenerated in some cases after they have reacted with H₂S. Points with horizontal bars (Figure 6) were determined by examining samples after they were equilibrated in specific H₂/H₂S mixtures at various temperatures. The low-temperature end of the bar indicates the highest temperature, at which Pd₄S was found, and the high-temperature end shows the lowest temperature at which Pd₄S was not found; the Pd/Pd₄S phase boundary lies between these two temperatures. For example, the phase boundary lies in the 450–475°C range for samples exposed to 10% H₂/8 ppm H₂S/balance He. The results (Figure 6) suggest that ANL-3e membranes should be able to withstand NETL test protocol conditions, considering that tests are required at 300–600°C with p(H₂S)/p(H₂) of 4E-05

in Test 2A and 1E-04 in Test 3.
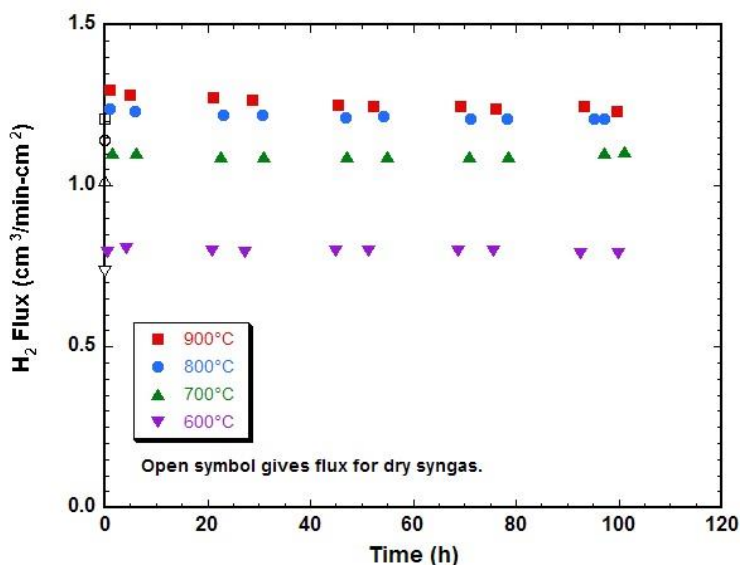
Figure 7: **Time Dependence of Hydrogen Flux for ≈0.3-μm-Thick ANL-3e Membrane at 600–900°C Using Feed Gas Initially Composed of Dry 52.7% H_2/10.1% CO/8.0% CO_2/0.6% CH_4/Balance He and Then 52.7% H_2/20.6% H_2O/10.1% CO/8.0% CO_2/0.6% CH_4/Balance He**

Figure 7 plots the hydrogen flux at 600–900°C for a ≈0.3-μm-thick ANL-3e membrane in tests using simulated "syngas" as the feed gas. The composition of the feed gas was 52.7% H_2/20.6% H_2O/10.1% CO/8.0% CO_2/0.6% CH_4/balance He. The initial values were measured in dry syngas. Then moisture was added by bubbling the syngas through water at a temperature of ≈ 60°C. When moisture was added at 600 and 700°C, the flux initially increased slightly then remained stable for >100 h. There was also a slight initial increase in the flux during tests at 800 and 900°C, but the flux decreased very slightly over longer times. Calculation of the equilibrium gas compositions (Figure 7) suggests that the initial increase in flux at each temperature resulted from an increase in hydrogen concentration in the feed gas. The fact that the flux remained stable at 600–700°C after an initial small increase indicates that the membrane is stable under these conditions.

In addition to providing high hydrogen flux and being chemically stable, practical membranes must be available in shapes with a large active area (e.g., tubes). To fabricate

tubular cermet membranes, a paste-painting method was used to prepare a disk-shaped membrane that gave the record high hydrogen flux for ANL-3e membranes. In the paste-painting method, porous alumina tubes are first produced by cold isostatic pressing of alumina hydrate powder. After a tube is pre-sintered, it is painted with a slurry of cermet components and sintered at high temperature to produce a porous tube coated with a thin (≈20 μm), dense membrane. Using this method, Argonne has fabricated tubular thin-film membranes composed of either Pd (60 vol. %)/ZrO_2 or Pd (60 vol. %)/CeO_2.

Cermet membranes must also have sufficient mechanical strength to withstand stress caused by changes in temperature and feed gas composition. Changes in temperature produce stress in ANL-3e membranes because they contain two materials with different coefficients of thermal expansion. Changes in feed gas composition produce stress because the lattice parameter of Pd depends on the hydrogen concentration in the feed gas. Because membranes will inevitably encounter changes in temperature and feed gas composition during operation, Argonne evaluated the "cyclability" of ANL-3e membranes (i.e., their ability to withstand the effects of cyclical changes in temperature and feed gas). Neither thermal nor hydrogen cycling caused significant changes in either hot-pressed or thin-film ANL-3e samples. Pd particles on the surface of polished hot-pressed samples were attributed to the coalescence of Pd left behind by the polishing. Growth of the particles did not noticeably affect helium leakage through the samples. Likewise, in situ measurements made during hydrogen cycling of a thin-film sample showed that its hydrogen flux did not change during cycling at 400°C and 500°C. Helium leakage through the sample did not change during cycling at 500°C, and the slight change during cycling at 400°C is within the range of experimental uncertainty.

Critical factors influencing cermet membrane performance in product streams from coal gasification were explored during the bench-scale development effort. The membranes were tested at feed pressure ≤350 psig in feed gas containing ≤400 ppm H_2S [8, 26]. They withstood cycling in temperature and feed gas composition without degradation in

performance. Large-scale membranes will be needed to meet DOE goals; the bench-scale effort demonstrated that tubular membranes can be made by conventional ceramic processing techniques.

Like metallic membranes, dense cermet membranes provide high hydrogen flux and high hydrogen selectivity, because a metal phase provides the path for hydrogen transport in both types of membrane, and hydrogen's diffusivity and solubility in the metal are much higher than the diffusivity and solubility of other gases. The ceramic phase in cermet membranes provides an important advantage over metallic membranes, however, because it provides structural support for the metal phase at high temperature and high pressure, conditions that the metal might be unable to withstand by itself. Mechanical support from the ceramic phase is also important during changes in feed gas composition, because changes in the metal's hydrogen content can cause large changes in its volume, which can cause a thin-film metal membrane to crack or spall from its support structure.

1.5   Problem Statement

Growing attention to the development of an environmentally benign, inexpensive technology for separating hydrogen from water [4, 26] and/or syngas [5, 27] has motivated research on hydrogen transport membranes (HTMs). Cost-effective, membrane-based reactor and separation technologies are of considerable interest to DOE's FutureGen program to develop advanced coal-based power and fuel technologies.

Most HTM research currently focuses on separation technology and hydrogen flux characterization. No significant work has been performed on thermo-mechanical properties of HTMs at elevated temperatures and/or under various chemical environments.

Cermet for hydrogen separation consists of a ceramic and a metallic phase contiguous in a dense matrix. In a cermet one may combine one state-of-the art pure proton conductor

with a highly electron-conducting metallic phase, and thereby circumvent the problem of having both electronic and ionic conduction in one and the same oxide.

Dense cermet membranes exhibit protonic or mixed protonic-electronic conductivity in hydrogen or water atmospheres without significant oxygen transport [5, 6]. These membranes, although with high hydrogen permeability, are either too thin to be self-supporting and too weak to resist differential pressures or they become brittle in hydrogen-reduced atmospheres. A novel dense HTM was created by ANL for high hydrogen permeance, where metals are evenly dispersed throughout a thermodynamically and mechanically stable ceramic matrix [6]. This HTM technology could facilitate hydrogen extraction from myriad fluids. However, its thermo-mechanical properties need a complete evaluation before this HTM can be used in industry. A correlation between intrinsic factors (such as grain size and phase content/distribution) and extrinsic factors (such as temperature and atmosphere) is required to set up a finite element model. This will ultimately lead to development of an improved process for manufacturing HTMs in the future.

1.6   Research Objectives

Modeling is becoming an acceptable method for identifying candidate material for membranes. In particular, many recent efforts have focused on predictive modeling of candidate metallic alloys from first principles. Ideally, specific performance features such as hydrogen permeability, hydrogen embrittlement and possibly thermal and chemical stabilities are modeled as a function of metal composition or structure. In combination with predictive structural models, it is useful to have experimental techniques to characterize or confirm their structures, which can be used to refine the predictive model.

Mechanical properties are important for real-world applications. This is an area where data is insufficient or non-existent, particularly in high temperature. In addition to the

thermal expansion and the problem of thermal cycling, membrane standing in chemical gradients may suffer from chemical expansion, so that one side expands relative to the other as a result of a gradient in defect concentrations. This results in stresses and bending of the membrane, and is well known in oxygen separation membranes, where the effects can be large [28]. One may investigate this with controlled atmosphere dilatometry or high-temperature X-ray diffraction.

For thin metal membranes, the permeability behavior may differ significantly from that of bulk metals of similar composition. This is due to the increase in the dominance of surface phenomena, defects, grain boundaries, thermal dilation, and lattice defects on the permeability behavior. This divergence emphasizes how critical it is to characterize the behavior for thin metal structures as opposed to mere inference from bulk metal behavior. It should be noted that the processing and production techniques must also be sufficiently able to manipulate the defect structure. Perhaps the biggest hurdle which is faced by all classes of hydrogen separation membrane is the lack of chemical stability. Water, sulfur containing species, acid vapors and carbon oxides are the most commonly encountered problematic contaminants which must be dealt with. The combined results of these chemicals and thermal performance issues ultimately determine the cost and viability of a given hydrogen membrane. Therefore, the importance of characterization of the HTM's chemical and thermal stability, mechanical strength, and ceramic engineering to make dense, thin membranes on porous supporting substrates for high-performance membranes for hydrogen separation at high temperatures cannot be over emphasized. While an incomplete understanding of the mechanical and structural properties of HTM remains, mechanical testing and analytical studies of its microstructural properties will play a critical role. In the interim, a practical solution has been to utilize the metal combined with ceramic as a composite or so called "cermet" material, which can be engineered to be less susceptible to cracks and their propagation.

Cermet for hydrogen separation consists of a ceramic and a metallic phase contiguous in

a dense matrix. In a cermet one may combine one state-of-the-art pure proton conductor with a highly electron-conducting metallic phase, and thereby circumvent the problem of having both electronic and ionic conduction in one and the same oxide. A novel dense HTM cermet membrane was developed by Argonne National Laboratory (ANL) for high hydrogen permeance (ANL-3e HTM), and was provided to the University of Alaska Fairbanks.

The objective of the thesis is to understand the structure-property correlation in hydrogen transport membranes (HTMs) and to characterize (1) thermo-mechanical properties under different reducing environments and thermal cycles (thermal shock), (2) stability of novel HTM materials, and (3) modeling of membranes that could lead to an improved design for their manufacture.

Durability of a HTM is determined by its thermal, chemical, and mechanical stability is critical to its performance. While a standard protocol for testing the durability of HTM has not been established, various mechanical tests can be used to assess its properties. Such useful tests include the following: fracture mechanics, slow strain-rate tensile tests, stress/strain controlled fatigue tests at room and elevated temperatures. Other microanalytical methods also play a vital role in assessing the durability and performance of HTM in the bulk and at the surface. Physical defects (e.g., holes, cracks, etc.) are assessed by fractography, and scanning electron microscope (SEM) after subjecting the membrane to extreme operating conditions (high pressure and temperature over an extended period). Therefore, thermo-mechanical properties of the as-received and the reduced HTM at several elevated temperatures in different ambient air and reducing environments will be determined. Mechanical properties to be evaluated include elastic properties, Vickers hardness and fracture toughness, thermal expansion behavior, and flexural and equibiaxial strength of this novel HTM. The effect of thermal cycles or thermal shock on mechanical properties and the stability of these membranes are also critical; these will be addressed using a custom-designed thermal cycling rig. The

porosity and density values for all HTM samples will be determined by Archimedes' principle. In general, the following tests/analyses will be evaluated based on the research objectives of this thesis work:

(1)   Physical properties - bulk density and porosity;

(2)   Elastic properties - Young's Modulus (E), Shear Modulus (G) and Poisson's Ratio (υ);

(3)   Vickers hardness number (HV);

(4)   Modulus of rupture (MOR) or flexural strength;

(5)   Slow crack growth (SCG);

(6)   Fractography characterization analysis by Scanning Electron Microscopy (SEM) with energy dispersive spectrometers (EDS);

(7)   Coefficient of thermal expansion (CTE);

(8)   Thermal analysis by Thermogravimetry (TG) and differential temperature analysis (DTA);

(9)   X-ray Diffraction (XRD) phase analysis;

(10)   X-Ray Diffraction (XRD) texture analysis;

(11)   Residual stress by X-ray $\sin^2\psi$ Techniques;

(12)   X-ray spectrometry analysis by X-ray florescence (XRF) and the electron microprobe with energy dispersive spectrometers (EDS);

(13)   Effect of thermal cycling on residual stress and other micro-structural properties;

1.7   Plan of Work

To develop the correlation between microstructural properties and thermo-mechanical performance of the HTM material, the following tasks are therefore identified:

Task 1: Literature Review

A comprehensive literature review of the status of HTM membrane development conducted to gather information on key subjects that pertain to this study, such as currently available HTM technologies, will be presented in Chapter I.

Task 2: Experimental Design and Material Section

Based on the research objectives, a detailed laboratory testing plan will be developed to characterize thermal and mechanical properties and microstructure of HTM system. Laboratory investigations and the equipment used for the investigations will be presented in Chapter II.

Task 3: Laboratory Results and Analyses

Laboratory results of thermo-mechanical and microstructural property data of the HTM bulk samples and HTM raw powder will be statistically analyzed. Based on statistical analyses, the significance of thermo-treatment such as high sintering temperature and thermal cycling or thermal shocks will be presented in Chapter III. Several selected structural ceramic substrates such as Al_2O_3, Yttria-stabilized Tetragonal Zirconia Polycrystalline (Y-TZP), and Ceria-stabilized Tetragonal Zirconia Polycrystalline (Ce-TZP) will be studied in order to compare thermal mechanical and microstructural properties of the HTM bulk samples. Results of the analyses will be presented in Chapter IV.

Task 4: Correlation of Microstructural and Thermo-Mechanical Properties

Correlation of both mechanical properties and microstructural characterization for HTM cermet and the selected structural ceramics are discussed and analyzed for the correlation among the physical properties, thermal and mechanical properties, and microstructural characterization and are presented in Chapter V. The effect of temperature and thermal

cycling on the thermo mechanical properties are also presented in Chapter V.

Task 5: Conclusions and Recommendations

Based on the results and analysis, conclusions for the correlation of the thermo-mechanical properties and microstructural properties are summarized in Chapter VI. Future recommended works are also discussed in Chapter VI.

CHAPTER II: MATERIAL AND LABORATORY INVESTIGATION

2.1   Material

The structure of HTM system is composed of a dense and thin cermet (thin-layers) as the functional layer and a porous structural ceramic as the support layer. In this research, the HTM cermet and several structural ceramics are selected to characterize the micro-structural and thermo-mechanical properties for the materials both as-received and after thermal cycling treatment.

2.1.1   Synthesis of HTM Samples and Its Research Plan

Novel hydrogen transport membrane (HTM) cermet was sintered at Argonne National Laboratory (ANL) and provided to University of Alaska Fairbanks (UAF) for characterization of its thermo-mechanical and microstructural properties. The HTM discs were sintered at 1450ºC for 5 hours in air with the heating & cooling rate of 120ºC/hour. Most often, the porous alumina substrates are prepared by mixing 3 wt.% carbon with alumina powder, pressing disks/pellets and pre-sintering at 1000ºC for 10 hours in air (Heating & cooling rate: 120ºC/hour). HTM cermet bulk sample was processed in both disc and bar shape, as shown in Figure 8 (a) and (b). Geometry of the disc-shaped and plate-shaped HTM cermet samples is summarized in Table 2 and Table 3, respectively. Laboratory tests for characterization of mechanical properties and microstructural studies for the HTM cermet solid are summarized in Table 4.

(a) Disc-Shaped HTM Cermet

26
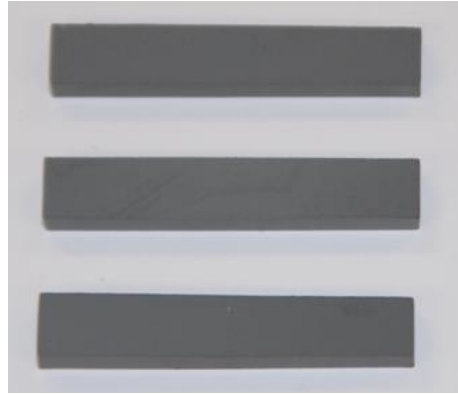
(b) Bar-Shaped HTM Cermet

Figure 8:   HTM Solid Cermet Sintered at Argonne National Laboratory (ANL), Chicago, IL

Table 2:   Geometry of HTM Disc-Shaped Samples

Sample ID	Diameter (mm)	Thickness (mm)
ANL-3e-HTM-Disk#1	28.39	3.98
ANL-3e-HTM-Disk#2	28.28	3.93
ANL-3e-HTM-Disk#3	28.39	4.02

0

Table 3:   Geometry of HTM Bar-Shaped Samples

Sample ID	Thickness(mm)	Width(mm)	Length(mm)
ANL-3e-HTM-Bar#1	3.98	6.60	37.23
ANL-3e-HTM-Bar#2	3.85	6.45	37.41
ANL-3e-HTM-Bar#3	3.69	6.49	37.60

The HTM raw powder (shown in Figure 9 (a)) was provided by ANL to compare the change in the microstructural properties after being processed to HTM solid sample at high temperature and pressure. The HTM raw powder was characterized and analyzed for the selected microstructural properties as summarized in Table 5. The pure palladium metal (shown in Figure 9 (b)) was also selected for TG/DTA study as summarized in Table 5.

Table 4: **Summary of Laboratory Tests for HTM Cermet**

Properties	Laboratory Investigation and Technique
Physical and Mechanical Properties	1. Density and Porosity 2. Elastic Properties, i.e. Young's Modulus (E), Shear Modulus (G) and Poisson Ratio (υ) 3. Vickers Hardness Number (VH) 4. Modulus of Rupture or Flexural strength (σ_{fs}) 5. Residual Stress by X-Ray Diffraction (XRD) $\sin^2\psi$ Technique
Thermal Properties	1. Coefficient of Linear Thermal Extension (CTE) 2. Thermogravimetry /Differential Thermal Analysis (TG/DTA)
Microstructural Properties	1. Fractography by Optical Microscope and Scanning Electron Microscopy (SEM) 2. Surface Morphology Analysis by Optical Microscope and Scanning Electron Microscopy (SEM) 3. Elemental Tracing and Analysis by SEM with Energy Dispersive Spectroscopy (EDS) 4. X-Ray Diffraction (XRD) Phase Analysis 5. XRD Surface Texture Analysis 6. Phase Morphology and Elemental Composition Analysis by Microprobe with EDS

(a) HTM raw powder   (b) Pd Metal

Figure 9: **HTM Raw Powder Supplied by ANL and Commercial Palladium (Pd)**

Table 5:   **Summary of Laboratory Tests for HTM Cermet Raw Powder and Commercial Palladium (Pd) Metal**

Material ID	Microstructural Properties
ANL HTM-Powder	1) XRD Phase Analysis 2) TG/DTA 3) XRD Texture Characterization 4) XRD $\sin^2\psi$ Stress Measurement 5) SEM Analysis
Pd Metal	1) TG/DTA

2.1.2   Selected Structural Ceramics and Research Plan

Two selected structural dense ceramic materials, i.e. Alumina 96 wt% (AL-96) supplied by LSP Industrial Ceramics and Yttria-stabilized tetragonal zirconia polycrystalline (Y-TZP) supplied by Superior Technical Ceramics Corporation (STC), were machined and processed into standard Modulus of Rupture (MOR) Type B bars as specified in the ASTM (C1161-02c), the specimens are shown in Figure 10 and Figure 11, respectively.

Figure 10:   **Specimen of the Structural Ceramic Alumina 96 wt% (AL-96)**
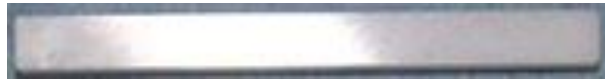
Figure 11:   **Specimen of the Structural Ceramic Yttria-stabilized Tetragonal Zirconia Polycrystalline (Y-TZP)**

The laboratory tests to characterize the thermomechanical and microstructural properties of these selected dense structural ceramic materials are summarized in Table 6 and Table 7, respectively.

Table 6:   **Summary of Laboratory Tests for the Structural Ceramic Material (Al_2O_3 wt 96% (AL-96))**

Material	Material ID	Thermo-Mechanical Properties	Microstructural Properties
Alumina wt. 96%	AL-96	1. Density and porosity 2. Elastic properties (E, G, υ) 3. Vickers hardness (VH) number 4. MOR or flexural strength (σ_{fs}) 5. Slow crack growth (SCG) 6. XRD $\sin^2\psi$ Residual stresses 7. CTE 8. TG/DTA	1. Fractography analysis by SEM with EDS 2. XRD phase analysis 3. XRD texture analysis 4. TG/DTA 5. Coefficient of linear thermal extension (CTE)

Table 7:   **Summary of Laboratory Tests for the Structural Ceramic Material (Yttria-Stabilized Tetragonal Zirconia Polycrystalline (Y-TZP))**

Material	Material ID	Thermomechanical Properties	Microstructural Properties
Yttria-stabilized tetragonal zirconia polycrystalline	Y-TZP	1. Density and porosity 2. Elastic properties (E, G, υ) 3. Vickers hardness (VHN) 4. Coefficient of linear thermal extension (CTE) 5. TG/DTA	1. Fractography analysis by SEM with EDS 2. XRD phase analysis

Two selected porous substrates, 25% ceria-stabilized tetragonal zirconia polycrystalline (25Ce-TZP) and 50% ceria-stabilized tetragonal zirconia polycrystalline (50Ce-TZP) were previously used for the Oxygen Transfer Membrane (OTM) project [28], are shown in Figure 12 (a) and (b). Laboratory tests conducted to characterize the thermomechanical and microstructural properties of these two porous substrates are summarized in Table 8.

(a) 25% Ceria-Stabilized Tetragonal Zirconia Polycrystalline (25Ce-TZP)

(b)   50% Ceria-Stabilized Tetragonal Zirconia Polycrystalline (50Ce-TZP)

**Figure 12:   Specimen of the Porous Substrate Ceria-Stabilized Tetragonal
Zirconia Polycrystalline (Ce-TZP)**

**Table 8:   Summary of Laboratory Tests for the Porous Substrate Ceria-
Stabilized Tetragonal Zirconia Polycrystalline (Ce-TZP)**

Material	Material ID	Thermomechanical Properties	Microstructural Properties
Ceria-stabilized tetragonal zirconia polycrystalline	Ce-TZP	1. Density and porosity 2. Elastic properties (E, G, υ) 3. Coefficient of linear thermal extension (CTE)	1. XRD phase analysis 2. Residual stress 3. TG/DTA 4. X-ray spectrometry

2.2   Laboratory Investigations for Physical & Mechanical Properties

2.2.1   Bulk Density and Porosity Measurement

The densities of HTM were measured based on Archimedes' principle by following these
steps:

1st Procedure: Measure the Density of Water

Step 1: Measure the net weight of the 10 ml graduated cylinder (W_c) ;

Step 2: Measure the total weight of the container filled with water (W_{c+w});

Step 3: With the known volume of the container (V_c), the density of water (ρ_w) can be

calculated as:

$$\rho_w = \frac{W_{c+w} - W_c}{V_c} \qquad\qquad\qquad\qquad Equation\ 6$$

2nd Procedure: Measure the Density of Solid Samples

Step 1: Measure the dry weight of the solid sample (W_d);

Step 2: Measure the total of the solid sample in the 10 ml cylinder filled with water (W_t);

Step 3: Measure the surface dry weight of the solid sample (W_s);

Step 4: Calculate the volume of the solid sample (V_s) based on Archimedes' principle:

$$V_s = \frac{W_s + W_{c+w} - W_t}{\rho_w} \qquad\qquad\qquad Equation\ 7$$

Step 5: Calculate the density of solid sample (ρ_s) based on:

$$\rho_s = \frac{W_d}{V_s} \qquad\qquad\qquad\qquad Equation\ 8$$

Step 6: Calculate the porosity of solid sample (P_s) based on:

$$P_s = \frac{W_s - W_d}{\rho_w} \qquad\qquad\qquad\qquad Equation\ 9$$

2.2.2   Elastic Properties

Three elastic properties: dynamic Young's modulus (E), shear modulus (G), and Poisson's ratio (υ), were determined by measuring the fundamental resonant frequency (f) of test specimens by impulse excitation vibration technique as prescribed in ASTM C1259-08. In this procedure, an elastic ceramic sample is tapped lightly with a small impulse tool, causing the solid to vibrate at its natural frequencies. Although an elastic solid can vibrate in several modes simultaneously (flexural, torsional, and longitudinal), the sample is supported and struck in such a way that only one mode of vibration is prevalent. The schematic diagram of the testing facility of Buzz-O-Sonic in Ceramic Membrane Research Lab (CMRL) is shown in Figure 13.
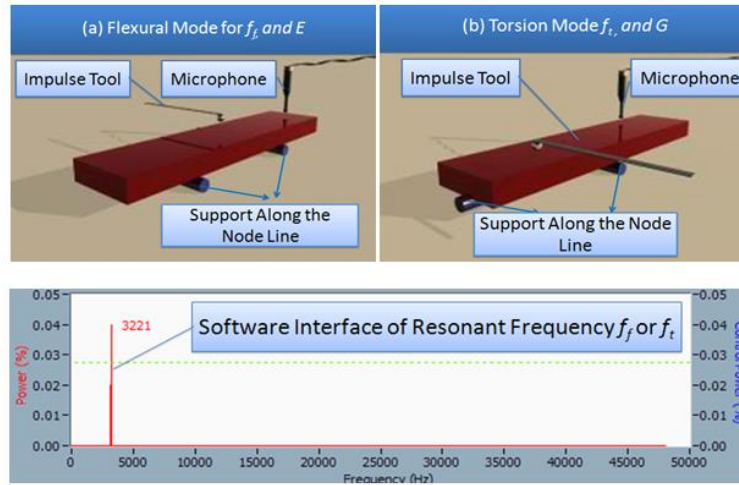
Figure 13: **Schematics of the Modes of Vibration and a Clean Spectrum for Elastic Properties Investigation by Impulse Excitation Technique**

Test environments were set at ambient temperature and at a high temperature. The system setup and specimen measurement of elastic properties at room temperature are shown in Figure 14.

The elastic properties can be calculated based upon observed resonant frequencies and on the measured geometry and mass of the specimens, as given below:

Dynamic Young's modulus (E) is calculated as [29]:

$$E = 0.9465 \left(\frac{m f_f^2}{b}\right)\left(\frac{L^3}{t^3}\right) T_1 \qquad\qquad \text{Equation 10}$$

where,

E = dynamic Young's modulus, Pa

m = mass of the bar, g

b = width of the bar, mm

L = length of the bar, mm

t = thickness of the bar, mm

f_f = fundamental resonant frequency of the bar in flexure, Hz,

T_1 = correction factor for fundamental flexural mode to account for finite

thickness of bar, Poisson's ratio, etc. If $L/t \geq 20$, T_1 can be calculated as:

$$T_1 = 1.00 + 6.585 \left(\frac{t}{L}\right)^2$$

Equation 11

Shear modulus (G) is calculated as [29] :

$$G = \frac{4Lmf_t^2}{bt} R$$

Equation 12

where,

G = dynamic shear modulus, Pa

m = mass of the bar, g

b = width of the bar, mm

L = length of the bar, mm

t = thickness of the bar, mm

f_t = fundamental resonant frequency of the bar in torsion, Hz,

$$R = \left[\frac{1+\left(\frac{b}{t}\right)^2}{4-2.521\frac{t}{b}\left(1-\frac{1.991}{e^{\pi\frac{b}{t}}+1}\right)}\right]\left[1+\frac{0.00851b^2}{L^2}\right] - 0.060 \left(\frac{b}{L}\right)^{\frac{3}{2}} \left(\frac{b}{t}-4\right)^2$$

Equation 13
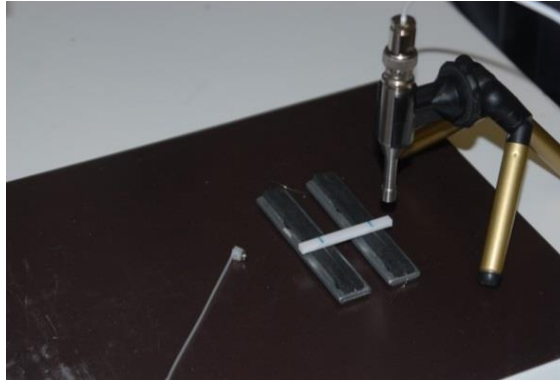
Figure 14:   Specimen Setup for Elastic Properties Measurement at Room Temperature

Poisson's ratio (υ) is calculated as [29]:

$$v = \left(\frac{E}{2G}\right) - 1$$

Equation 14

34

where,

υ = Poisson's ratio

E = dynamic Young's modulus, Pa

G= dynamic shear modulus, Pa

Measurement of dynamic Young's modulus was also made at elevated temperatures to 850°C by a customized E-test furnace, as shown in Figure 15 and Figure 16. The specimens were conditioned and tested for E-value in the E-test furnace for three stages (Figure 17):

1st Heating Stage: Samples were heated and tested every 2 minutes from room temperature to the designated temperature of 850°C.

2nd Dwelling Stage: Samples were dwelled and tested at the target temperature for 2 hours;

3rd Cooling Stage: Samples were cooled to room temperature and tested.

The calculated dynamic Young's modulus (E_t) was corrected for thermal expansion effects using the following equation [29]:

$$E_t = E_0 \left[\frac{f_t}{f_0}\right]^2 \left[\frac{1}{1+\alpha\Delta t}\right] \qquad\qquad Equation\ 15$$

where,

E_t = dynamic Young's modulus at temperature T, Pa

E_0 = dynamic Young's modulus at room temperature, Pa

f_t = fundamental resonant frequency at temperature T, Hz

f_o = fundamental resonant frequency at room temperature, Hz

α = average linear thermal expansion (mm/mm.°C) from room temperature to test temperature

Δt = temperature differential in °C between test temperature T and room temperature
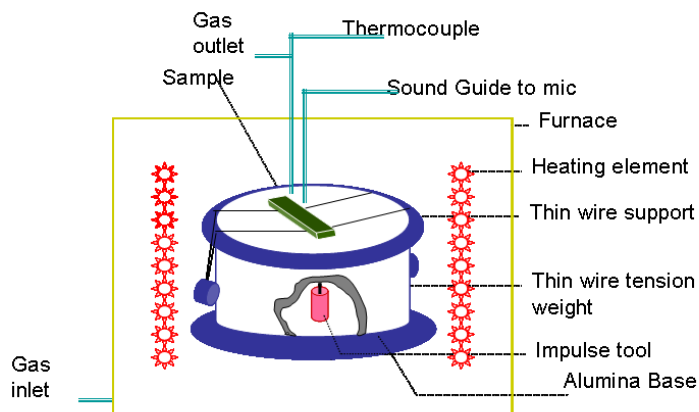
Figure 15:   Schematic Diagram of High Temperature Equipment Setup for Young's Modulus (E) Measurement

(a) System Setup for Young's Modulus Measurement at High Temperature

(b) Specimen Setup for Young's Modulus Measurement at High Temperature
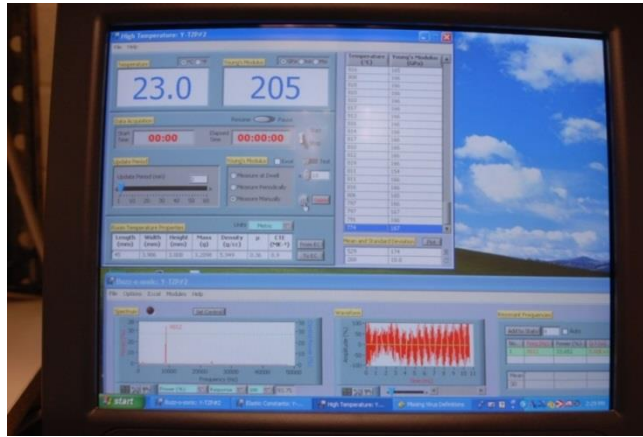
(c) Computer Interface of Buzz-O-Sonic Software for High Temperature Module

Figure 16: **Actual Equipment & Specimen Setup and Buzz-O-Sonic Software Interface for Young's Modulus Measurement at Elevated Temperature**
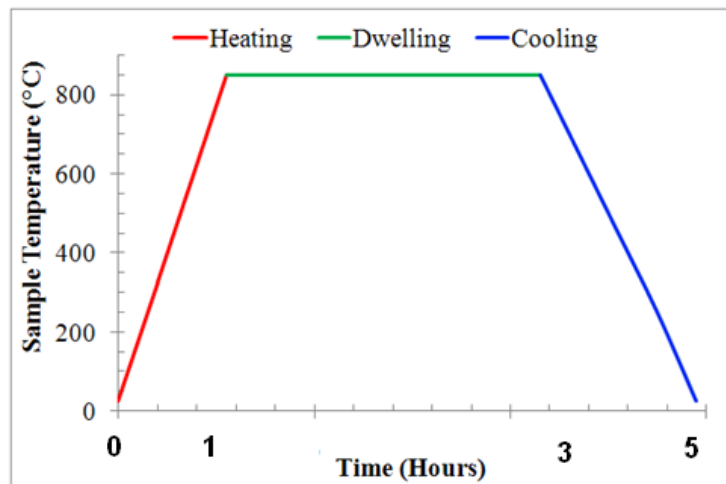
Figure 17: **Schematic Diagram of Temperature-Time Frame for E-test at Elevated Temperature**

2.2.3 Vickers Hardness Number (HV)

Vickers hardness number (*HV*) is calculated by dividing the applied force by the surface area of the permanent impression as designated in ASTM C1327 and E384. A Vickers indenter is the square-based, pyramidal-shaped, diamond indenter with face angles of

136°00' shown in Figure 18. Due to its simplicity, nondestructive nature, and minimal machining requirement, the Vickers hardness test is generally used to characterize many properties of advanced ceramics [30]. Vickers hardness number can be calculated as [30]:

$$HV = 0.0018544 \left(\frac{P}{d^2}\right) \hspace{4cm} Equation\ 16$$

where,

HV = Vickers hardness number in GPa

P = load, N

d = average length of the two diagonals of the indentation, mm

The mean hardness $\overline{HV}$ is calculated as:

$$\overline{HV} = \frac{\sum HV_n}{n} \hspace{4cm} Equation\ 17$$

where,

HV_n = Vickers hardness number obtained from n^{th} indentation, GPa

n = total number of indentations

The standard deviation, S, is calculated as

$$S = \sqrt{\frac{\sum(\overline{HV} - HV_n)^2}{n-1}} \hspace{3cm} Equation\ 18$$
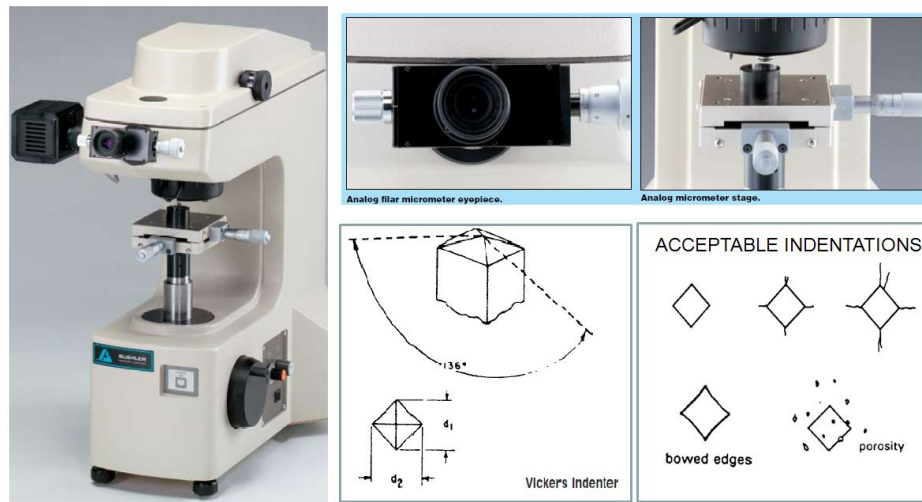
Figure 18:   Buehler Vickers Hardness Indentation and Indenters

38

For tracking the indentation on the specimens, suggested lab procedures are illustrated in Figure 19.

1. Mark on the polished surface using a marker pen

2. Give the indentation in a pattern (at a particular load) closer to the ink mark

3. It is easy to locate the ink mark in microscope than the indentation mark
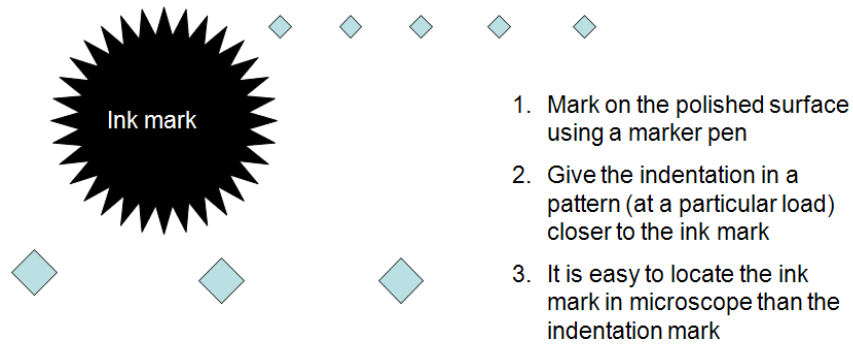
Figure 19:   Lab Procedures to Track Indentations on Specimens

Vickers hardness tests were conducted at several different applied loads (100, 200, 300, 500, and 1000g) for a period of 15s. After completion of the Vickers hardness test, an indentation image was captured with an Olympus BX 60 Microscope (Figure 20).
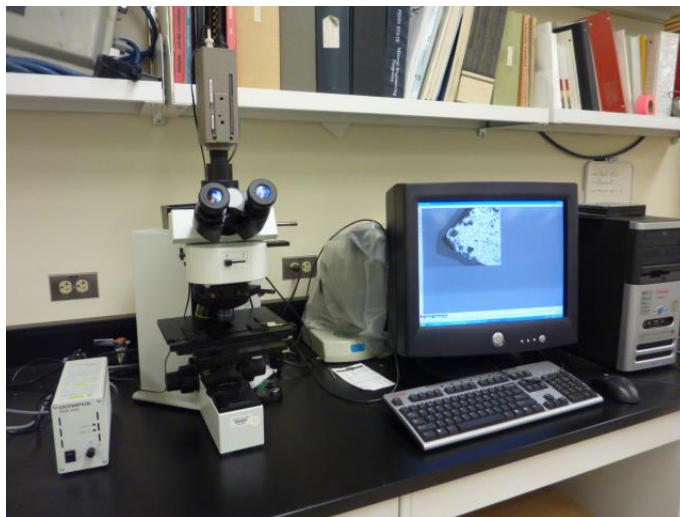
Figure 20:   Olympus BX 60 Light Microscope

2.2.4   Modulus of Rupture (MOR) or Flexural Strength (σ_{fs})

As designated in ASTM C1161, flexural strength (σ_{fs}), also known as modulus of rupture

(MOR), bending strength, or fracture strength, is a measure of the ultimate strength of a specific beam in bending. The flexural strength test is a reasonable substitute for the tensile strength (σ_T) of ceramic materials. The geometry of test specimens used for the research are rectangular bars that conform to the ASTM MOR Bar Type-A or Type-B, as shown in Figure 21.

(a) Type-A MOR Bar
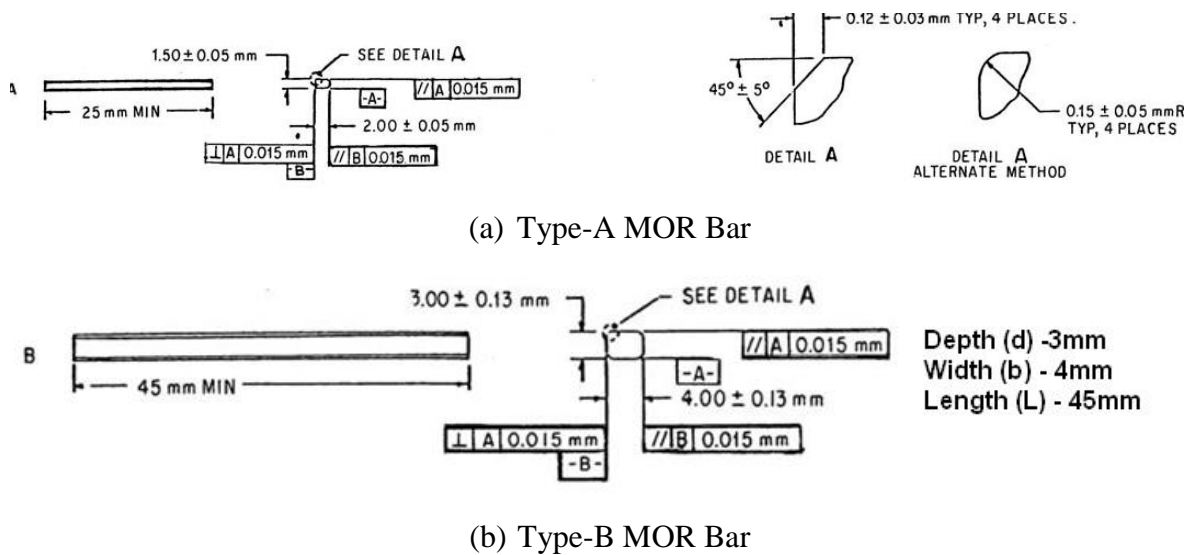
(b) Type-B MOR Bar

Figure 21:   Geometry Diagram for ASTM Type-A (a) and Type-B (b) MOR Sample Bar for Flexural Strength Test

A free body diagram (FBD) of the applied test for the HTM sample bar (Type-A MOR Bar) is schematically presented in Figure 22. This configuration is known as the "four-point bending," and produces uniform bending moment (M) over the center section of the beam, as illustrated in Figure 22. Since the maximum tensile stress occurs at the bottom of the beam, the standard formula for calculating the flexural strength of a beam in a four-point-1/4 point flexure is:

$$\sigma_{fs} = \frac{3PL}{4bd^2}$$

Equation 19

where,

σ_{fs} = flexural strength or stress (MPa)

P = break force (N)

L = length of the bar, mm

b = width of the bar, mm

d = thickness of the bar, mm

The mean flexural strength, $\overline{\sigma_{fs}}$, is calculated as:

$$\overline{\sigma_{fs}} = \frac{\Sigma \sigma_n}{n}$$
Equation 20

where,

σ_n = flexural strength obtained from n^{th} test (MPa)

n = total number of flexural tests

The standard deviation, SD, is calculated as

$$SD = \sqrt{\frac{\Sigma(\overline{\sigma}-\sigma_n)^2}{n-1}}$$
Equation 21

In order to verify the crack origin and its positioning, a diagram was plotted (Figure 23) for a numerical positioning of the crack origin. Fracture patterns were recorded according to the commonly observed fracture patterns [31] illustrated in Figure 24. Breaks outside the inner gage section that occur due to misalignment or error were not included in the calculations.
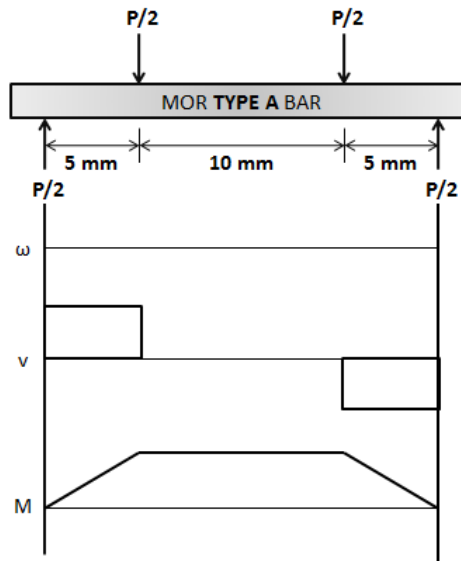
Figure 22: **Free Body Diagram (FBD) of the 4-Point Bending Type-A MOR Bar**
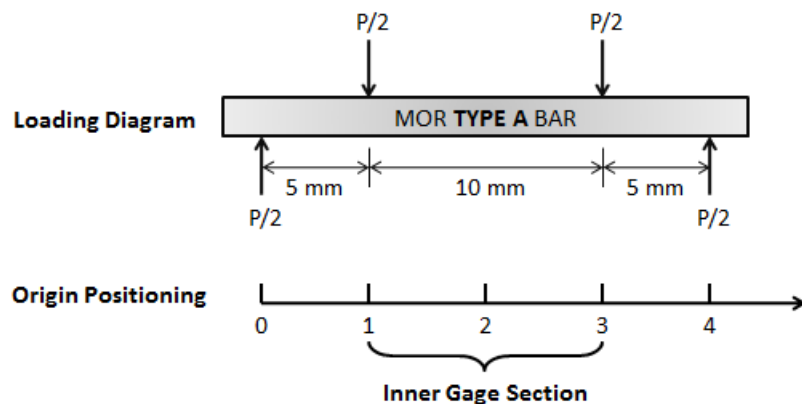
Figure 23: **Diagram for Positioning the Crack Origin for Type-A MOR Bar after Flexural Strength Test**

(a) Low Energy Failure

42

A SECONDARY FRACTURE CAUSED BY THE ELASTIC RELEASE WAVE - REFLECTION OFF OF THE END FACES.

NOTE THIS OFTEN OCCURS AT LOAD PINS.

NOTE THE MIRROR IS ON WHAT ORIGINALLY WAS THE COMPRESSION SIDE.

SECONDARY BREAK - OFTEN AT AN ANGLE

PRIMARY FRACTURE - ORIGIN

SECONDARY FRACTURE AT A LOAD PIN

PRIMARY - ORIGIN NEAR, BUT NOT DIRECTLY AT A LOAD PIN

BREAK AT OR NEAR LOAD PIN. BEWARE OF MISALIGNMENTS OR TWISTING ERRORS

NOTE ANGLE TO TENSILE SURFACE

(b) Medium High Energy Failure

CRACK BRANCHES AND CURVES BACK TO TENSILE FACE

SECONDARY BREAK

ORIGIN

HIGH ENERGY FAILURE
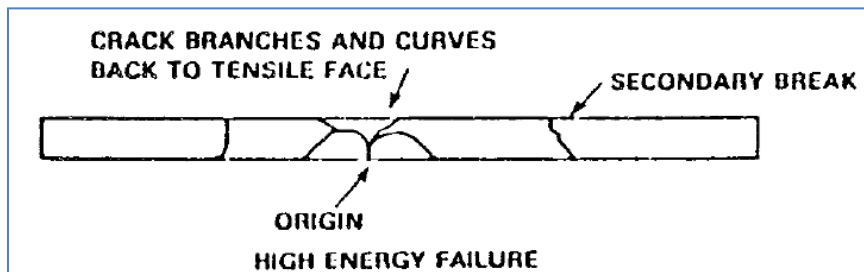
(c) High Energy Failure

Figure 24:   Typical Fracture and Cracks of Flexural Specimens [11]

The strength distribution of the reference material is described by a Weibull distribution

as [32]:

$$f(x) = m(x)^{m-1} exp(-x^m) \qquad \qquad Equation\ 22$$

Where, $f(x)$ is the frequency distribution of the random variable x and m is the shape factor (usually referred to as the Weibull modulus). The random variable x is defined as σ/σ_0, where σ is the failure stress (MPa) and σ_0 is a normalizing parameter. Replacing the x by σ/σ_0 in Equation 22, the survival probability (S), the fraction of samples that would survive a given stress level can be derived as:

$$S = \int_{\frac{\sigma}{\sigma_0}}^{\infty} f\left(\frac{\sigma}{\sigma_0}\right) d\left(\frac{\sigma}{\sigma_0}\right) \qquad \qquad Equation\ 23$$

or

$$S = exp\left[-\left(\frac{\sigma}{\sigma_0}\right)^m\right] \qquad \qquad Equation\ 24$$

Taking the natural log of both sides in Equation 24 twice yields:

$$lnln\frac{1}{S} = mln\frac{\sigma}{\sigma_0} = mln\sigma - mln\sigma_0 \qquad \qquad Equation\ 25$$

Or

$$-lnln\frac{1}{S} = -mln\frac{\sigma}{\sigma_0} = -mln\sigma + mln\sigma_0 \qquad \qquad Equation\ 26$$

Where σ_0 is the stress level at which the survival probability is equal to 1/e, or 0.37. For a total N number of samples, the survival probability of the ranked j^{th} specimen is statistically calculated as [32]:

$$S_j = 1 - \frac{j-0.3}{N+0.4} \qquad \qquad Equation\ 27$$

By plotting $-lnln(\frac{1}{S})$ versus $ln\sigma$, the least-squares fit to the resulting line, the Weibull modulus (m-value) can be calculated. With an increase of the Weibull modulus m, more uniformity of the microstructure is expected, although the material specimen may be very weak. In the Ceramic Membrane Research Lab (CMRL) at UAF, an in-house custom-designed loading scheme and force measuring system (Figure 25) was used to measure σ_{fs} at various ranges of temperature. The specimens with dimensions of Type-A or Type-B MOR bars were selected and tested in situ in an autoclave mounted on the servo-electric loading frame shown in Figure 25 (a). The loading of the specimen was done on a

Type-A or Type-B 4-point bending fixture, as shown in Figure 25 (b) and (c) respectively.

(a) In-House Autoclave Setup
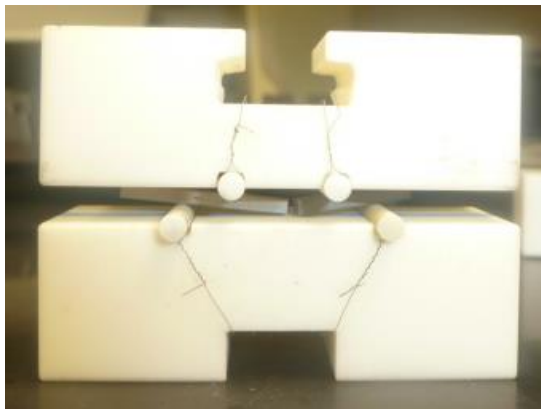
(b) Type-A 4-Point Bending Fixture   (c) Type-B 4-Point Bending Fixture
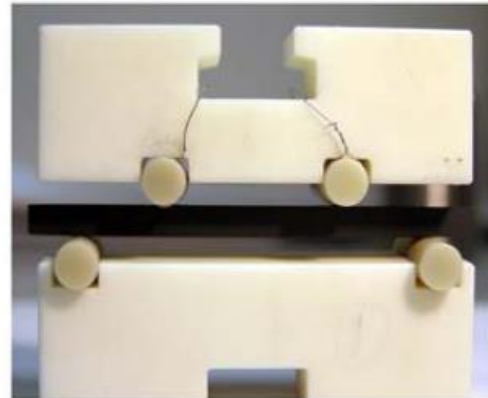
Figure 25:   **In-House Designed Autoclave and 4-Pointe Bending Fixtures Used for Flexural Strength and Slow Crack Growth (SCG) Tests**

2.2.5   Residual Stress by XRD $\sin^2\psi$ Technique

Residual stress is stress that remains after its original cause (external forces, heat gradient) has been removed [33]. X-ray diffraction (XRD) $\sin^2\psi$ technique was employed to measure the residual stress of the samples, based on the principle as illustrated in Figure 26 [34]. Angle ψ defines the angle between the normal of the surface and the incident (S)

and diffracted (D) beam bisector. Figure 26 (a) shows that the presence of a tensile stress ($\psi=0°$) in the sample reduces the lattice spacing, which slightly increases the diffraction angle 2θ. Figure 26 (b) shows that the tensile stress ($\psi>0°$) present in the material increases the lattice spacing, which decreases the diffraction angle 2θ. Because the X-ray diffraction stress measurement is confined to the surface of the sample, a plane-stress elastic model in Figure 27 could be assumed to exist for the studied material [34].

The definition of the angles psi (ψ) and phi (φ) are shown in Figure 28. The stress and strain at a point p under investigation can be obtained with the aid of the stress and strain ellipsoids in Figure 28.

(a) $\Psi=0$	(b) $\Psi=\psi$ (Sample rotated angle ψ)
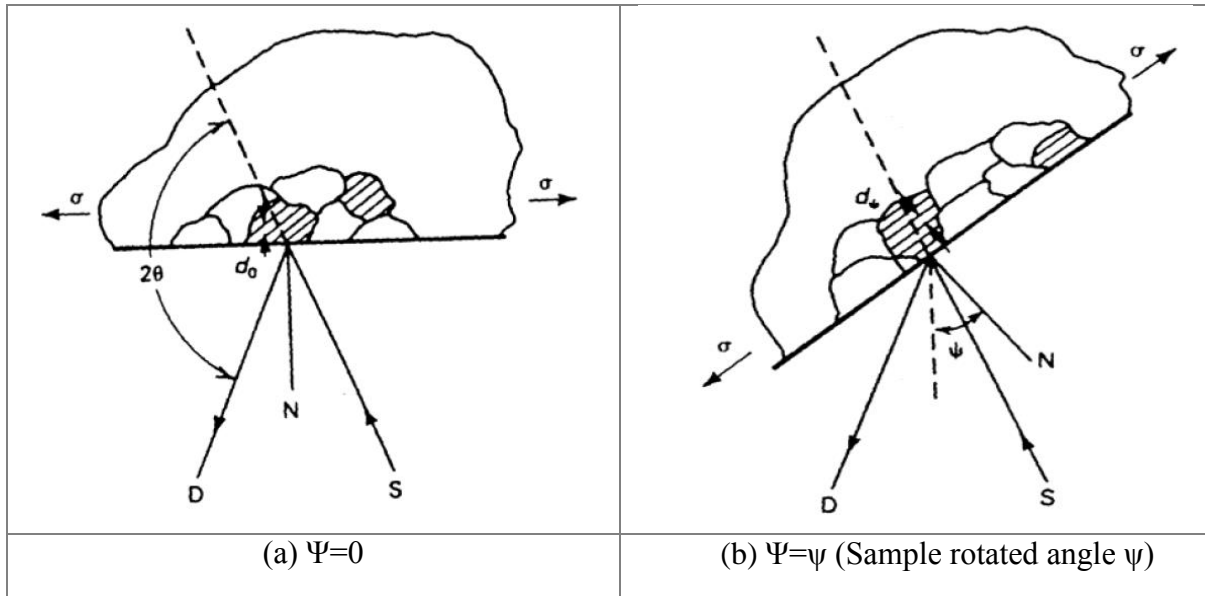
Figure 26:   Diagram of the Principle of Residual Stress Measurement by X-ray Diffraction (XRD) sin²ψ Technique (D, X-ray Detector; S, X-ray Source; N, Normal to the Surface) [34]

From strain transformation and the angles shown in Figure 28, the normal strain $\varepsilon_{\varphi\psi}$ is given by the following equation [35]:

$$\varepsilon_{\varphi\psi} = \varepsilon_1\alpha_1^2 + \varepsilon_2\alpha_2^2 + \varepsilon_3\alpha_3^2 \qquad\qquad \textit{Equation 28}$$

where,

$$\alpha_1 = \cos\varphi\sin\psi$$

$$\alpha_2 = sin\,\varphi\,sin\,\psi$$

$$\alpha_3 = cos\,\psi = \sqrt{1 - sin\,^2\psi}$$
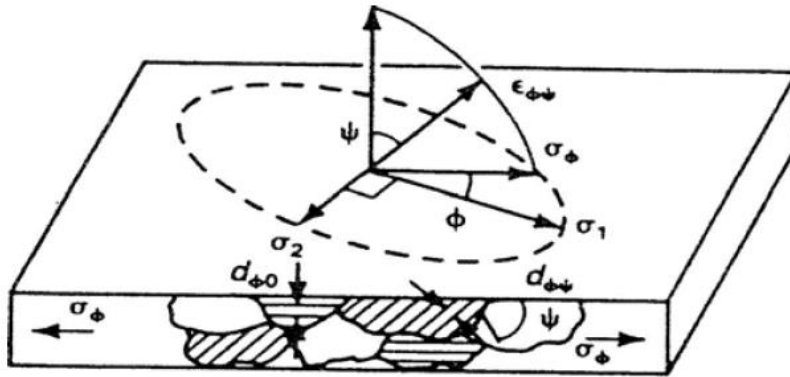
Figure 27: **Plane-Stress Elastic Model for Residual Stress Measurement [34, 36]**
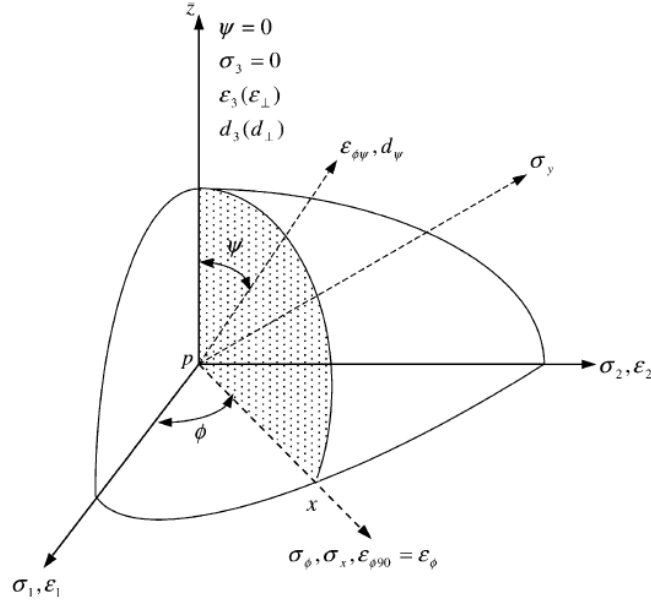
Figure 28: **Stress and Strain Ellipsoids at the Point p [34, 35]**

The strain $\varepsilon_{\varphi\psi}$ in the direction defined by the angles φ and ψ is then [34]:

$$\varepsilon_{\varphi\psi} = \left[\frac{1+\upsilon}{E}(\sigma_1\,cos\,^2\varphi + \sigma_2\,sin\,^2\varphi)\right] - \left[\frac{\upsilon}{E}(\sigma_1 + \sigma_2)\right] \qquad \textit{Equation 29}$$

And

$$\sigma_\varphi = \left(\sigma_1 \cos{}^2\varphi + \sigma_2 \sin{}^2\varphi\right) \qquad\qquad \textit{Equation 30}$$

Substitution of Equation 30 into Equation 29 results in an equation that can be used to calculate the residual stress:

$$\varepsilon_{\varphi\psi} = \left[\frac{1+v}{E}\sigma_\varphi\right] - \left[\frac{v}{E}(\sigma_1 + \sigma_2)\right] \qquad\qquad \textit{Equation 31}$$

And the strain could be expressed in terms of the changes in the linear dimensions of the crystal lattice:

$$\varepsilon_{\varphi\psi} = \frac{\Delta d}{d} = \frac{d_{\varphi\psi} - d_0}{d_0} = \left[(\frac{1+v}{E})_{hkl}\sigma_\varphi\right] - \left[\left(\frac{v}{E}\right)_{hkl}(\sigma_1 + \sigma_2)\right] \qquad \textit{Equation 32}$$

Because $E \gg (\sigma_1 + \sigma_2)v$, the σ_φ may be calculated using the following formula:

$$\sigma_\varphi = \left(\frac{E}{1+v}\right)_{hkl}\frac{1}{d_{\varphi 0}}\left(\frac{\partial d_{\varphi\psi}}{\partial \sin{}^2\psi}\right) \qquad\qquad \textit{Equation 33}$$

where,

E is the modulus of elasticity,

v is Poisson's ratio

$d_{\varphi 0}$ is the unstressed lattice spacing

By assuming the existence of plane-stress elastic model conditions as shown in Figure 27, the residual stress is calculated by using Equation 33. The residual stress can be determined by measuring the lattice spacing for multiple ψ tilts. A straight line is fitted by least-square regression, and the stress is calculated from the slope of the best fit line using Equation 33[34]. The maximum and minimum normal residual stresses, shown as σ_1 and σ_2 in Figure 27 and Figure 28, and their orientation relative to a reference direction can be calculated using Mohr's circle for stress if the stress σ_φ is determined for three different values of φ based on Equation 30.

The effects of the average crystallized grain size (τ) on Bragg peak broadening (β, in radians) can be calculated as a first approximation by [37]:

$$\tau = \frac{\lambda}{\beta \cos\theta}$$
<div align="right">*Equation 34*</div>

where,

β - the peak's full width at half maximum (FWHM), radians

λ - is the wavelength, in the case of Cu Kα_1, λ=0.15916nm

θ - Bragg angle

Collected with a PANalytical X'Pert PRO Materials X-ray Diffractometer using Cu Kα radiation in a continuous scanning mode with preset parameters varied for different crystalline material, this diffraction pattern of the residual stress will be discussed with the results of residual stress measurement.

2.3   Laboratory Investigation for Thermal Properties

2.3.1   Coefficient of Thermal Expansion (CTE)

For isotropic material (such as ceramic), the coefficient of thermal expansion (CTE) can be estimated by measuring the linear thermal expansion. Thermo-dilatometry is a technique that measures a length of a substance under negligible load as a function of temperature. A single pushrod tube-type dilatometer such as the Netzch DIL 402 PC (Figure 29) can be used to determine CTE under the linear thermal expansion for isotropic materials. The CTE sample is heated from 50 °C up to 1200°C at a rate of 3°C/min in a single pushrod dilatometer.

Instantaneous CTE-value at a temperature T is defined as [38]:

$$\alpha_t = \frac{1}{L_0}\left(\frac{dL}{dT}\right)_T$$
<div align="right">*Equation 35*</div>

where,

α_t = instantaneous coefficient of linear thermal expansion at any temperature T (μm/mm.°C)

L_0 = original length of specimen at temperature T_0, mm

Mean CTE-value for a range of temperatures is defined as [38]:

$$\alpha_m = \frac{1}{L_0}\frac{\Delta L}{\Delta T}$$

Equation 36

where,

α_m = mean coefficient of linear thermal expansion (μm/mm.°C)

L_0 = original length of specimen at temperature T_0, mm

ΔL = change in length of specimen between any two temperatures, μm

ΔT = temperature difference, °C
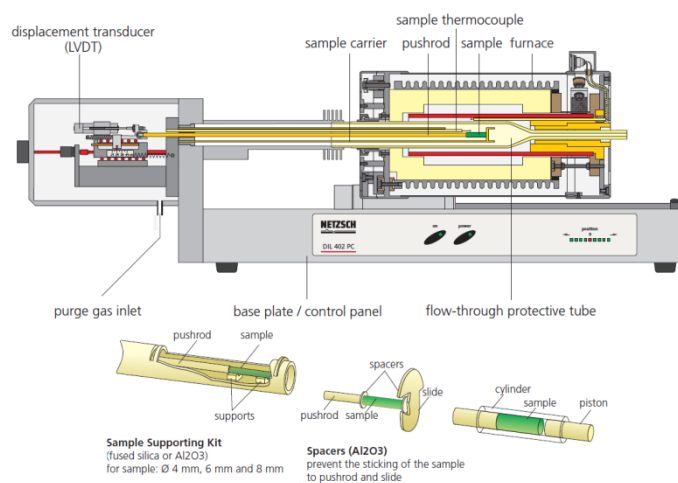
Figure 29:   Netzch DIL 402PC Dilatometer and Single Pushrod Tube

2.3.2   Thermogravimetry/Differential Thermal Analysis (TG/DTA)

TG analysis and DTA were simultaneously performed on the samples by a simultaneous TG/DTA analyzer (Perkin Elmer Diamond TG/DTA), as shown in Figure 30, in both air or in the inert nitrogen (N$_2$). Inert gas of nitrogen (N$_2$) was introduced as a purge gas at a rate of 200 ml/min by an input gas control system, as shown in Figure 31. The Perkin

50

Elmer Diamond TG/DTA analyzer was connected directly to a computer-controlled system with Pyris software v 6.0 to control the testing parameters.
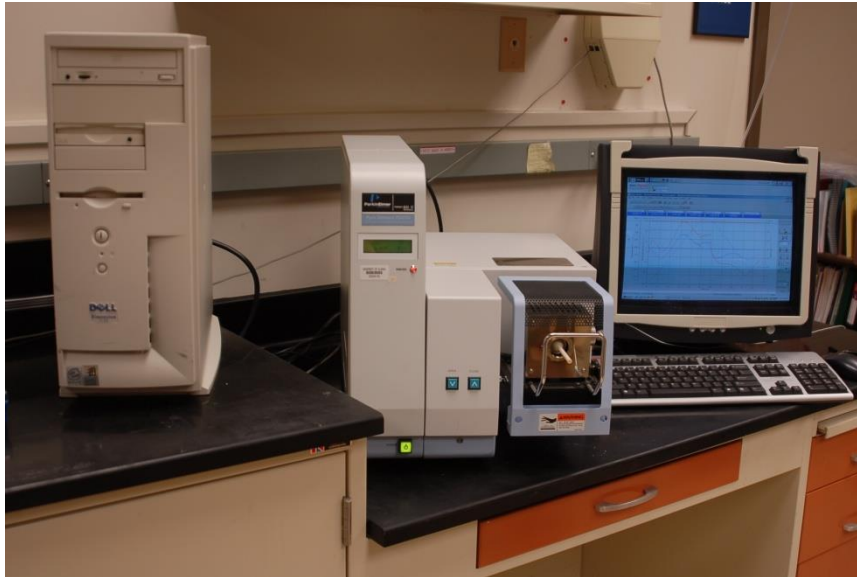
Figure 30:   Perkin Elmer Diamond TG/DTA Analyzer and the PC with Pyris v6.0

Figure 31:   Omega Gas Flow-Rate and Temperature Control System

2.4   Laboratory Investigation for Microstructural Properties

2.4.1   Fractography Analysis

As specified in ASTM C1322, subsequent to the flexural tests of the sample, the mating halves were preserved and a fractography analysis was conducted according to the

procedures shown in the . Segments of the samples with fracture were sectioned longitudinally. They were then cleaned with acetone in the Branson 2510 ultrasonic cleansing system. These fracture portions, both fracture surface and bottom surface, were then analyzed and observed, as illustrated in . Then, the samples were visually inspected with an Olympus BX 60 microscope at maximum magnification of 50X. Finally, the fractured portions of the mating halves were sputter-coated with carbon or Pd-Au coating for SEM observations.

Store the mating halves after flexural strength tests

Section the fracture parts from mating halves and clean by ultrasonic system

Visually inspect the fracture surface and evaluate crack patterns and general location of fracture origin

Examine the fracture surface by Olympus BX60 microscope at 5-50X magnification

Examine the fracture surface by IRIS SEM at 100-2500X

Figure 32: Fractography Analysis Procedures

With a focused beam of high-energy electrons, SEM systematically scans the surface of the specimen. The ISI-SR-50 (Figure 34) with a SEM column and specimen chamber can be operated from 2–30kv and can achieve sub-50nm resolution.

This microscope is generally used to visualize and understand: (1) surface morphology of

52

solid-state specimens; (2) elemental tracing and analysis for a certain area; (3) pore size distribution and surface porosity estimation, and for this thesis (4) fractography or characterization of fracture origins in solid-state advanced ceramics.
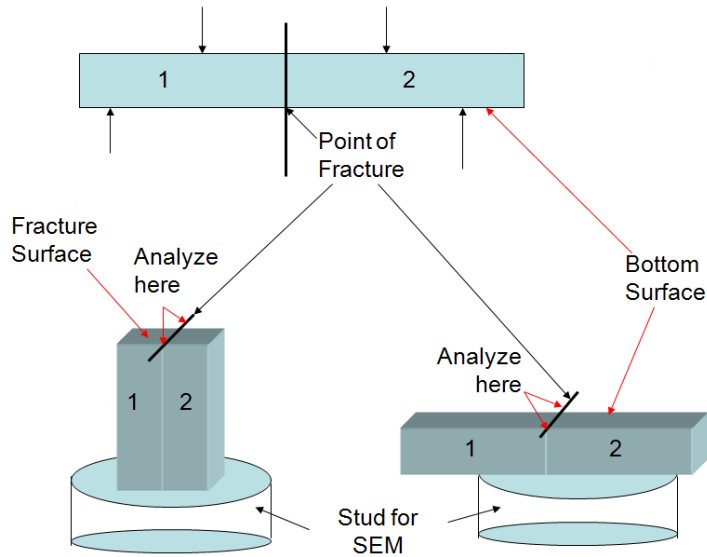
Figure 33: **Diagram of Fractographic Inspection for Mating Halves of Tested Bar after Flexural Strength Test**

Figure 34: **Scanning Electron Microscope (SEM) ISI-SR-50 Automated with iXRF Software/Hardware and EDS Detector**

The samples for SEM tests were prepared by sputter coating with either Au-Pd for the structural ceramics or carbon for HTM samples. The current beam was set at 15–30kv with a working distance (WD) ranged from 10mm to 40mm and the magnifications ranged from 40X up to 10000X. Scanning Electron Microscopy–Energy Dispersive Spectroscopy (SEM-EDS) was used to elementally analyze the chemical composition of the specimen by means of X-ray spectrum acquisition and X-ray mapping.

2.4.2   Phase Analysis and Surface Texture Analysis

X-ray Diffraction (XRD) technology is a widely accepted method to study the crystal structure of mineral and crystal material. For HTMs or other thin-film or membrane composite material, XRD techniques were used to determine: (1) phase identification and semi-quantitative analyses; (2) surface texture; and (3) residual stresses for the HTM cermet both as-received and after thermal cycling treatment. The geometrical illusion of Braggs' Law and its equation is displayed as Figure 35. Braggs' law is the basic principle for employing XRD to determine the lattice parameters for any crystal material.

The PanMRD X'Pert PRO X-ray diffraction (K_αCu Radiation) system (Figure 36) was used as the basic platform for various applications, including phase analysis, texture measurement, and residual stress measurements on HTM cermet and substrate materials.

Specifically, the graded multilayer parabolic X-ray mirror (Figure 37) was used as a special kind of beam conditioner for its ability to convert the divergent X-ray beam from a line focus tube to an intense monochromatic quasi-parallel beam. The mirror was applied for measurements at a fixed angle of incidence (ω) on thin film for the purposes of reflectivity measurement, phase identification, layer structural analysis, thickness estimation, and surface texture analysis.

$$2d_{hkl}\sin\theta_{hkl} = n\lambda$$
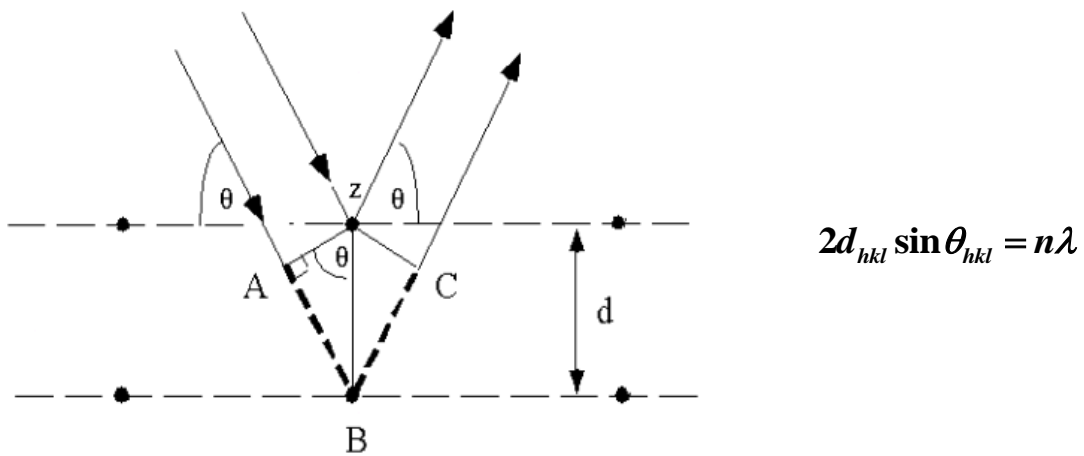
Figure 35:   Geometrical Illustration of Braggs' Law and its Equation

Figure 36:   PANalytical PW3040/60 X'Pert PRO Instrument Enclosures
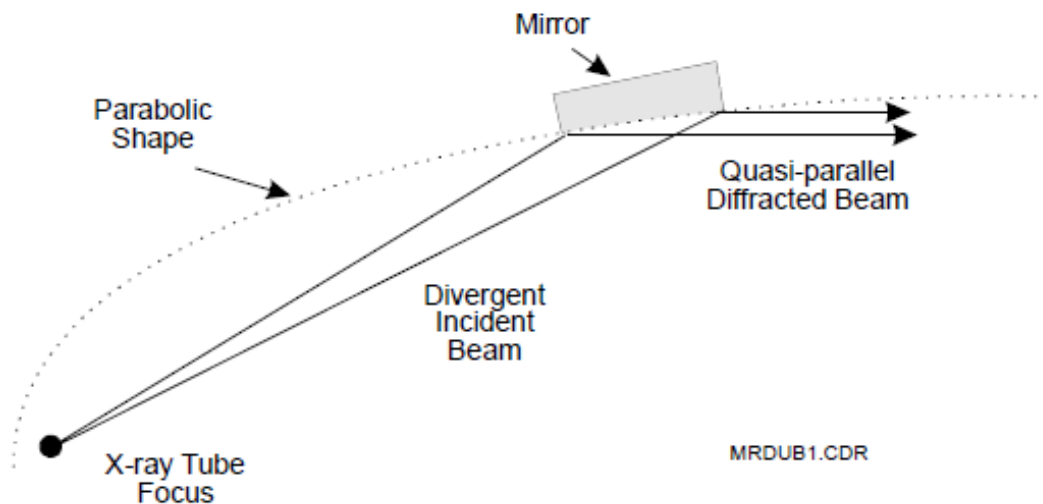
Figure 37:   Graded Multilayer Parabolic X-ray Mirror

Texture is seen in almost all engineered materials and can greatly influence material properties [39]. For this thesis, texture was initially analyzed for the distribution of crystallographic orientations of a polycrystalline reference sample. This was accomplished by using a pole figure, in which a specified crystallographic axis (or pole) from each of a representative number of crystallites was plotted in a stereographic projection shown in Figure 38 and Figure 39[40].
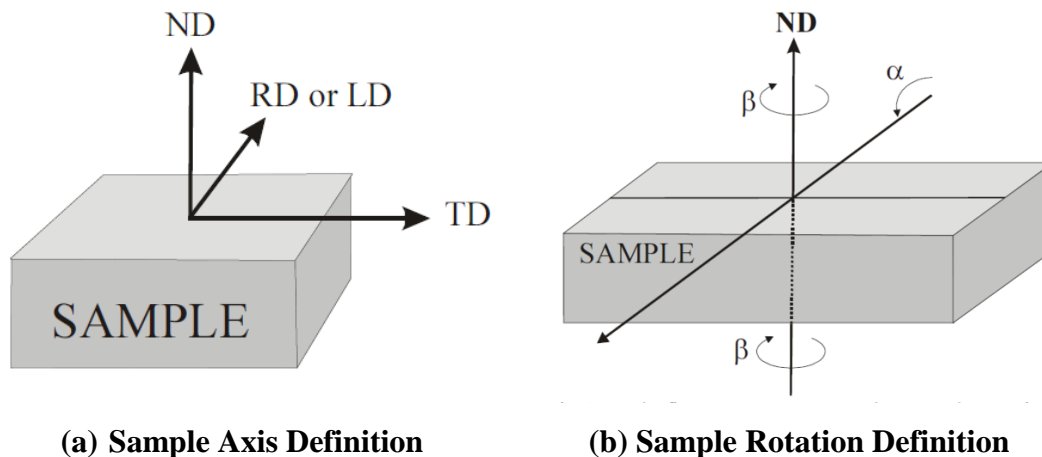
(a) Sample Axis Definition   (b) Sample Rotation Definition

Figure 38:   Axis Definition for Pole Figure Measurement [40]

Pole figures were then characterized by rotating α (or ψ) and β (or φ), where parameter

56

value of α (or ψ) was set to range from 0° at the center to 90° at the edge, and parameter value of β (or φ) was set to range from 0° to 360°.
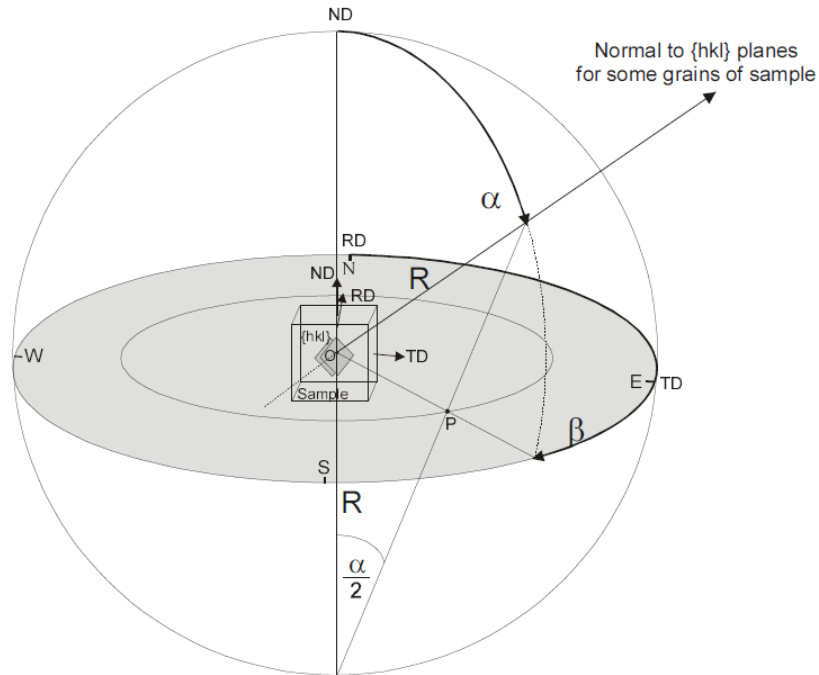
Figure 39:   **Principle of Using Stereographic Projection to Create Pole Figure [40]**

2.4.3   X-ray Spectrometry Analysis

Elemental composition analysis and semi-quantitative analysis were performed by the Panalytical Axios four kilowatt wavelength X-ray florescence (XRF) shown in Figure 40 and the electron microprobe Cameca SX50 that is equipped with EDAX energy dispersive spectrometers (EDS) shown in Figure 41.

The hardware and software configuration are summarized in Table 9 for the system used. The electron beam conditions of the EDS spectrometry were selected by changing the beam accelerating voltage (in keV) and the beam size (in μm) as shown in Table 10.

57

Figure 40: **Panalytical Axios Four Kilowatt Wavelength Dispersive Spectrometer (WDS) X-ray Florescence (XRF)**

Figure 41: **CAMECA SX-50 Electron Microprobe with EDAX EDS System**

2.5 Laboratory Investigation for the Effect of Thermal Cycling on both Microstructural and Mechanical Properties

Failure as a result of rapid heating or cooling is known as thermal shock. Because of their brittleness and low thermal conductivities, ceramics are prone to thermal shock and will

58

crack when subjected to large thermal gradients [41]. The effect of thermal cycling with a designed time frame (Figure 42) on the mechanical properties and stability of the reference material was investigated using the customized thermal cycling equipment shown in Figure 43.

Table 9:   X-ray Spectrometry Employed for the Research

X-ray Spectrometry	System Model	System Software
X-ray florescence (XRF)	Panalytical Axios XRF system	SuperQ
Energy dispersive spectrometer (EDS)	Cameca SX50 with EDAX EDS system	QuantZAF

Table 10:   Selected Beam Conditions for EDS Spectrometry

No.	Beam Voltage (keV)	Beam Current (nA)	Beam Size (µm)
1	5	20	1
2	10	20	1
3	15	20	1
4	20	20	1
5	15	20	5
6	15	20	10
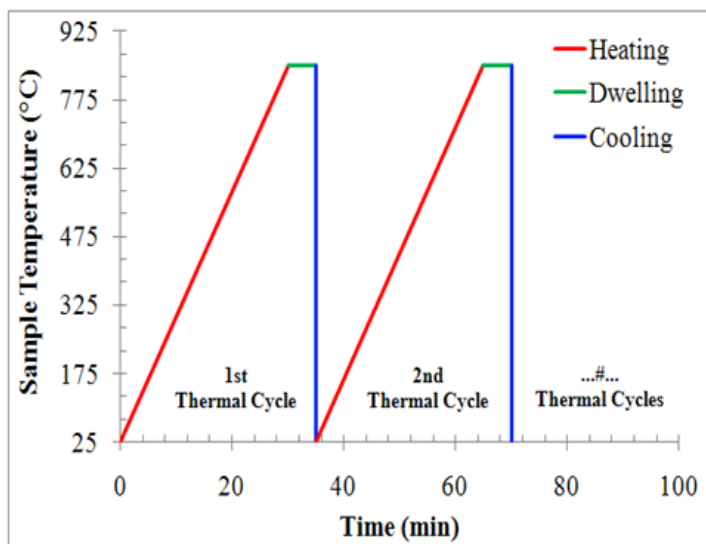
Figure 42: **Diagram of Time Frame and Sample Temperatures for Thermal Cycling Processes**

Figure 43: **Customized Thermal Cycling Furnace Designed by Carbolite Inc.**

CHAPTER III: CHARACTERIZATION OF MICROSTRUCTURAL AND THERMO-MECHANICAL PROPERTIES OF HTM CERMET

3.1   Characterization of Physical and Mechanical Properties

3.1.1   Bulk Density and Porosity Measurement

The average density of the HTM cermet sample was evaluated at ambient temperature based on Archimedes' principle. The calculated density of this novel HTM cermet is approximately 11.3 g/cc, as shown in Table 11. The estimated porosity of 0% revealed that HTM cermet is visually dense material.

Table 11:   Estimated Density and Porosity for HTM Cermet Material

Sample ID	W_d (g)	W_t (g)	W_s (g)	V_s (ml)	ρ (g/cc)
HTM-Bar#2	8.35	57.23	8.35	0.69	12.12
HTM-Bar#3	8.22	57.058	8.22	0.79	10.41
Average (*g/cc*)	11.26				

3.1.2   Elastic Properties for HTM As-Received and after Thermal Cycling

The elastic properties of the novel HTM materials were evaluated based on pulse excitation techniques, and the results are shown in Table 12. Though the difference in sample shape can affect the experimental values of elastic modulus (E-value and shear modulus (G-value), the estimated result of Poisson ratio (υ), calculated from both experimental values of E and G, is not affected. Dynamic Young's modulus (E-Value) for the bar-shaped sample is approximately 151 GPa while for the disc-shaped sample the E-value is about 141 GPa. Actual difference (10 MPa) in the E values for the disk and bar-shaped samples is within the range of experimental errors. Young's modulus could, therefore, be averaged as 145.5 MPa for the HTM cermet as-received. The Poisson ratios (υ) are very identical and approximately 0.34 as tested on these two differently shaped

samples. Though the difference in sample shape can affect the experimental values of elastic modulus (E-value) and shear modulus (G-value), the estimated result of Poisson ratio (v), calculated from both experimental values of E and G, is not affected.

Table 12:   Elastic Properties for HTM Cermet As-Received

Sample Shape	Dimension (mm)	Mass (g)	E (GPa)	G (GPa)	Poisson Ratio v
HTM-Bar	37.44 (Length) 6.44 (Width) 3.78 (Thickness)	8.35	150.62	56.40	0.34
HTM-Disc	28.25 (Diagonal) 3.93 (Thickness)	22.24	140.74	52.18	0.35

Effect of thermal cycling on Young's modulus (E-value) was evaluated for the HTM samples, the calculated result are shown in Table 13. Young's modules for the HTM samples did not change significantly due to thermal cycling (up to 500 cycles).

Table 13:   Results of Young's Modules for HTM Cermet with and without Thermal Cycling Treatment

Sample ID	Conditions	Density (mg/m3)	E_{out} (Gpa)	E_{in} (Gpa)	Eav (Gpa)
HTM-Bar#2	As-Received	9.1662	148.80	151.70	150.25
	120 Thermal Cycles	9.1560	147.00	150.90	148.95
	500 Thermal Cycles	9.1560	148.50	151.00	149.75

3.1.3   Vickers Hardness Number (*HV*)

Vickers Hardness (*HV*) numbers were evaluated for the as-received HTM cermet supplied by ANL. Loads were applied at five different forces varying from 100–1000 grams, with each force applied for 15 seconds. The mean calculated HV values ($(\overline{HV})$ are shown in Table 14 and plotted in Figure 44. The $\overline{HV}$ numbers of the as-received HTM cermet average in the range of 2.0 ~ 2.2 GPa, regardless of the loading force. While there is a trend of a decreased $\overline{HV}$ value with increased load (from 100–1000 grams) for the

selected structural alumina 96% material (refer to Chapter 4.1), the $\overline{HV}$ numbers for the HTM cermet was not influenced by the change of loading force. The indentation marks after each loading were observed with an Olympus BX 60 optical microscope in the magnification of 50X, as shown in Figure 45. In contrast to the indentation marks for AL-96, the two direct diagonal diameters are identical at each loading rate, and this is attributed to the isotropic characteristics of the HTM material. The uniform and isotropic character might be the reason for identical $\overline{HV}$ numbers despite changing loading force. With increase of loading force from 100–1000 grams, the diagonal diameter is increased as well, as shown in Figure 45.

Table 14:   Vickers Hardness Number (HV) for HTM Cermet As-Received

Load (g)	Hardness (GPa)	Standard Deviation (GPa)
1000	2.11	0.06
500	2.22	0.10
300	2.02	0.08
200	2.10	0.05
100	2.00	0.16
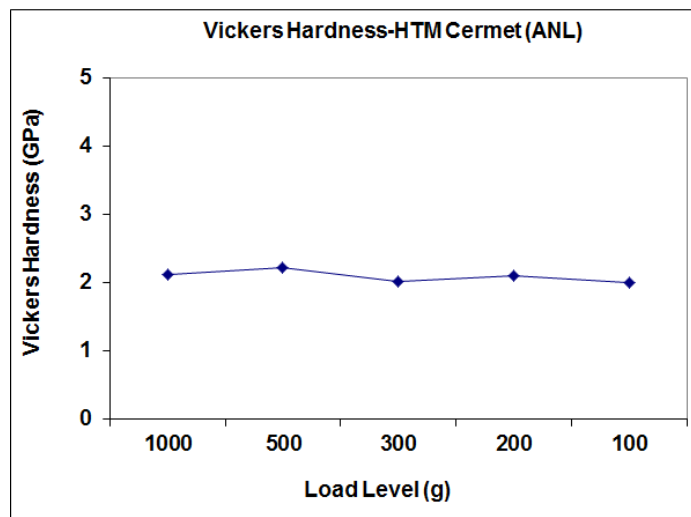
Figure 44:   Vickers Hardness Number ($\overline{HV}$) for HTM Cermet As-Received
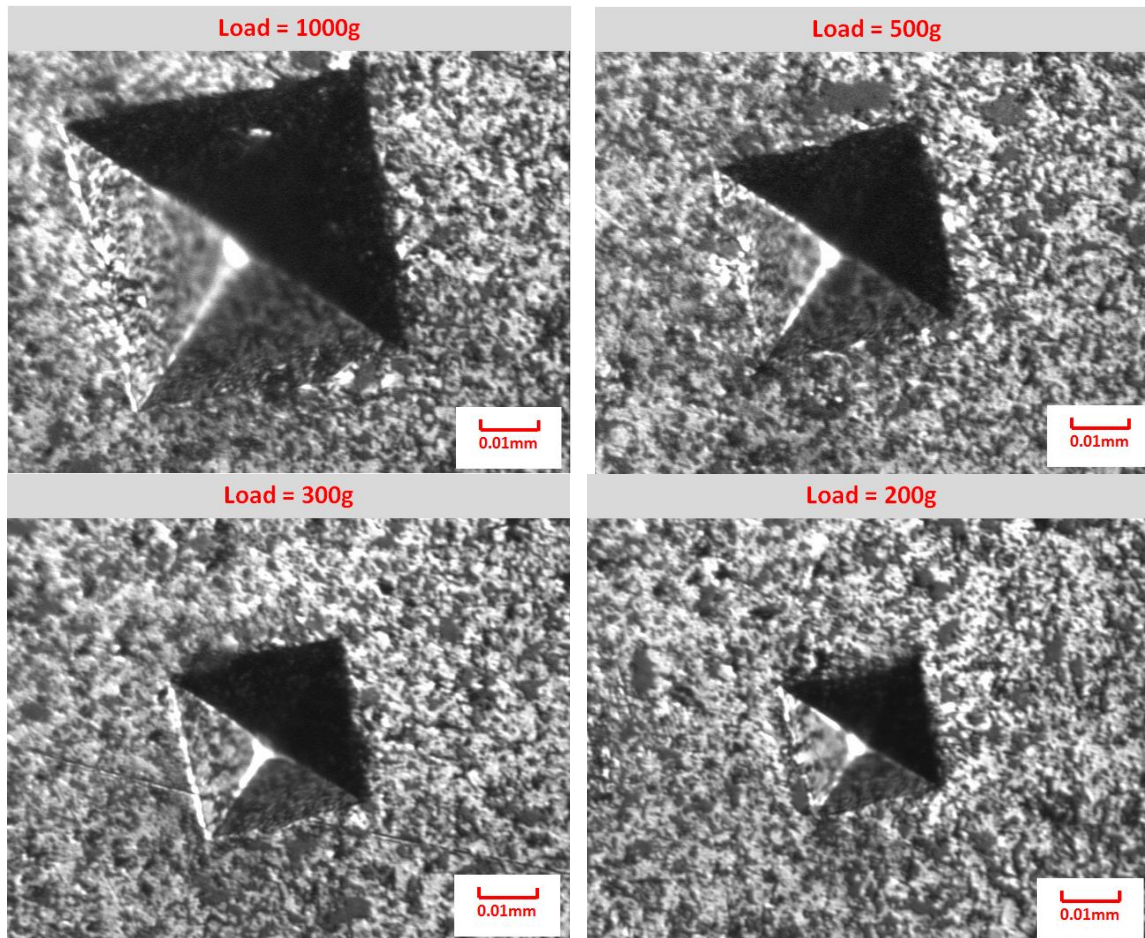
Figure 45: **Vickers Indentation Marks for HTM Cermet after Different Loading Forces of 200 ~ 1000 Grams**

3.1.4 Modulus of Rupture (MOR) or Flexural Strength (σ_{fs})

The flexural strength (σ_{fs}) of the HTM cermet was evaluated at the crosshead loading rate of 600μm/min at both ambient temperature (25°C) and an elevated temperature of 850°C, in the environment of both air and inert N_2 gas atmosphere. The load-displacement results for all four tests above are graphically presented in Figure 46. The flexural strength calculated from the maximum loading forces and the simple formula, is shown in Table 15. The mean σ_{fs} calculated from the two HTM MOR bars (i.e., HTM#1 and HTM#4) is about 356 MPa for the HTM cermet at room temperature. Though the HTM#4 was previously used for CTE analysis with heating and cooling in the temperature range of 50

to 1200°C in air, its load-displacement curves (Figure 46) during the flexural strength is shown to be identical to HTM#1, which is a non-thermally treated and as-received sample bar. Difference of testing atmosphere (air or N_2) has insignificant effect on the load-displacement curves during the flexural strength test at an elevated temperature of 850°C for the HTM cermet, as shown in Figure 46. With testing temperature at 25°C, the load-displacement curves are in elastic stage and HTM failed more like brittle solid without any plastic deformation (Figure 46).

With the testing temperature increased to 850°C, the load-displacement curves for HTM initially result in an elastic deformation, and then are followed by some obvious plastic deformation. The total displacement for HTM at 850°C is about 3 times to that at room temperature. Flexural strength calculated from the peak load for HTM at 850°C is only 284 MPa, as compared to 356 MPa for HTM at room temperature, though the stain energy for HTM at 850°C is much higher. From the above, it can be stated that HTM cermet behaves much more like elastic material at room temperature. With the temperature increased to 850°C, the HTM cermet behaves much more like a metallic material with fractures preceded by plastic deformation as shown Figure 46.

After HTM Disc#2 was subjected to 500 thermal cycles between 50–850°C, two MOR Type-A bars (i.e. HTM-TC500#1 and HTM-TC500#2) were processed for the flexural strength test at cross-head rate of 600µm/min as designated in ASTM C1161. The experimental results for the load-displacement for these two tests are plotted in Figure 47. The flexural strengths calculated from the maximum loading force are shown in Table 16. The mean σ_{fs} was calculated to be about 422 MPa for HTM cermet after 500 thermal cycles, whereas, for the as-received HTM sample, it was 356 MPa. Flexural strengths for both the HTM as-received and after 500 thermal cycles, as well as the effect of temperature (25°C and 850°C on the flexural strength are graphically presented in Figure 48. Thermal cycling in air is beneficial to the development of flexural strength, which might be attributed to chemical reaction of Pd with oxygen in air to form a strong oxide

layer of PdO, which is later verified by both Microprobe and SEM. This PdO layer provided an enhanced compressive residual stress, thus, the HTM sample was found to have better resistance to tensile stress.
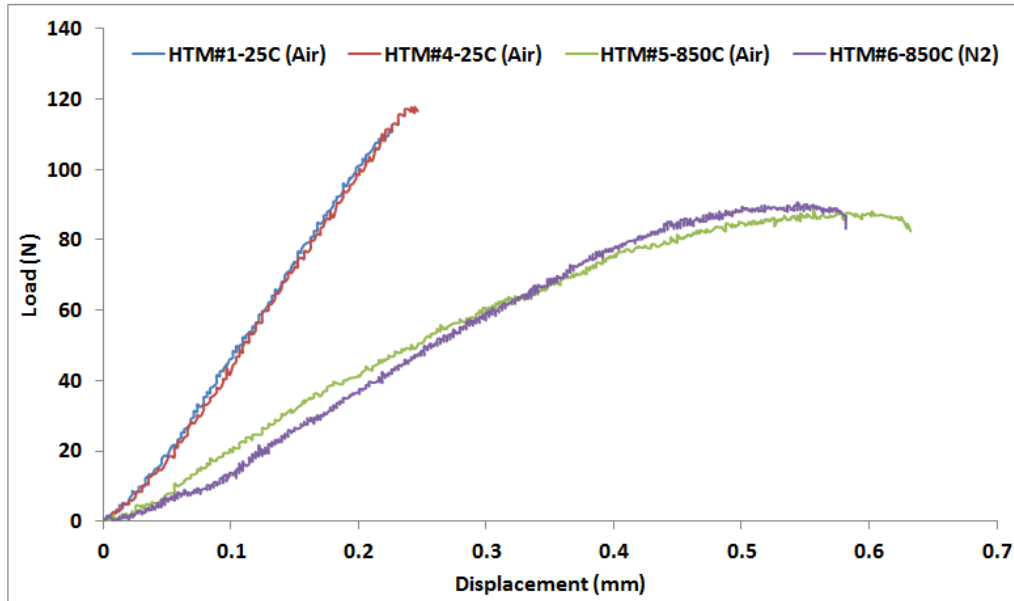
Figure 46: **Load Displacement Curves for 4-Point Bending Test of HTM at Room Temperature (25°C) and the Elevated Temperature of 850°C**

Table 15: **Flexural Strength of HTM at Room Temperature (25°C) and the Elevated Temperature of 850°C**

Sample ID	Temperature (°C)	Atmosphere	Thickness (mm)	Width (mm)	Length (mm)	Load P (N)	σ_{fs} (Mpa)	σ_{fs} (Mpa)
HTM#1	25°C	Air	1.54	2.05	19.72	112.11	342.51	356.56
HTM#4	25°C	Air	1.52	2.03	19.72	117.86	370.61	
HTM#5	850°C	Air	1.50	2.04	19.72	88.50	284.74	284.50
HTM#6	850°C	N2	1.52	2.03	19.72	90.64	284.25	

Table 16: **Flexural Strength (σ_{fs}) for HTM As-Received (HTM-TC0) and after 500 Thermal Cycles (HTM-TC500)**

Sample ID	Thickness (mm)	Width (mm)	Length (mm)	Load P (N)	σ_{fs} (Mpa)	σ_{fs} (Mpa)
HTM#1	1.54	2.05	19.72	112.11	342.51	356.56
HTM#4	1.52	2.03	19.72	117.86	370.61	
HTM-TC500#1	1.53	2.01	19.72	137.45	432.92	422.09
HTM-TC500#2	1.53	2.01	19.72	130.90	411.26	
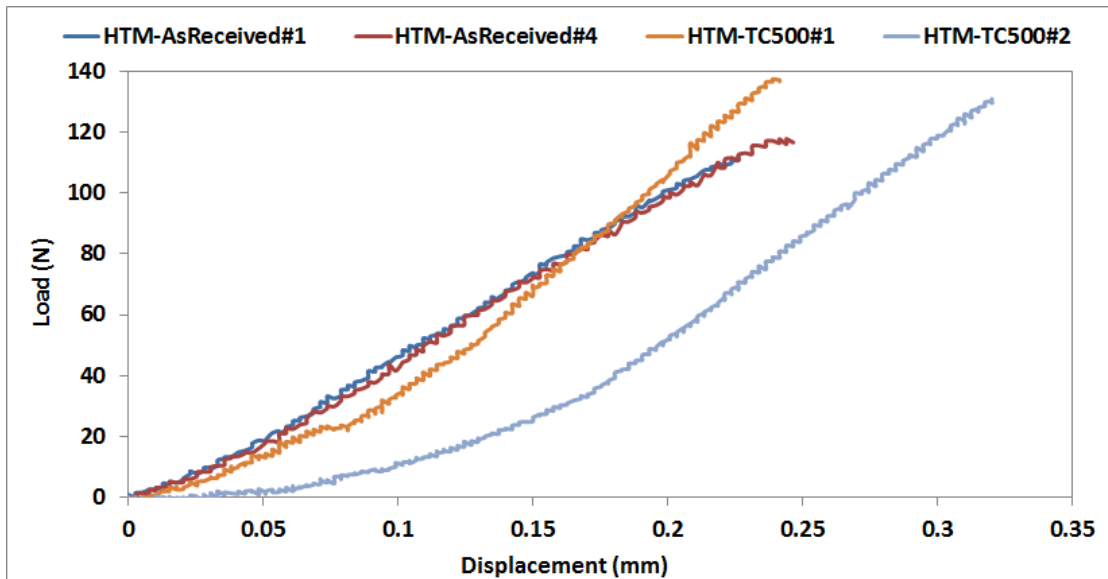
Figure 47: Load Displacement Curves for 4-Point Bending Test of HTM As-Received (TC0) and after 500 thermal cycles (TC500)
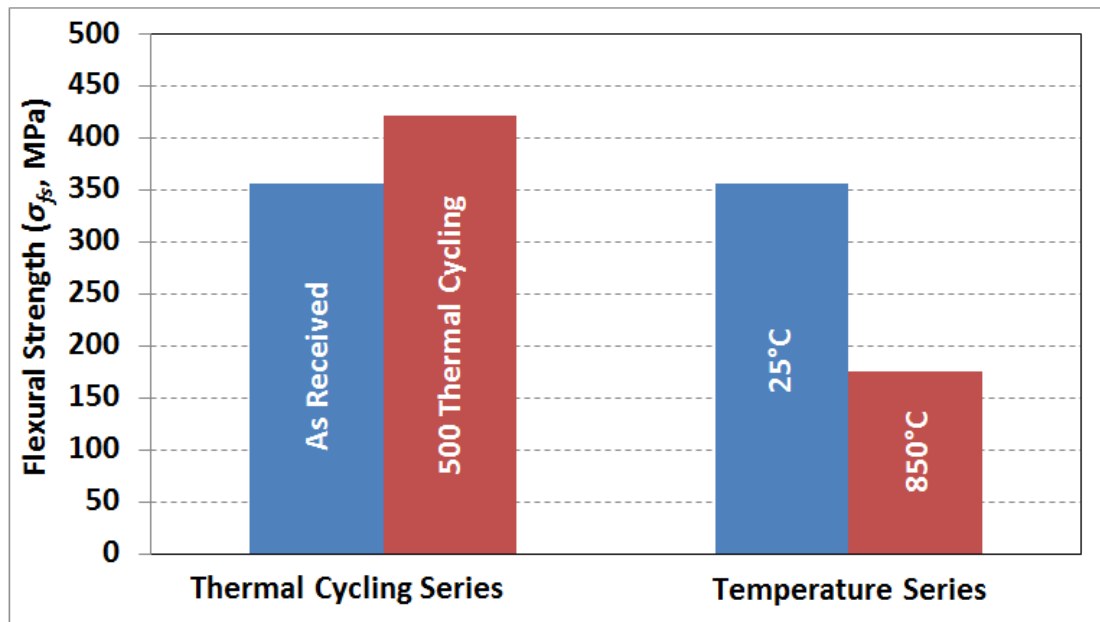
Figure 48: Flexural Strength (σ_{fs}) for HTM both As-Received (HTM-TC0) and after 500 Thermal Cycles (HTM-TC500) and at 25°C and 850°C

3.1.5   Residual Stress for HTM Cermet

3.1.5.1   Residual Stress and Mohr's Circle

The residual stress was measured at different diffraction peak angles of the Pd phase by changing the incidence beam conditions, which varied from 2 square millimeters (1mm x 2mm) to 64 square millimeters (8mm x 8mm), as provided in Table 17. Both the as-received surface and polished surface were measured for their residual stress based on the selected Palladium's crystallographic planes. In order to verify the effects of instrument parameters on the residual stress measurement, different step-sizes and scan-times were selected for some of the residual stress measurements, as summarized in Table 17.

The lattice displacement change ($\Delta d_{\psi\varphi}$) versus $\sin^2\psi$ for all tested crystallographic planes for all five stress measurements are plotted in Figure 49 to Figure 54. The calculated bulk residual stresses from all experiments are found to be consistent about -150 MPa.

Elastic constant of each crystallographic plane can be estimated based on Stress#1 and Stress#2 measurements for Pd polycrystalline material. If it is assumed that the Young's modulus E_{331} and Poisson ratio for the Pd(331) crystallographic plane are consistent with the referenced metal palladium, and the values are 121 GPa and 0.39 respectively [39], then, the value of σ_φ can be calculated for the as-received surface Pd(331) for Stress#1. The results are shown in Table 18:

$$\sigma_\varphi = \left(\frac{E}{1+\upsilon}\right)_{331} \frac{1}{d_{\varphi 0}} \left(\frac{\partial d_{\varphi\psi}}{\partial \sin^2\psi}\right) = \left(\frac{121E9}{1+0.39}\right)_{331} \frac{1}{0.8936}(-0.0016)$$
$$= -154.72 MPa$$

It is assumed that the residual stress (σ_φ) is constant for any crystallographic plane of a phase in polycrystalline materials such as the HTM cermet. The elastic constant for any

crystallographic plane (h k l) could, thus be estimated and calculated based on the above assumption as:

$$\sigma_\varphi = \left[\left(\frac{E}{1+v}\right)_{331} \frac{1}{d_{\varphi 0}} \left(\frac{\partial d_{\varphi\psi}}{\partial \sin^2\psi}\right)\right]_{331} = \left[\left(\frac{E}{1+v}\right)_{hkl} \frac{1}{d_{\varphi 0}} \left(\frac{\partial d_{\varphi\psi}}{\partial \sin^2\psi}\right)\right]_{hkl} \qquad \textit{Equation 37}$$

Table 17:   X-ray Diffraction Instrument Parameters and Crystallographic Planes Selected for Residual Stress Measurement for HTM Cermet

Test No. (Sample Surface Condition)	XRD Parameters			Crystallographic Plane	2θ	Phi (φ)	Psi (ψ)
	Width x Height (mm)	Step Size	Scan Time (s) /Step				
Stress#1 (As-Received Surface)	4x4	0.02	8	Pd[200]	44.5 ~ 48.5	0	0
				Pd[400]	102.5 ~ 106.5		6.24 12.6 18.43
				Pd[331]	117.1 ~ 121.1		26.53
				Pd[420]	122.3 ~ 126.3		33.21 39.23
Stress#2 (Polished Surface)	8x8	0.02	8	Pd[111]	38.0 ~ 42.0	0	0 6.24 12.6 18.43 26.53 33.21 39.23
				Pd[200]	44.5 ~ 48.5		
				Pd[220]	66.0 ~ 70.0		
				Pd[311]	79.9 ~ 83.9		
				Pd[222]	84.5 ~ 88.5		
				Pd[400]	102.5 ~ 106.5		
				Pd[331]	117.1 ~ 121.1		
				Pd[420]	122.3 ~ 126.3		
Stress#3	8x8	0.02	8	Pd[331]	117.1 ~ 121.1	0 30	0 12.6
				Pd[420]	122.3 ~ 126.3	60 90	26.53 39.23
Stress#4	2x1	0.01	20	Pd[331]	117.1 ~ 121.5	0 60 120	0 39.23
Stress#5	2x2	0.01	30	Pd[331]	117.1 ~ 121.5	0 60 120 180	0 39.23

Based on measurements of Stress # 1 and Stress # 2, the elastic constant $(\frac{E}{1+v})_{hkl}$ values were calculated from Equation 37 as presented in Table 18 and Table 19, for the as-received surface and the polished surface, respectively. From Table 18 and Table 19, it

can be seen that the surface morphology has very little influence on the residual stress for both the as-received and polished surface. The elastic constants for the four tested crystallographic planes: Pd(200), Pd(400), Pd(331), and Pd(420) (from the residual stress values of Stress#1) are found to be consistent with that of the measured values from Stress#2.

Table 18: **Estimation of Elastic Constants Based on the Results of Residual Stress Measurement *Stress#1* of Pd Phase on As-Received Surface for HTM Cermet**

Lattice Plane	$d_{\varphi 0}$	Slope of $d_{\varphi\psi}$ vs. $\sin^2\psi$	Least Square Regression (R^2)	Residual Stress (MPa)	Calculated Elastic Constant $E/(1+v)$ GPa
Pd[200]	1.9475	-0.0066	0.9965	-154.72	45.54
Pd[400]	0.9738	-0.0032	0.9738	-154.72	47.40
Pd[331]	0.8936	-0.0016	0.9968	-154.72	87.05
Pd[420]	0.8709	-0.0019	0.9824	-154.72	69.12

Table 19: **Estimation of Elastic Constants Based on the Results of Residual Stress Measurement *Stress#2* of Pd Phase on Polished Surface for HTM Cermet**

Lattice Plane	$d_{\varphi 0}$	Slope of $d_{\varphi\psi}$ vs. $\sin^2\psi$	Least Square Regression (R^2)	Residual Stress (MPa)	Calculated Elastic Constant $E/(1+v)$ GPa
Pd[111]	2.2488	-0.0038	0.9994	-138.56	82.39
Pd[200]	1.9475	-0.0065	0.9998	-138.56	41.35
Pd[220]	1.3771	-0.0026	0.9994	-138.56	74.40
Pd[311]	1.1744	-0.0028	0.9974	-138.56	57.57
Pd[222]	1.1244	-0.0017	0.9985	-138.56	91.74
Pd[400]	0.9738	-0.0028	0.9973	-138.56	48.41
Pd[331]	0.8936	-0.0014	0.9974	-138.56	87.05
Pd[420]	0.8709	-0.0019	0.9991	-138.56	64.37

In addition, the elastic constants for a parallel crystalline plane such as Pd(200) and Pd(400) are identical to both the residual stresses measurements (Stress#1 and Stress#2). The assumption of constant residual stress for any selected crystalline plane is therefore, proved to be correct and an acceptable value of elastic constant for all crystallographic

planes for a polycrystalline material can be calculated using Equation 37. All crystalline planes of Pd phase from lower diffraction angles to higher diffraction angles could also be used to precisely evaluate the residual stress, if the XRD powder diffraction pattern provides a diffraction peak of suitable intensity and free of interference from neighboring peaks [34].
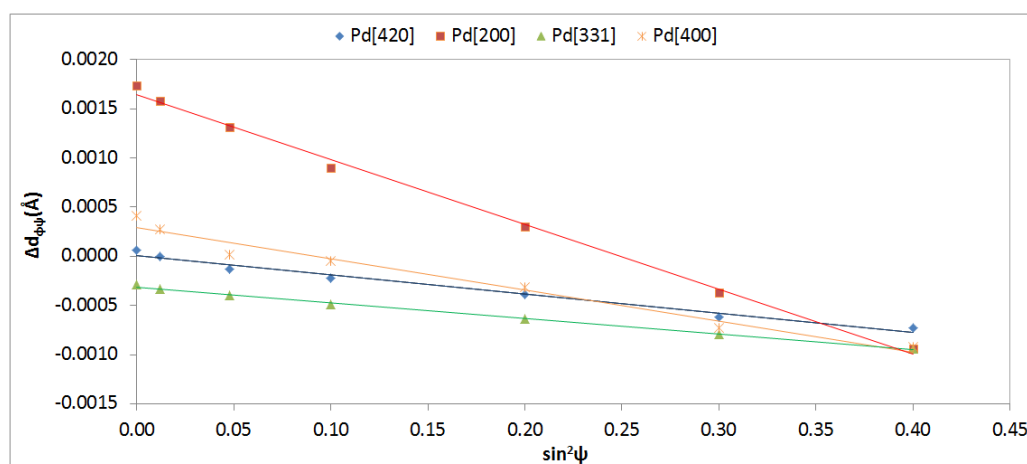
Figure 49: **Residual Stress Measurement *Stress#1* of Pd Phase on As-Received Surface of HTM Cermet Material**
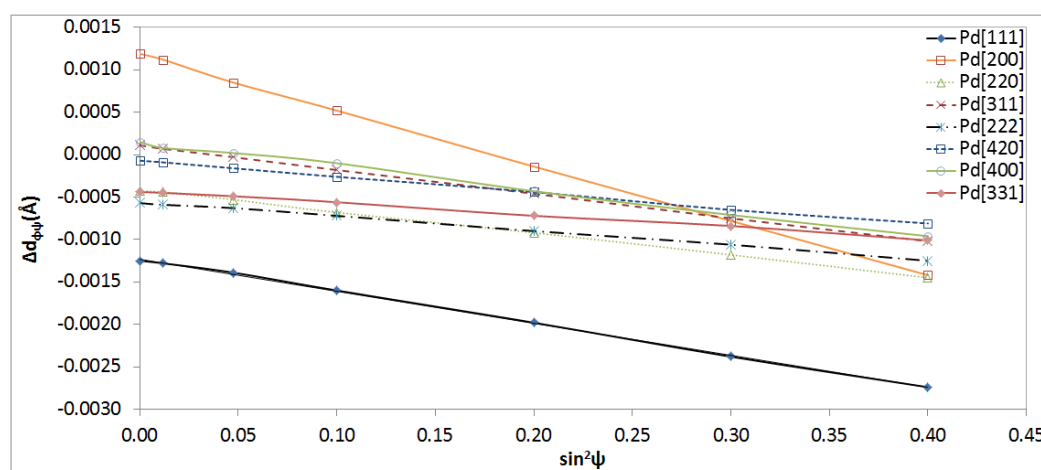
Figure 50: **Residual Stress Measurement *Stress#2* of Pd Phase on Polished Surface of HTM Cermet Material**

In order to calculate the maximum principle stress (σ_1) and minimum principle stress (σ_2) along with the maximum shear stress based on Mohr's circle, four φ values (0°, 30°, 60° and 90°) were selected for Stress#3 based on the crystallographic planes of Pd(331) and Pd(420). Respective changes in lattice displacement ($\Delta d_{\varphi\psi}$) versus $\sin^2\psi$ for Stress#3 are plotted in Figure 51 and Figure 52 for Pd(331) and Pd(420). During the stress measurements in Stress # 3, the incident beam was set at 8mm for its horizontal mask width and 8mm for its vertical divergence slit height. The residual stress values for Stress#3 are presented in Table 20. The residual stress is consistently in the range from -130 to -140MPa, with the φ angles varying from 0 to 90 for both Pd (331) and Pd (420).
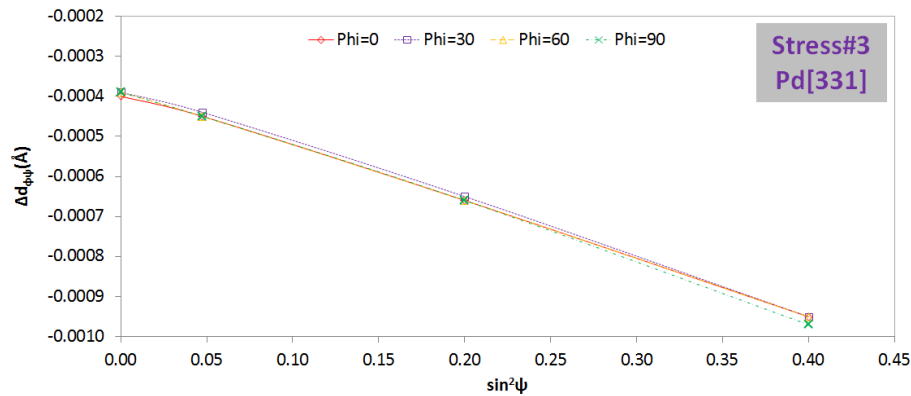
Figure 51: **Residual Stress Measurement *Stress#3* Based on Pd (331) for HTM Cermet at Four Phi (φ) Angles: 0, 30, 60, And 90°**
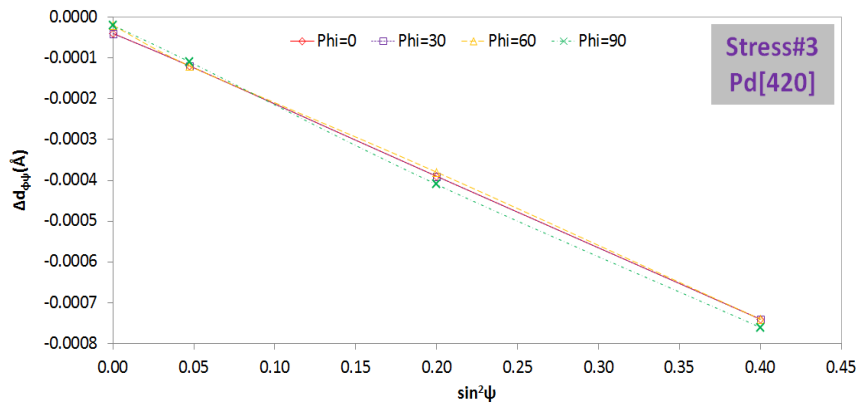
Figure 52: **Residual Stress Measurement *Stress#3* Based on Pd (420) for HTM Cermet at Four Phi (φ) Angles: 0, 30, 60, And 90°**

Table 20: **Residual Stress Measurement** *Stress#3* **of Pd Phase on Polished Surface of HTM Cermet Material**

Lattice Plane	Phi (φ)	$d_{\varphi 0}$	Estimated Elastic Constant $E/(1+v)$ Gpa	Slope of $d_{\varphi\psi}$ vs. $\sin^2\psi$	Least Square Regression (R^2)	Residual Stress (MPa)
Pd[331]	0	0.8936	87.05	-0.00139	0.9974	-135.14
	30	0.8936	87.05	-0.00141	0.9974	-137.52
	60	0.8936	87.05	-0.00140	0.9974	-136.76
	90	0.8936	87.05	-0.00145	0.9991	-141.52
Pd[420]	0	0.8709	64.37	-0.00175	0.9991	-129.64
	30	0.8709	64.37	-0.00175	0.9991	-129.64
	60	0.8709	64.37	-0.00178	0.9991	-131.80
	90	0.8709	64.37	-0.00186	0.9991	-137.15

Because the residual stress determined by x-ray diffraction is the arithmetic average stress in the area defined by the dimensions of the x-ray beam, consideration should be given to appropriate beam size for the investigated stress [34]. For Stress#4 and Stress#5 measurements, a smaller irradiated area was set by changing the incident beam from 8mm to 1~2mm for its horizontal mask width and from 8mm to 2mm for its vertical divergence slit height.

The respective changes in lattice displacements ($\Delta d_{\varphi\psi}$) versus $\sin^2\psi$ for Pd(331) are plotted in Figure 53 and Figure 54, for Stress#4 and Stress #5. The residual stress values of Stress#4 and Stress#5 are presented in Table 21 and Table 22. As compared to the residual stress values from Stress#3, the differences are very insignificant. Because HTM cermet is homogeneous in terms of its microstructure and mechanical properties in all direction, the size of selected diffraction areas does not influence the results of the residual stress.

The other selected instruments parameters, such as step size and stepping time, played insignificant roles for HTM cermet. The residual compressive stress in the HTM cermet has a value somewhere in between -130 to -150 MPa.
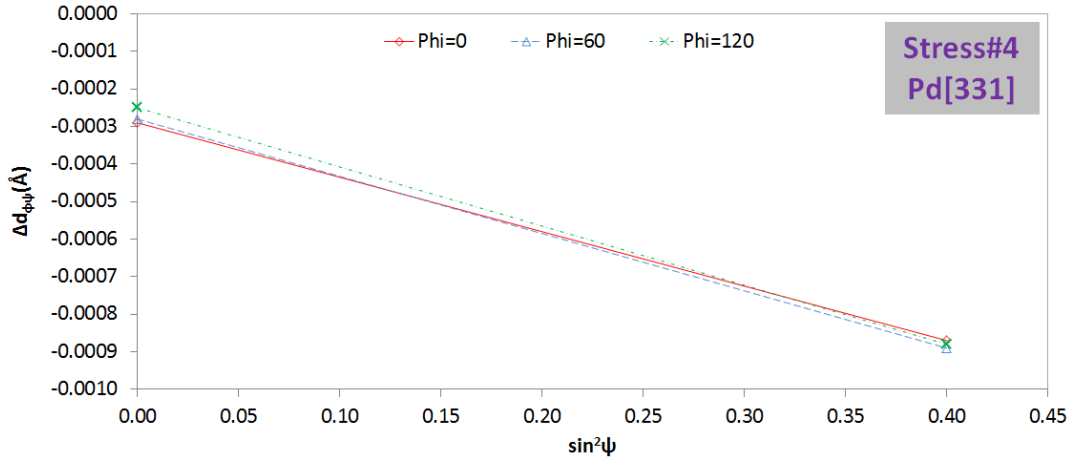
Figure 53: Residual Stress Measurement *Stress#4* of Pd (331) on Polished Surface of HTM Cermet Material at Three Different Phi (φ) Angles: 0, 60, And 120°

Table 21: Residual Stress Measurement *Stress#4* of Pd Phase on Polished Surface of HTM Cermet Material

Lattice Plane	Phi (φ)	$d_{φ0}$	Estimated Elastic Constant $E/(1+v)$ Gpa	Slope of $d_{φψ}$ vs. $\sin^2 ψ$	Least Square Regression (R^2)	Residual Stress (MPa)
Pd[331]	0	0.8936	87.0504	-0.00145	1.0000	-141.26
	60			-0.00153	1.0000	-148.57
	120			-0.00158	1.0000	-153.44
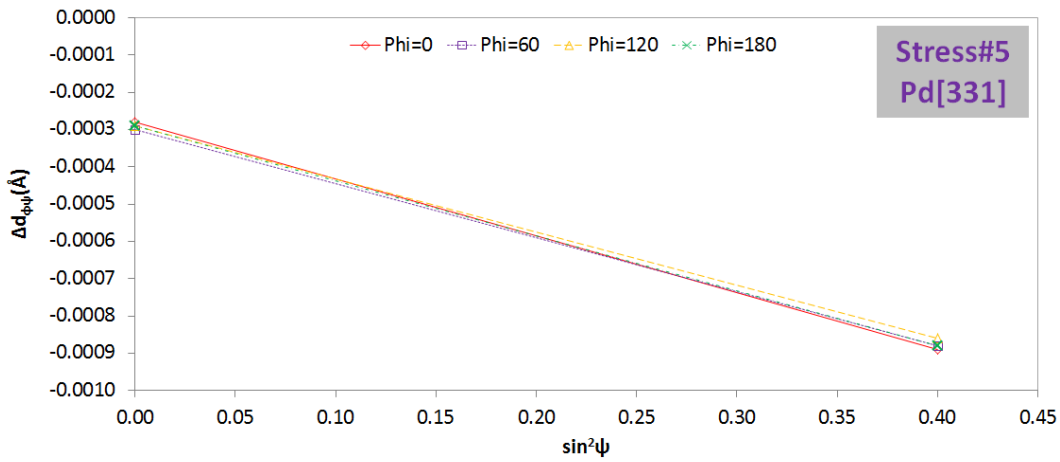
Figure 54: Residual Stress Measurement *Stress#5* of Pd (331) on Polished Surface of HTM Cermet Material at Four Phi (φ) Angles

Table 22: **Residual Stress Measurement *Stress#5* of Pd Phase on Polished Surface of HTM Cermet Material**

Lattice Plane	Phi (φ)	$d_{\varphi0}$	Estimated Elastic Constant E/(1+v) Gpa	Slope of $d_{\varphi\psi}$ vs. $\sin^2\psi$	Least Square Regression (R^2)	Residual Stress (MPa)
Pd[331]	0	0.8936	87.05	-0.00153	1.0000	-148.57
	60			-0.00145	1.0000	-141.26
	120			-0.00143	1.0000	-138.83
	180			-0.00148	1.0000	-143.70

Maximum and minimum principle stress and the maximum shear stress were calculated from the selected σ_φ at three different selected φ angles according to Equation 30. The results for maximum normal and shear stresses are shown in Table 23, with the Mohr's circle for each calculation shown in Figure 55. The residual stress is found to be mainly in the principle compressive in the magnitude between -135 and -155MPa. One the other hand, shear stress is only 10MPa, which is much smaller than the principle compressive stress.

Table 23: **Mohr's Circle of Principle Stress and Shear Stress on Polished-Surface of HTM Cermet Material**

Stress Measurement No.	Maximum Principle Stress σ_1 (MPa)	Minimum Principle Stress σ_2 (MPa)	Maximum Shear Stress τ_{max} (MPa)	Calculated Phi φ_0	Three Selected Phi Angles
Stress#3 Pd[331]	-130	-138	4	52°	φ_0+0 φ_0+30 φ_0+60
Stress#3 Pd[420]	-129	-134	2.5	165°	φ_0+0 φ_0+30 φ_0+60
Stress#4 Pd[331]	-141	-155	7	-9.5°	φ_0+0 φ_0+60 φ_0+120
Stress#5 Pd[420]	-137	-149	6	84°	φ_0+0 φ_0+60 φ_0+120

Even the calculated shear stress increases accordingly with the increasing maximum

principle stress as shown in Figure 55, the setting of XRD incident beams conditions and instrument parameters are found to have very little effect on residual stress. In order to compare theoretical value with experimental value, one additional phi (φ) was selected for comparison of Stress#3 and Stress#5 values. The results are shown in Table 24. The theoretical values based on Equation 30 and Mohr's circle is found to be consistent with the experimental values as shown in Table 24.

Table 24:   Comparison of Theoretical Value Based on Mohr's Circle and Experimental Value for Pd Phase of HTM Cermet Material

Stress Measurement No.	Selected Phi Angles	Theoretical Value (MPa)	Experimental Value (MPa)
Stress#3 Pd[331]	φ_0+90	-133	-141
Stress#3 Pd[420]	φ_0+90	-133	-137
Stress#5 Pd[420]	φ_0+90	-141	-143
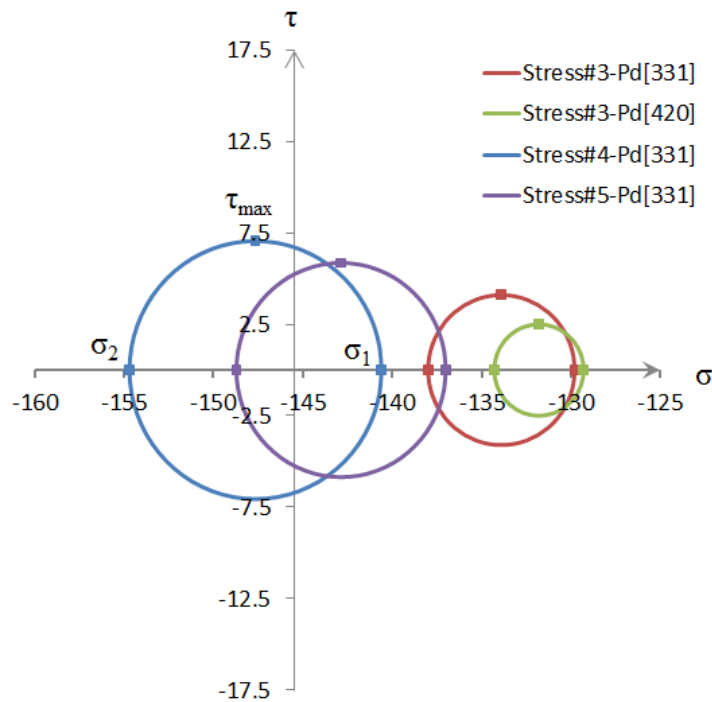
Figure 55:   Mohr's Circle Calculation from Residual Stress Measured at Three Different Phi (φ) Angles for Stress#3, Stress#4, and Stress#5 for HTM Cermet

3.1.5.2   Residual Stress for HTM Cermet after 120 and 500 Thermal Cycles

From XRD phase analysis, the oxidation of Pd (PdO) was identified from the powder diffraction pattern of HTM cermet after 120 and 500 thermal cycles. In the absence of any Young's modulus (E-value) and Poisson ratio (υ) value for PdO, the E-value of 169 GPa which is based on the estimation by the lattice energy (U) was used (41). For the crystalline tetragonal YSZ, the Young's modulus is assumed to be equal to 204 GPa [42, 43] and Poisson ratio (υ) is 0.39.

As compared to the HTM as-received material, the residual stress in all the existing phases in the HTM cermet after 120 thermal cycles were measured by XRD $\sin^2\psi$ technique. The (h k l) indexed planes for XRD residual stress measurement were selected, considering higher angles and noninterference with other Bragg peaks [34, 36]. For the HTM phase of Palladium Oxide (PdO), three different Bragg peaks, PdO (100) at 2θ $\approx 29.396°$, PdO (110) at 2θ $\approx 42.005°$, and PdO(112) at 2θ $\approx 54.887°$, were measured for residual stress at 4 different ψ angles from 0° to 39.23°.

Similarly, a total of three different Pd phases, Pd (111) at 2θ $\approx 40.063°$, Pd (200) at 2θ $\approx 46.598°$, and Pd (331) at 2θ $\approx 119.008°$, were selected in order to evaluate the residual stress. YSZ phases including both tetragonal and monoclinic phases were also tested for the XRD residual stress based on the selected peaks, T-YSZ(101) at 2θ $\approx 30.228°$, M-YSZ(-111) at 2θ $\approx 28.340°$, and M-YSZ(111) at 2θ $\approx 31.478°$. The XRD experimental parameters and the selected crystallographic planes for HTM cermet after 120 thermal cycles are summarized in Table 25.

Results of change of d-spacing ($\Delta d_{\varphi\psi}$) vs. $\sin^2\psi$ for different crystallographic planes of HTM after 120 thermal cycles are plotted in Figure 56. The residual stresses calculated from the slope of d-spacing vs. $\sin^2\psi$ are summarized in Table 26.

Table 25:   **X-ray Diffraction Experimental Parameters and Crystallographic Planes of HTM Cermet after 120 Thermal Cycles**

Phase	Crystallographic Plane	2θ Scan Range	Step Size	Scan Time (s/Step)	Phi (φ)	Psi (ψ)
HTM-Pd	Pd(111)	39.00 ~ 41.00	0.01	30	0	0
	Pd(200)	45.50 ~ 47.50				12.6
	Pd(331)	117.75 ~ 120.75				26.53
						39.23
	Pd(331)	117.75 ~ 120.75			60 120 180 240	0 39.23
HTM-PdO	PdO(100)	27.00 ~ 32.00			0	0
	PdO(110)	40.50 ~ 43.50				
	PdO(112)	52.41 ~ 56.41				12.6
HTM-YSZ& ZrO2	T-YSZ(101)	27.00 ~ 32.00				26.53
	M-ZrO2(-111)	27.00 ~ 32.00				39.23
	M-ZrO2(111)	27.00 ~ 32.00				

Different phases in the HTM cermet have substantial differences in residual stresses. For example, the PdO phase has an average of about 700 MPa in compressive stress as compared to 120 Mpa for the Pd phase. The Tetragonal yttria-stabilized zirconia (T-YSZ) phase has about 530 MPa in compressive stress as compared to 160 MPa for the monoclinic zirconia phase (M-ZrO2). The difference of residual stress in different phases in the HTM cermet is due to the disparities in the coefficient of thermal expansion between the various phases during thermal cycling.

79
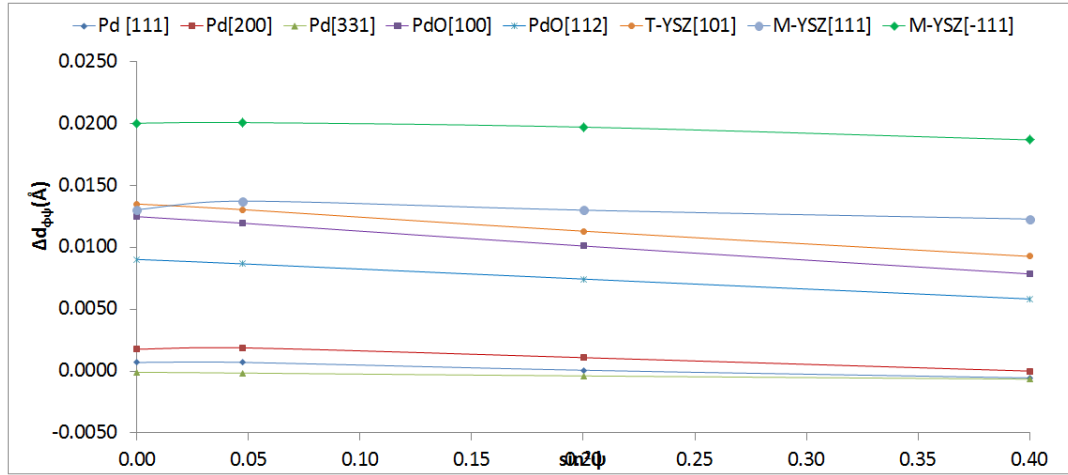
Figure 56:   Results of Change of d-Spacing ($\Delta d_{\varphi\psi}$) vs. $\sin^2\psi$ for Residual Stress for HTM Cermet after 120 Thermal Cycles (HTM-TC120)

Table 26:   Results of Residual Stress for HTM Cermet after 120 Thermal Cycles

Phases	Lattice Plane	d_0	E/(1+v) GPa	Slope of $d_{\varphi\psi}$ vs. $\sin^2\psi$	Least Square Regression (R^2)	Residual Stress (MPa)	Mean Value (MPa)
Pd	Pd(111)	2.25	82.39	-0.0033	0.9871	-121	-119
	Pd(200)	1.95	41.35	-0.0047	0.9699	-100	
	Pd(331)	0.89	87.05	-0.0014	0.9986	-137	
PdO	PdO(110)	2.15	135.20	-0.0117	0.9998	-736	-693
	PdO(112)	1.67	135.20	-0.0080	1.0000	-649	
T-YSZ	T-YSZ (101)	2.95	146.76	-0.0107	0.9993	-531	-531
M-ZrO$_2$	M-ZrO2 (-111)	3.15	146.76	-0.0035	0.9297	-162	-162

In order to calculate the maximum principle stress (σ_1) and the minimum principle stress (σ_2) along with the maximum shear stress using Mohr's circle in HTM cermet after 120 thermal cycles (HTM-TC120), five different φ values (0, 60, 120, 180, and 240°) were

selected for residual stress measurement and Mohr's circle calculation based on the selected crystallographic planes of Pd (331). The lattice displacements (d-spacing) versus $\sin^2\psi$ are plotted in Figure 57 for Pd (331). Residual stress values of Pd (331) at different φ angles are shown in Table 27, and the principle stresses calculated by selecting three different φ angles are shown in Table 28.
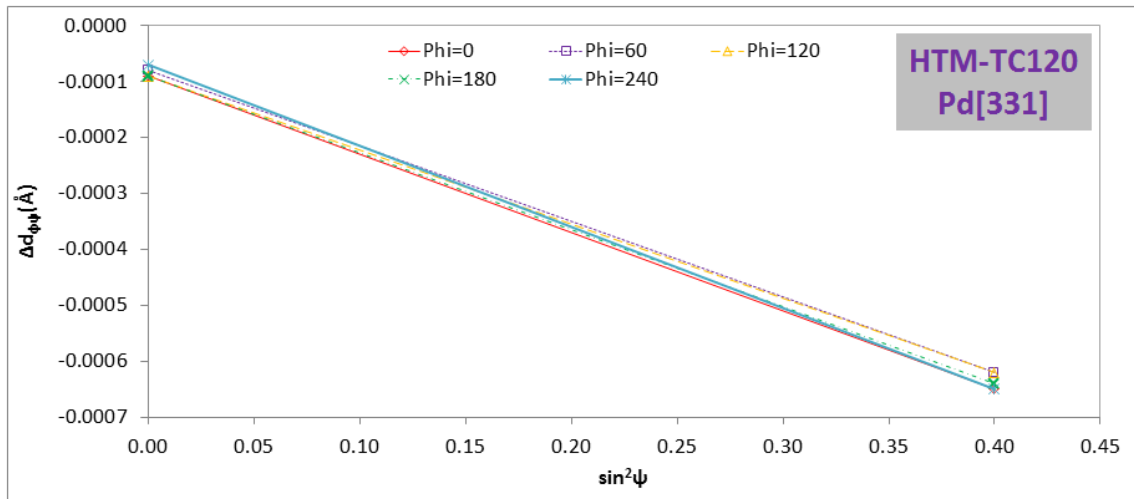
Figure 57:   **Results of $\Delta d_{\varphi\psi}$ vs. $\sin^2\psi$ of Pd(331) for HTM Cermet after 120 Thermal Cycles (HTM-TC120) at Different Phi (φ) Angles**

Table 27:   **Results of Residual Stress of Pd (331) for HTM Cermet after 120 Thermal Cycles (HTM-TC120) at 5 Different φ Angles: 0°, 60°, 120°, 180°, and 240°**

Lattice Plane	Phi (φ)	$d_{\varphi 0}$	Estimated Elastic Constant E/(1+v) Gpa	Slope of $d_{\varphi\psi}$ vs. $\sin^2\psi$	Residual Stress (MPa)
	0			-0.00140	-136.47
	60			-0.00135	-131.52
Pd(331)	120	0.89	87.05	-0.00133	-129.08
	180			-0.00138	-133.95
	240			-0.00145	-141.26

The residual stress is found to be consistent and uniform and in the range of -130 to -140

MPa with φ angles varying from 0 to 240 for Pd (331). The residual stress is found to be mainly as the principle compressive stress, and in magnitude ranging between -130 and -140 MPa, whereas, the shear stress is very small, within the magnitude of 5 MPa as shown in both Table 28 and Figure 61. In order to compare the theoretical value with the experimental value, the two additional φ values were therefore selected for the comparison of stress measurements, and the results are shown in Table 29. Theoretical value based on Mohr's circle and Equation 30 is consistent with the experimental value as shown in Table 27.

Table 28: **Calculation of Principle Stresses and Maximum Shear Stress of the Mohr's Circle for HTM after 120 Thermal Cycles (HTM-TC120)**

Stress Measurement No.	Principle Stress σ_1 (MPa)	Principle Stress σ_2 (MPa)	Shear Stress τ_{max} (MPa)	Orientation of φ_0	Three Selected Phi Angles
HTM-TC120 Pd(331)	-129	-139	5	-119°	0°,60°,120°

Table 29: **Comparison of Theoretical Value Based on Mohr's Circle with Experimental Value for HTM Cermet after 120 Thermal Cycles (HTM-TC120)**

Stress Measurement No.	Selected Phi Angles	Theoretical Value (MPa)	Experimental Value (MPa)
Pd(331)	Φ_0+180	-132	-134
	Φ_0+240	-137	-141

After 500 thermal cycling treatments of the HTM cermet disc, residual stress in two Palladium Oxide (PdO) phases, PdO (110) at $2\theta \approx 42.005°$ and PdO (112) at $2\theta \approx 54.887°$ at two different ψ angles of 0° and 39.23° were measured. Similarly, a total of two different Pd phases, Pd (111) at $2\theta \approx 40.063°$ and Pd (200) at $2\theta \approx 46.598°$, were selected to evaluate the residual stress. The XRD experimental parameters and the selected crystallographic planes are summarized in Table 30.

Table 30: **X-ray Diffraction Experimental Parameters and Crystallographic Planes of HTM Cermet after 500 Thermal Cycles**

Phase	Incident Beam		Crystallographic Plane	2θ Scan Range	Step Size	Scan Time (s) /Step	Phi (φ)	Psi (ψ)
	Width (mm)	Height (mm)						
Pd	2	2	Pd(111)	39.00 ~ 42.70	0.01	30	0	0
			Pd(200)	45.50 ~ 47.50			0 60 120 180 240	
PdO			PdO(110)	39.00 ~ 42.70			0	39.23
			PdO(112)	53.00 ~ 56.00			0 60 120 180 240	

Table 31 summarizes the residual stress of HTM cermet after 500 thermal cycling. Phases of PdO and Pd in HTM cermet after 500 thermal cycles are found to have decreased compressive residual stress as compared to HTM as-received and after 120 thermal cycles. In order to calculate the maximum principle stress (σ_1) and the minimum principle stress (σ_2) along with the maximum shear stress using Mohr's circle of HTM cermet after 500 thermal cycles (HTM-TC500)., five different φ values (0, 60, 120, 180 and 240°) were selected for residual stress measurement, as shown in Figure 58, Figure 59 and Figure 60. The Mohr's circle calculations are based on the selected crystallographic planes of Pd (200) and PdO (112), as shown in Figure 61.

The residual stress of Pd (200) and PdO (112) at different φ angles are presented in Table

32, and the principle stresses calculated from three selected different φ angles, are shown in Table 33. The residual stress of Pd(200) varied significantly from a positive value of 60 MPa to a negative value of -120 MPa with φ angles varying from 0 to 240 degrees. The residual stress of PdO (112) is, however, found to be mainly as the principle compressive stress, in magnitude between -200 to -350 MPa and shown in Table 31 and Table 32.

Table 31:   Results of Residual Stress for HTM Cermet after 500 Thermal Cycles (HTM-TC500)

Crystalline Phases	Lattice Plane	d_0	Estimated Elastic Constant $E/(1+\nu)$ GPa	Slope of $d_{\varphi\psi}$ vs. $\sin^2\psi$	Residual Stress (MPa)
Pd	Pd(111)	2.25	82.39	-0.0030	-110
	Pd(200)	1.95	41.35	-0.0000	58
PdO	PdO(110)	2.15	135.20	-0.0049	-120
	PdO(112)	1.67	135.20	-0.0039	-313
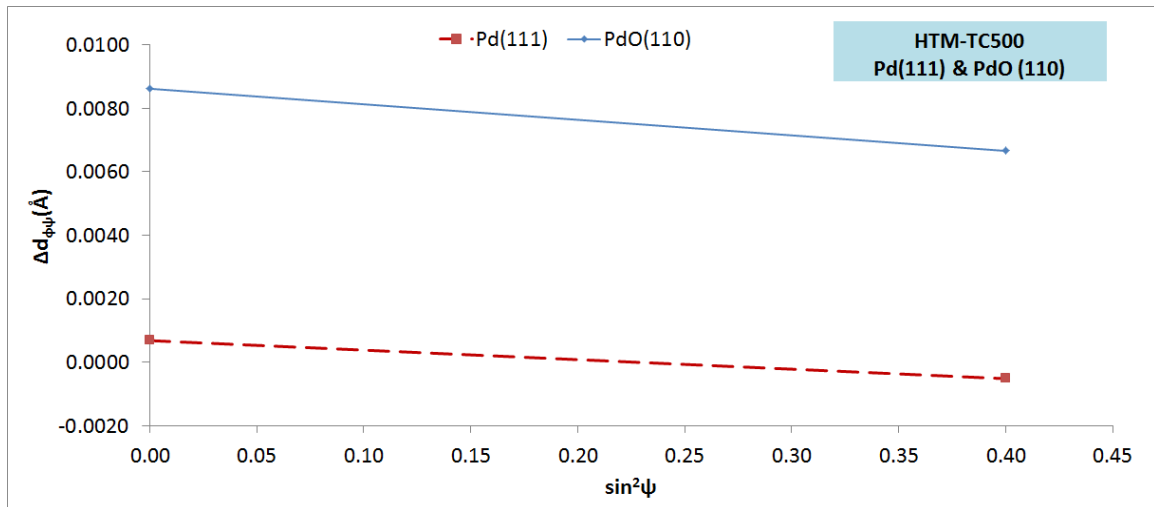
Figure 58:   Results of $\Delta d_{\varphi\psi}$ vs. $\sin^2\psi$ for HTM Cermet after 500 Thermal Cycles (HTM-TC500)

84

Mohr's circles for both Pd (200) and PdO (112) are presented in Figure 61 for HTM cermet. In order to compare the theoretical value with the experimental value, the two additional φ values were selected for stress measurement. Results are shown in Table 34.

Table 32:   Results of Residual Stress of Pd (200) and PdO(112) for HTM Cermet after 500 Thermal Cycles (HTM-TC500) at 5 Different Phi (φ) Angles: 0°, 60°, 120°, 180°, and 240°

Lattice Plane	Phi (φ)	$d_{\varphi 0}$	Elastic Constant $E/(1+v)$ Gpa	Slope of $d_{\varphi\psi}$ vs. $\sin^2\psi$	Residual Stress (MPa)
Pd(200)	0	1.95	41.35	-0.00003	-0.53
	60			0.00275	58.39
	120			-0.00338	-71.66
	180			-0.00553	-117.32
	240			-0.00280	-59.49
PdO(112)	0	1.67	135.20	-0.00388	-313.47
	60			-0.00320	-258.87
	120			-0.00248	-200.22
	180			-0.00405	-327.63
	240			-0.00303	-244.71

At some φ angle, the residual stress is found to be as tensile stress. This weakens most ceramic, thus, develops the macroscopic cracks that can be observed by naked eyes as well as by a microscope (Figure 98 and Figure 97). The PdO phase in HTM cermet is found to have compressive residual stress, but the value decreased from -700 MPa after 120 thermal cycles to -120 MPa after 500 thermal cycles.

After 500 thermal cycles, the theoretical residual stress value of the HTM, based on the Mohr's circle and Equation 30 is not always consistent with the experimental value (Table 34). This observation is quite different from the result for the as-received HTM

85

cermet and after 120 thermal cycles.
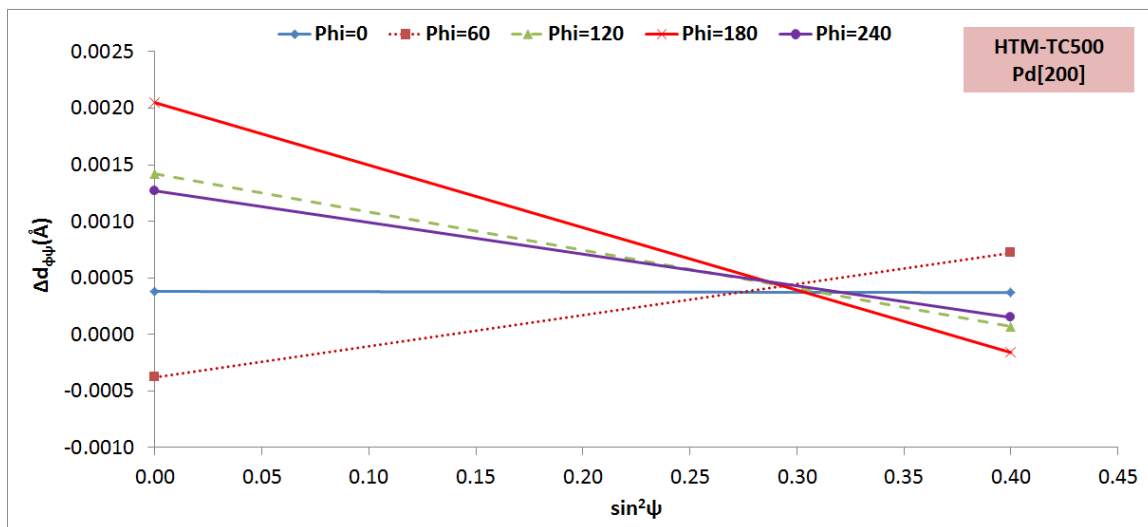
Figure 59: Results of $\Delta d_{\varphi\psi}$ vs. $\sin^2\psi$ of PdO(200) for HTM Cermet after 500 Thermal Cycles (HTM-TC500) at Different Phi (φ) Angles
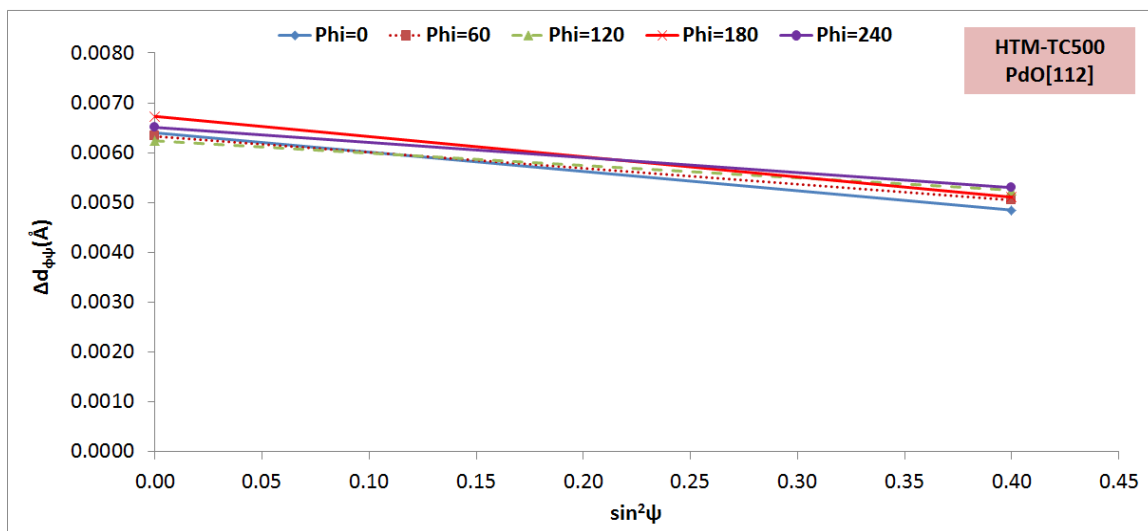
Figure 60: Results of $\Delta d_{\varphi\psi}$ vs. $\sin^2\psi$ of PdO(112) for HTM Cermet after 500 Thermal Cycles (HTM-TC500) at Different Phi (φ) Angles

Table 33: **Calculation of Principle Stresses and Maximum Shear Stress for Mohr's Circle for HTM after 500 Thermal Cycles (HTM-TC500)**

Stress Measurement No.	Principle Stress σ_1 (MPa)	Principle Stress σ_2 (MPa)	Shear Stress τ_{max} (MPa)	Orientation of φ_0	Three Selected φ Angles
HTM-TC500 Pd(200)	145	-119	132	70°	60°,120°,180°
HTM-TC500 PdO(112)	-189	-320	65.5	153°	0°,60°,120°

Table 34: **Comparison of the Theoretical Value Based on Mohr's Circle with Experimental Value for HTM Cermet after 500 Thermal Cycles (HTM-TC500)**

Stress Measurement No.	Selected Phi Angles	Theoretical Value (MPa)	Experimental Value (MPa)
Pd(200)	Φ_0	143	0
	Φ_0+240	-32	-59.49
PdO(112)	Φ_0+180	-195	-327
	Φ_0+240	-250	-245

Figure 61: **Calculated Mohr's Circle Based on Residual Stress Measurement of Pd(200) and PdO(112) for HTM Cermet after 500 Thermal Cycles (HTM-TC500)**

3.1.5.3   **Residual Stress for HTM both As-Received and after Annealing in N$_2$ Environments**

In order to verify the accuracy of the XRD $\sin^2\psi$ technique used and the equipment setup, residual stress in HTM cermet both as-received and after annealing in an inert environment (such N$_2$ at both room temperature and high temperature) was measured. A total of two HTM as-received samples (Sample ID: PC#1 and PC#2) were cut and polished before they were used for the residual stress measurement. After the base measurement, the two samples (PC#1 and PC#2) were soaked for the annealed processes for 48 hour continuously in the gaseous environments in the range of 3.8 to 13 psi above one atmospheric pressure (approximately 14.7 psi) at either room temperature (25°C) or the elevated temperature (900°C). The test plan for the HTM cermet is summarized in Table 35.

Table 35:   **Residual Stress for HTM both As-Received and after Annealing Treatments in the Inert Nitrogen Environment**

Sample ID	Residual Stress	
	Controlled Sample	Soaking Environment
PC#1	HTM As-Received in air, 25°C	N$_2$, 25°C
PC#2	HTM As-Received in air, 25°C	N$_2$, 900°C

The digital pictures of the HTM cermet both as-received and after soaking in N$_2$ (both at room and high temperature) are shown in Figure 62. No change of surface color in HTM samples after soaking in N$_2$ at room temperature for 48 hours (Figure 62) could be observed when compared to as-received sample. However, the surface lost its brightness and shiny silver surface color after the as-received HTM sample was soaked in N$_2$ for 48 hours at an elevated temperature of 900°C (Figure 62).

This change in color is called *thermochromism,* which is defined as the property of substances to change color due to a change in temperature [44]. Virtually all inorganic

compounds are thermo chromic to some extent [45]. Thermochromism for most oxides is due to a possible tiny loss of oxygen atoms in the oxide phases such as the Y_2O_3-Stablized-Zirconia (Y_2O_3-ZrO_2) in the HTM sample at a temperature of 900°C [45]. Thermochromism in palladium metal is also reported in the literature [46].
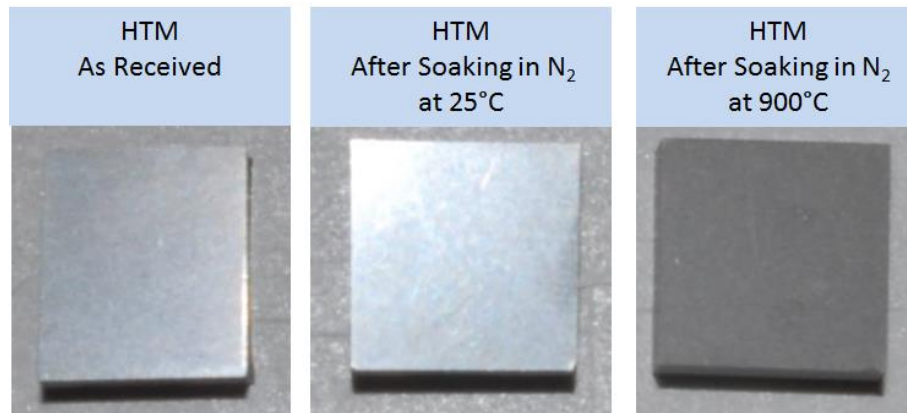
Figure 62:   HTM As-Received and after Soaking in N_2 Environment at Room Temperature of 25°C, and High Temperature of 900°C

For residual stress measurements in HTM for both controlled and after annealing or soaking the sample at various environments, the selected XRD instrument parameters and the crystallographic planes are summarized in Table 36.

The residual stress values for HTM Sample PC#1 both as-received and after soaking in N_2 at room temperature are summarized in Table 37 and graphically presented in Figure 63. For the selected crystalline plane Pd (200) and Pd (331), the residual stress is found to be as compressive residual stress. The residual stress is much higher in YSZ phase based on the selected crystalline plane of T-YSZ (101) as compared to the Pd phases, as shown in both Table 37 and Figure 63.

There is an insignificant decrease in the residual stress value for the sample soaked in N_2 at room temperature for 48 hours, and concluded based on all the selected peaks for both Pd and YSZ phases of HTM cermet, as shown in Figure 63.

Table 36:   X-ray Diffraction Experimental Parameters and Crystallographic Planes of HTM Cermet As-Received and after Soaking in N$_2$ at both Room Temperature and High Temperature

Sample ID	Environment	Phase	Crystallographic Plane	2θ Scan Range	Step Size	Scan Time (s)/Step
PC#1	As-Received	Pd	Pd(200)	44.5 ~ 48.5	0.02	8
			Pd(331)	117 ~ 122		
		T-YSZ	YSZ(101)	26 ~ 37		
	Soaking in N$_2$ at Room Temperature	Pd	Pd(200)	44.5 ~ 48.5	0.02	8
			Pd(331)	117 ~ 122		
		T-YSZ	YSZ(101)	26 ~ 37		
PC#2	As-Received	Pd	Pd(200)	44.5 ~ 48.5	0.02	8
			Pd(331)	117 ~ 122		
		YSZ	YSZ(101)	26 ~ 37		
	Soaking in N$_2$ at High Temperature	Pd	Pd(200)	44.5 ~ 48.5	0.02	8
					0.005	8
					0.001	8
			Pd(331)	117 ~ 122	0.02	8
					0.005	8
		YSZ	YSZ(101)	26 ~ 37	0.02	8

Table 37:   Results of Residual Stress for HTM Sample PC#1 As-Received and after Soaking in N$_2$ at Room Temperature (25°C)

Sample ID	Condition	Lattice Plane	$d_{\phi 0}$	Estimated Elastic Constant E/(1+v) Gpa	Slope of $d_{\phi\psi}$ vs. $\sin^2\psi$	Least Square Regression (R^2)	Residual Stress (MPa)
PC#1	As Received	Pd[200]	1.9475	41.35	-0.00601	0.9998	-127.52
		Pd[331]	0.8936	87.05	-0.00110	0.9994	-107.05
		T-YSZ[101]	2.9558	111.69	-0.00904	0.9979	-341.75
	Soaked in N$_2$ at 25ºC	Pd[200]	1.9475	41.35	-0.00583	0.9981	-123.84
		Pd[331]	0.8936	87.05	-0.00109	0.9955	-106.19
		T-YSZ[101]	2.9558	111.69	-0.00848	0.9903	-320.25
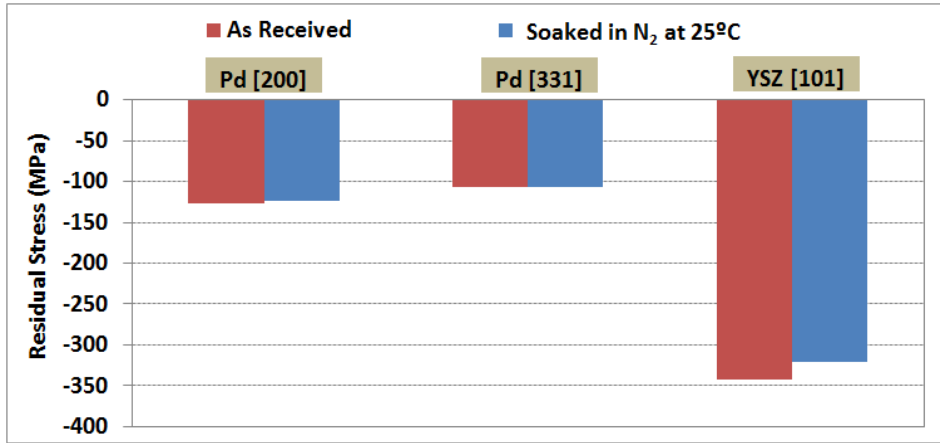
Figure 63: **Result of Residual Stress for HTM Sample PC#1 As-Received and after Soaking in N₂ at Room Temperature (25°C)**

The residual stress values in HTM Sample PC#2, both as-received and after annealing in N₂ at 900°C are summarized in Table 38 and graphically presented in Figure 64. Based on all the selected peaks of both Pd and YSZ phases of the HTM cermet sample, the residual compressive stresses are found to be greatly reduced after the HTM is soaked or annealed in N₂ at 900°C for 48 hours. The annealing treatment of HTM in N₂ at 900°C for 48 hours is the main reason to substantially reduce the residual stress.

Table 38: **Residual Stress for HTM Sample PC#2 As-Received and after Annealing in N₂ at 900°C**

Sample ID	Condition	Lattice Plane	$d_{\phi 0}$	Estimated Elastic Constant $E/(1+v)$ Gpa	Slope of $d_{\phi\psi}$ vs. $\sin^2\psi$	Least Square Regression (R^2)	Residual Stress (MPa)
PC#2	As Received	Pd[200]	1.9475	41.35	-0.00640	0.9774	-135.92
		Pd[331]	0.8936	87.05	-0.00116	0.9992	-112.95
		T-YSZ[101]	2.9558	111.69	-0.01025	0.9971	-387.45
	Annealing in N₂ at 900ºC	Pd[200]	1.9475	41.35	-0.00026	0.1690	-5.54
		Pd[331]	0.8936	87.05	-0.00012	0.7389	-11.62
		T-YSZ[101]	2.9558	111.69	-0.00197	0.9989	-74.40
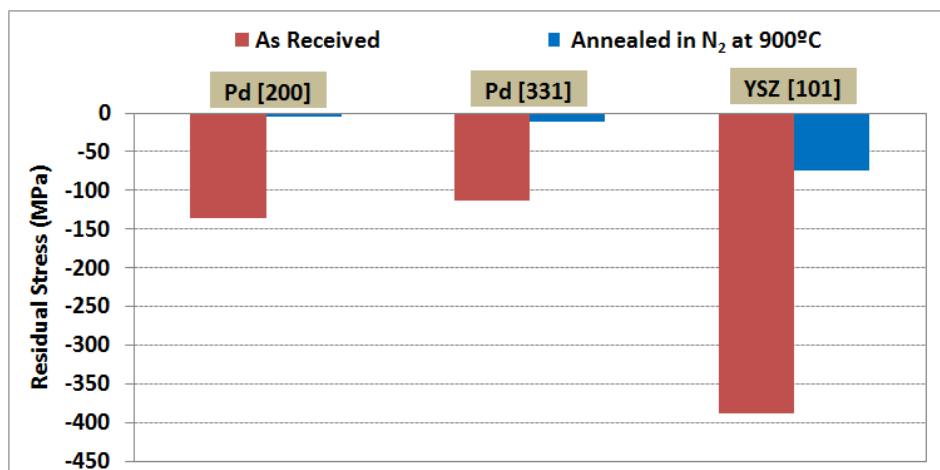
Figure 64: **Residual Stress for HTM Sample PC#2 As-Received and after Soaking in N$_2$ at 900°C at a Scanning Step Size of 0.02°**

Since the least square regression (R^2) values for the HTM Pd (200) and Pd (331) are only 0.1690 and 0.7389 (Table 38), it was necessary to get a better measurement of the residual stress. Therefore, smaller step sizes of 0.005° and 0.001° were selected for the residual stress measurement of HTM after soaking in N$_2$ at high temperature of 900°C. For HTM Sample PC#2, after annealing in N$_2$ at 900°C for 48 hours, the residual stresses measured by using different step sizes, 0.02°, 0.005°, and 0.001° are shown in Table 39 and Figure 65.

Table 39: **Residual Stress for HTM Sample PC#2 after Annealing in N$_2$ at 900°C at Selected Scanning Step Sizes**

Sample ID	Lattice Plane	Step Size (°)	$d_{\phi 0}$	Estimated Elastic Constant E/(1+v) Gpa	Slope of $d_{\phi\psi}$ vs. Sin$^2\psi$	Least Square Regression (R^2)	Residual Stress (MPa)
PC#2	Pd[200]	0.02	1.9475	41.35	-0.00026	0.1690	-5.54
		0.005	1.9475	41.35	-0.00106	0.9455	-22.42
		0.001	1.9475	41.35	-0.00110	0.9463	-23.29
	Pd[331]	0.02	0.8936	87.05	-0.00012	0.7389	-11.62
		0.005	0.8936	87.05	-0.00017	0.8708	-16.67

The results of the residual compressive stress are much improved with the step size

decreasing from 0.02° to 0.005° and 0.001° for the selected crystalline plane Pd[200] as shown in Figure 65.
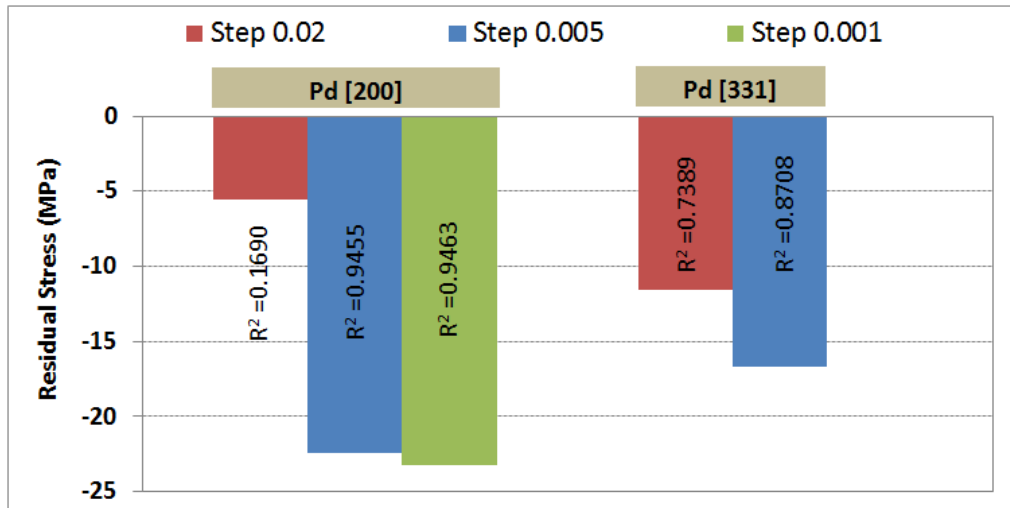
Figure 65:   **Residual Stress for HTM Sample PC#2 after Soaking in N_2 at High Temperature at Different Scanning Step Sizes**

The R^2 value is found to be much improved from 0.7 to 0.8 as the step size decreased from 0.02° to 0.005°v crystalline plane Pd[331]. As compared to Pd (331) with 2θ centered around 119°, Pd(200) is centered much smaller 2θ around 46.6°. With a much smaller residual stress, selection of the instrument parameters such as step size becomes more critical for those peaks which are centered on smaller 2θ angles as compared with higher 2θ angles.

Based on this observation, both lower 2θ peak and the higher 2θ peak would give accurate results if a suitable step size is selected for the measurement. Furthermore, the lower 2θ peak was used to scan at a much smaller step size in order to have better results and higher R^2 value. The residual compressive stress based on both Pd[331] and Pd[200] is found to be significantly lower with an annealing environment of N_2 at high temperature as compared to the controlled value of 135 MPa for HTM as-received sample without annealing, as shown in Table 39.

3.1.5.4   Residual Stress Analysis for HTM Cermet Powder

The (h k l) indexed planes for XRD residual stress measurement were selected considering higher angles and noninterference with other Bragg peaks [34, 36]. The residual stress in the HTM raw powder was measured in the range of $2\theta \approx 117{-}122°$ with the peak centered at $2\theta \approx 119°$ for Pd (331) by 4 different ψ angles from $0°$ to $39.23°$. It was assumed that there would be no peak shift for the residual-stress-free powder sample, and was verified by the powder diffraction patterns shown in Figure 66 for the as-received HTM raw powder.
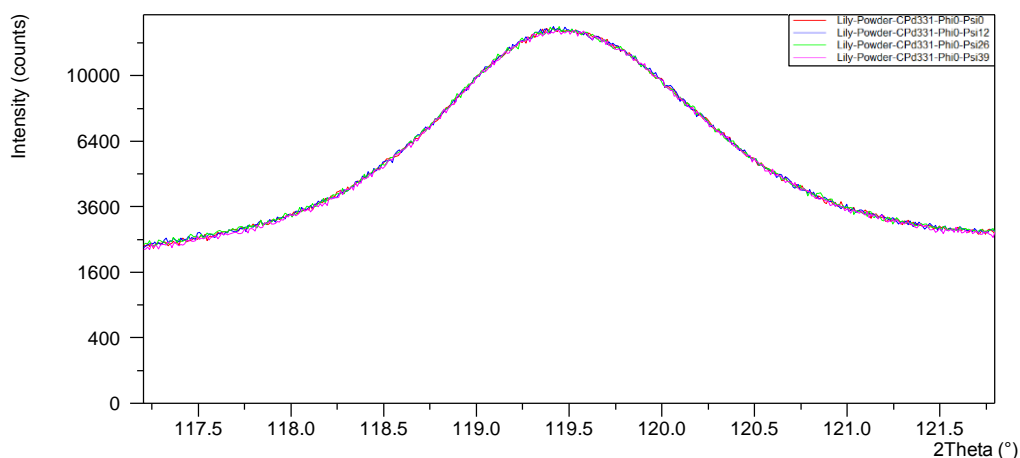
Figure 66:   Powder Diffraction Pattern for HTM Raw Powder Residual Stress Analysis Based on Palladium Crystal Plane Pd (331)

3.2   Characterization of Thermal Properties for HTM Cermet

3.2.1   Coefficient of Thermal Expansion (CTE)

The instantaneous coefficient of thermal expansion, CTE or Alpha (α_t), of the HTM cermet flexural bar (MOR Type A Bar) were measured in the temperature range of 50–1000°C at a constant heating rate of 3°C/min in both air and inert nitrogen (N_2) environments. Sample bars for the CTE experiments were first processed from the HTM

cermet plate and disc, according to the geometry of MOR Type A bars (2.0 mm (width) x 1.5mm (depth) x 25mm (length) as designated in ASTM C1161-02c (Figure 67).
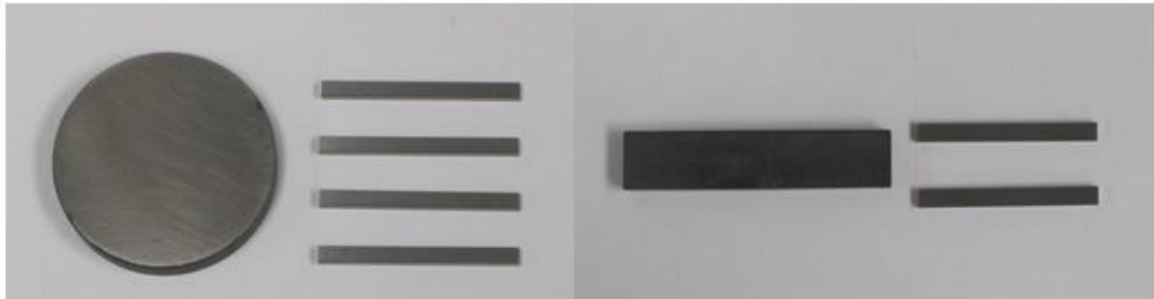
Figure 67:   HTM Type-A Bending Sample Bars as Processed from Both HTM Cermet Plates and Discs for both Flexural Strength Tests and CTE Measurement

The CTE values of HTM cermet bars in air and inert gas N_2 are plotted in Figure 68. The average CTE, α_{avg}, of HTM cermet in air is approximately 10×10^{-6}/K, and very similar to that of HTM cermet in N_2. However, the instantaneous coefficient of thermal expansion, α_t, of HTM cermet in air slowly increases with increasing environmental temperature from 500–650ºC. It sharply increases in temperature from 650–750ºC, and then, sharply decreases in the temperature range of 825–875ºC (Figure 68 (a)).

In an inert (Nitrogen) testing environment, however, no increase in the CTE value of HTM cermet was observed (Figure 68 (b)). Meanwhile, in temperature ranges of 675–825°C and in the inert gas environment of N_2, there was a significant decrease in the instantaneous coefficient value of the thermal expansion, α_t, (Figure 68 (b)).

The expansion of the HTM cermet during the CTE test in air may be related to the chemical reaction of the palladium (Pd) metal phase with the oxygen in air. The shrinkage of the sample bar is related to the softening of the palladium phase at high temperature in both nitrogen and air environment. Another reason for the shrinkage could be the dissociation of palladium oxide (PdO) back to palladium at high temperature.
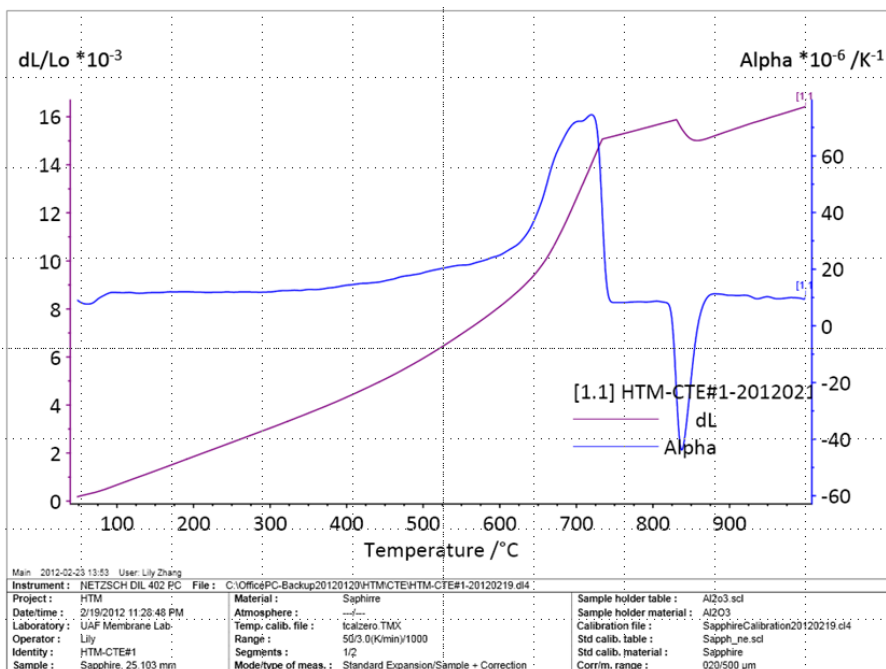
(a) CTE in Air
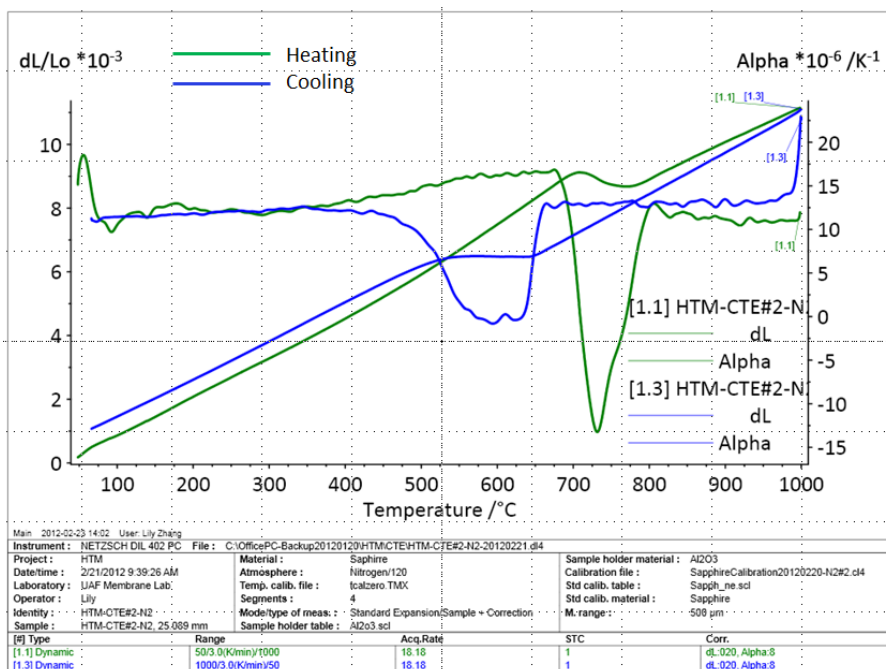
(b) CTE in N$_2$

Figure 68: **CTE Instantaneous Physical Alpha (α_t) and dL/L$_0$ on Heating Rate of 3°K/min for HTM Cermet between 50–1000°C in (a) Air and (b) N$_2$**

The sample bars before and after the CTE tests are shown in Figure 69 (a) and (b) for the testing environments of air and inert N_2, respectively. The sample bar after the CTE test in air (Figure 69 (a)) is more distorted than the sample bar after the CTE test in N_2 (Figure 69 (b)). This physical observation is consistent with the change of instantaneous coefficient of thermal expansion, α_t, of HTM cermet in air and N_2 previously discussed.
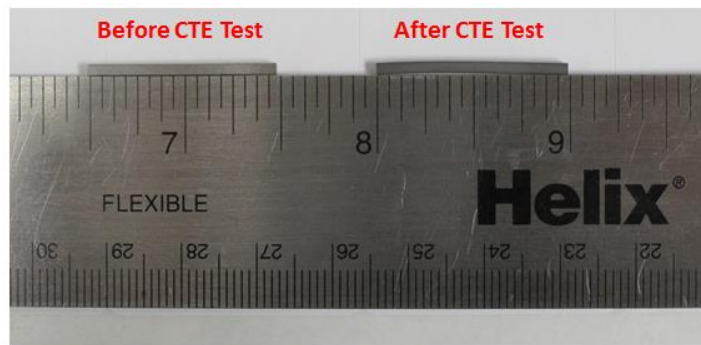
(a) CTE in Air
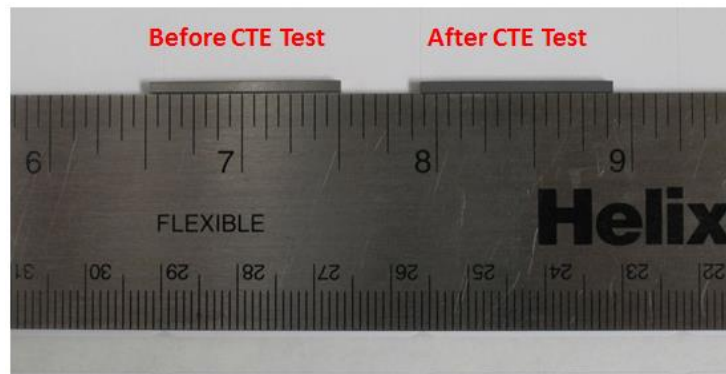
(b) CTE in N_2

Figure 69:   HTM Sample Bar before and after CTE Measurement in Temperature Range of 50–1000°C in (a) Air; (b) N_2

3.2.2   Thermogravimetry/Differential Thermal Analysis (TG/DTA)

3.2.2.1   TG/DTA for HTM Cermet Solid

The TG/DTA experiments were simultaneously performed on HTM cermet solid samples

in both air and an inert nitrogen environment at a constant heating or cooling rate of 10°C/min. The TG/DTA curves for the HTM cermet solid are presented in Figure 70.
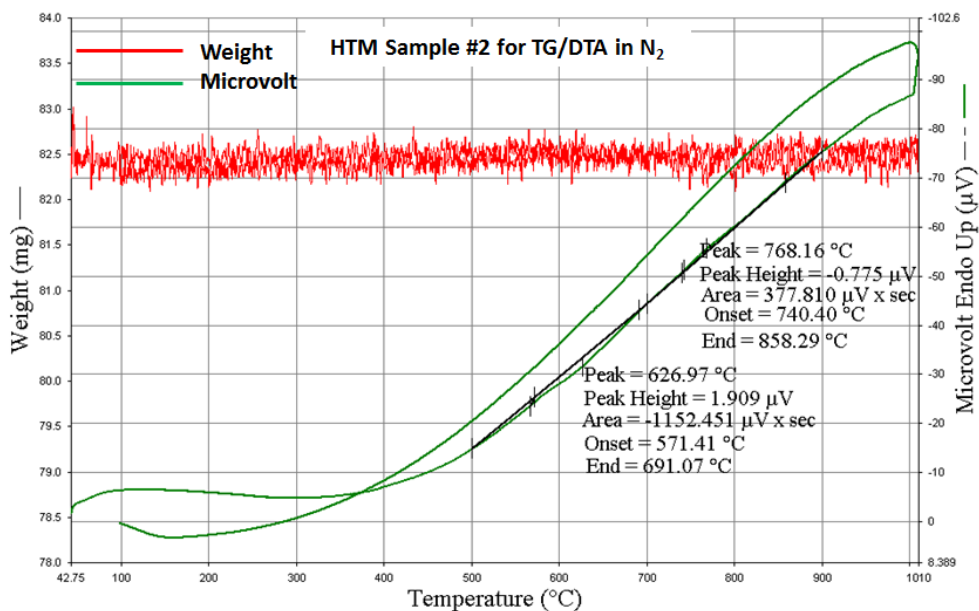
(a)   In N$_2$ Environment
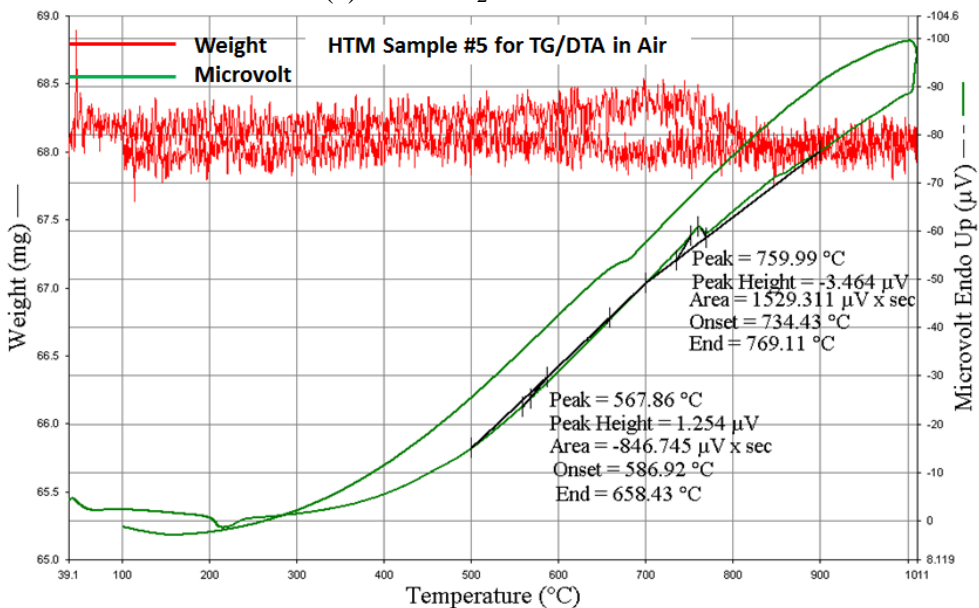
(b) In Air Environment

Figure 70:   TG/DTA Curves for HTM Cermet Solid Sample in the Temperature Range between 40–1000ºC at a Heating/Cooling Rate of 10°C/Min in (a) N$_2$; (b) Air

No obvious weight change or any energy changes can be detected from the TG/DTA curves for HTM cermet solid sample in N_2 environment (Figure 70 (a)). A small endothermic peak along with a small weight gain (Figure 70(b)) can be observed in the TG/DTA curves for HTM cermet solid in air. Based on the TG/DTA's thermal analysis software, Pyris Version 6.0, the endothermic peak occurs around the temperature of 766°C on the DTA heating curves for the HTM cermet solid in air.

A weight gain could also be observed during the heating process due to the chemical reaction of palladium (Pd) metal with oxygen to form palladium oxide (PdO). With continued temperature increase, unstable PdO is dissociated back to metal Pd and oxygen. Therefore, there is both weight gain and weight loss during the heating in air as can be seen from Figure 70(b). Because the bulk sample has a small surface area, the peak for both TG and DTA is not as obvious as that of the powder sample. Therefore, HTM cermet powder provided by ANL was also tested for TG/DTA for a better understanding of the thermal properties.

3.2.2.2 TG/DTA for HTM Cermet Powder

Thermogravimetry (TG) and differential thermal analysis (DTA) of the HTM powder were conducted simultaneously in the temperature range of 50–1000°C at various scanning rates ranging from 3°C/min up to 40°C/min in both air and in an inert environment of nitrogen (N_2). All the experimental parameters and parameters of TG/DTA of HTM powder used in the analysis are summarized in Table 40.

Three repetitive tests for each powder sample were conducted at various scanning rates, ranging from 3 to 40°C/min in order to find the kinetic effect of scanning speed on the thermal property. With the system software, Pyris V6.0, peak parameters, such as onset temperature (T_i), peak temperature (T_p) and end temperature (T_e), peak height (H_p), peak area (A_p) and weight change (ΔW) in percentage (%) and milligram (mg) for each

observed peak were calculated and analyzed for the heating and cooling processes. The result of TG/DTA for the HTM powder in N_2 is shown in Figure 71.

Table 40:   Research Plan of TG/DTA for HTM Powder Provided by ANL

Category	Sample Material	Weight (mg)	Temperature (°C)	Environment	Scanning Rates (°C/min)	Repetitive Tests
Experimental Parameters	HTM Powder	40-60	50-1000°C	Air N_2	3 10 20 40	TC1-1st test TC2-2nd test TC3-3rd test
Analyzed Peak Parameters	T_i – Onset Temperature (°C) T_p - Peak Temperature (°C) T_e - End Temperature (°C) H_p - Peak Height (μV) A_p - Peak Area (μV x Sec or Micro Joules) ΔW - Weight Change (% and mg)					
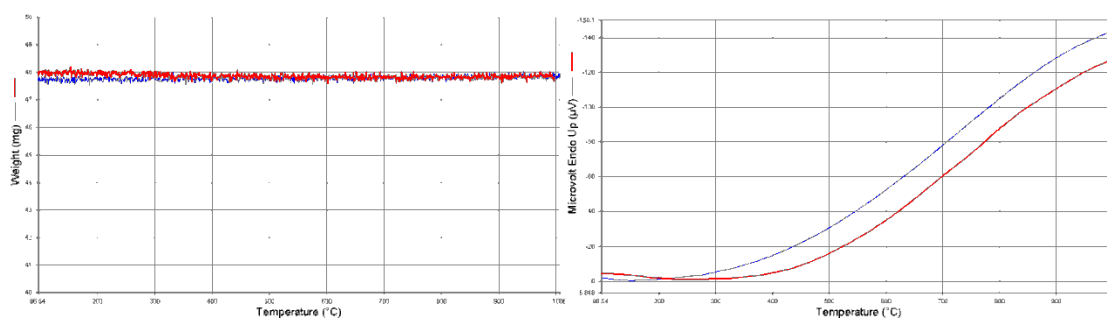
(a) TG in N_2 (b) DTA in N_2

Figure 71:   Thermogravimetry and Differential Thermal Analysis (TG/DTA) Curves for HTM Powder in N_2 at Scanning Rate of 10°C/min between 50–1000°C

An insignificant amount of weight loss in the temperature range from 200–400°C, could be observed in the TG curve in Figure 71 (a), whereas, no endothermic/exothermic peak occurred in the heating/cooling processes for the DTA shown in Figure 71 (b). This weight loss is mainly attributed to the decomposition of a small amount of polymeric

binder present in the HTM raw powder. No other chemical reaction or phase transformation could be observed of HTM raw powder TGA/DTA in the inert (N_2) environment. Therefore, in the inert environment of N_2, HTM raw powder was not evaluated for its thermodynamic and kinetic analysis at other scanning rates.

The DTA curves of HTM powder in the heating process in air are shown in Figure 72. Selected peak parameter results are summarized in Table 41.
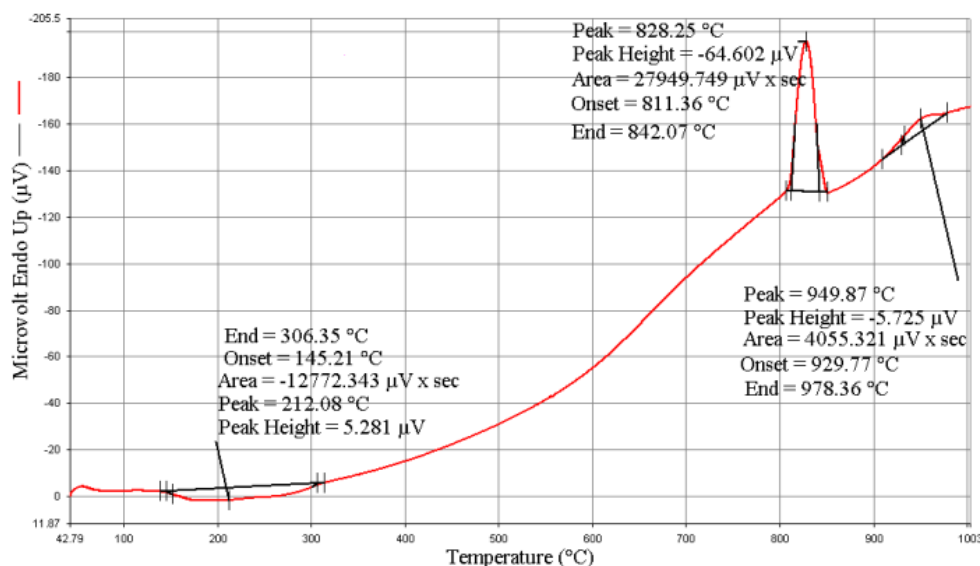
Figure 72: **Characteristic Differential Thermal Analysis (DTA) Curves for HTM Cermet Powder during Heating Process at Different Heating Rates between 50–1000°C in Air for Three Repetitive Heating Processes**

Two endothermic peaks and one exothermic peak (Heating Endothermic Peak #1, Heating Endothermic Peak #2, and Heating Exothermic Peak #1) can be seen on the DTA curve during the heating process of HTM powder in air. Heating Endothermic Peak #1, with peak temperature (T_p) centered at 830°C, can be seen on all the DTA heating curves at all scanning rates ranging from 3 to 40°C/min, as shown in Table 41 and Figure 72. Heating Endothermic Peak #2, with peak temperature centered at 950°C, is only found in the heating process at the lowest scanning rate of 3°C/min, as shown in Table 41 and Figure 72.

Table 41:   Results of Peak Parameters for HTM Cermet during Heating Process of DTA Thermal Analysis

(a) Heating Endothermic Peak #1						
Scan Rate (°C/Min)	**Number of Heating Cycles**	**T_i (°C)**	**T_p (°C)**	**T_e (°C)**	**H_p (µV)**	**A_p (µV·Sec)**
3	TC1	811.360	828.250	842.070	-64.602	2799.749
	TC2	806.630	822.910	836.280	-45.833	20021.540
	TC3	805	823.590	837.030	-45.581	19850.586
10	TC1	808.650	835.620	860.770	-105.444	20739.774
	TC2	803.470	828.230	847.950	-72.348	12852.133
	TC3	804.350	828.800	850.770	-63.714	12246.637
20	TC1	808.180	843.430	873.020	-143.377	17366.206
	TC2	803.450	835.220	859.100	-97.037	10620.473
	TC3	801.750	834.380	858.150	-94.196	10325.360
40	TC1	806.830	853.150	902.090	-139.407	11862.045
	TC2	801.420	851.480	884.950	-91.485	7436.772
	TC3	803.360	849.130	879.990	-98.524	7206.001
(b) Heating Endothermic Peak #2						
Scan Rate (°C/Min)	**Number of Heating Cycles**	**T_i (°C)**	**T_p (°C)**	**T_e (°C)**	**Peak Height H_p (µV)**	**Peak Area A_p (µV·Sec)**
3	TC1	929.770	949.870	978.360	-5.725	4055.321
	TC2	942.930	950.920	949.530	-3.981	2134.650
	TC3	940.580	950.220	960.920	-3.175	1429.881
(c) Heating Exothermic Peak #1						
Scan Rate (°C/Min)	**Number of Heating Cycles**	**T_i (°C)**	**T_p (°C)**	**T_e (°C)**	**Peak Height H_p (µV)**	**Peak Area A_p (µV·Sec)**
3	TC1	145.210	212.080	306.350	5.281	12772.34

10	TC1	161.440	234.360	332.280	11.361	-8402.518
20	TC1	174.420	262.000	356.190	22.293	-8309.044
40	TC1	186.140	285.400	386.360	45.820	-8444.791

However, the peak area (A_p) is greatly reduced from 4055 mJ in the first heating process of TC1 to 1430 mJ in the third heating process of TC3, as Table 41. Since the peak area is related to the total energy change for the chemical system, the HTM powder became less active with each subsequent heating process. It is also very important to select a scanning rate equal or lower than 3°C/min in order to detect Heating Endothermic Peak#2 for the HTM cermet powder.

Heating Exothermic Peak #1, with peak temperature (T_p) between 200 and 300°C, occurred only in the first heating process for the DTA curves at all heating rates from 3 to 40°C/min, as shown in both Table 41 and Figure 72. Generally, the peak parameters except for peak area (A_p) are found to increase or shift positively with increasing heating rate. (The A_p is approximately -14000 mJ at the scanning rate of 3°C/min, whereas, the A_p at other scanning rates stays consistently around -8400mJ (Table 41). Heating Exothermic Peak #1 failed to occur with the subsequent heating processes of TC2 and TC3 for all DTA heating curves at all scanning rates, as shown in Table 41.

The Differential thermal analysis (DTA) curves for HTM powder in the process of cooling of TG/DTA in air are presented in Figure 73. The results of the peak parameters, i.e. Onset Temperature (T_i), Peak Temperature (T_p), End Temperature (T_p), Peak Height (H_p) and Peak Area (A_p) are summarized in Table 42. Two consecutive exothermic peaks, i.e. Cooling Exothermic Peak #1 and Cooling Exothermic Peak #2, are manifested in all the DTA curves in the process of cooling for the HTM powder, shown in Figure 73. The Cooling Exothermic Peak #1 with the peak temperature (T_p) centered around 725-775°C

occurred in all the DTA heating curves at all different scanning rates, as shown in Figure 73 and Table 42.
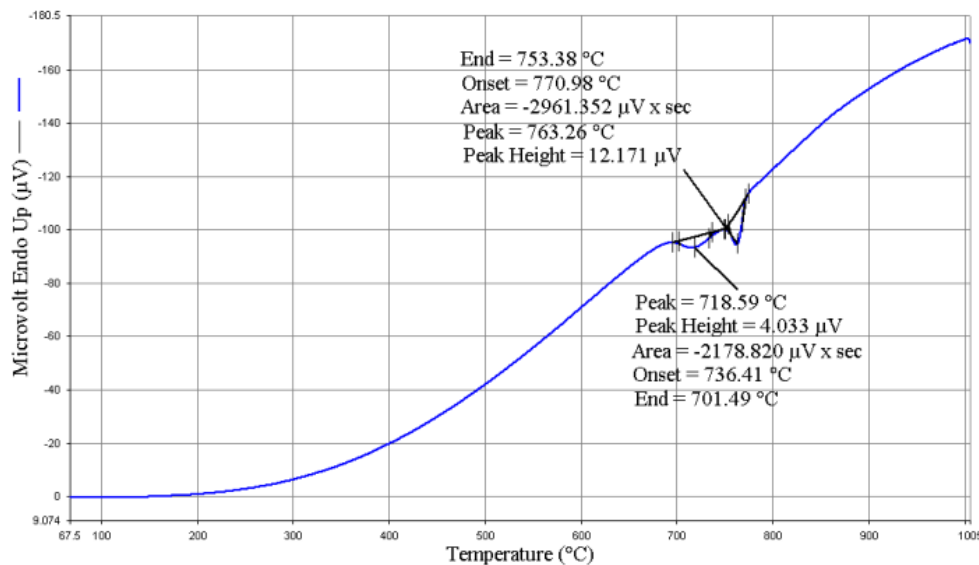
Figure 73:   An Example of Differential Thermal Analysis (DTA) Curves for HTM Cermet Powder during Cooling Process at Different Cooling Rates between 50–1000°C in Air for Three Repetitive Cooling Processes

Because the peak parameters are not only affected by the kinetics such as the heating rate but also the sample weight and the microstructures [47]. When the heating rate is increased from 3°C/min to 40°C/min, Cooling Exothermic Peak #1 shifted to lower peak temperature, and is less distinguishable from the Cooling Exothermic Peak #2 and, thus has the tendency to merge as one unique peak at the DTA cooling curve, shown in Figure 73.

The Cooling Exothermic Peak #2 with the peak temperature (T_p) centered around 680-725°C occurred in all the DTA heating curves at all different scanning rates as shown in Figure 73 and Table 42. The peak parameters are not only affected by the kinetics such as the cooling rate but also the sample weight and microstructures [47]. Thermogravimetry (TG) curves for HTM powder in TG/DTA heating and cooling processes are shown in Figure 74. Weight change (ΔW) results are also summarized in Table 43. Both weight gain and weight loss exhibited in the heating process, whereas, only weight gain is seen

again in the cooling process for all three repetitive tests at different heating rates.

Table 42:   **Results of Peak Parameters for HTM Cermet Powder during Cooling Process of DTA Thermal Analysis**

(a) Cooling Exothermic Peak #1						
Scan Rate (°C/Min)	Number of Heating Cycles	T_i (°C)	T_p (°C)	T_e (°C)	Peak Height H_p (μV)	Peak Area A_p (μV·Sec)
3	TC1	770.980	763.260	753.380	12.171	-2961.352
	TC2	766.160	758.530	748.240	9.063	-2279.451
	TC3	763.120	754.620	743.780	7.940	-2429.220
10	TC1	759.540	748.540	734.890	17.050	-1700.660
	TC2	754.840	744.050	727.000	13.410	-1366.996
	TC3	749.270	741.270	724.850	12.725	-1218.870
20	TC1	750.960	737.840	721.800	19.631	-1164.482
	TC2	745.530	733.510	719.640	14.325	-771.155
	TC3	741.770	730.870	717.970	12.323	-596.296
40	TC1	742.620	727.870	713.600	13.055	-402.400
	TC2	736.110	722.040	707.960	11.388	-351.165
	TC3	733.020	720.010	707.840	10.182	-289.323
(b) Cooling Exothermic Peak #2						
Scan Rate (°C/Min)	Number of Heating Cycles	T_i (°C)	T_p (°C)	T_e (°C)	Peak Height H_p (μV)	Peak Area A_p (μV·Sec)
3	TC1	736.410	718.590	701.490	4.033	-2178.820
	TC2	729.040	713.040	700.280	4.222	-2022.968
	TC3	723.800	712.340	698.440	4.831	-2315.800
10	TC1	723.890	704.540	684.200	7.582	-1220.161
	TC2	720.740	702.850	683.070	7.407	-1119.963
	TC3	719.970	701.640	681.040	7.657	-1183.662

Table 42 continued

20	TC1	715.340	695.280	671.080	10.056	-838.288
	TC2	713.410	693.650	671.030	9.722	-767.789
	TC3	713.160	693.140	670.360	9.782	-781.412
40	TC1	707.770	682.370	655.530	11.222	-557.195
	TC2	505.960	681.920	656.500	11.539	-551.791
	TC3	705.020	680.550	654.550	11.977	-573.633

Table 43:   Weight Change (ΔW) for HTM Cermet Powder for TG Test

Scan Rate (°C/Min)	Number of Heating Cycles	Weight Change ΔW (mg)			Weight Change ΔW (%)		
		Heating		Cooling	Heating		Cooling
		Weight Gain (mg)	Weight Loss (mg)	Weight Gain (mg)	Weight Gain (%)	Weight Loss (%)	Weight Gain (%)
3	TC1	6.317	-6.386	3.094	10.894	-11.093	5.455
	TC2	1.292	-4.403	2.972	1.996	-7.155	4.996
	TC3	1.225	-4.205	2.827	1.949	-6.915	4.642
10	TC1	4.797	-4.969	1.802	9.389	-9.836	3.508
	TC2	1.077	-2.756	1.616	1.896	-5.466	3.328
	TC3	1.077	-2.756	1.616	1.781	-5.072	3.163
20	TC1	3.983	-4.223	1.376	8.283	-8.270	2.906
	TC2	0.877	-2.251	1.370	1.722	-4.599	2.720
	TC3	0.995	-2.296	1.403	1.682	-4.268	2.321
40	TC1	3.427	-3.695	1.331	6.191	-6.221	2.379
	TC2	0.827	-2.076	1.120	1.385	-3.590	1.856
	TC3	0.770	-1.910	1.020	1.285	-3.404	1.840

Total weight of the powder sample only increased after the first TG analysis; it remained constant during the second and third TG analysis (Figure 74). Weight gain (+ΔW) in the first heating process (TC1) is much larger than it is in the two heating process of TC2 and TC3, at all four heating rates.

106

(a) TC1

(b) TC2

(c) TC3

━━━━━ Heating Process   ━━━━━ Cooling Process

**Figure 74:   Example of TG Analysis for HTM Cermet during Heating/Cooling
Process at Different Heating/Cooling Rates between 50–1000°C in Air**

The $+\Delta W$ is consistent in TC2 and TC3, as shown in Table 43. The maximum percentage of weight gain ($+\Delta W$), approximately 11%, occurred during the first TG analysis heating process at the lowest heating rate of 3°C/min. During the first heating process (TC1), the weight loss ($-\Delta W$) is very close to the weight gain ($+\Delta W$), as shown in Table 43 and Figure 74.

However, during the second and third heating processes (TC2 and TC3), the weight loss ($-\Delta W$) is much greater than the weight gain ($+\Delta W$). Amount of Weight loss ($-\Delta W$) shows a relatively consistent value in TC2 and TC3. The maximum percentage of 11% weight loss ($-\Delta W$) occurred in the first heating process of TG analysis at the lowest heating rate of 3°C/min. The first time weight loss ($-\Delta W$) decreased with increase of the heating rate from 3 to 40°C/min.

Meanwhile, second and third heating process weight loss ($-\Delta W$) varied insignificantly with change of heating rates, as shown in Table 43. Weight gain ($+\Delta W$) in the TG analysis process of cooling has little changes in value for all three repetitions, as seen from Figure 74 and Table 43. This weight gain ($+\Delta W$) in the process of cooling generally decreases with increase of heating rate from 3 to 40°C/min, as shown in Table 43 (c).

The weight changes in the processes of heating and cooling for TG analysis, two new concepts of total weight gain ($+\Delta W_T$) and total weight loss ($-\Delta W_T$) are defined as:

$$(+\Delta W_T)=(+\Delta W_c)+(+\Delta W_h) \qquad\qquad \textit{Equation 38}$$

where, $+\Delta W_T$ -total weight gain after one complete cycle of heating and cooling process

$+\Delta W_c$-weight gain in the previous cooling process

$+\Delta W_h$ - weight gain in the current heating process

$$(-\Delta W_T)=(-\Delta W_h) \qquad\qquad \textit{Equation 39}$$

where, $-\Delta W_T$ -total weight loss after one complete cycle of heating and cooling process

$-\Delta W_h$ - weight gain in the current heating process

The results for total weight gain ($+\Delta W_T$) and total weight loss ($-\Delta W_T$) are summarized in Table 44 based on TG analysis of three repetitive tests at different heating/cooling rates.

Table 44:   Total Weight Gain ($+\Delta W_T$) and Total Weight Loss ($-\Delta W_T$) in Percentage (%) for HTM Cermet Powder for TG Analysis

Scan Rate (°C/Min)	Cycles	$+\Delta W_C$ (%)	$+\Delta W_H$ (%)	$+\Delta W_T$(%)	$-\Delta W_T$ (%)
3	TC1	/	10.894	10.894	-11.093
	TC2	5.455	1.996	7.451	-7.155
	TC3	4.996	1.949	6.945	-6.915
10	TC1	/	9.389	9.389	-9.836
	TC2	3.508	1.896	5.404	-5.466
	TC3	3.328	1.781	5.109	-5.072
20	TC1	/	8.283	8.283	-8.270
	TC2	2.906	1.722	4.628	-4.599
	TC3	2.720	1.682	4.402	-4.268
40	TC1	/	6.191	6.191	-6.221
	TC2	2.379	1.385	3.764	-3.590
	TC3	1.856	1.285	3.141	-3.404

It could be observed that $+\Delta W_T$ is always equal to $-\Delta W_T$ for one TG analysis, which includes the heating and cooling process. The ratio of Total weight gain ($+\Delta W_T$)/total weight loss ($-\Delta W_T$) decreases gradually with continuous heating/cooling treatment for the same HTM powder, as shown in Table 44. From Figure 73, it could be concluded that PdO did not completely changed to Pd at high temperature during the heating and cooling process. This explains why more PdO was produced with the HTM cermet exposed to

120 and 500 thermal cycles by XRD phase analysis. With thermal cycling up to 3, total weight gain ($+\Delta W_T$)/total weight loss ($-\Delta WT$) also decreased with increase of the heating rate from 3 to 40°C/min.

Oxidation behavior of platinum metals is of great importance in applications at high temperatures, such as application of heating element material for crucibles and linings in containers for melting special glasses or growing single crystals for catalysts [48]. Therefore, the employed experimental technique of thermogravimetry and differential temperature analysis (TG/DTA) could provide the free energy change for any chemical reaction or phase transition. The free energy function G, which defines the equilibrium or unstable system, was defined by Gibbs as [49, 50]

$$G = H - TS \qquad\qquad\qquad Equation\ 40$$

Free energy changes occurring during any reaction or transformation are given by [49]:

$$\Delta G = \Delta H - T\Delta S \qquad\qquad\qquad Equation\ 41$$

where, ΔG is the free energy change for a closed system

ΔH is the enthalpy change between the reacted products and the reactants

ΔS is the total changes of all forms of product

The function is called the Gibbs free-energy function, comprises of two terms, the enthalpy, H and the entropy, S [49]. The enthalpy content of a crystal is given by:

$$H^T - H_{form}^{298} = \int_{298}^{T} C_{p,comp} dT \qquad\qquad Equation\ 42$$

where H^T is the heat content for a compound at temperature T (K)

H_{form}^{298} is the enthalpy formation of a compound at 298K from its elements.

$C_{p,comp}$ is the heat capacity for the compound at a designated pressure, and is often expressed in the empirical form shown below:

$$C_p = A + BT + \frac{C}{T^2}$$

Equation 43

Disorder constitutes entropy as the atoms or ions vibrate in a solid [49]. The thermal entropy S_T is defined by the following expression:

$$dS_T \equiv \frac{dq_{rev}}{T} = \frac{C_p}{T}dT$$

Equation 44

and for any substance,

$$\Delta S_T = \int_0^T \frac{C_p}{T}dT$$

Equation 45

As stated as the third law of thermodynamic systems, the entropy of a perfect crystal at absolute zero is exactly equal to zero [47]. The implication of the third law is that every substance has a certain amount of entropy, "S", associated with it at any given temperature above absolute 0 DEG K.

As stated in the first law of thermodynamics, the change in the internal energy of a closed system is equal to the amount of heat supplied to the system, minus the amount of work performed by the system on its surroundings [51]. The law of conservation of energy, same as the first law of thermodynamics, states that the energy of an isolated system is constant [51, 52]. Therefore, the amount of heat supplied to or released from the system during the TG/DTA tests could be used to calculate the Gibbs free energy changes as:

$$\Delta G = \Delta Q$$

Equation 46

where, ΔG is defined as the free energy change previously defined.

ΔQ is the heat supplied to the system in the heating and cooling processes of TG/DTA

The hydrogen transport membrane (HTM) powder has mainly two components, metal Pd and the ceramic yttria-stabilized zirconia (YSZ), verified by the XRD phase analysis and the XRF analysis. Palladium is an unreactive metal, palladium oxide is difficult to produce, however, it decomposes relatively easily [50, 53]. The heating of Pd powder in air will result in a weight gain corresponding to the oxidation of palladium initiating at about 840°K or 600°C [54]. Oxidation continues until reaching the decomposition temperature of the PdO to Pd at approximately 1080°K or 800°C [54]. The transformation between the Pd and the PdO is represented by the following reaction:

$$2PdO(s) \rightleftarrows 2Pd(s) + O_2$$
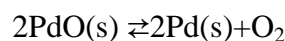
As discussed in the TG analysis, the first trace of PdO with the weight increase could be seen already at 400°C for the 1st time heating process for TG analysis. Oxidation is completed approximately at 800°C and dissociation of PdO takes place rapidly at a temperature which is in the range of 800–900°C, and varied as a function of the heating rates. During cooling, the weight increases in the temperature range of 800–600°C,, which is attributed to the partial re-oxidation of the palladium powder that decomposed from PdO [54]. With repetitive TG analysis for the same (powder) sample, oxidation of the metal palladium and the resultant weight gain could be seen in temperatures of 600–800°C, and dissociation taking place rapidly in the same temperature range as before.

Oxidation of Pd to PdO is a chemical (combustion) reaction with heat released from the closed system, and an exothermic peak is exhibited in DTA curves. The dissociation of PdO back to Pd is a reverse process with heat absorbed into the closed system; as a result, an endothermic peak is seen in the DTA curves. As previously discussed for DTA of HTM powder in both heating and cooling, Heating Endothermic Peak #1 is initiated in the temperature range of 800–900°C, which corresponds to the dissociation of PdO to Pd

and cooling. Cooling Exothermic Peak #1 and #2 are seen in the temperature range of 600–800°C, which is corresponding to the re-oxidation of Pd to PdO. There is no trace of an exothermic peak corresponding to the oxidation of Pd to PdO during heating for all DTA, and it could be attributed to several factors.

The one possible reason is that the temperature range of the oxidation of Pd to PdO during heating is very wide (from 400–800°C), as a result, the oxidation takes much longer time than that of the dissociation of PdO to Pd during heating or the re-oxidation process during cooling. The energy released from the system is extremely low is undetectable by the TG/DTA system used. Another possible reason could be attribute to the phase transformation of the YSZ phase present in the HTM powder. The TG/DTA curves for the YSZ material: Y-TZP, 50% CeSZ, 25% CeSZ, and YSZ-A, are shown in Figure 75 in the temperature range of 50–850°C. A very broad endothermic peak can be traced at 400°C or about 20 min and ends at 800°C or about 45min. The endothermic energy might compensate the exothermic energy released from the oxidation of Pd to PdO, resulting in the distinguished exothermic peak in the DTA curves.

In order to find a kinetic factor such as heating rate on the thermodynamic properties, a concept of free energy change per mol is introduced. Results for free energy change per mol (ΔG/mol) associated with the transformation $2PdO(s) \rightleftarrows Pd(s)+O_2$ are calculated for Heating Endothermic Peak #1 and Cooling Exothermic Peak #1 and #2 for the HTM powder. The system heat absorption per mole calculated from the weight loss (in mole) during the dissociation of PdO to Pd and total peak area in joules are presented in Table 45. Though there is a big difference in the total heat exchange (ΔQ) during the 1st time heating process for DTA, the average heat exchange per mole is approximately 71 J/mol, and it does not vary significantly for DTA at a heating rate equal to or lower than 20°C/min, although a large difference in the ΔQ/mol value could be observed for TG/DTA at the heating rate of 40°C/min.

Table 45: **Heat Exchange (ΔQ) per Mole for HTM Cermet during DTA Heating Process**

Heating Endothermic Peak #1							
Rate (°C/min)	Cycles	ΔW (mg)	ΔW (mol)	Peak Area (mJ)	ΔQ/mol (KJ/mol)	Average ΔQ/mol (KJ/mol)	Standard Deviation (%)
3	TC1	-6.386	0.399	27949.75	70.03	72.77	3.78%
	TC2	-4.403	0.275	20021.54	72.76		
	TC3	-4.205	0.263	19850.59	75.53		
10	TC1	-4.969	0.311	20739.77	66.78	70.83	5.54%
	TC2	-2.756	0.172	12852.13	74.61		
	TC3	-2.756	0.172	12246.64	71.10		
20	TC1	-4.223	0.264	17366.21	65.80	71.08	6.90%
	TC2	-2.251	0.141	10620.47	75.49		
	TC3	-2.296	0.144	10325.36	71.95		
40	TC1	-3.695	0.231	11862.05	51.36	56.35	8.12%
	TC2	-2.076	0.130	7436.77	57.32		
	TC3	-1.910	0.119	7206.00	60.36		
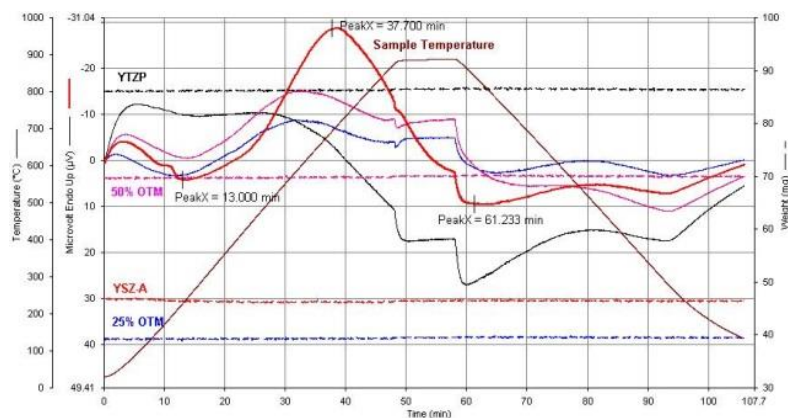
Figure 75: **DTA Curves for Several Toughened Zirconia Materials: Y-TZP, 50%Ce-TZP, 25%Ce-TZP and YSZ-A, between 50–1000ºC in Air**

As the Using the standard value of the enthalpy and entropy change of transformation between 2PdO(s) $\rightleftharpoons$ Pd(s)+O$_2$ at 298 DEG K, [48]: as ΔH_{298}=-27.37Kcal/mol and ΔS_{298}=-24.00cal/(mol·°C), and the heat capacity equation as [48]:

$$\Delta C_p = -6.08 + 12.32 \times 10^{-3}T + 0.20 \times 10^5 T^{-2}$$

the free energy change (ΔG) is calculated for the dissociation of PdO to Pd:

$\Delta H_{1073} = \Delta H_{298} + \int_{298}^{1073}(-6.08 + 12.32 \times 10^{-3}T + 0.20 \times 10^5 T^{-2})dT = -27.37 + 1.83 = -25.54 Kcal/mol = -106.82 KJ/mol$

$\Delta S_{1073} = \Delta S_{298} + \int_{298}^{1073} \frac{-6.08 + 12.32 \times 10^{-3}T + 0.20 \times 10^5 T^{-2}}{T} dT = -24 + 1.83 = --21.71/mol \cdot °C = -0.09 KJ/mol \cdot °C$

Therefore,

$$\Delta G = \Delta H - T\Delta S = -106 - (800) * (-0.09) = -34 KJ/mol$$

Based on the above discussion, the free energy change (ΔG) is quite consistent with the heat energy change based on the TG/DTA. System heat release per mol is calculated from the weight increase (in mole) during the re-oxidation of Pd to PdO and total peak area (joules). The results are shown in Table 46. The unit heat energy released from the system during cooling is relatively much smaller than the heat energy absorbed during heating, which might be attribute to the energy absorption of the zirconia phase transformation during the cooling process, as shown in (Figure 75) and also discussed in Chapter 4.2 and 4.3.

These are several factors that could lead to the experimental errors during TG/DTA, such as thermal drifts, gas drifts, etc, and a discussion of these factors is beyond the scope of the present work.

Table 46:   **Heat Exchange (ΔQ) per Mole for HTM Cermet during DTA Cooling Process**

Cooling Exothermic Peak #1+Cooling Exothermic Peak#2							
Scan Rate (°C/Min)	Number of Heating Cycles	ΔW (mg)	ΔW (mol)	Total Peak Area (mJ)	ΔQ (KJ/mol)	Average ΔQ (KJ/mol)	Standard Deviation (%)
3	TC1	3.094	0.193	5140.17	26.58	25.53	8.06%
	TC2	2.972	0.186	4302.42	23.16		
	TC3	2.827	0.177	4745.02	26.86		
10	TC1	1.802	0.113	2920.82	25.93	24.78	4.37%
	TC2	1.616	0.101	2486.96	24.62		
	TC3	1.616	0.101	2402.53	23.79		
20	TC1	1.376	0.086	2002.77	23.29	18.99	20.48%
	TC2	1.370	0.086	1538.94	17.97		
	TC3	1.403	0.088	1377.71	15.71		
40	TC1	1.331	0.083	959.60	11.54	12.66	8.08%
	TC2	1.120	0.070	902.96	12.90		
	TC3	1.020	0.064	862.96	13.54		
	TC2	1.120	0.070	902.96	12.90		
	TC3	1.020	0.064	862.96	13.54		

3.2.2.3   TG/DTA for Pure Palladium (Pd)

Thermogravimetry (TG) and differential thermal analysis (DTA) for pure palladium (Pd) were measured simultaneously in the temperature range between 50–1000°C at a constant heating/cooling rate of 3°C/min in air. Three repetitive tests for a pure Pd sample were conducted in a simulated treatment as the thermal cycling. With system software Pyris V6.0, peak parameters such as Onset Temperature (T_i), Peak Temperature (T_p) and End

Temperature (T_e), Peak Height (H_p), Peak Area (A_p) and Weight Change (ΔW) in both percentage (%) and milligram (mg) for each observed peak were calculated and analyzed for both heating and cooling processes for all TG/DTA.

Macroscopic optical observation of the surface of the Pd sample was conducted with a digital camera after TG/DTA (Figure 76). A layer of dark grey by-product can be observed on the Pd sample after being heated as high as 1000ºC, which is in contrast to the as-received sample. The result is consistent with observation of the HTM cermet subjected to thermal cycling in air between 50–850°C.
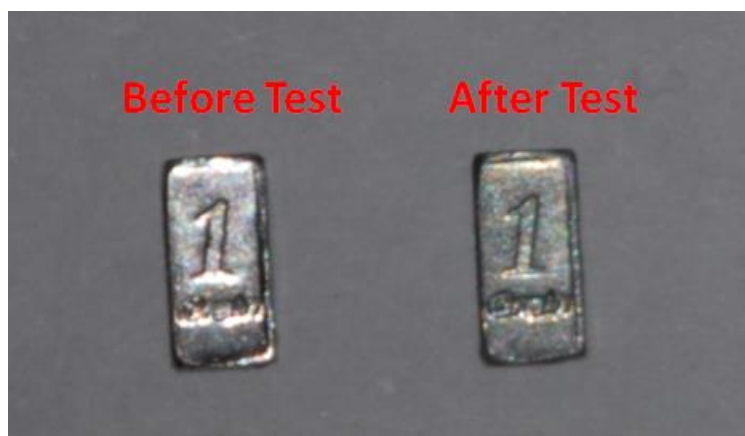
Figure 76: **Pure Palladium (Pd) Sample before and after TG/DTA Test**

The existence of endothermic peaks for the DTA curve in the process of heating as well as cooling the pure Pd in the temperature range of 50–1000°C air can be observed in Figure 77. The heating Endothermic Peak #1 with peak temperature (T_p) centered at 810°C and the Cooling Endothermic Peak at 690°C, presented in Table 47. These peaks are related to the absorbed energy of Pd to form PdO, as previously discussed.

It is generally observed that each peak parameter remains generally constant regardless of the repetitive heating and cooling processes. The weight change is in the range of 0.4%, as shown in Table 47 which is associated with the reaction of Pd and Oxygen in air.
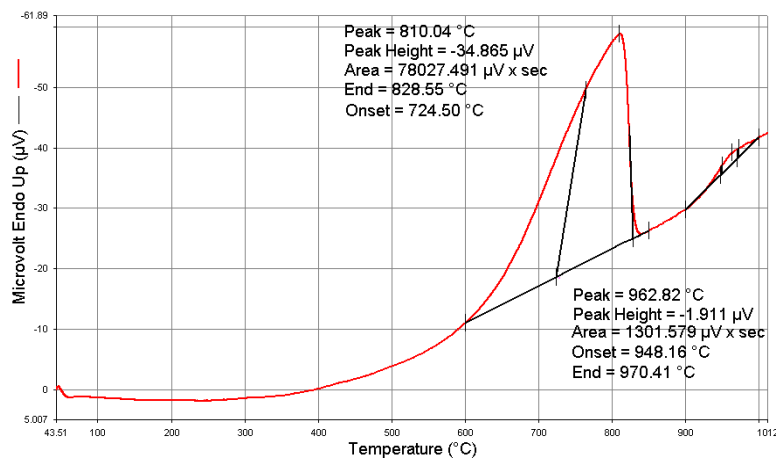
(a) DTA Curve in Heating Process
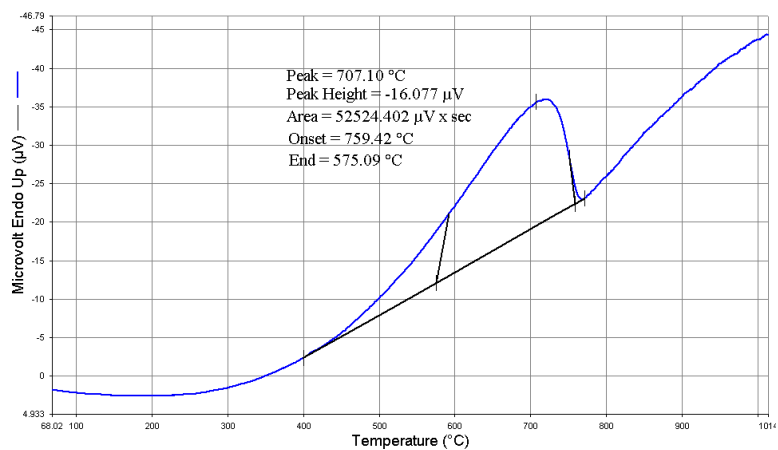
(b) DTA Curve in Cooling Process
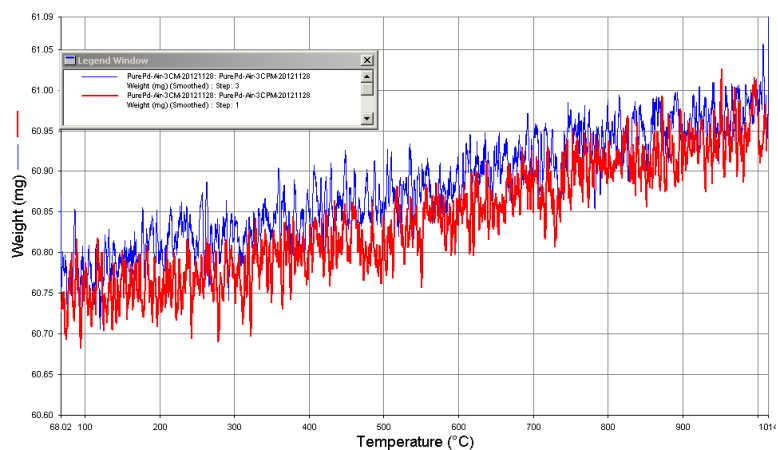
(c) TG Curves in Heating (Red) and Cooling (Blue) Processes

Figure 77: Examples of Pd Metal in Three Repetitive TG/DTA Tests

Table 47:   **Results of Peak Parameters during Heating Processes of DTA for Pure Palladium Metal**

Process	Number of Heating Treatments	Onset Temp T_i (°C)	Peak Temp T_p (°C)	End Temp T_e (°C)	Peak Height H_p (μV)	Peak Area A_p (μV·Sec)	Weight Change (%)
Heating	TC1	724.50	810.04	828.55	-34.87	78027.49	0.423
	TC2	758.63	811.35	824.83	-31.77	82708.36	0.390
	TC3	732.51	813.30	829.01	-33.50	83911.48	0.404
Cooling	TC1	759.42	707.10	575.09	-16.08	52524.40	-0.405
	TC2	740.13	686.22	607.50	-14.27	45507.31	-0.394
	TC3	740.21	670.45	611.83	-10.38	32802.11	-0.386

The weight change is much smaller as compared to the HTM cermet powder, because the sample is solid with small surface area and much larger weight.

3.3   Characterization for Microstructural Properties

3.3.1   Fractography Analysis

Fractured MOR bars were sectioned with a slow cutting saw in order to get the broken halves for fractography analysis for HTM sample bars after their flexural strength tests. The broken halves for HTM sample bars are observed for its top, bottom and fractured surfaces by optical microscope Olympus BX60 in the magnification ranging from 5x to 50x. The cracking lines on the top surface of the sample bars are shown in Figure 78, and they are characterized by straight cutting surface, which was perpendicular to the direction of the tensile stress.

The cracking lines on the bottom surface of the sample bars are shown in Figure 79. The crack surface for sample bars tested at room temperature (Figure 79 (a) and (b)) are

characterized by straight cutting surface which is perpendicular to the tensile stress shown in Figure 79 (a). Crack line for sample bars tested at the elevated temperature and the crack propagations are characterized by zig-zag line (Figure 79 (c) and (d)). Cutting surfaces are found to have a combination of both crack Mode I and II the tensile stress direction and the facture might be predominantly intergranular fracture, because the material started to show high toughness and ductility at the elevated temperature.

(a) HTM (as-received) at 25°C

(b) HTM (500 thermal cycles) at 25°C

(c) HTM (as-received) at 850°C in air

(d) HTM (as-received) at 850°C in N_2
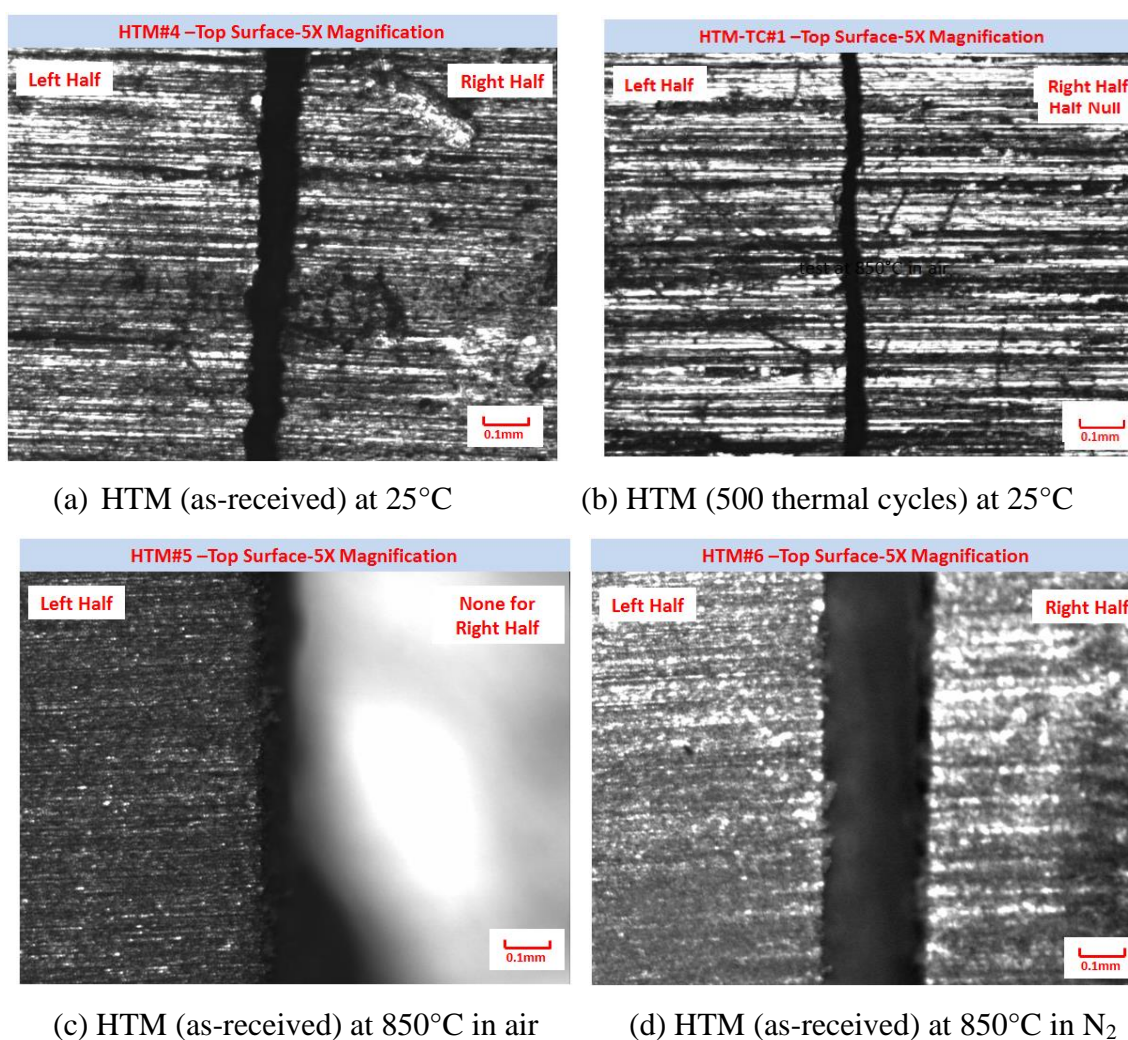
Figure 78: **Optical Observation from Top Surface of HTM Sample Bars after Flexural Strength Tests at different Temperatures (25°C and 850°C) in different Atmospheres (Air and N_2) for HTM As-Received and after 500 Thermal Cycles**

(a)   HTM(as-received) at 25°C

(b) HTM(500 thermal cycles) at 25°C

(c) HTM (as-received) at 850°C in air

(d) HTM (as-received) at 850°C in N$_2$
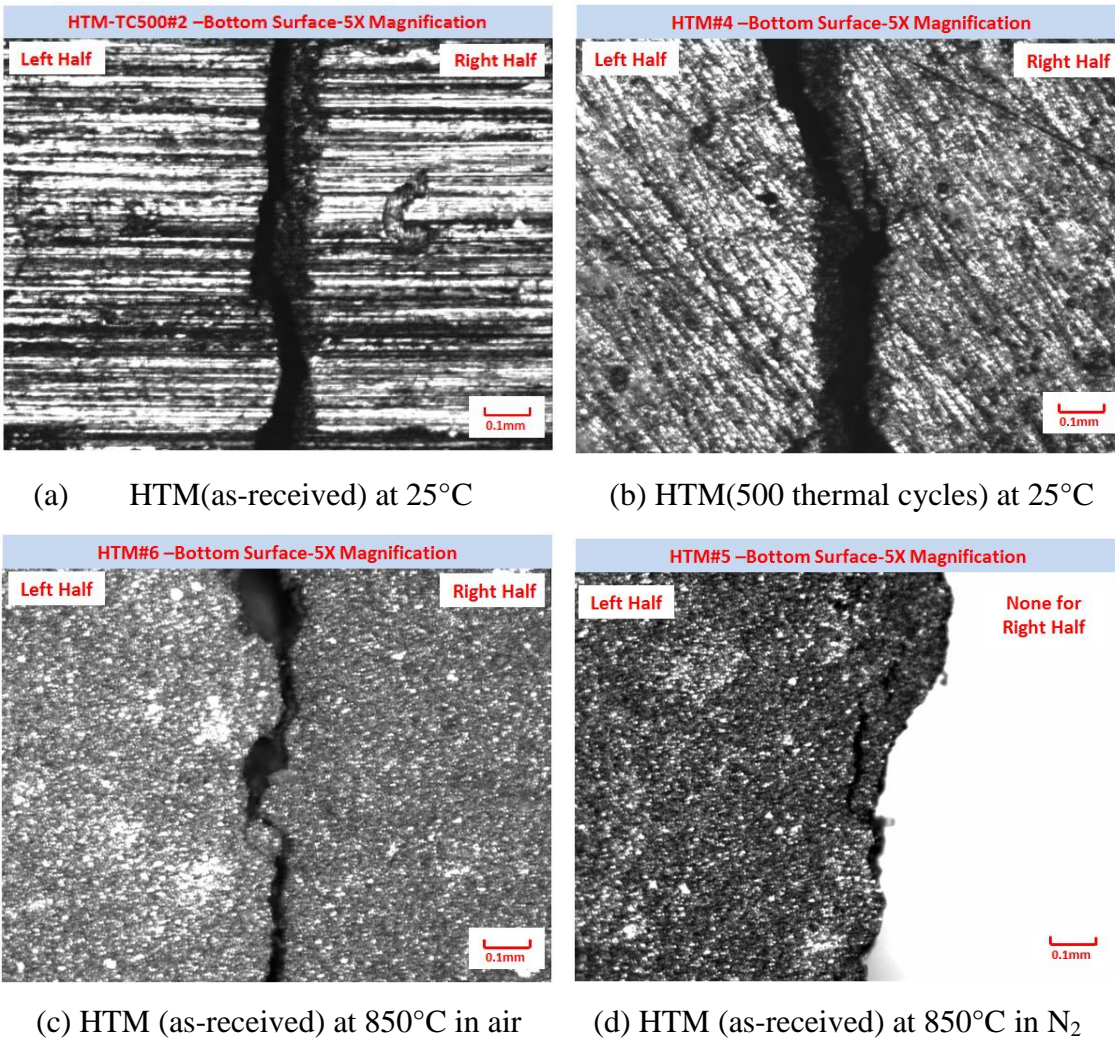
Figure 79:   Optical Observation from Bottom Surfaces of HTM Sample Bars after Flexural Strength Tests at 25°C and 850°C in Air and N$_2$ for HTM As-Received and after 500 Thermal Cycles

The crack propagation and the direction of the fracture surface based on the optical observation after flexural strength provides some basic information about the mode of the failure and characteristic of material such as brittle or ductile. Characteristic mirror-mist-hackle features are normally observed around the fracture origins, as shown schematically in Figure 80. In order to better understand the fracture mechanism of HTM cermet, a commonly used crack-branching pattern fractography was used for further evaluation by SEM. Crack origins and crack growths were captured by SEM as shown in

Figure 81 and for room temperature and Figure 82 for high temperature. For the HTM
MOR bar tested at room temperature, the type of fracture is appears to be intergranular
fracture, where the phases in the grain boundary is weak and brittle.
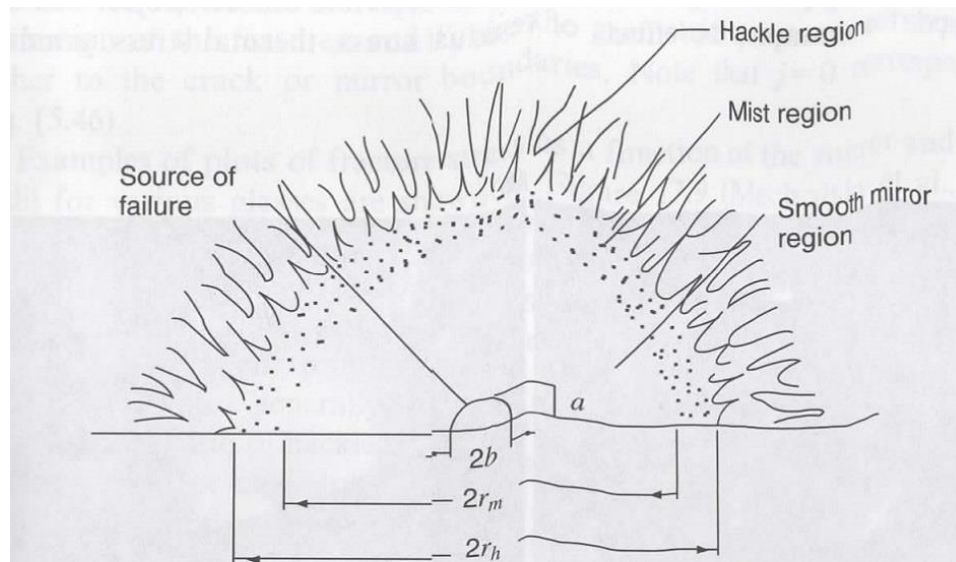
**Figure 80:   Schematic of Glass Fracture Surface Showing Fracture Mirrors, Mist
Region, and Hackle Region [55]**
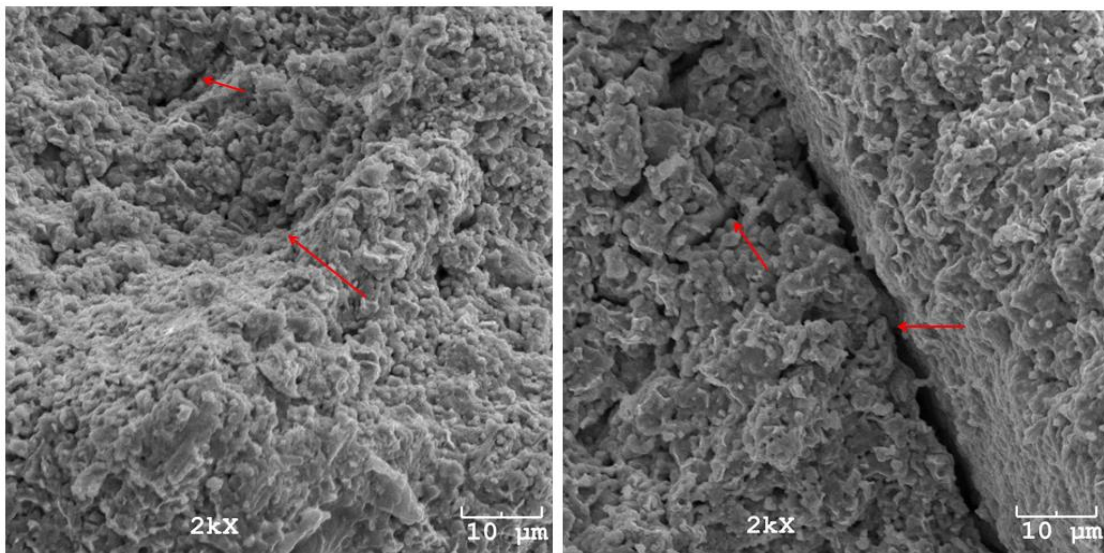
(a)   Inherited pore as crack origin   (b) Intergranular/Transgranular fractures

Figure 81:   SEM of HTM after Flexural Strength Tests at Room Temperature

(a)   850°C in air   (b)   850°C in N$_2$
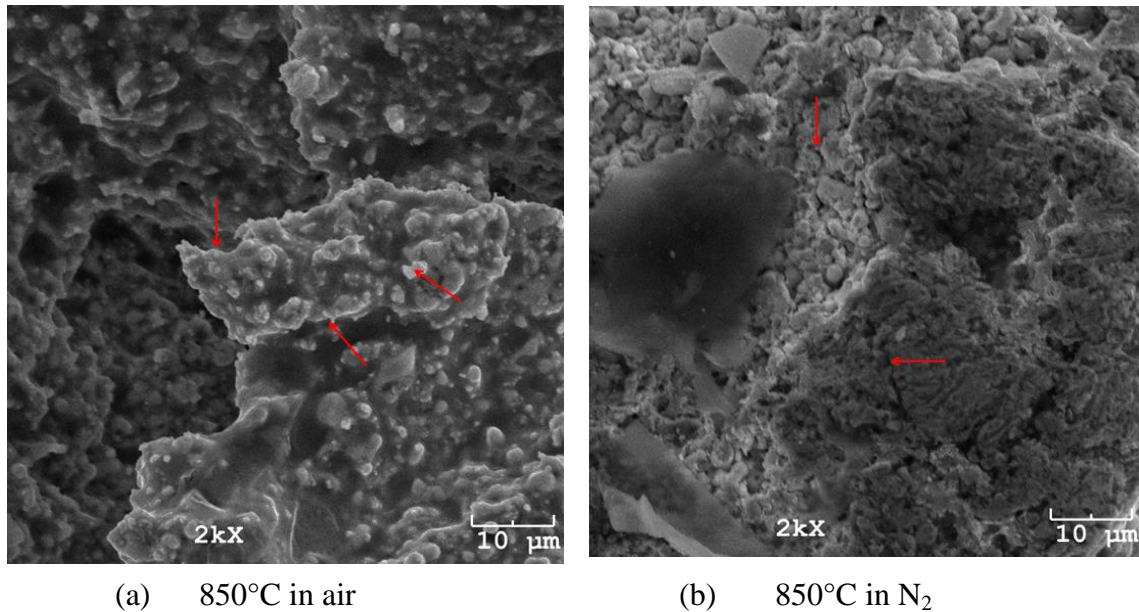
Figure 82:   Fast Transgranular Fracture with Increased Formation of Precipitate by SEM for HTM-MOR Bars after Flexural Strength at 850°C in (a) Air and (b) N$_2$

Fracture originated from existing pores and micro-cracks as shown in Figure 81 (a) and (b). Crack modes can be characterized as crack Mode I or the crack opening mode. For the HTM MOR bars tested at the elevated temperature of 850°C, the cracks also originated from existing pores and micro-cracks as shown Figure 82. The cracks are growing in combination of both transgranular and intergranular. The crack failed in Mode I and II, or tearing and opening modes.

3.3.2   Phase Analysis by XRD

3.3.2.1   Phase Analysis for HTM both As-Received and after Thermal Cycling

The XRD powder diffractions of HTM cermet are plotted with identified phases and the corresponding peaks as shown in Figure 83 (a). It is also compared with the powder diffraction reference pattern ICDD 04-015-0492 for pure palladium (Pd) [56], ICDD 01-075-9648 for tetragonal zirconia (T-ZrO$_2$) [57], and ICDD 01-080-0966 for monoclinic zirconia (M-ZrO$_2$) [58] as shown in Figure 83 (b).

Powder diffraction analysis of the HTM cermet is indexed for both the as-received sample and the sample after thermal cycling treatment up to 500 cycles in the range of 2θ between 10°~137°, as shown in Figure 84. With thermal cycling in the temperature range between 50 to 850ºC, there are new phases of PdO identified. Whereas, the peaks for palladium (Pd) are significantly decreased in the peak intensity. The higher peak intensity for PdO can be observed on the powder diffraction patterns with increasing thermal cycles. The monoclinic zirconia phase was first identified in the HTM as-received sample. However, after thermal cycling (both 120 and 500 thermal cycles), the M-ZrO$_2$ phase is transformed to the tetragonal YSZ.

3.3.2.2   Material Properties and Quantitative Analysis for HTM Cermet As-Received and after Thermal Cycling

Following identification of the existing phases by the powder diffractions for HTM, a summary of the fundamental material properties for the multi-phase system is provided in Table 48. It can be observed from Table 48, the selected metallic phase of Pd is found to have relatively similar coefficient of thermal expansion (CTE) as compared to YSZ. Therefore, the thermal mismatch due to inconsistent CTE values is significantly minimized by selecting the YSZ and Pd for the dense functional layer for the HTM system.

Based on all the identified phases of the HTM system, a semi-quantitative analysis is conducted based on the scale factor and the RIR (Reference Intensity Ratio, also known as I/I$_c$ values) values from the ICDD database. The estimated mass fractions of the accepted phases for HTM cermet are illustrate from the XRD software as shown in Figure 85. The results of the mass fractions for all the identified phases for HTM are also summarized in Table 49 and presented in Figure 86.
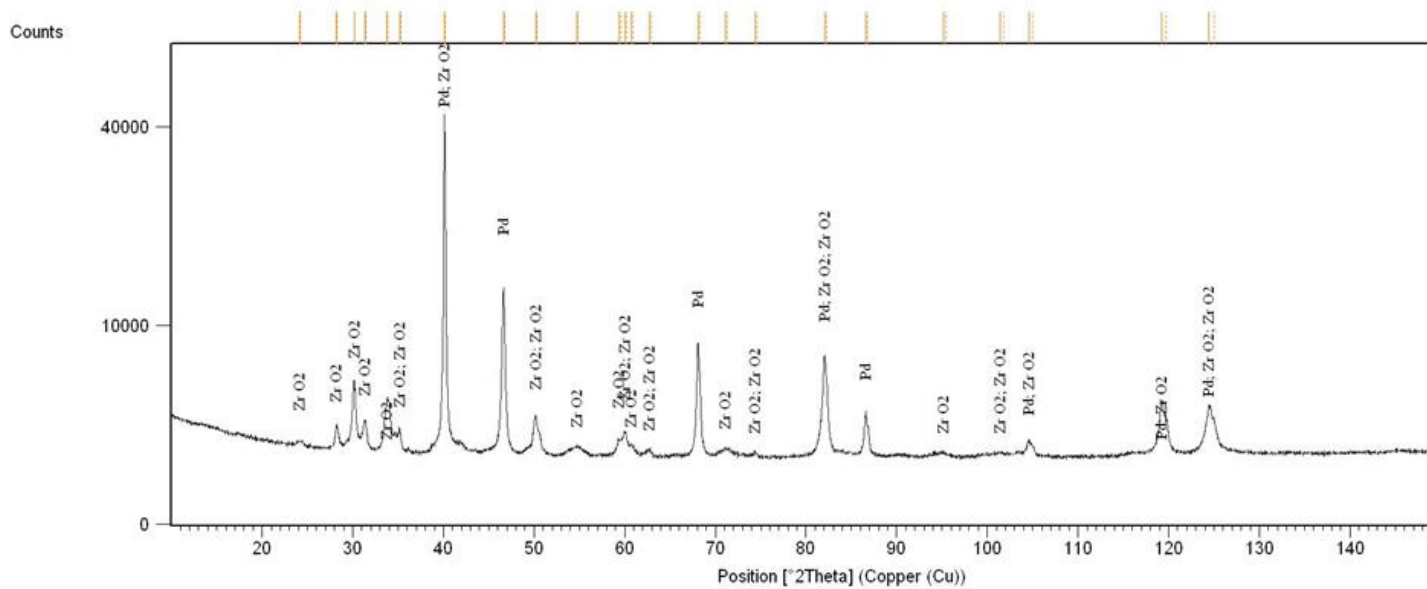
(a)   Powder Diffraction Pattern of As-Received HTM
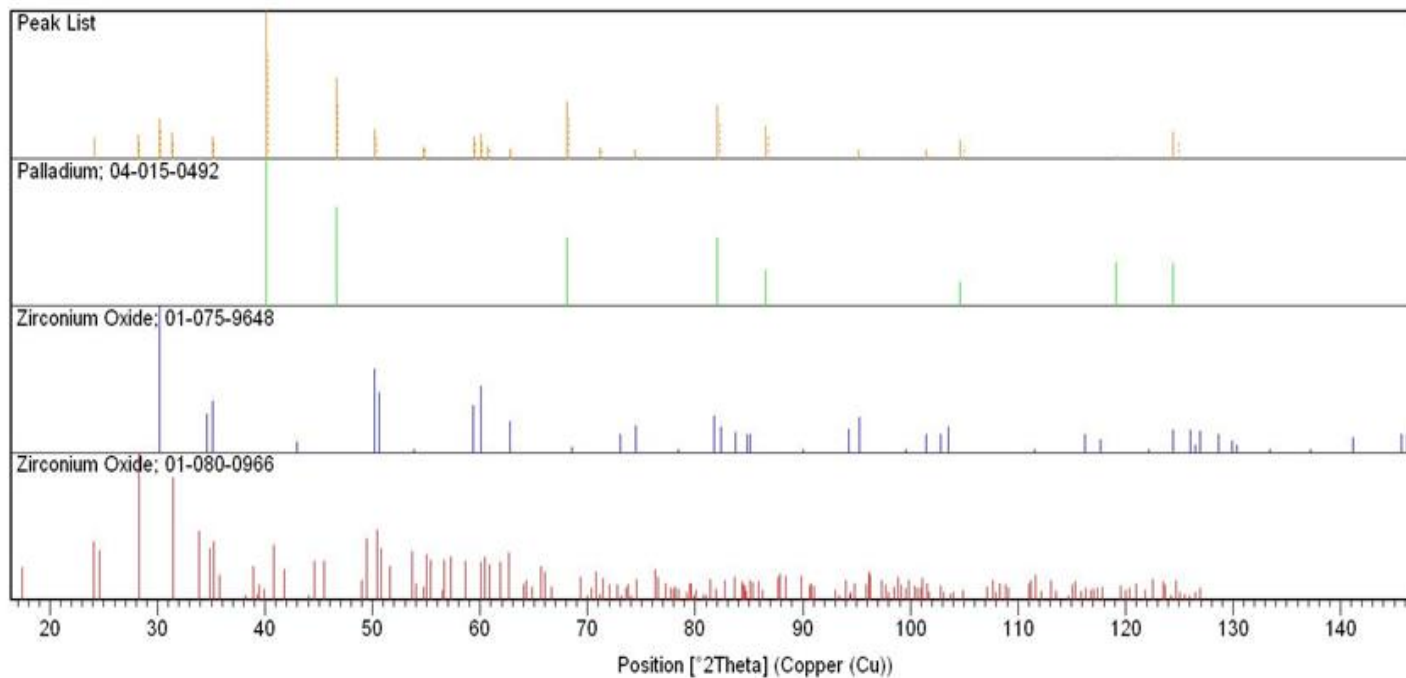
(b)   Comparison of Peaks to Reference Patterns

Figure 83:   Experimental Powder Diffraction Pattern and Phase Analysis for As-Received HTM Cermet at $20°<2\theta<150°$ and Corresponding Reference Patterns based on ICDD Database [56-58]
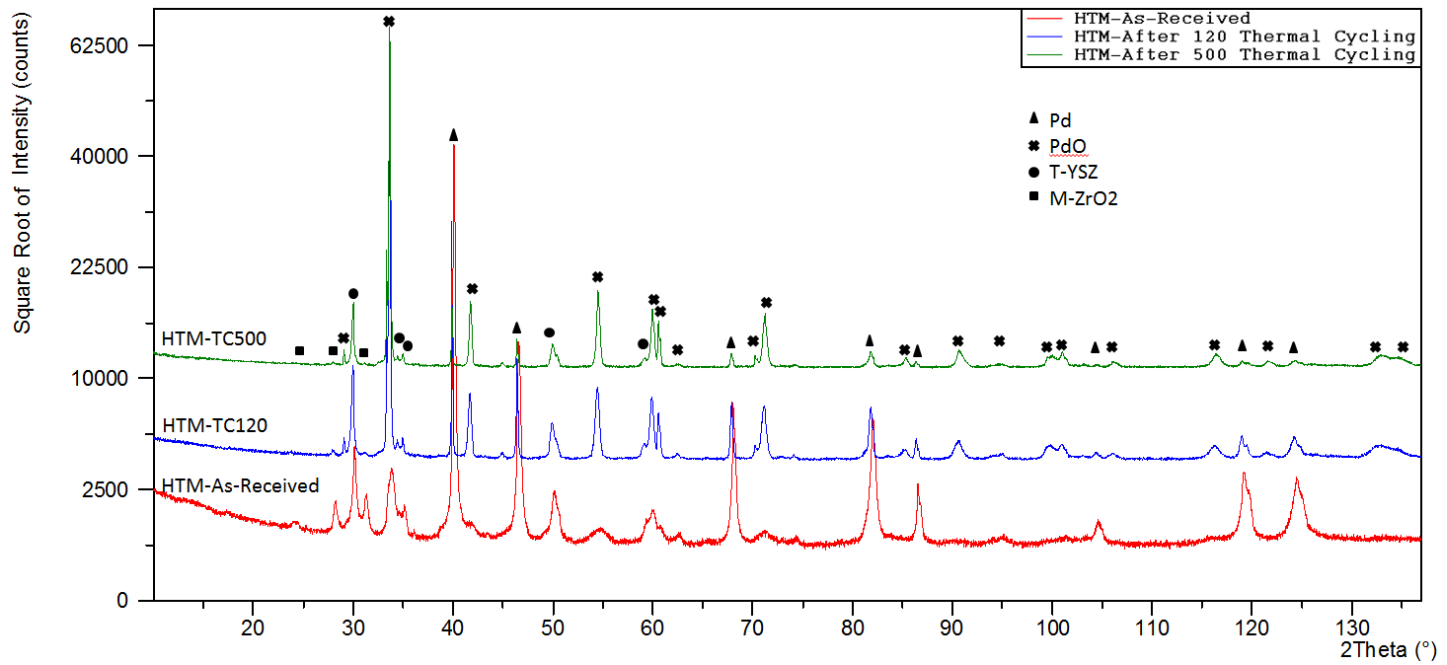
Figure 84:   XRD Phase Analysis for HTM Cermet As-Received and after 500 Thermal Cycles

Table 48: **Material Properties for the Multi Phases Identified inside HTM Cermet**

Phases	Molecular Formula	Crystal Structure	Density (g.cm^{-3})	Young's Modulus (GPa)	CTE (µm.m^{-1}.K^{-1})	Vickers Hardness (MPa)
Palladium	Pd	Cubic	12.02 [1]	121 [1]	11.8 [1]	461 [1]
Palladium Oxide	PdO	Hexagonal	8.30 [1]	n/a		
Yttria	Y$_2$O$_3$	Cubic	5.03 [2]	175 [3]	9.3 [2]	8000 [3]
Zirconia	ZrO$_2$	Monoclinic	5.68 [2]	190 [3]	7 [2]	13000 [3]
		Tetragonal	6.10 [2]		12 [2]	
Yttria Stabilized Zirconia	YSZ	Tetragonal	5.57 [4]	182.5 [4]	10.8 [4]	10500 [4]

Note: [1] Data referenced from Wikipedia

[2] Michael W Barsoum, Fundamentals of Ceramics, 2003, P96

[3] Michael W Barsoum, Fundamentals of Ceramics, 2003, P394

[4] Data is estimated by averaging the properties of Y$_2$O$_3$ and ZrO$_2$

As the treatment of thermal cycling increased from 0 to 120 cycles, the mass fraction of Pd is greatly reduced from 74% to 12%, whereas, increased amount of PdO is produced by the oxidation of Pd with O$_2$. The other zirconia phases, including both M-ZrO$_2$ and YSZ, did not change significantly with the treatment of thermal cycling between 50 to 850°C.

3.3.2.3 Phase Analysis for HTM Cermet As-Received and after Annealing in N$_2$ Environments

The phase analyses of HTM as-received and after soaking in N$_2$ at room temperature and annealing at high temperature are shown in Figure 87 and Figure 88. A clearer comparison for all three powder diffractions in smaller scales of diffraction ranges is shown in Figure 89 (a) to (e).

The powder diffraction pattern of HTM as-received is quite identical with the HTM after soaking in N$_2$ at room temperature (Figure 87). The HTM after annealing in N$_2$ at high temperature for 48 hours, however, gave a quite different powder diffraction pattern than the as-received sample (Figure 88).

The peaks of monoclinic zirconia phase at $2\theta \approx 28°$ and $31°$ are dissolved into tetragonal YSZ phase at $2\theta \approx 30°$, as shown in Figure 89 (a). All the Pd phase peaks of HTM after annealing in N_2 at high temperature display identical peak positions with more distinctly separated peaks by $K\alpha_1$ and $K\alpha_2$, as shown in Figure 89 (a) to (e). Most peaks' shapes become narrower and higher in intensity, plus the better separation of $K\alpha_1$ and $K\alpha_2$, which are all related to the better crystallographic structure of the Pd phase and larger crystallographic grain size [59]
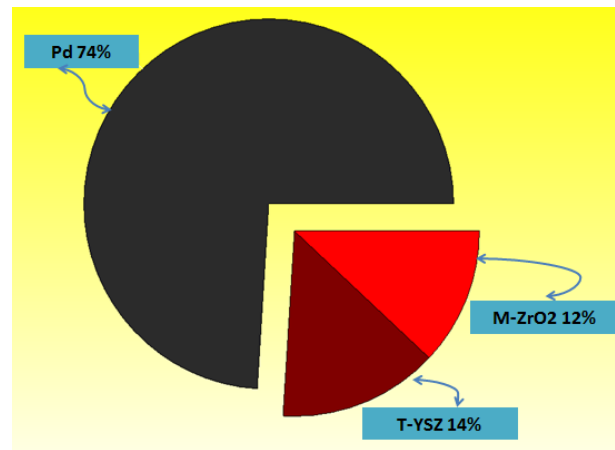
(a) HTM As-Received
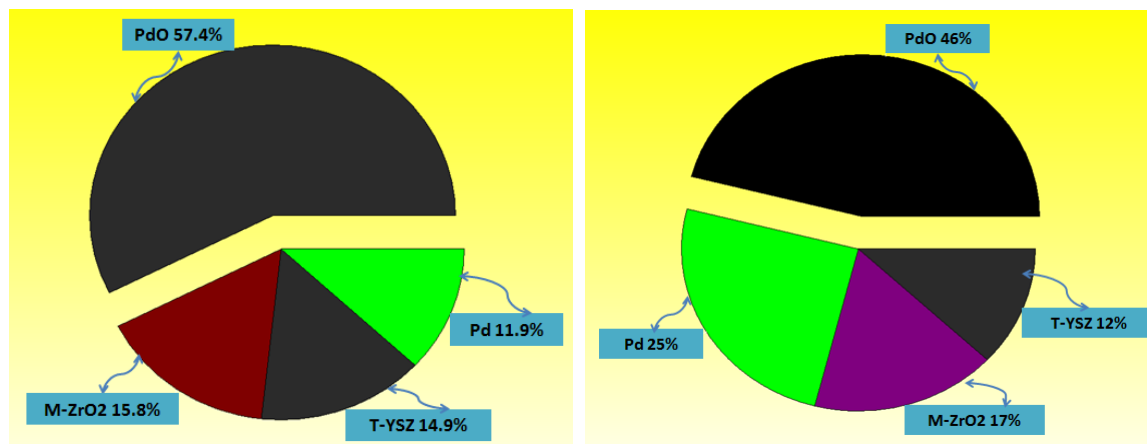
(b) HTM after 120 Thermal Cycles   (c) HTM after 500 Thermal Cycles

Figure 85:   Diagrams of Quantitative Analysis for Multi Phases inside HTM Cermet both As-Received and after Thermal Cycling (50-850°C)

129

Table 49: Mass Fraction (%) of all Identified Phases in HTM Cermet both As-Received and after Thermal Cycling (50-850°C)

Phase in HTM	Number of Thermal Cycles (50-850°C)	Estimated Mass Fraction (%)
Pd	0	74.0
	120	25.0
	500	11.9
PdO	0	0.0
	120	46.0
	500	57.4
T-YSZ	0	14.0
	120	12.0
	500	14.9
M-ZrO$_2$	0	12.0
	120	17.0
	500	15.8
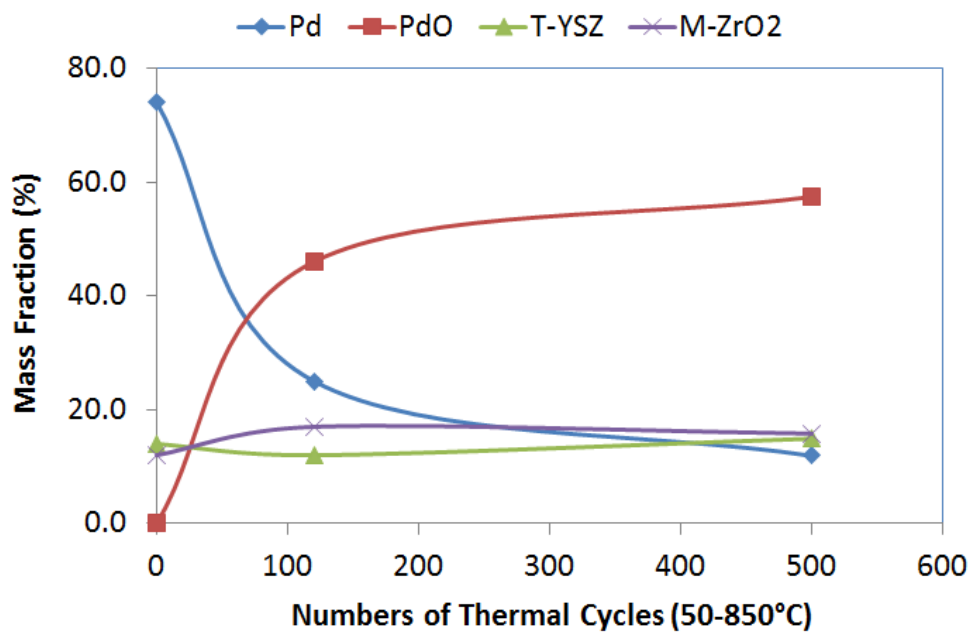
Figure 86: Results of Mass Fraction (%) for the Multi Phases in HTM both As-Received and after Thermal Cycling Treatment between 50-850°C

.
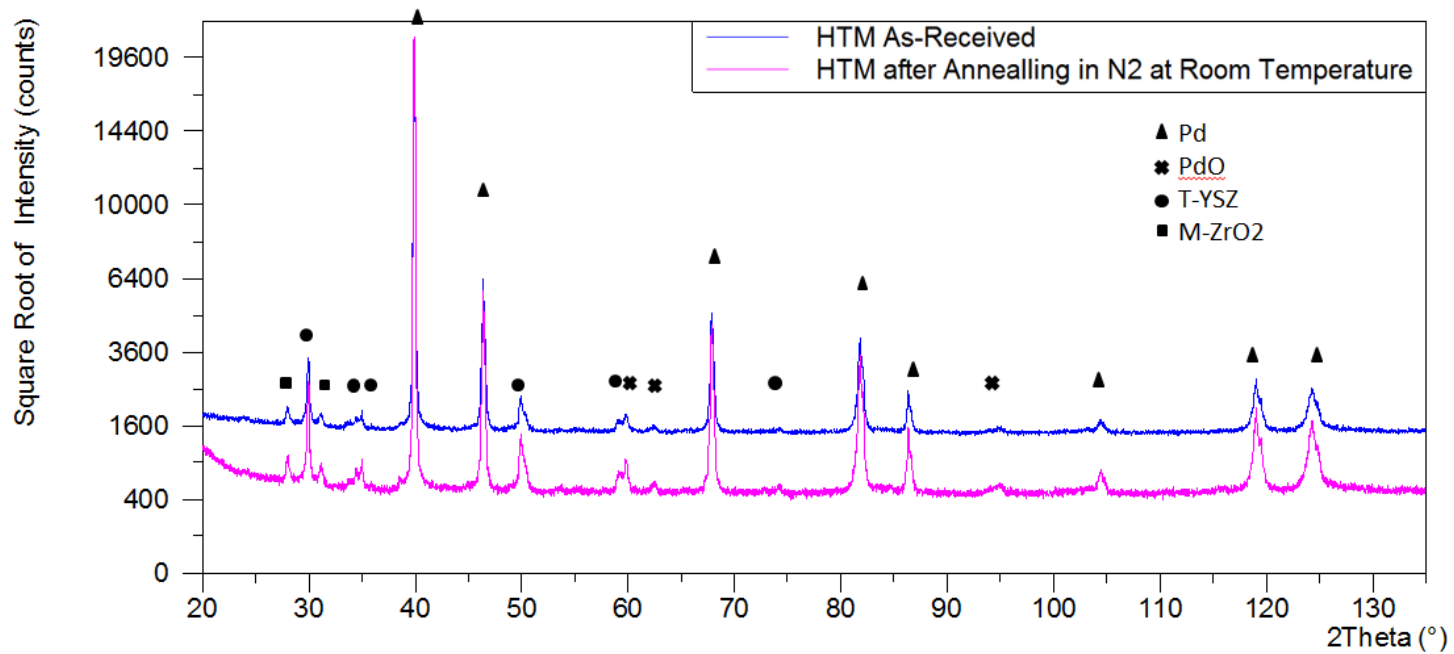
Figure 87: Phase Analysis for HTM As-Received and after Soaking in N_2 at Room Temperature (25°C)
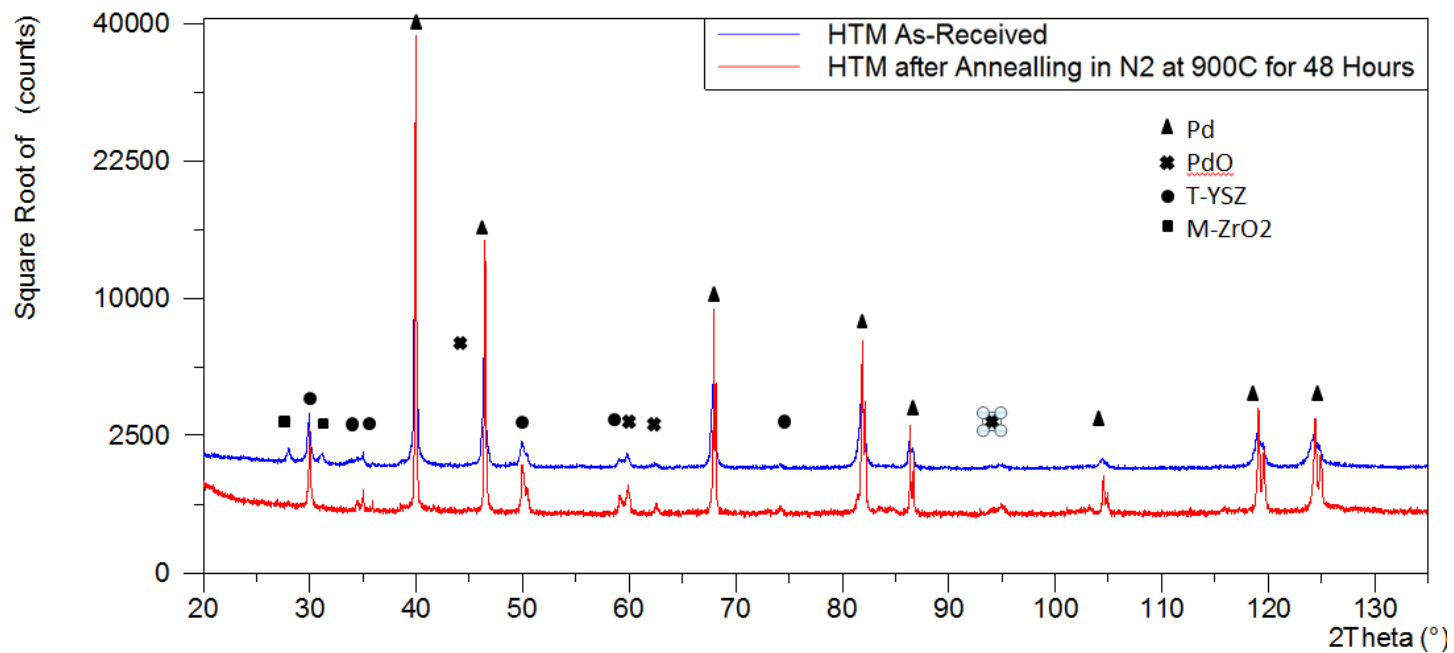
Figure 88: Phase Analysis for HTM As-Received and after Soaking in N_2 at the Elevated Temperature of 900°C
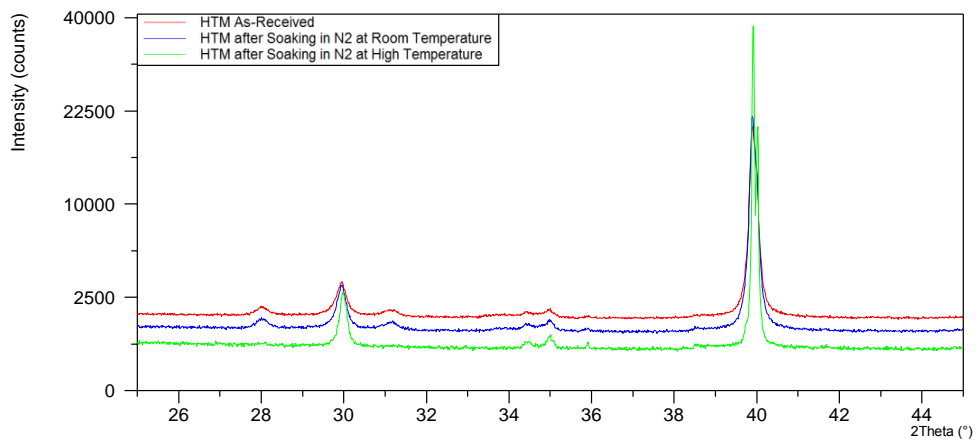
(a) $2\theta \approx 25\text{-}45°$
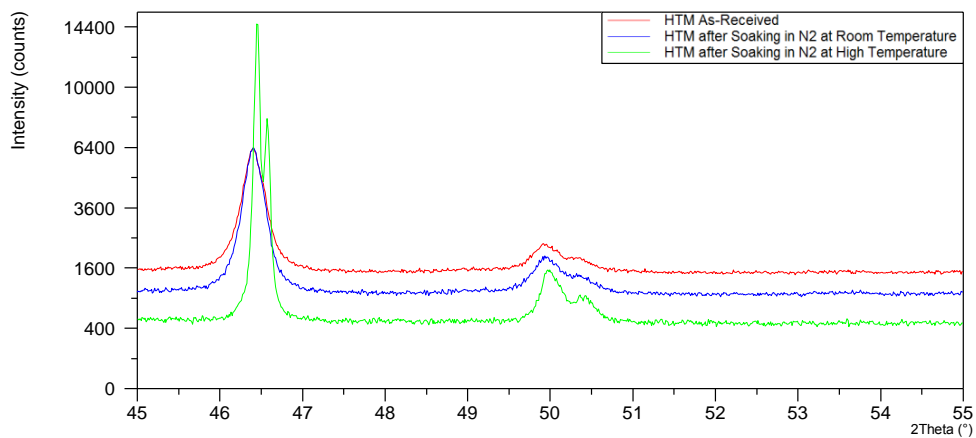
(b) $2\theta \approx 45\text{-}55°$
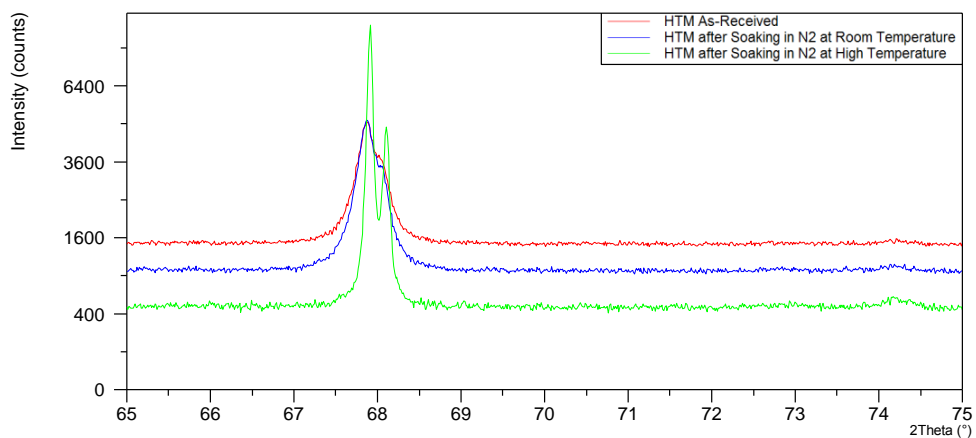
(c) $2\theta \approx 65\text{-}75°$
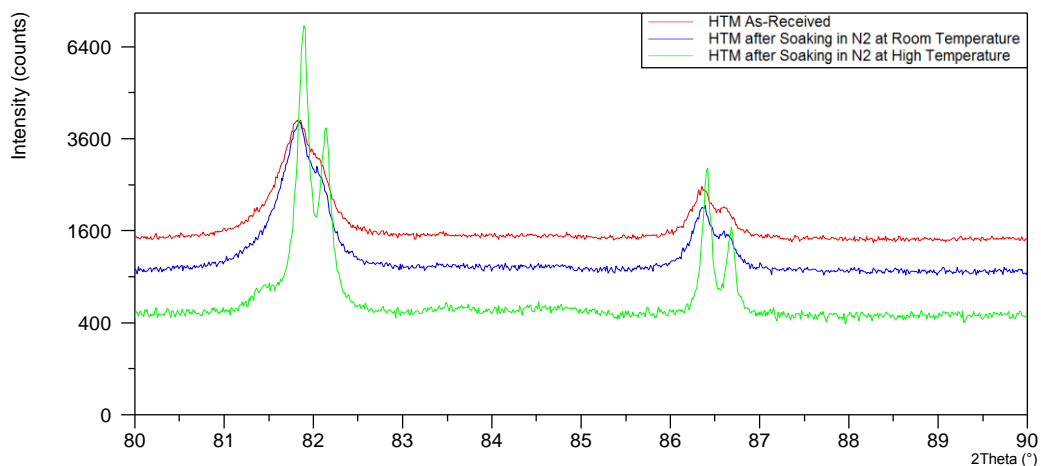
(d) $2\theta \approx 80\text{-}90°$
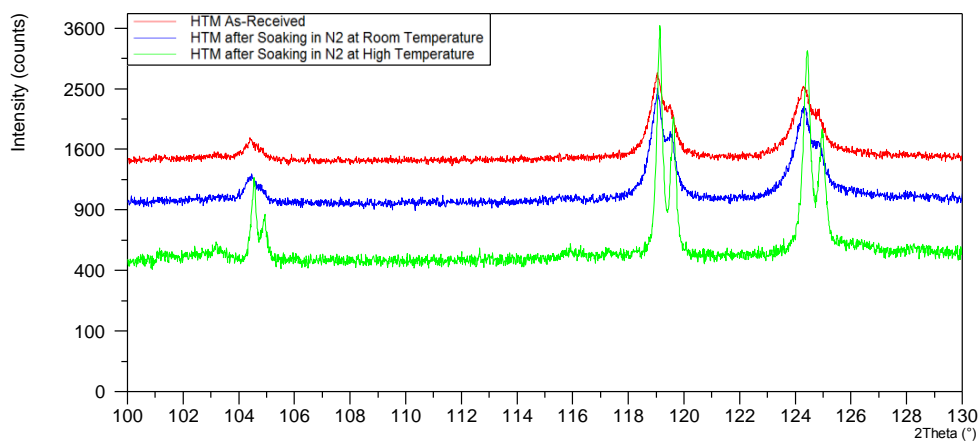
(e) $2\theta \approx 100\text{-}130°$

Figure 89: **Phase Comparison in Smaller Scales for HTM As-Received and after Soaking in N_2 at Room Temperature (25°C) and the Elevated Temperature (900°C)**

3.3.2.4   Phase Analysis for HTM Cermet Powder

The HTM raw powder was prepared for the XRD powder diffraction with the powder holder and XRD set up as shown in Figure 90. The powder diffraction analysis for the HTM raw powder and HTM cermet is indexed within the 2θ angles of $10°\sim137°$, as shown in Figure 91. These two powder diffraction patterns of HTM solid sample and HTM raw powder are very similar in composition of multi-phases of Pd, T-YSZ, and M-

ZrO2. However, there is also PdO phase peaks appeared in the powder diffraction pattern of HTM solid sample as opposed to HTM raw powder, as shown in Figure 91.

(a) Sample holder for powder   (b) Holder compressed with HTM powder
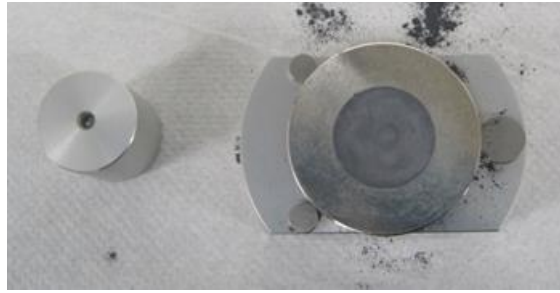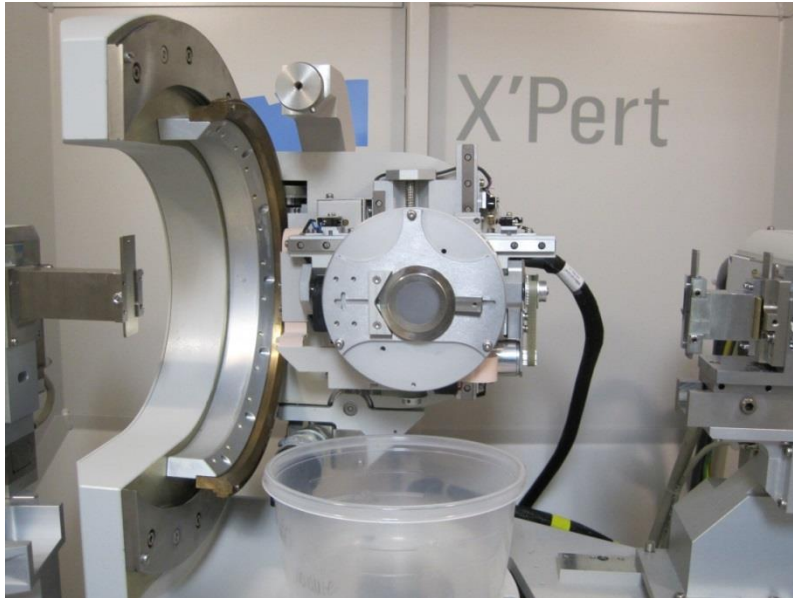
(c) Powder sample for XRD phase analysis and residual stress

Figure 90:   XRD System Setup for Powder Diffraction, Texture, and Residual Stress Measurement for HTM Raw Powder
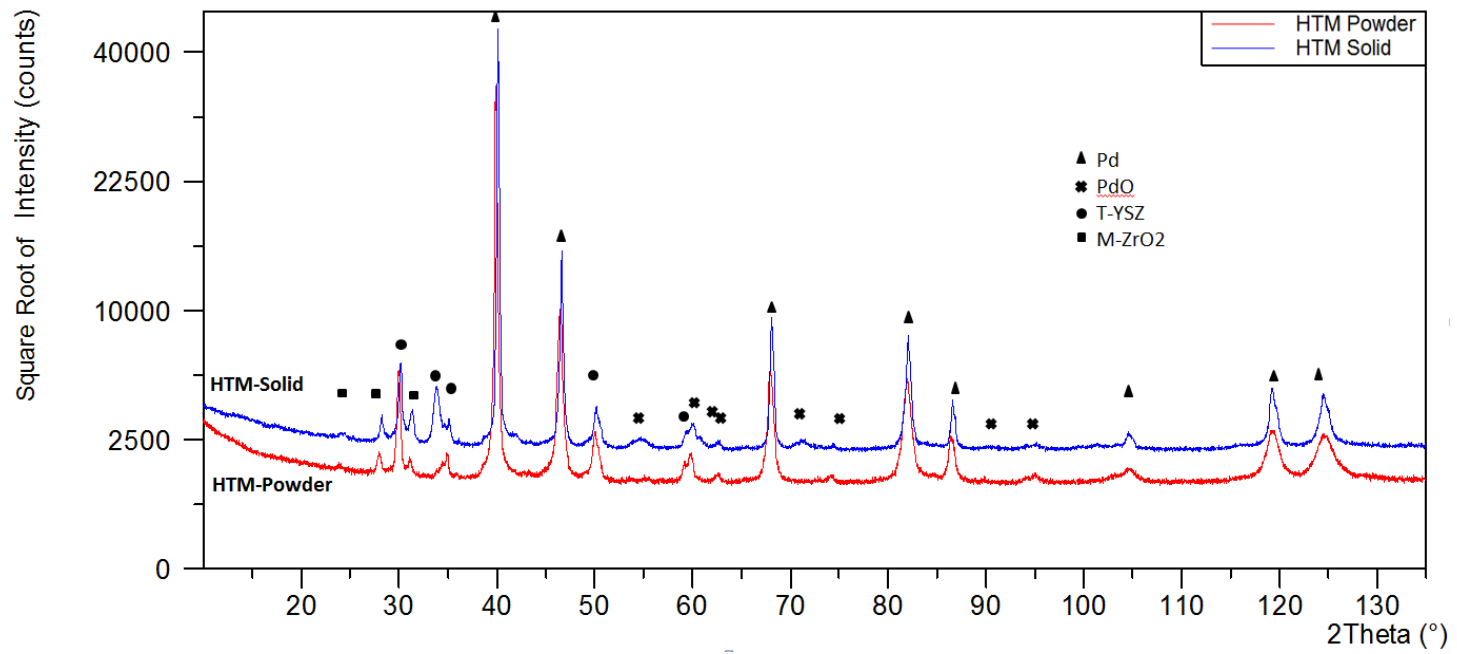
Figure 91: **XRD Phase Analysis for HTM Raw Powder and HTM Cermet Solid**

136

3.3.3   Texture Analysis by XRD Pole Figures

3.3.3.1   Texture Analysis for HTM Cermet Solid

Pole figures were measured at two selected peak 2θ values, $2\theta \approx 40°$ for Pd(111) and $2\theta \approx 68°$ for Pd(200), by rotating the sample using the parameters of psi (ψ) and phi (φ), as shown in Figure 92. The parameter of ψ was set to range from 0° at the center to 85° at the edge, and the parameter of φ was set to range from 0° to 360°. Because the overlapping occurred for most peaks for the tetragonal and monoclinic zirconia phases, texture analysis for these two zirconia phases in HTM was conducted for two selected peak 2θ values, $2\theta \approx 28°$ for M-ZrO2(-111) and $2\theta \approx 30°$ for T-ZrO2(101) as shown in Figure 93(a) and (b) for the as-received surface and polished surface, respectively. The pole figure for Pd phase in HTM cermet were conducted based on the two selected 2θ values, $2\theta \approx 40°$ for Pd(111) and $2\theta \approx 46°$ for Pd (200) as shown in Figure 94 (a) and Figure 94 (b) for the as-received surface and polished surface, respectively. Both Figure 93 and Figure 94 demonstrate that the surface morphology significantly impacts the integrity of the pole figure, as the parameters φ and ψ change and the sample rotate along with these two parameters.
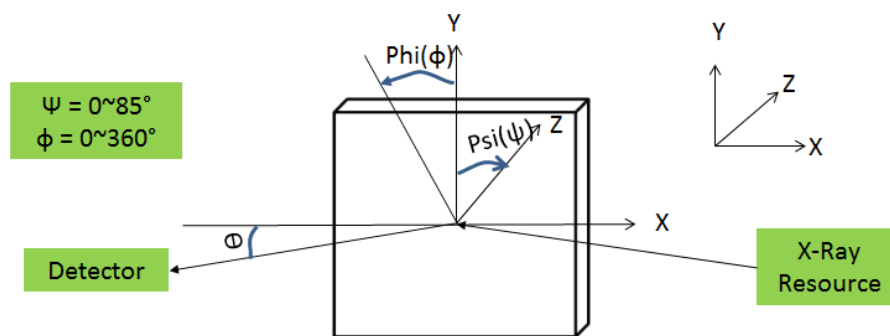
Figure 92:   Axis and Angle Definition for Pole Figure Construction for Texture Analysis

(a) As-Received Surface
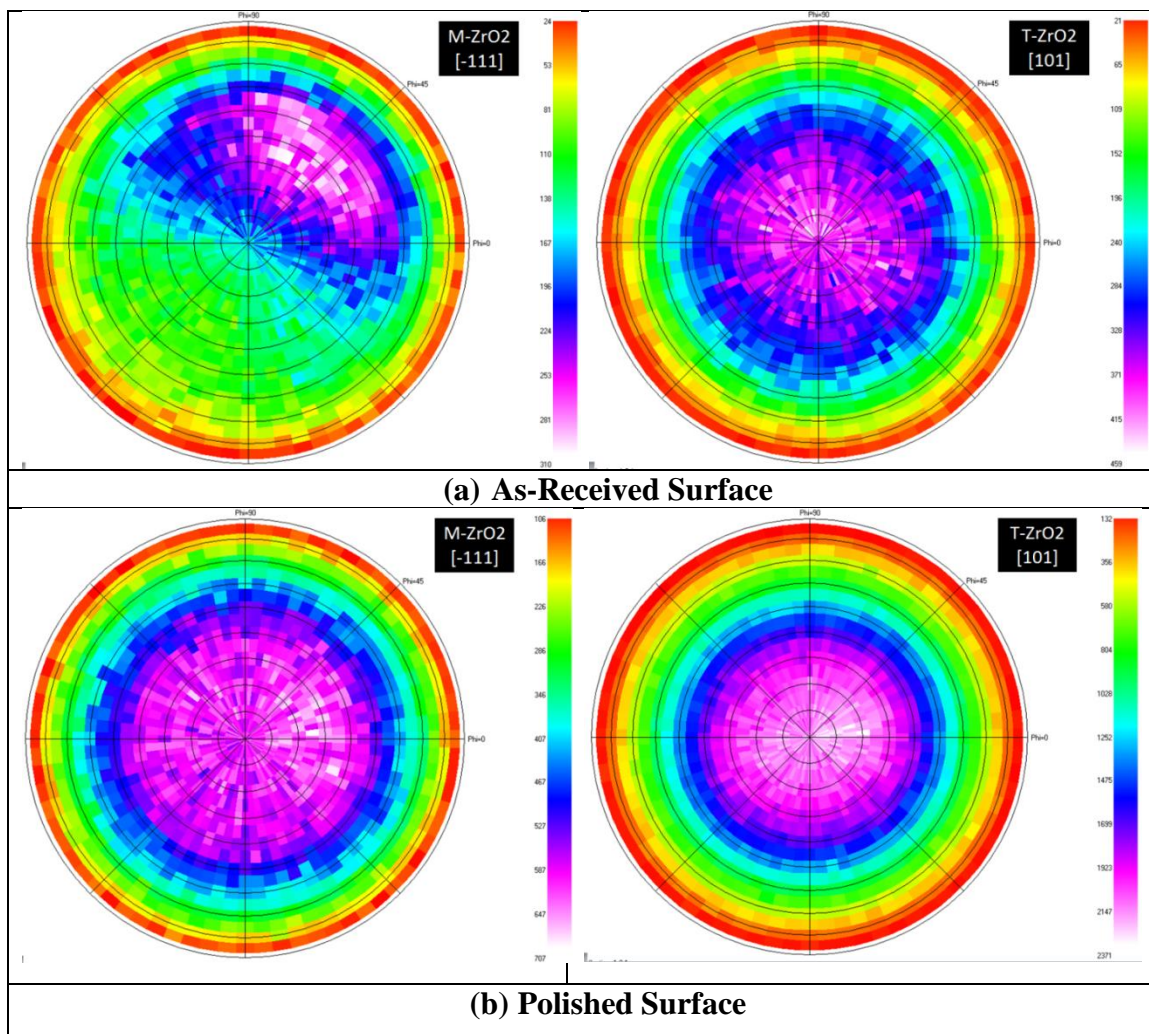
(b) Polished Surface

Figure 93:   Pole Figure For HTM Cermet Polished Surface Texture Analysis based on Zirconia Crystallographic Planes, M-ZrO$_2$(-111) and T-ZrO$_2$(101)

Based on the cubic crystallographic structure of Pd, the a-axis in the unit cell of the crystallographic structure is perpendicular to the crystallographic plan of Pd (200). As shown in Figure 94, with the parameter value of ψ tilting from 0 to 45°, the intensity of the pole figure of Pd (200) can be observed to be slowly decreased due to the effect of tilting of incident XRD plane. The same trend is also true for all other selected crystallographic plans for the phase of Pd as show in Figure 95. Therefore, the studied HTM cermet is a non-textured materials based on the pole figures by XRD technique.

138

(a) As-Received Surface
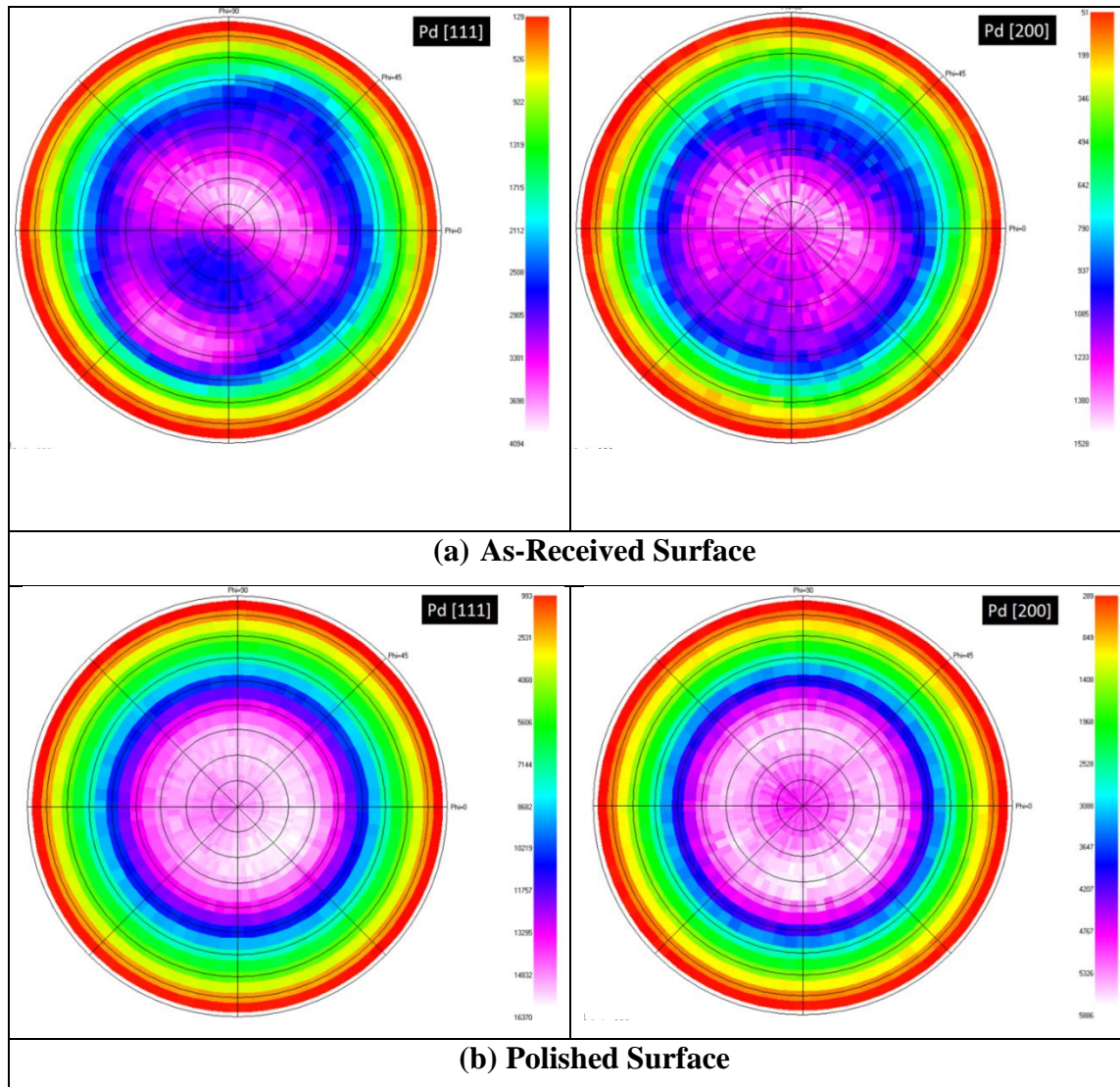
(b) Polished Surface

Figure 94:   Pole Figure for HTM Cermet Texture Analysis based on Palladium Crystallographic Planes of Pd(111) and Pd(200) for both (a) As-Received Surface and (b) Polished Surface
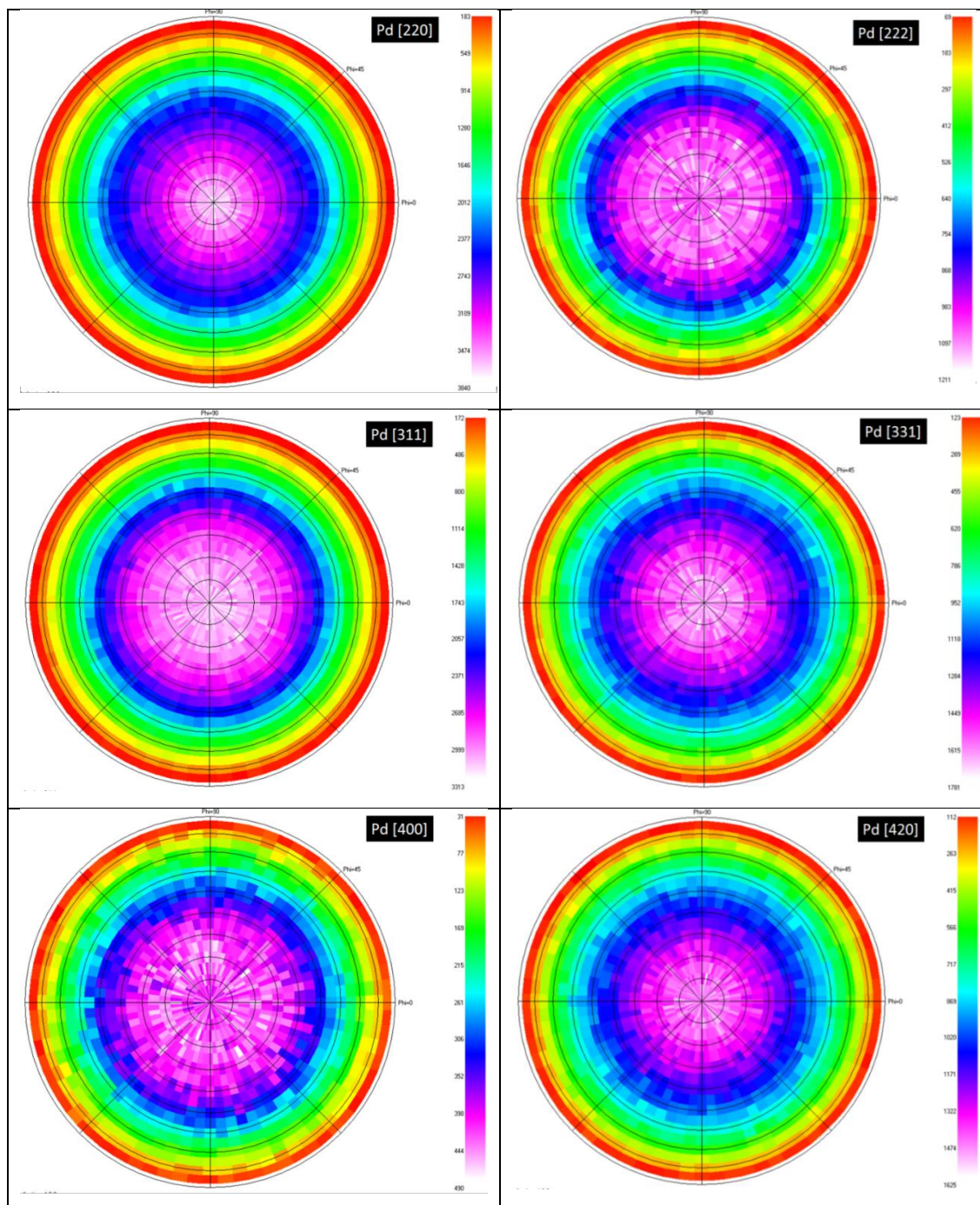
Figure 95:   Pole Figure for HTM Polished Cermet Based on Palladium Crystallographic Planes, Pd(220), Pd(222), Pd(311), Pd(331), Pd(400), and Pd(420)

140

3.3.3.2 Texture Analysis for HTM Cermet Powder

At three selected peak 2θ values: $2\theta \approx 40°$ for Pd(111), $2\theta \approx 68°$ for Pd(200), and $2\theta \approx 86°$ for Pd(222), pole figures were measured by rotating the sample using the parameters of psi (ψ) and phi (φ). The parameter of ψ was set to range from 0° at the center to 85° at the edge, and the parameter of φ was set to range from 0° to 360°. The pole figures based on the selected Pd phases are shown in Figure 96 for the HTM raw powder sample. It is generally known that powder sample should have no texture, which is verified from the three pole figures by XRD texture analysis for HTM raw powder.
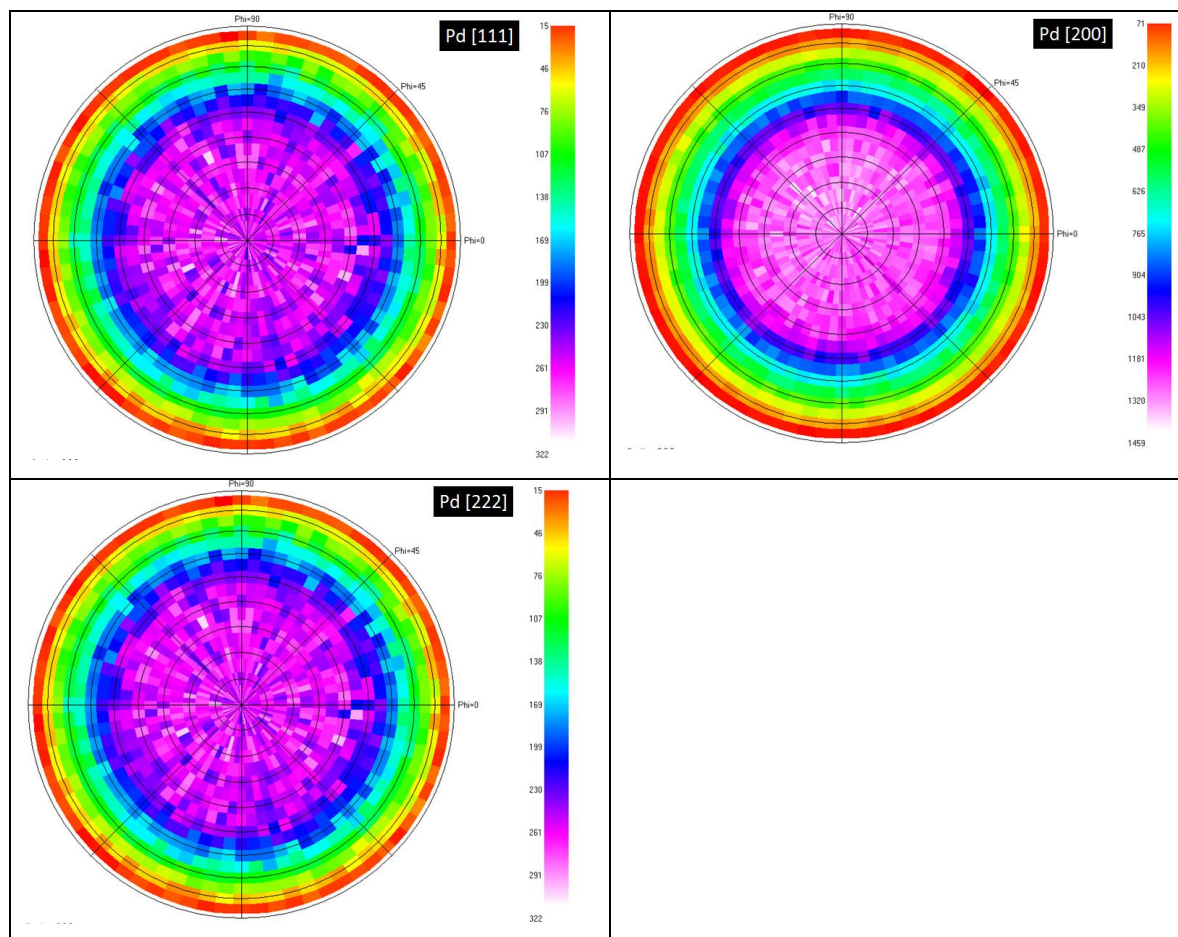
Figure 96:   Pole Figure of HTM Raw Powder Based on Palladium Crystallographic Planes: Pd(111), Pd(200), and Pd(222)

3.3.4 Surface Morphologies for HTM As-Received and after Thermal Cycling by Visual and Optical Observation

Visual surface morphologies for HTM both as-received and after 500 thermal cycles (polished and unpolished surface) were recorded by a digital camera and are shown in Figure 97 (a) to (c). There is one major crack propagated from the edge to the center on the polished surface as shown in Figure 97 (b). On the unpolished surface, many tiny cracks are observed to propagate along the circular edge as seen from Figure 97 (c).
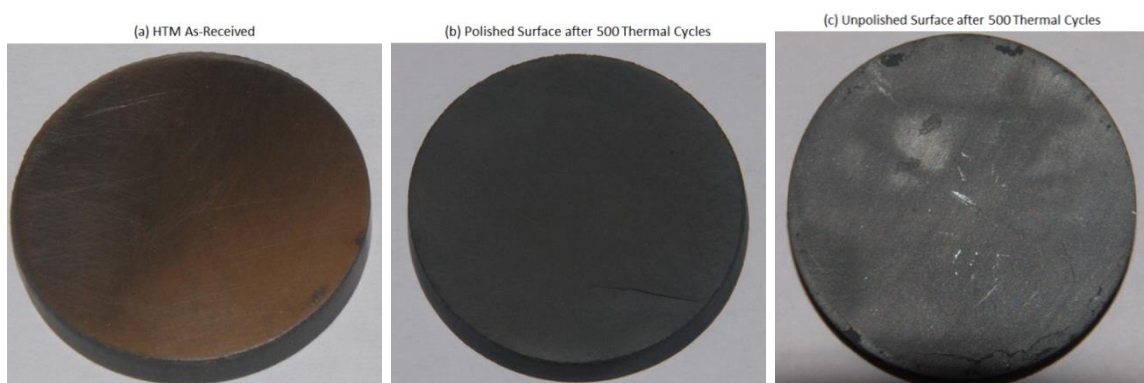
Figure 97: **Visual Observation of Surface Morphology by Digital Camera for HTM Cermet both As-Received and after Thermal Cycling Treatment**

Optical observation on the surface morphology was studied under magnification from 5x to 50x by the Olympus BX 60 microscope. Change of surface morphology as an effect of thermal cycling was first observed in the pictures shown in Figure 98 (a) to (d) for HTM as-received (polished and not polished), after 120 thermal cycles, and after 500 thermal cycles, respectively.

With the thermal cycling up to 120 cycles between 50–850ºC, HTM cermet started to have some micro-cracks that could be observed only by microscope under the magnification 50x as shown in Figure 98 (c). There are some macro-cracks which could be seen by naked eyes on the surface of the HTM cermet after 500 thermal cycles as seen from Figure 98 (d).

Before Polishing – Magnification 5x

Before Polishing – Magnification 50x

0.1mm

0.01mm
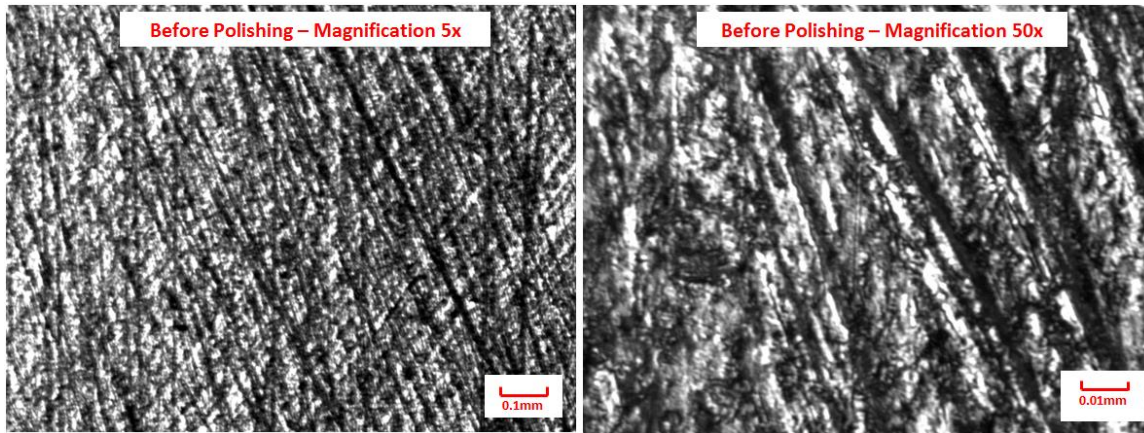
(a) HTM Cermet As-Received without Polishing

After Polishing – Magnification 5x

After Polishing – Magnification 50x

0.1mm

0.01mm
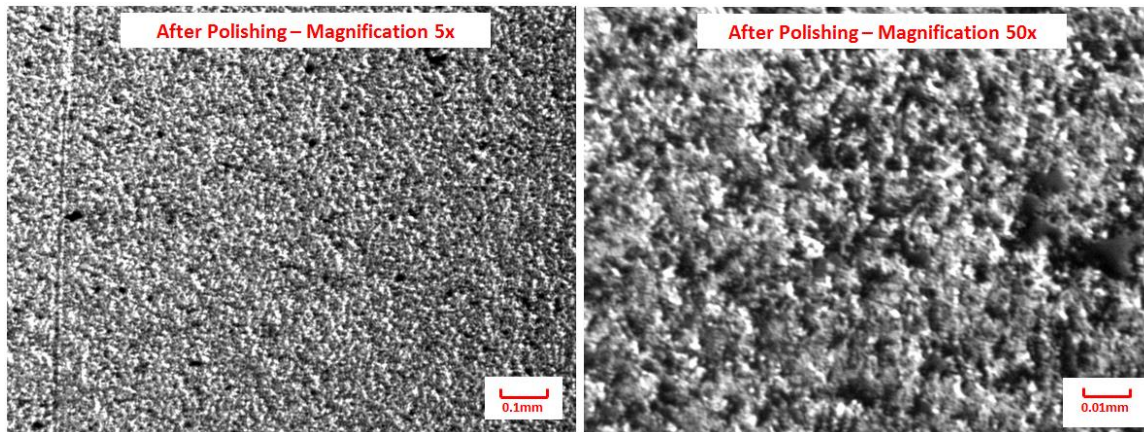
(b) HTM Cermet As-Received after Polishing

HTM after 120 Thermal Cycling
Magnification 5X

HTM after 120 Thermal Cycling
Magnification 50X

0.1mm

0.01mm
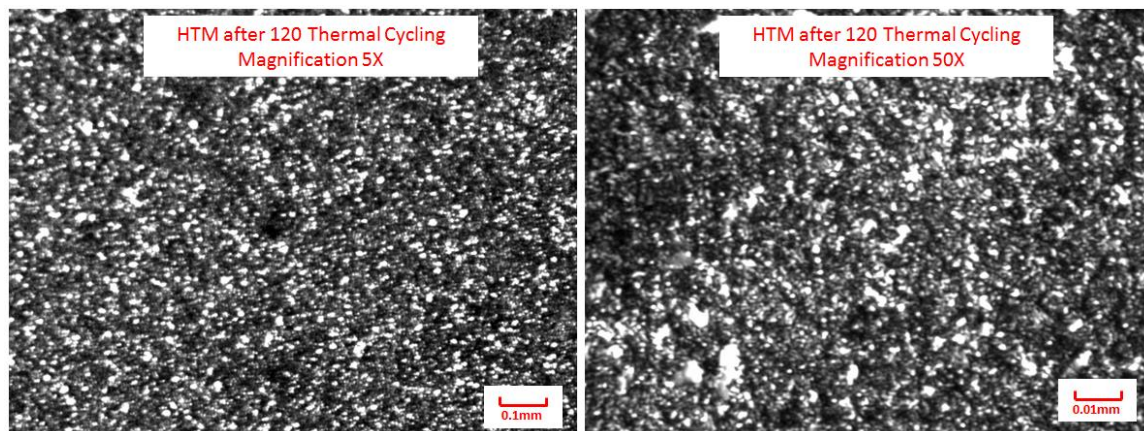
(c) HTM Cermet after 120 Thermal Cycles
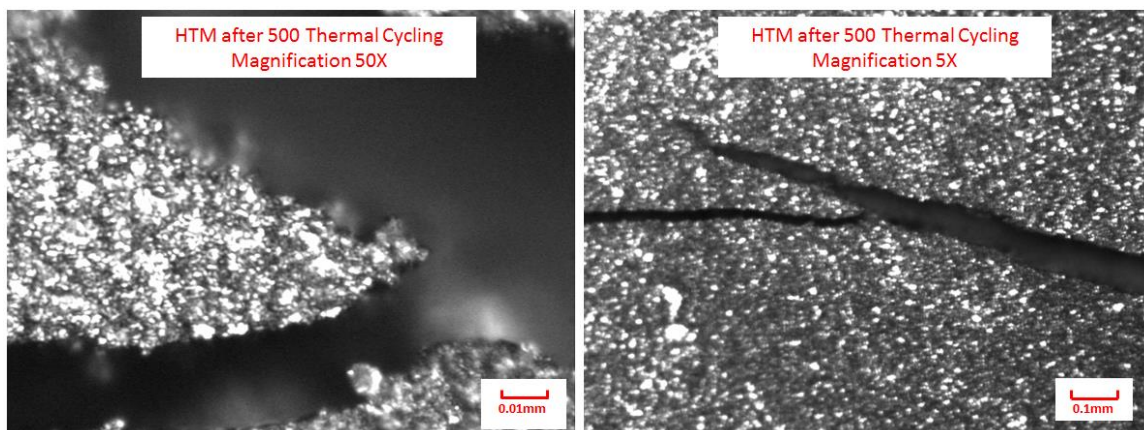
(d) HTM Cermet after 500 Thermal Cycles

Figure 98: **Optical Observation for Surface Morphology by Olympus BX 60 Microscope for HTM Cermet (a) As-Received; (b) after 120 Thermal Cycles; (c) after 500 Thermal Cycles**

A total of four HTM cermet pieces were polished to 0.25μm diamond precision to represent the top surface and the cross-section of HTM cermet both as-received and after 500 thermal cycles. These HTM cermet pieces were embedded into permanent epoxy to get ready for further microstructural studies, as shown in Figure 99.

The schematic diagram of the cross-section for HTM after 500 thermal cycles is shown in Figure 100. Three distinctive layers could be observed on the cross-section for HTM cermet after 500 thermal cycling treatments between 50–850°C in air. The top and bottom layers are light green color observed by naked eyes, whereas the middle layer is the same grey color as the cross-section of as-received HTM. As discussed in the XRD powder diffraction phase analysis and TG/DTA, the top and bottom layers could be composed mainly of Palladium oxide (PdO), the unreactive Pd or dissociated Pd phase, and the YSZ phases. The middle layer of the HTM Disc sample is therefore estimated unreactive after 500 thermal cycles and is mainly composed of the same Pd and YSZ phases as the raw material.

There are also three visible cracks with different crack lengths on the sample cross-

144

section of the HTM cermet, as seen from Figure 100. The shortest crack is closest to the center of the HTM sample disc, while the longest crack is near the disc edge, as illustrated in Figure 100. These three visible cracks are mainly in the middle layer, in the center of the cross-section of HTM cermet as a result of 500 thermal cycling.
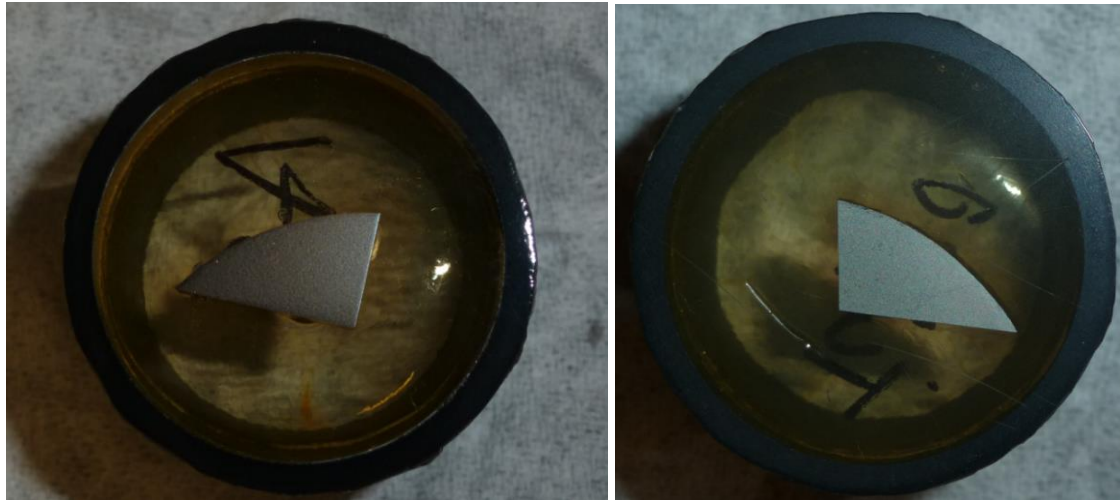
(a) Top Surface of HTM (As-Received)   (b) Top surface of HTM (500 Thermal Cycles)

(c) Cross-section of HTM (As-Received)   (d) Cross-section of HTM (500 Thermal Cycles)

Figure 99:   Polished HTM Cermet for Top Surface and Cross-Section of HTM Cermet As-Received and after 500 Thermal Cycles
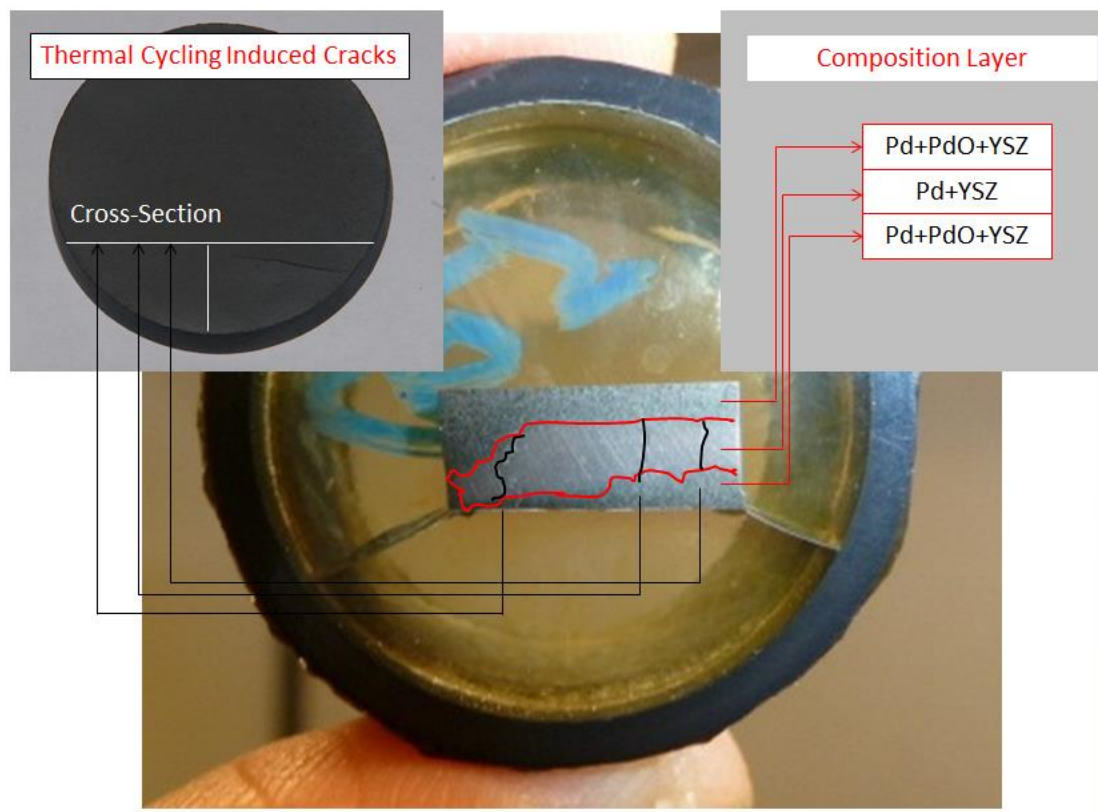
Figure 100:   Schematic Diagram of Composition Layer and Thermal-Cycling-Induced Cracks on the Cross-Section for HTM after 500 Thermal Cycles between 50-850°C

The microscopic optical observation for these different HTM cermet pieces (i.e., top surfaces and cross-section surfaces for HTM as-received and after 500 thermal cycles in Figure 100) was firstly captured with Olympus BX60 microscope before the samples were carbon-coated and prepared for SEM and microprobe analysis. The microscopic morphology of the top surfaces for the HTM both as-received and after 500 thermal cycles is shown in Figure 101.

The top surface became more porous with the discontinuous phases after 500 thermal cycling processes as compared with HTM as-received as shown in Figure 101. Microscopic optical observations for the cross-section are captured by the microscope for HTM both as-received and after 500 thermal cycling, as shown in Figure 102. The Cross-

section surface morphology is composed of two interconnected phases as it is similar to that of the top surface for the as-received HTM. With the thermal cycling process for up to 500 cycles, the surface morphology of the cross-section of the top and bottom layers as illustrated in Figure 100 became more porous and new phase appeared.

HTM As-Received Top Surface	HTM 500 Thermal Cycled Top Surface
Pd & YSZ Dual Phases	PdO & Pd &YSZ Multi-Phases
(a) 5X	
(b) 50X	
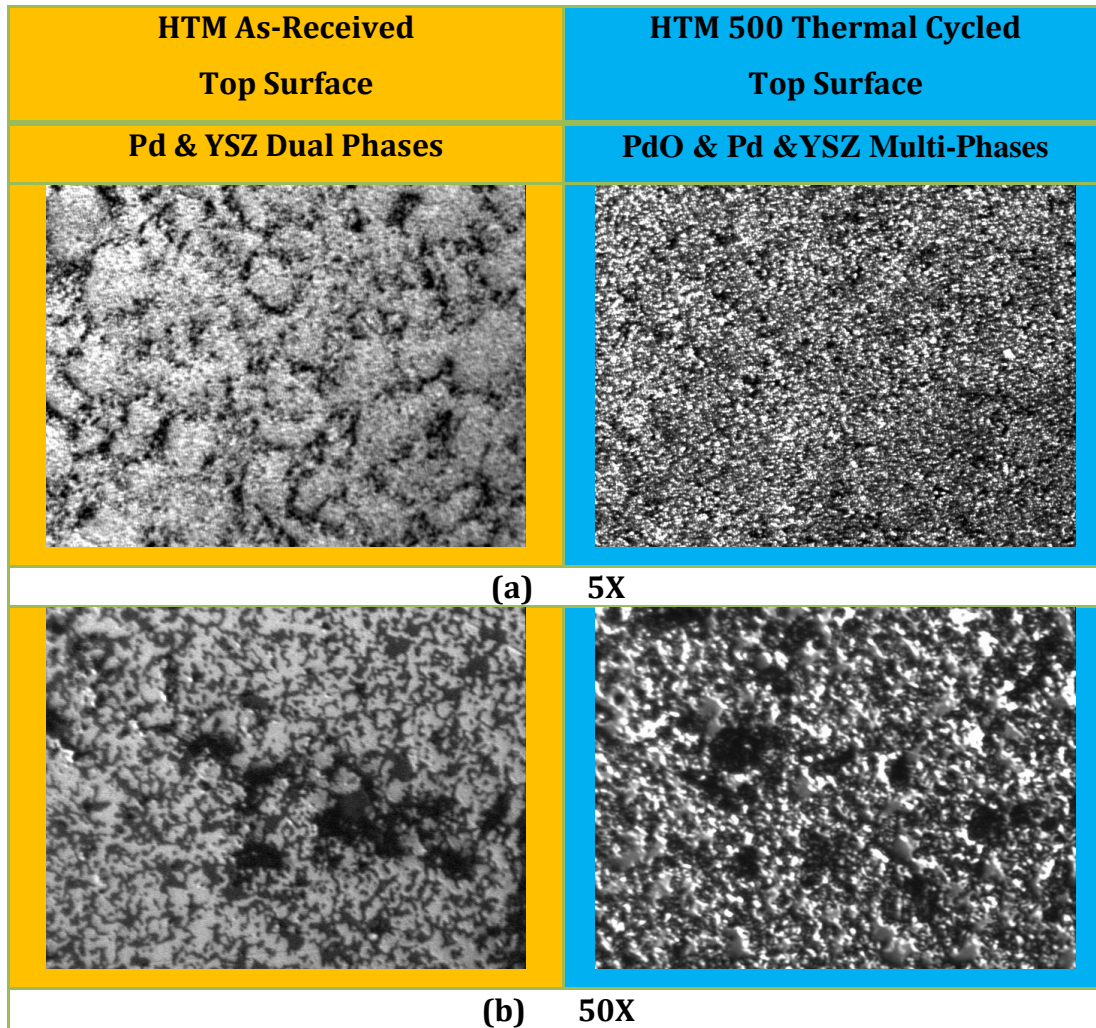
Figure 101:   Optical Observation on Top Surface for HTM As-Received and after 500 Thermal Cycles between 50–850°C in Air

The surface morphology on the middle layer is found to have several vertical micro-cracks while the rest are still composed of continuous and intense Pd-YSZ dual phase system as shown in Figure 102. The temperature gradient during thermal cycling

produced more micro-cracks inside the HTM disc, whereas the chemical reaction between Pd and oxygen (O_2) to form PdO disturbed the continuity of Pd-YSZ dual interconnection system from surface to interior.

HTM As-Received Cross-Section	HTM 500 Thermal Cycled Cross-Section	
Pd+YSZ Composition	PdO+Pd+YSZ Composition Top & Bottom Layer	Pd+YSZ Composition Middle Layer
(a) 5X		
(b) 50X		
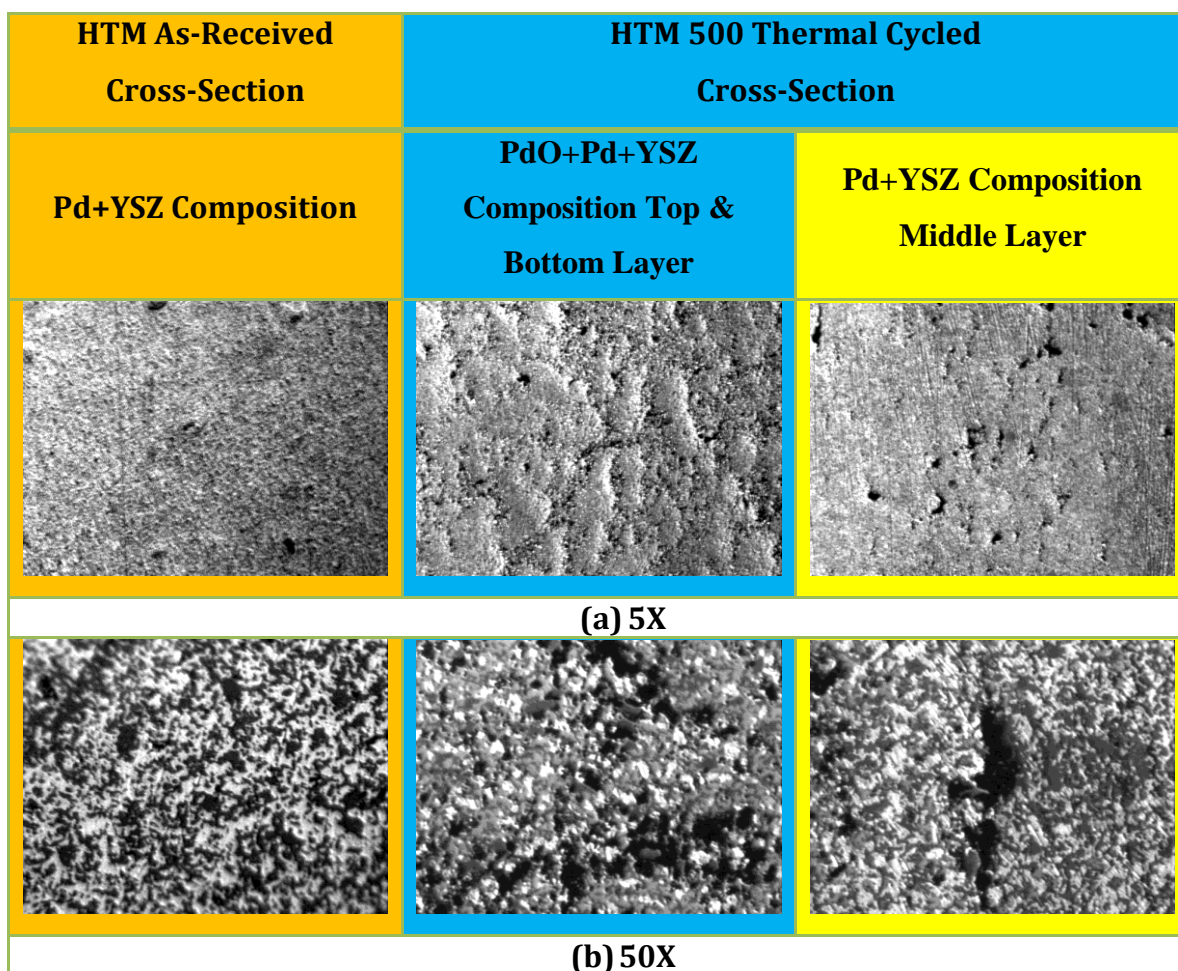
Figure 102:   Optical Observation of Cross Section for HTM As-Received and after 500 Thermal Cycles between 50–850°C in Air

3.3.5   SEM Observation and EDS Elemental Tracing Analysis

HTM cermet pieces (i.e., top surfaces and the cross-section for HTM as-received and after 500 thermal cycles in Figure 100) were carbon-coated and EDS analysis were performed using SEM. The cracked part on the polished surface of HTM after 500 thermal cycling was slowly sectioned by diamond saw as pictured in Figure 103. The

148

sectioned cracked part was also carbon-coated before it was analyzed by EDS.
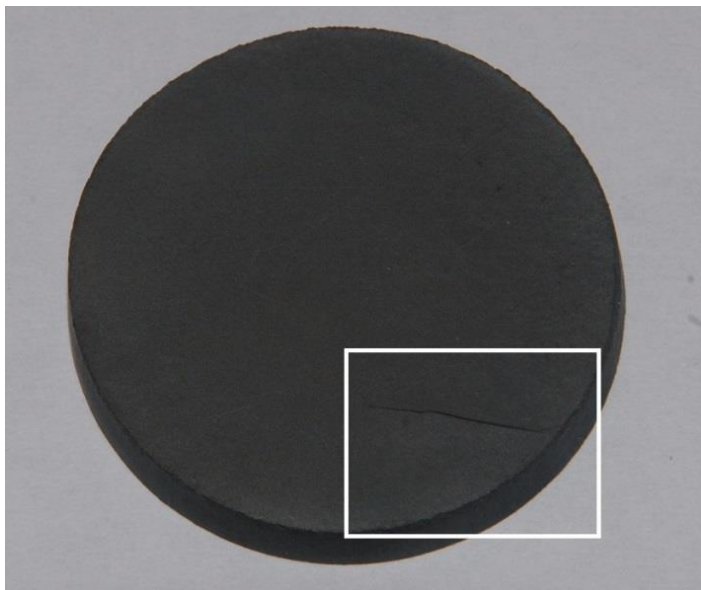
Figure 103: **Diagram of the Cracked Sample Sectioned from HTM Cermet Disc after 500 Thermal Cycles**

SEM images and EDS elemental trace for the top surface of the as-received HTM are shown in Figure 104. The morphologies for both Pd and YSZ phases in the HTM cermet are pointed out in the figure. It is observed that Pd phase and YSZ phase are interconnected and dissolved with each other for as-received HTM sample, however, there is some agglomerate of YSZ gains and the inherited cracks from the agglomerate could be found along the YSZ grain boundary, as shown in Figure 104.

SEM images and EDS analysis for the cracks on the top surface of HTM after 500 thermal cycles are shown in Figure 105. The elemental analysis in Figure 105 shows that the dark and tetragonal grains in HTM system are mainly YSZ phase, while the light and bright phase is Pd-related phase.

It could be assumed that the original Pd-YSZ dual phase system in HTM cermet was first broken by the chemical reaction between Pd and O_2 to form a new layer of PdO. With

thermal cycling treatment, more Pd will be transformed to PdO and the interconnected Pd-YSZ dual phases were broken to a multi-phases system of Pd, PdO and YSZ. A combination of trans granular and inter granular crack propagation could be seen around YSZ grains and PdO precipitates, as shown in Figure 105.
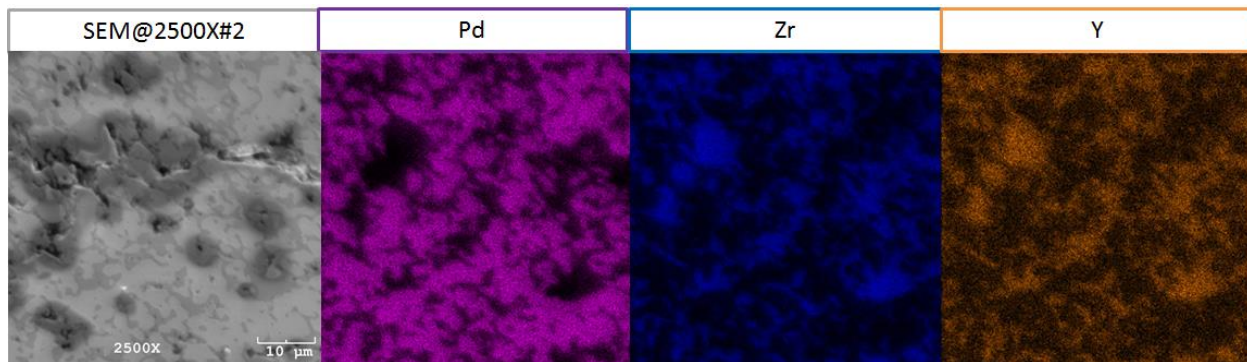
(a) EDS Elemental Tracing Analysis
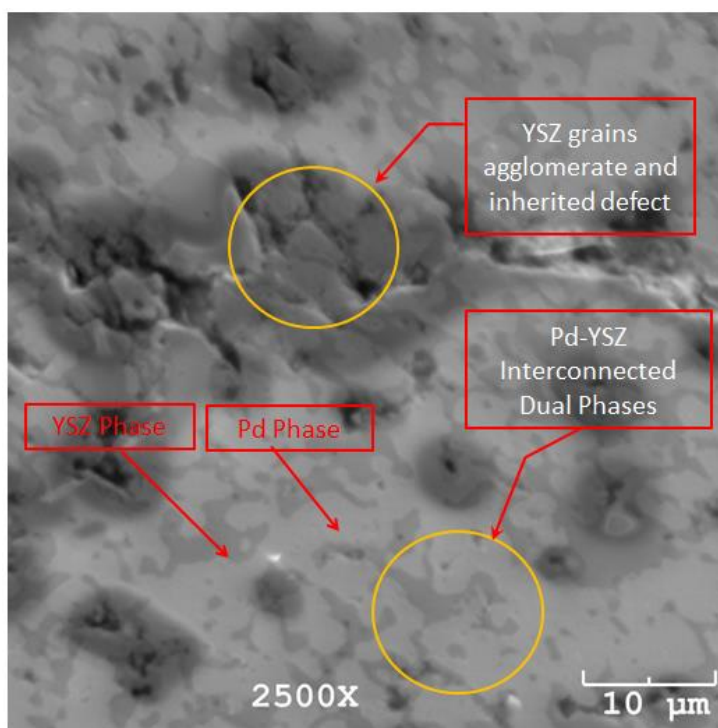
(b) SEM Image @2500X

Figure 104:   SEM with EDS Analysis on the Top Surface of HTM As-Received

FastMap-HTM-Disc#3-3400x#3

SEM

3400X   10 µm

Zr

Pd
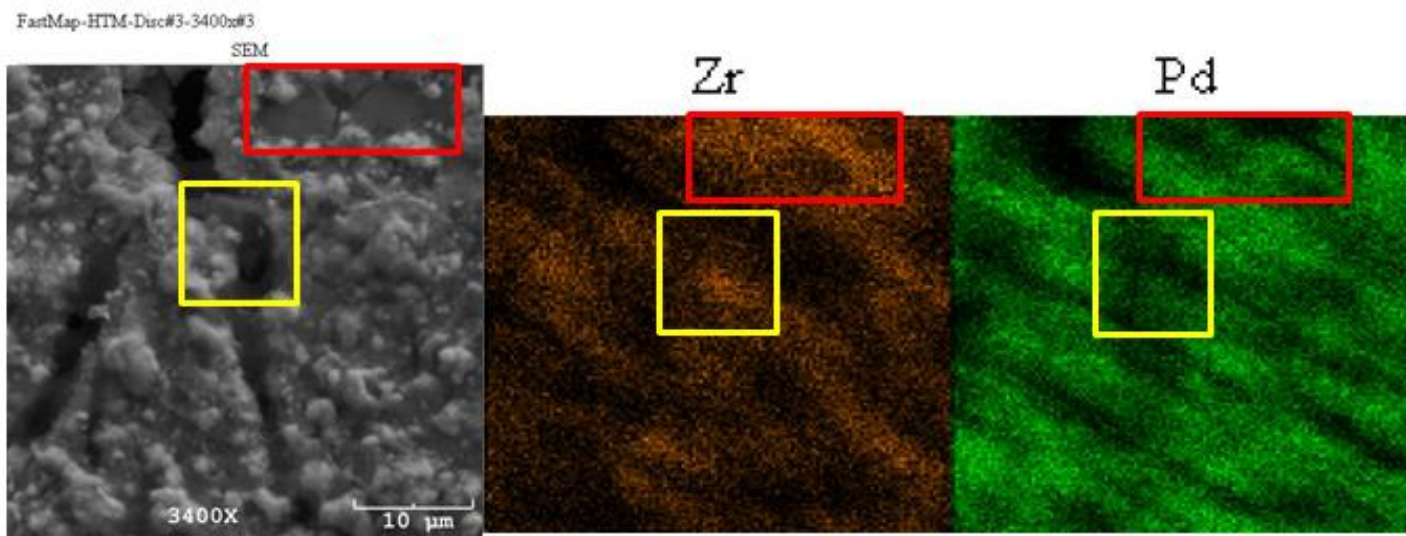
(a) EDS Elemental Tracing Analysis
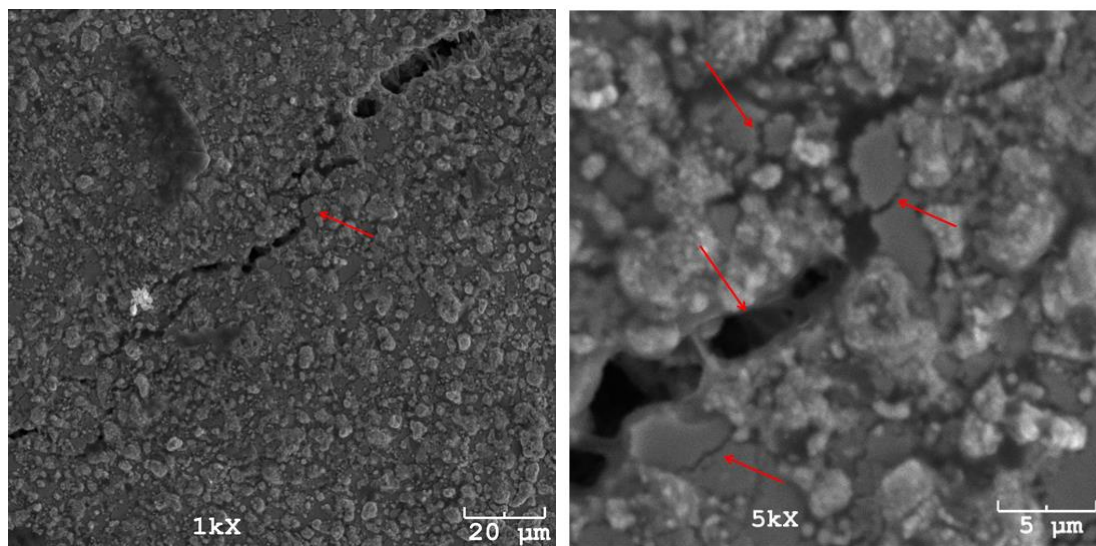
(b) SEM and Crack Propagation for Top Surface Cracks
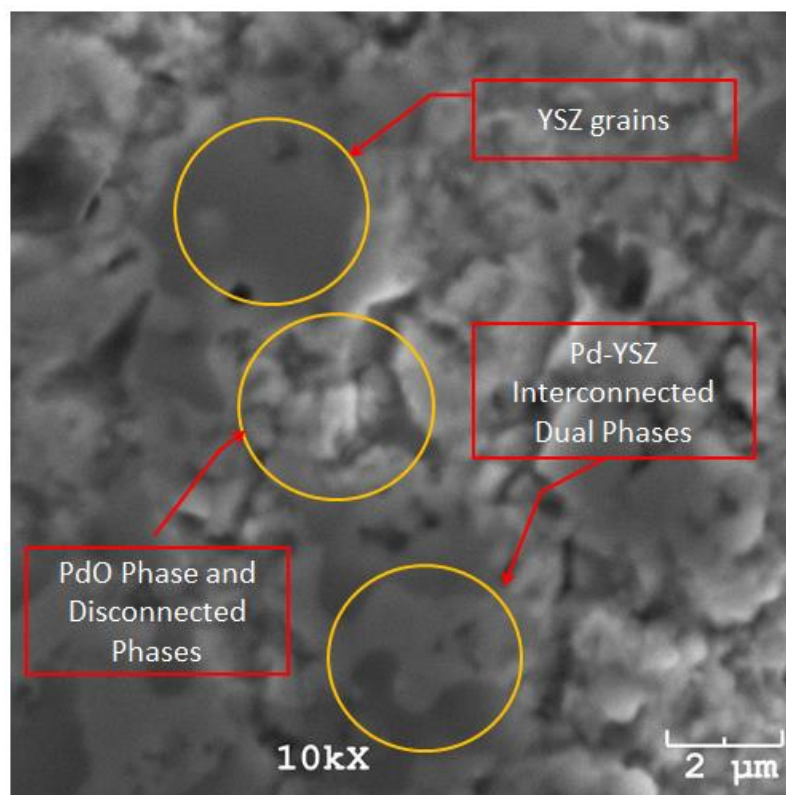
(c) SEM Imaging for Top Surface without Cracks

Figure 105: **SEM and EDS Analysis for the Cracked Part on Top Surface of the HTM Cermet after 500 Thermal Cycles**
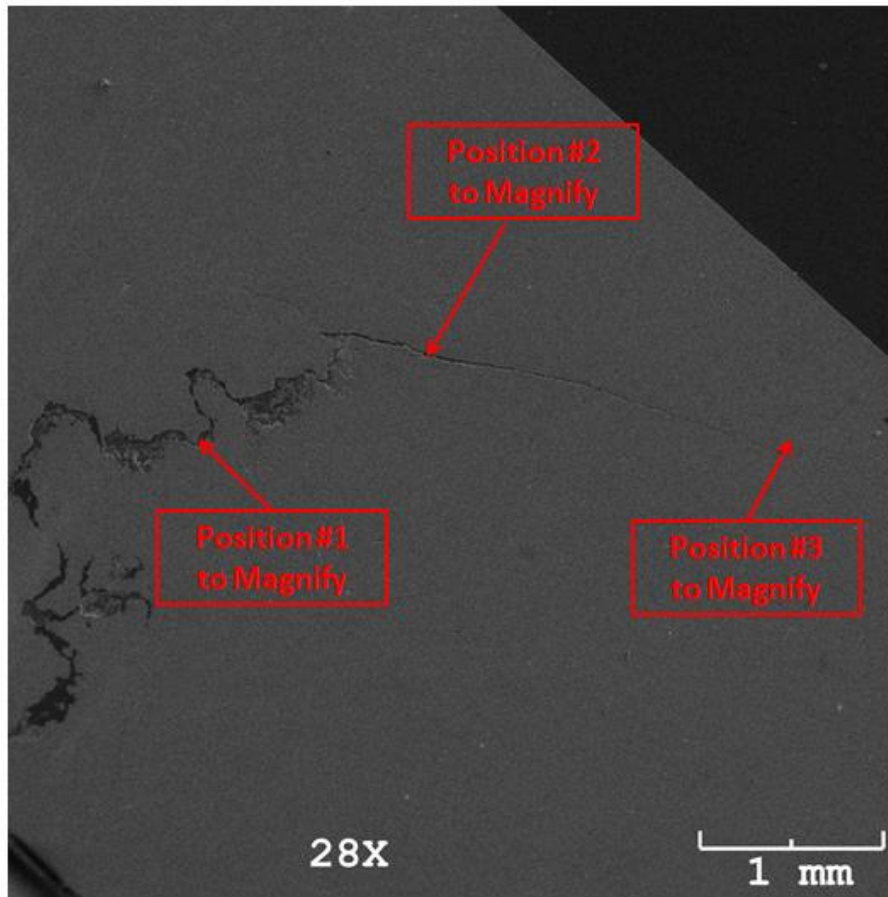
Figure 106: **Diagram of Selected Positions (i.e. Position #1, #2 and #3) along the Longest Cracks on the Cross-Section Surface of HTM after 500 Thermal Cycles**

SEM imaging for the longest crack on the cross-section of HTM after 500 thermal cycles are shown in Figure 106 and Figure 107. Three characteristic positions in Figure 106 are selected based on the middle of the cracks, tips of the cracks, and area near the tip of the crack. Both SEM imaging for Position #1 and Position #1 demonstrated that the crack grew along the grain boundary of YSZ phase and there is new precipitate of PdO formed along the crack boundaries.

The other non-cracked areas are still integrated with dual phases of Pd and YSZ as seen from Figure 107 (a) and (b). Therefore, the initial crack in the internal portion of the HTM disc might be caused by the thermal gradient during the thermal cycling process.

For Position #3 near the multiphase layer of the cross-section was found to start to have a break down with pores and micro-cracks of the melting of dual phases of Pd and YSZ as shown in Figure 107 (c).
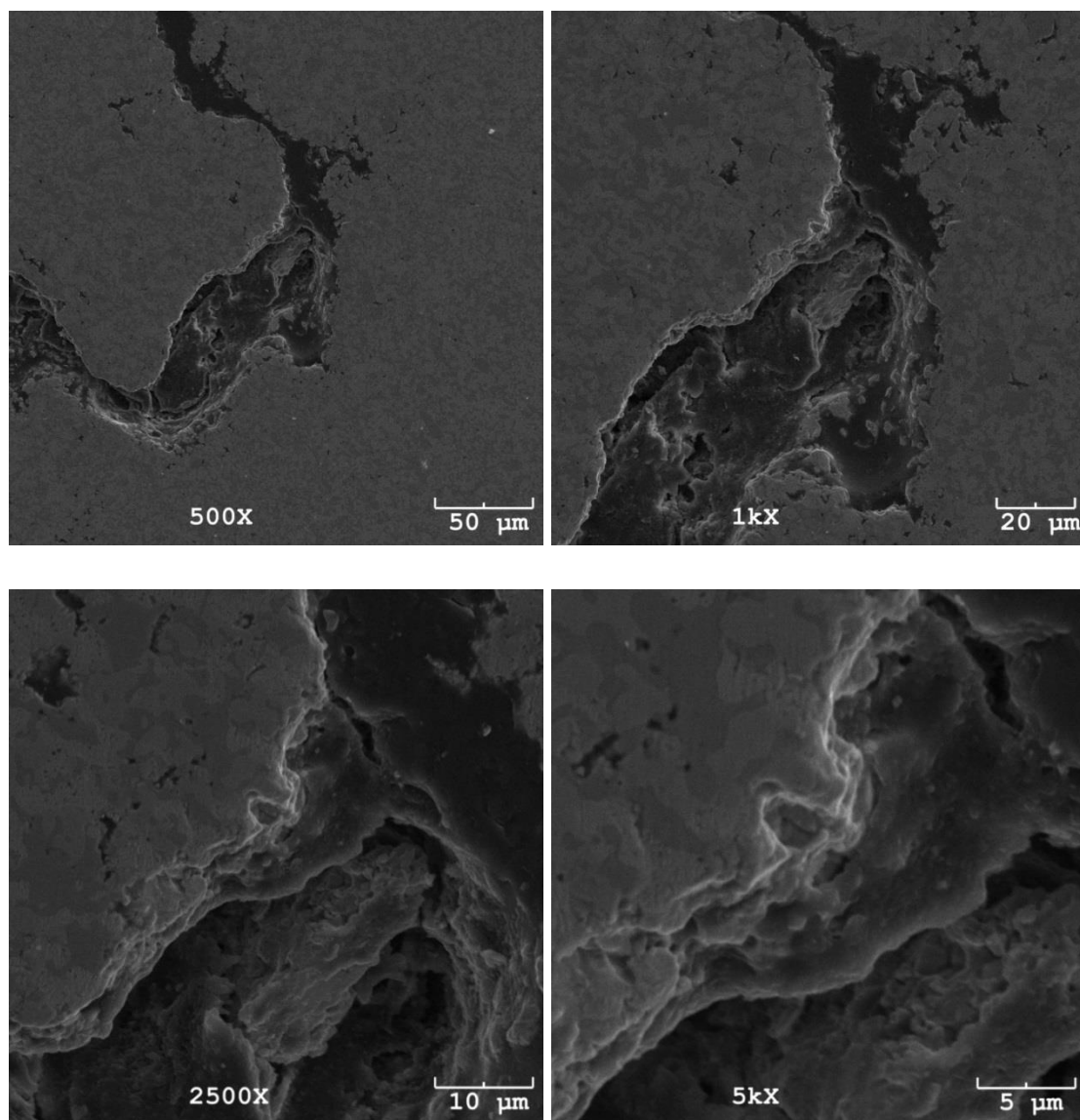
(a) Position #1
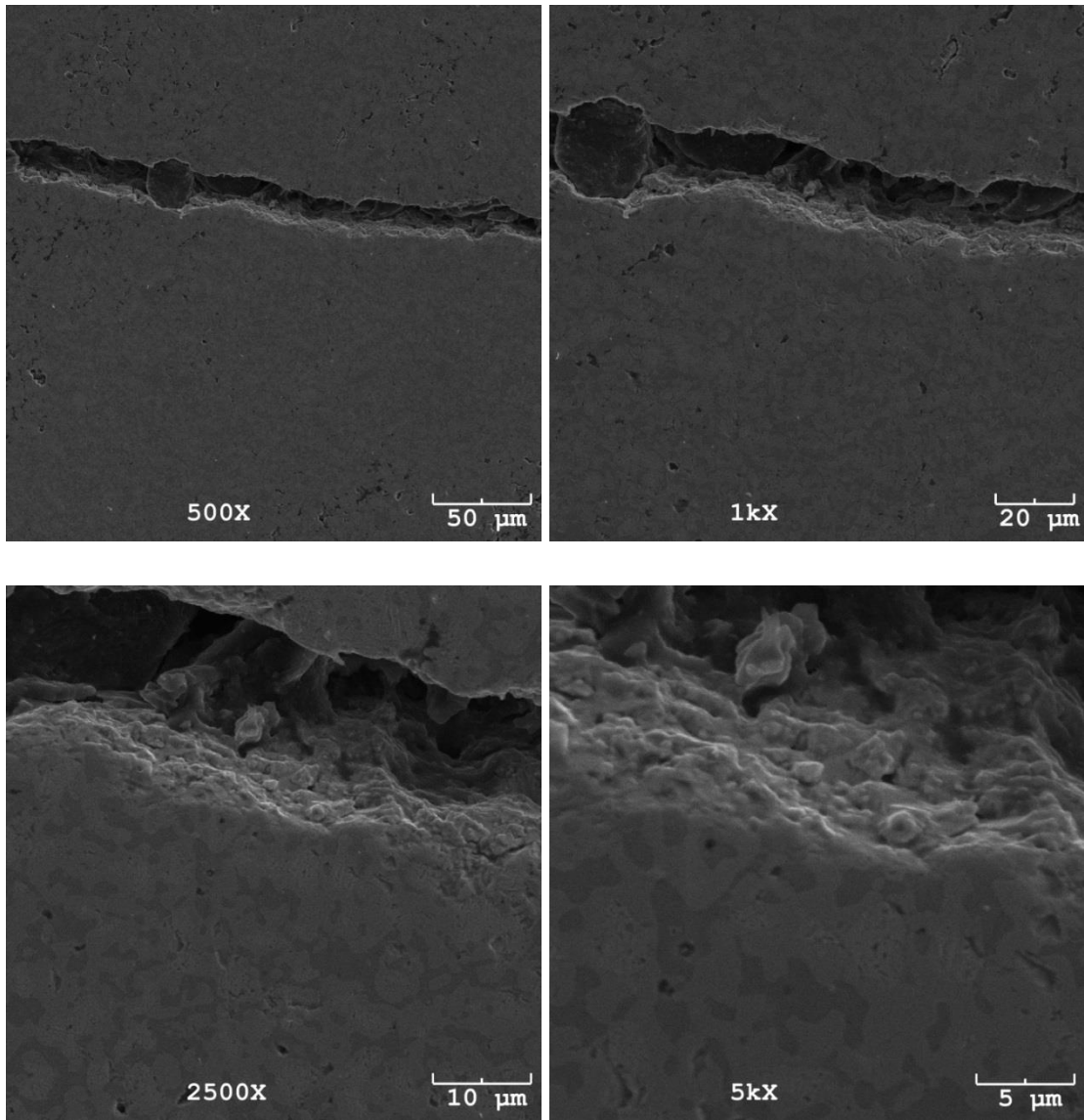
(b) Position #2
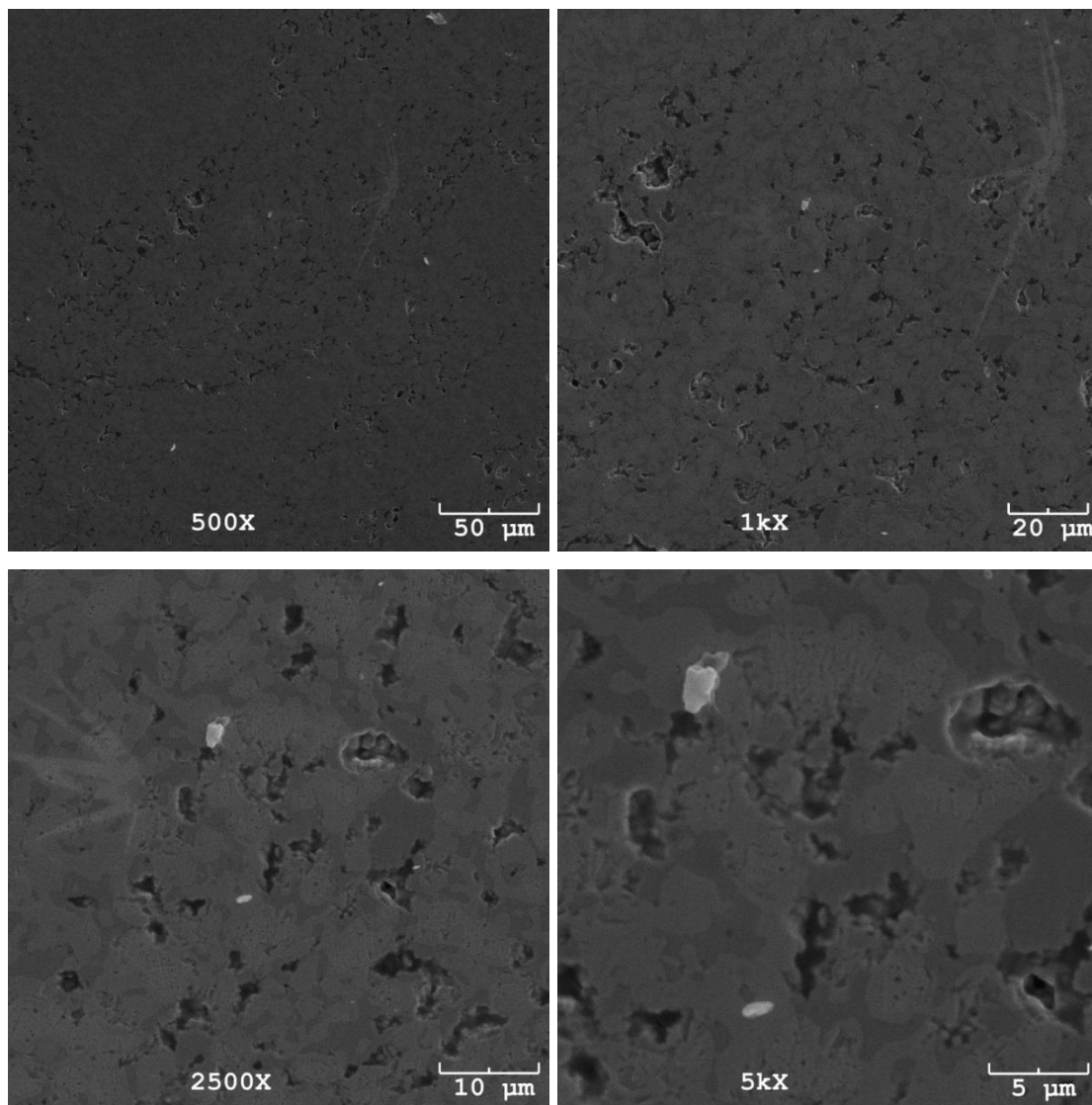
(c) Position #3

Figure 107:   SEM Pictures of the Selected Positions along the Longest Crack on the Cross-Section Surface of HTM Cermet after 500 Thermal Cycles (50-850°C)

3.3.6   X-Ray Microanalysis by Microprobe with EDS

The difference between Pd and PdO is not easily discerned by SEM and EDS technique, but it could be differentiated by the x-ray microanalysis technique such as Microprobe with EDS. Microprobe BSE Imaging on top surface and cross-section for as-received HTM are shown in Figure 108 and Figure 109, respectively. The main phases have been

verified with the SEM and EDS results which is the dual phase of Pd-YSZ, by which Pd is denoted by brighter color and YSZ is denoted by darker color.

(a)   Phase ZrO2

(b)   Phase Pd
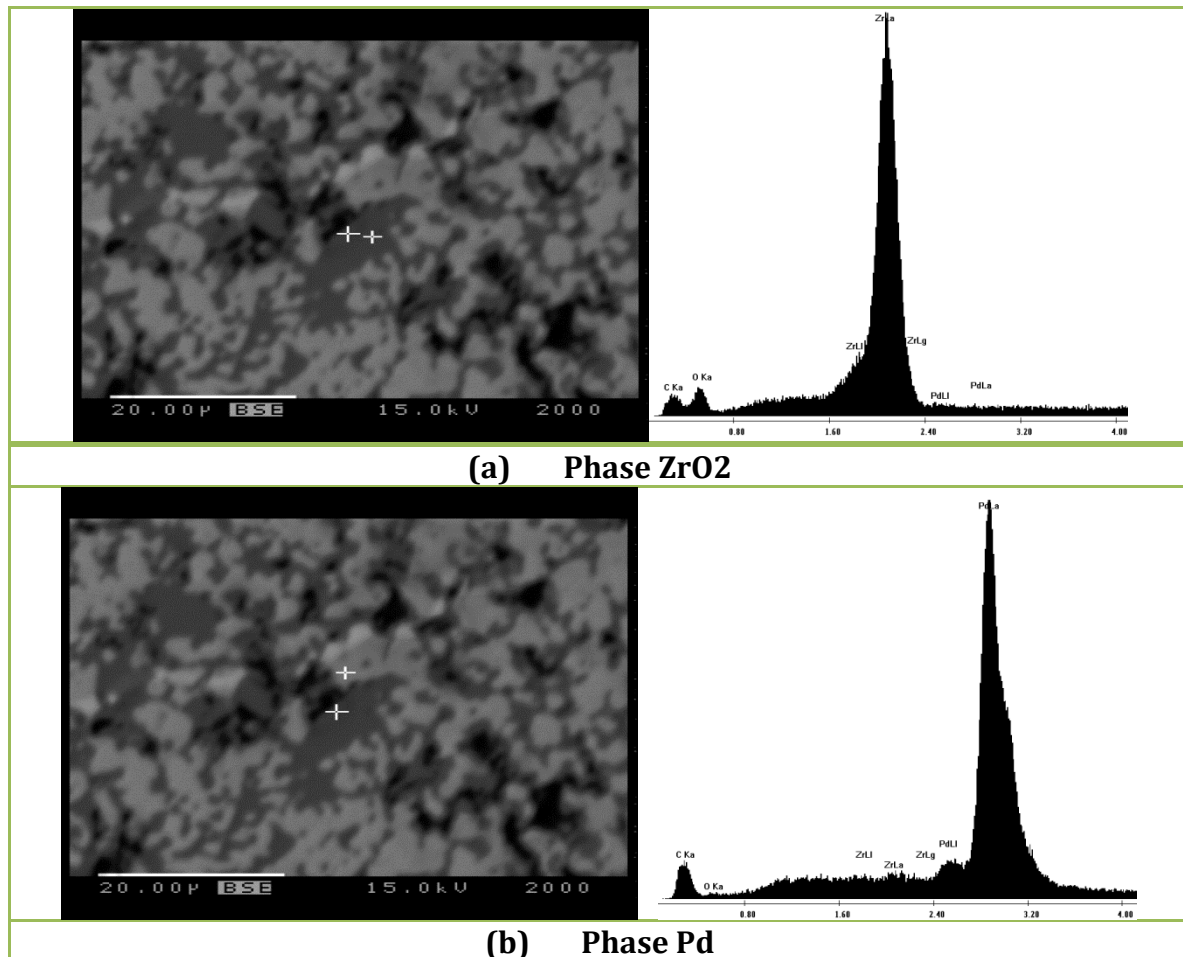
Figure 108:   Microprobe BSE Imaging on the Top Surface of HTM As-Received
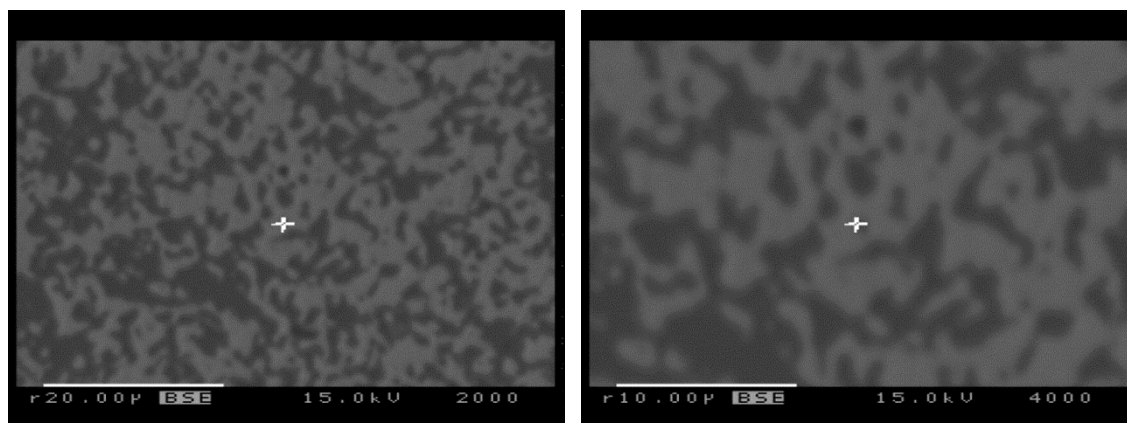
Figure 109:   Microprobe BSE Imaging on the Cross-Section of HTM As-Received

Microprobe BSE Imaging on top surface for HTM after 500 thermal cycling is shown in Figure 110. Microprobe BSE Imaging on the cross-section for HTM after 500 thermal cycling is shown in Figure 111 for the middle portion and Figure 112 the portion close to sample edges. Most of Pd phase near the sample edge had been oxidized to PdO while there are still interconnected Pd-YSZ dual phase in the middle portion of the cross-section as we compared Figure 111 and Figure 112. The macro pores are found to grow ahead of the crack tips, a characteristic discussed before by other researchers **[60]**.

(a)   PdO Phase

158

(b)   Pd Phase

(c)   ZrO2 Phase

(d)   PdO + ZrO2 Phase
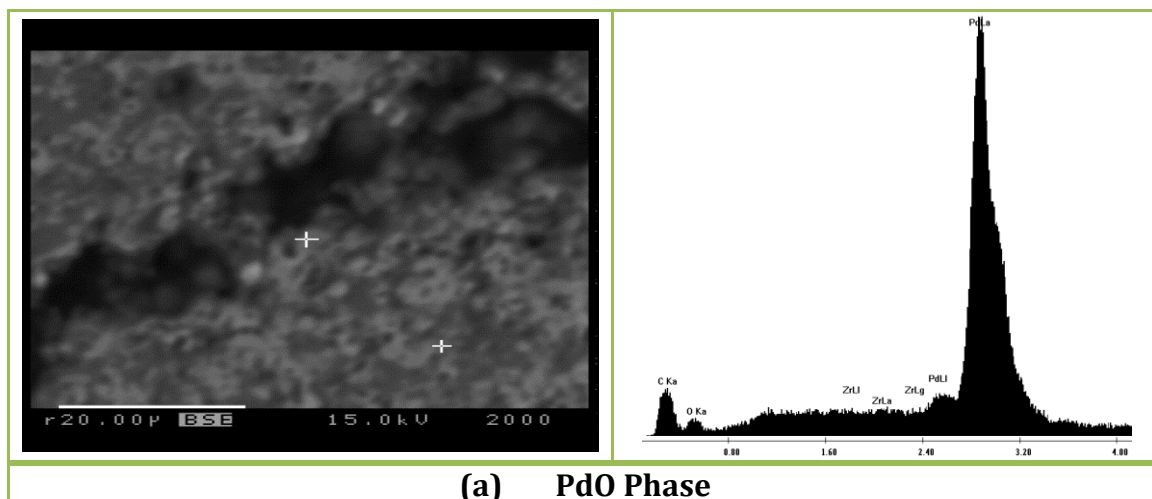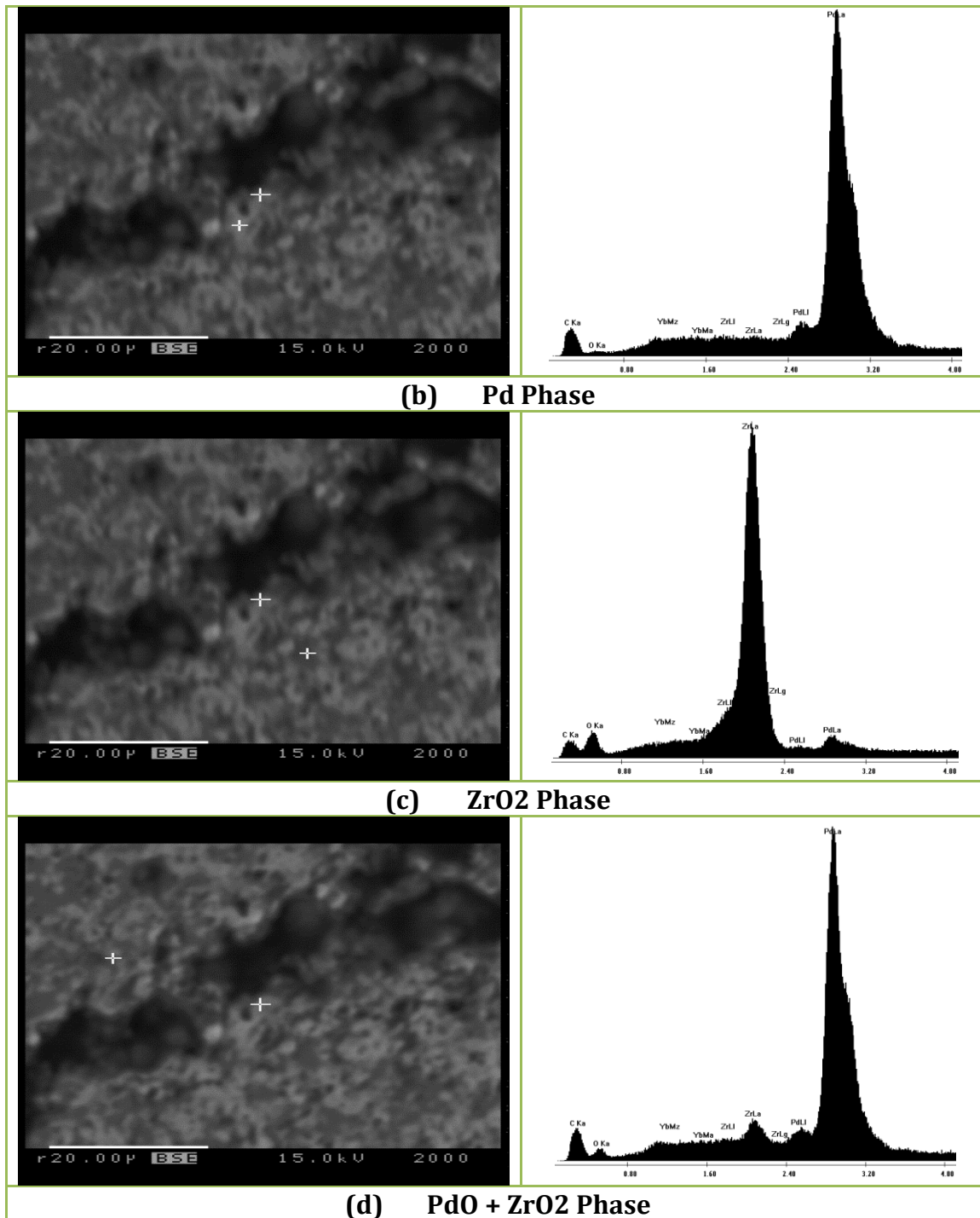
Figure 110:   Microprobe BSE Imaging and EDS Analysis of the Crack Areas on the Top Surface of HTM after 500 Thermal Cycles

(a) Pd Phase

(b) ZrO2 Phase
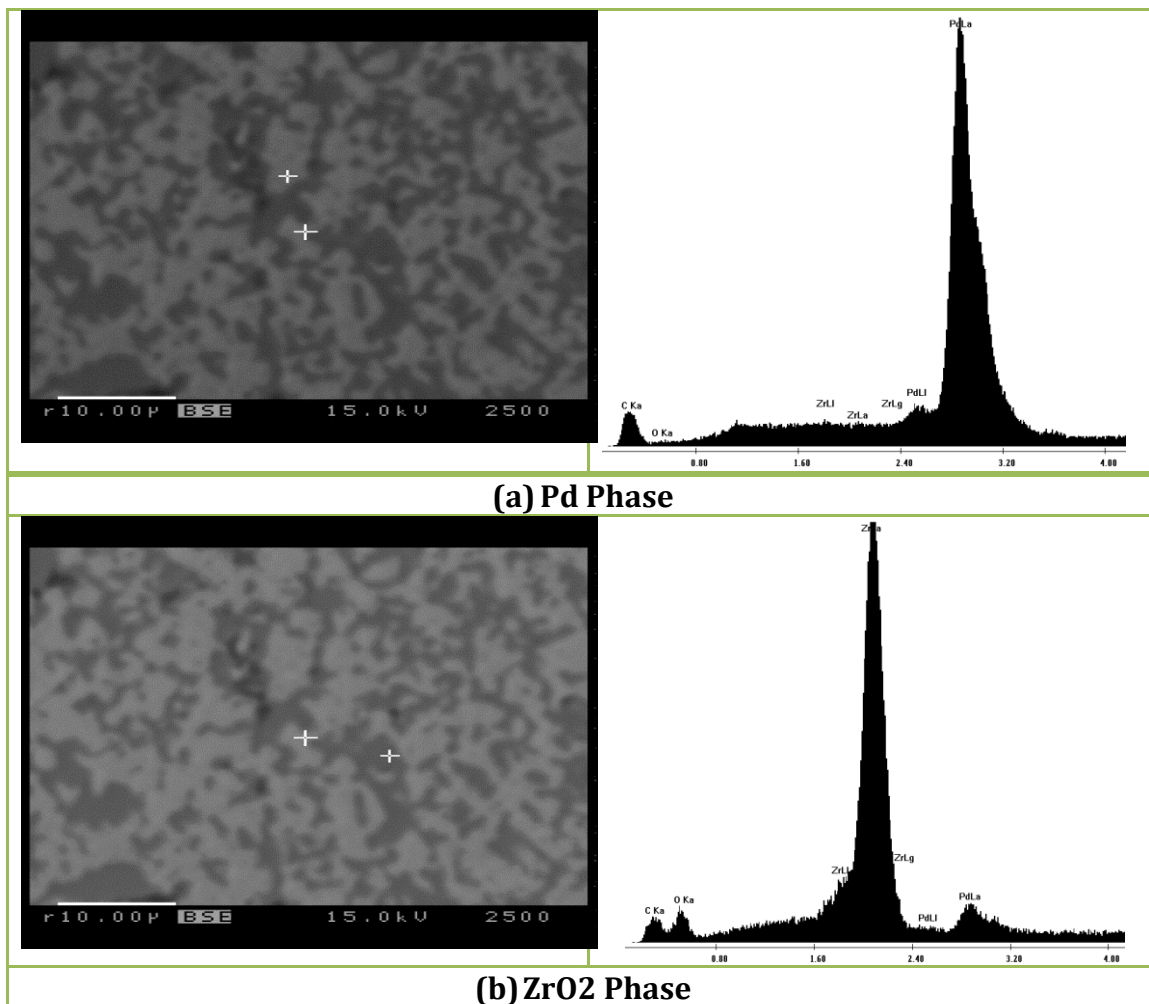
Figure 111:   Microprobe BSE Imaging and EDS Analysis of the Middle Part of the Cross-section of HTM after 500 Thermal Cycles

(a)   Pd Phase

(b)   PdO Phase

(c)   ZrO2 Phase
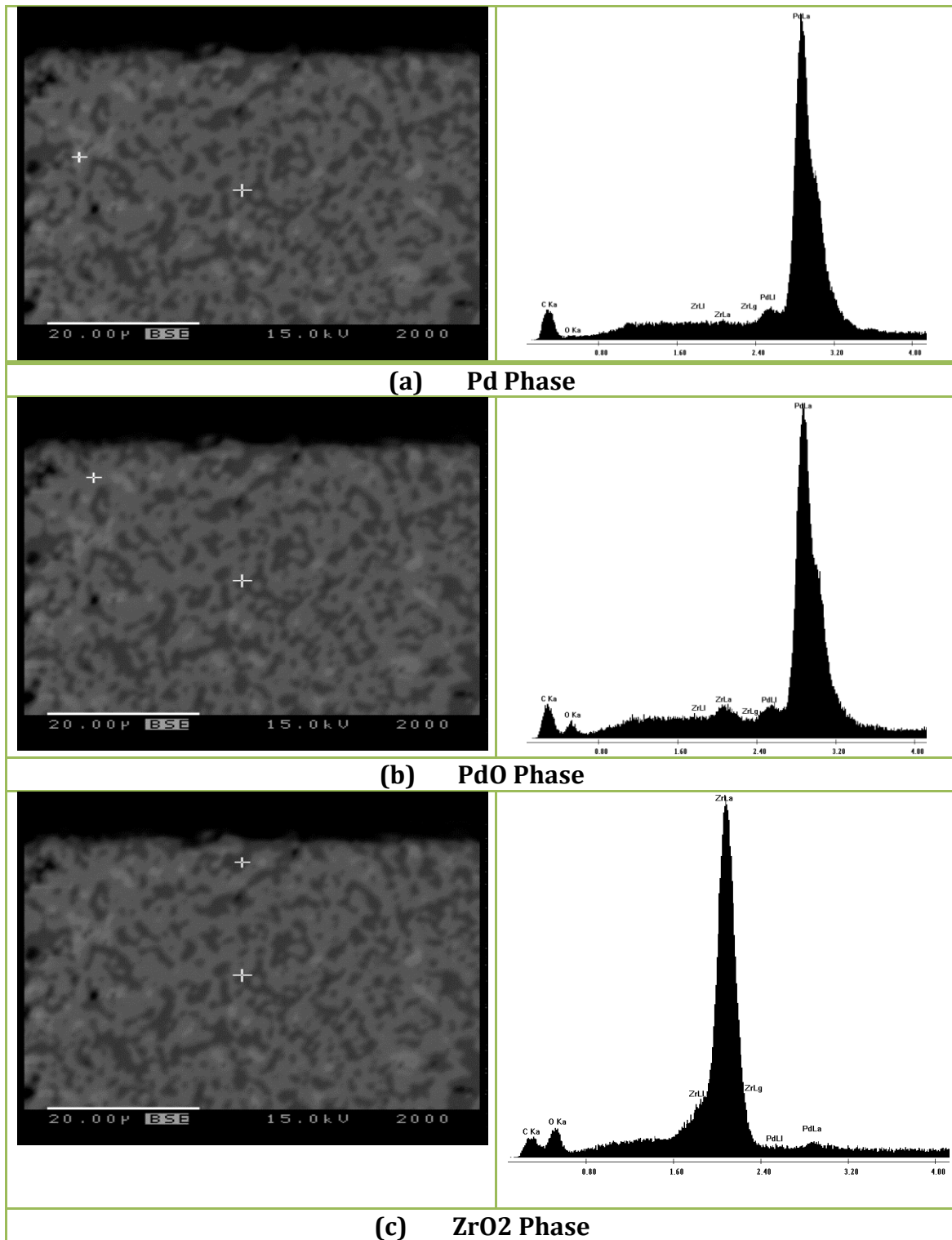
**Figure 112:   Microprobe BSE Imaging and EDS Analysis on the Cross-Section
Close to the Edge of the HTM Sample Bar after 500 Thermal Cycles**

CHAPTER IV: CHARACTERIZATION OF MICROSTRUCTURAL AND THERMO-MECHANICAL PROPERTIES OF THE SELECTED STRUCTURAL CERAMICS

4.1 Characterization of Thermo-Mechanical Properties and Microstructure for Selected Structural Ceramic – Al_2O_3

4.1.1 Bulk Density and Porosity Measurement

The density of the selected dense alumina (AL-96) was evaluated at ambient temperature based on the Archimedes' principle. Density of AL-96 is approximately 3.2g/cc as calculated based on the data in Table 50. The density result is consistent with the reference values published by the manufacturers online http://www.lspceramics.com.

Table 50: Density of the Selected Structural Ceramic, AL-96

Sample ID	W_d (g)	W_t (g)	W_s (g)	V_s (ml)	ρ (g/cc)
AL-96#1	1.98	51.10	1.98	0.63	3.14
AL-96#2	1.96	51.04	1.96	0.60	3.26
Average (*g/cc*)	3.20				

4.1.2 Elastic Properties

The elastic properties, including dynamic Young's modulus (E), dynamic shear modulus (G), and Poisson ratio (υ) of AL-96 were evaluated at ambient temperature (25°C). Results and the corresponding reference values specified by the manufacturer (LSP Industrial Ceramics, Inc. http://www.lspceramics.com) are shown in Table 51. Experimental results of the elastic properties are consistent with the published values of the material. Effects of temperature and thermal cycling on dynamic Young's modulus (E) of AL-96 are presented in Figure 113.

The thermally cycled samples were also selected to correlate the Young's modulus (E) value as a function of temperatures after 150, 650, and 1150 thermal cycles (Figure 113). A decrease in E-value can be observed for the specimen after 1150 thermal cycles, whereas, no significant difference could be observed for E-value after 150 and 650 thermal cycles.

Table 51: **Elastic Properties of the Selected Structural Ceramics (AL-96) at Room Temperature (25°C)**

Elastic Properties	Experimental Results	Reference Value
Young's Modulus (E)	334.7 GPa	331 GPa
Shear Modulus (G)	136.5 GPa	132.4 GPa
Poisson Ratio (υ)	0.226	0.25
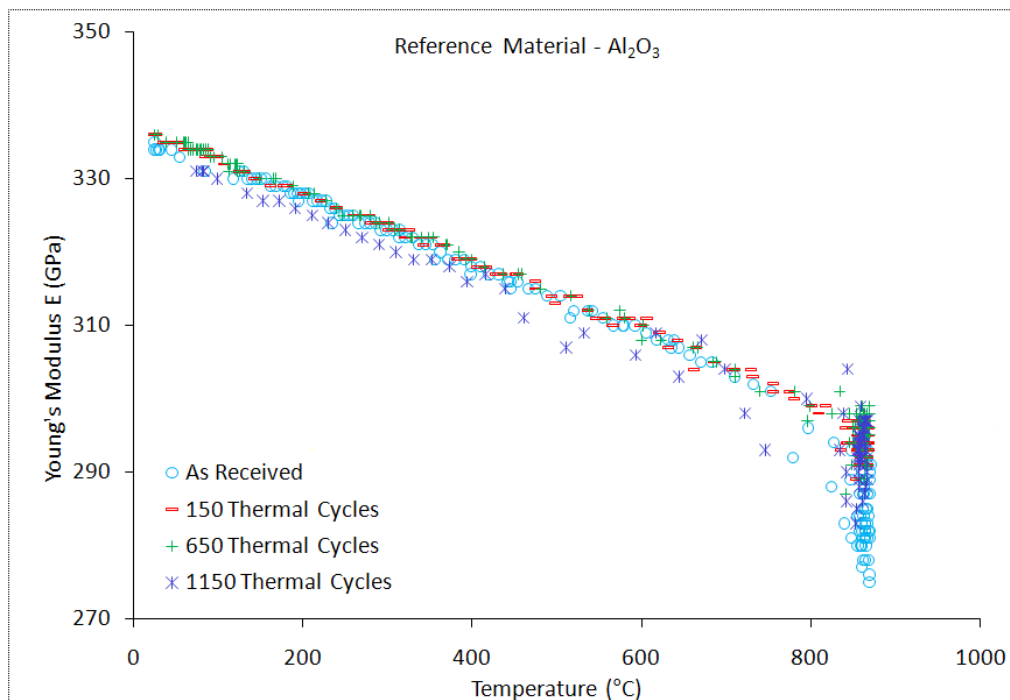
Figure 113: **E-Value vs. Temperature for Alumina 96%, As-Received and after Thermal Cycling (150, 650, and 1150 Thermal Cycles) between 50–850°C in Air**

As previously discussed, the specimen was thermally conditioned and tested for E-value at three stages. For both heating and cooling stages, the E-values are fairly constantly linear decreasing with the temperature ranges as shown in Figure 113.

The experimental value of E as a function of temperature can be represented by an interpolation formula [61]:

$$E=A-BT \hspace{4cm} Equation\ 47$$

where, E = dynamic Young's Modulus (GPa)

T = temperature of E-test Furnace (°C)

A = intercept constant for a specific testing environment

B = slope constant for a specific testing environment

The values of the intercepts and the slopes of the regression lines (E vs. T) are presented in Table 52 and shown in Figure 114. The results indicate that a decreasing trend for these two constants can be expected with increasing number of thermal cycles.

Table 52: **Results of Intercept (A) and Slope (B) to the Number of Thermal Cycles for the Linear Relationship of E as an Effect of Temperature**

Statistical Regression Formula for E vs. T: *E=A-BT*		
Number of Thermal Cycles	Intercept A	Slope B
0	339.9	0.062
150	338.4	0.051
650	338.4	0.051
1150	335.2	0.048

164
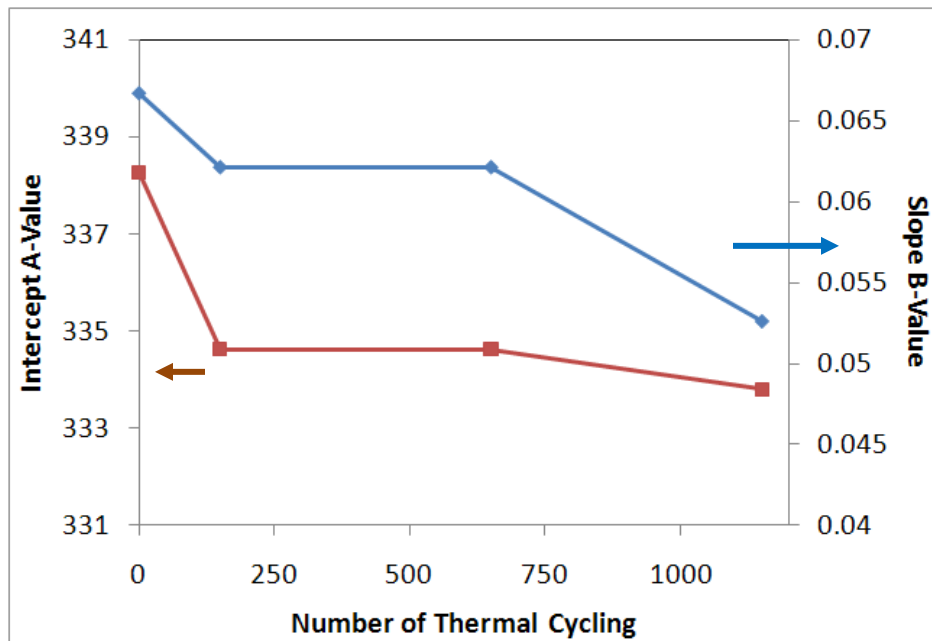
Figure 114: Relationship of Intercept (A) and Slope (B) for the Linear Relationship of E vs. Temperature for AL-96 after Thermal Cycling Processes

4.1.3   Vickers Hardness Number (HV)

Vickers hardness (HV) numbers were also evaluated for alumina both as-received and after 650 thermal cycles, and are presented in Table 53 and Figure 116. The indentation mark is captured by Olympus BX60 as presented in Figure 115.

Table 53:   Vickers Hardness Test for the Selected Structural Ceramics (AL-96) As-Received and after Thermal Cycling

Load (g)	Alumina As-Received		Alumina After #650 Thermal Cycles	
	$\overline{HV}$	Standard Deviation (S)	$\overline{HV}$	Standard Deviation (S)
1000	13.54	1.16	17.96	1.10
500	17.62	3.82	20.64	2.62
300	23.36	4.08	24.01	1.82
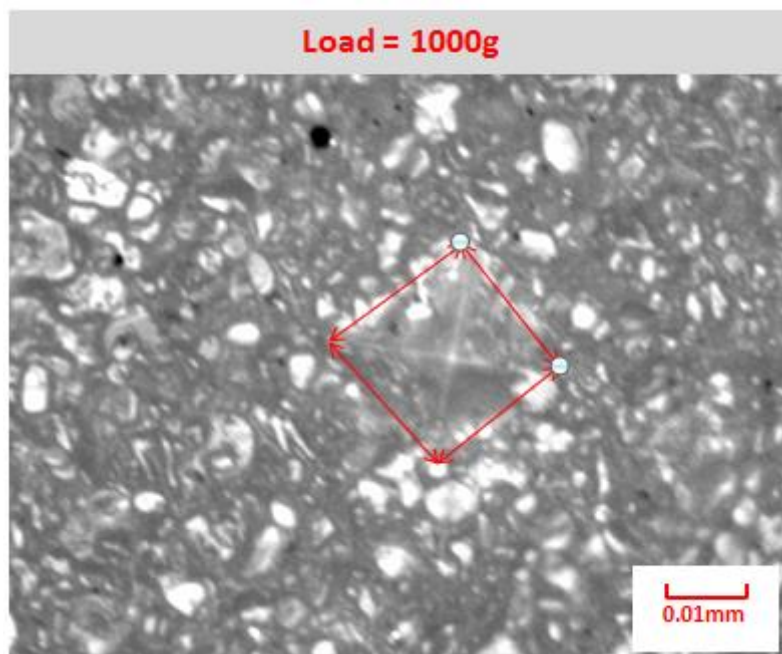
Figure 115: **Vickers Hardness Indentation for AL-96 As-Received**
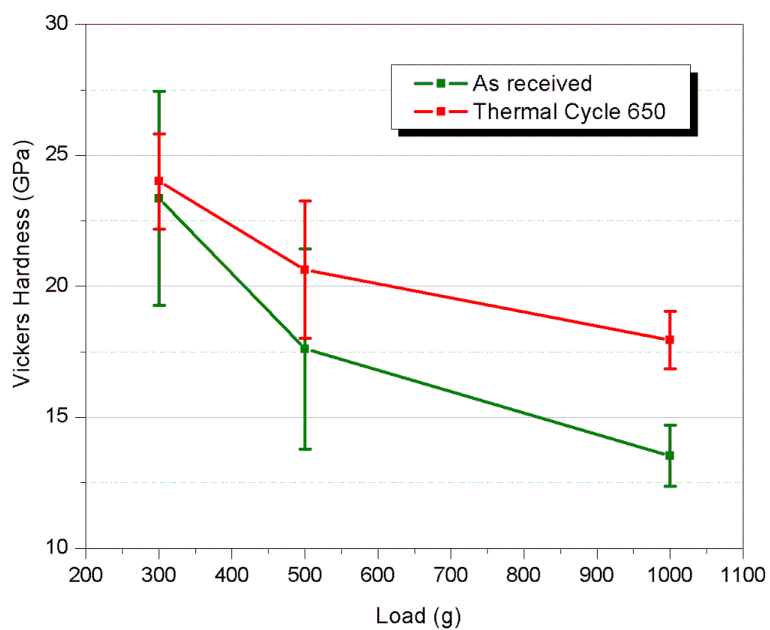
Figure 116: **Vickers Hardness Number ($\overline{HV}$) for AL-96 both As-Received and after Thermal Cycling**

The mean Vickers hardness numbers $\overline{(HV)}$ of the selected structural ceramic are within the range of the reference values between 13–23 GPa (1500–2000 HV1/15). These values are consistent with data presented in published literature [62, 63]. The results show a decreasing trend for $\overline{HV}$ with increasing load from 300g to 1000g (Figure 116). A 30% increase of $\overline{HV}$ for alumina at 1000 gm load was observed after 650 thermal cycles. The reason for the increased hardness number could be attributed to the change of microstructural such as the larger grain size which could increase the R-value for alumina.

4.1.4 Modulus of Rupture (MOR) or Flexural Strength (σ_{fs})

Using the standard specified in ASTM C1161, flexural strength (σ_{fs}) of the AL-96 was evaluated at an ambient temperature of 25 °C and at an elevated temperature of 850°C with a crosshead loading rate of 600 µm/min. Flexural strength results are summarized in Table 54 and the Weibull plots calculated from flexural strength are presented in Figure 117.

Table 54:   Results of Flexural Strength for Structural Ceramic AL-96

Temperature (°C)	Total Number of Testing Samples	Mean σ_{fs} (MPa)	Standard Deviation (MPa)
25	8	158.87	28.47
850	6	174.03	26.02

The m-values from the Weibull plots are approximately 6~7 at both room temperature and the elevated temperature. The high temperature testing environment of 850°C for 1 hour in air, however, increased the flexural strength of the material. This effect is due to the healing function of the surface and the inherent cracks in alumina [64].

Since the experimental value of the flexural strength of AL-96 is significantly lower than the manufacturer's reference value of 345 MPa, two other dense ceramics materials: alumina 99 wt% (manufactured by CoorsTek) and the yttria polycrystalline tetragonal

zirconia (Y-TZP) (manufactured by STC) were selected for further evaluation of flexural strength.
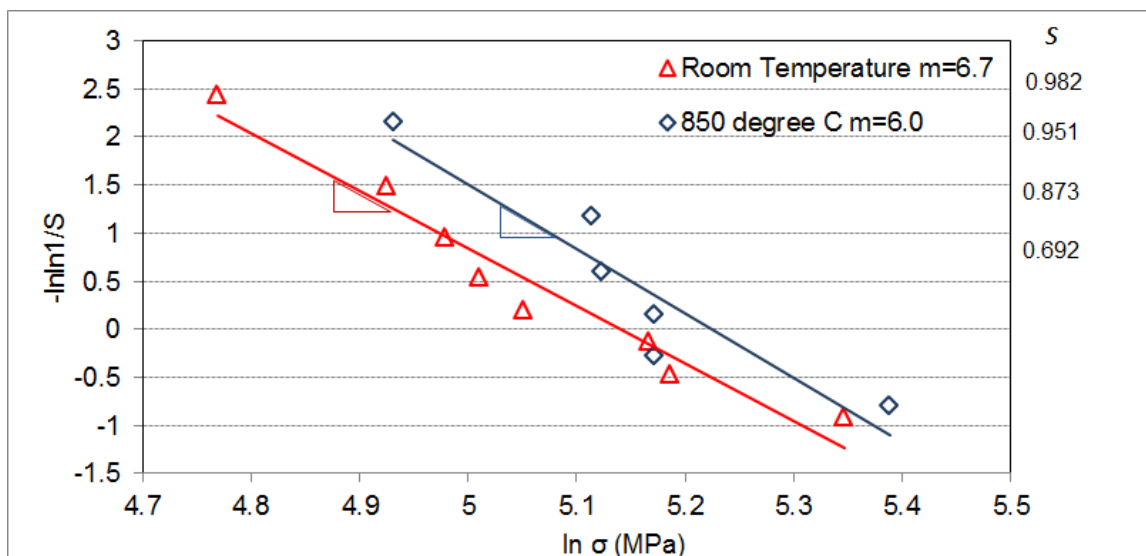
Figure 117:   Weibull Plots for the Selected Structural Material (AL-96) at Room Temperature (25°C) and Elevated Temperature (850°C)

Calculated flexural strengths or modulus of rupture (MOR) are summarized in Table 55. The experimental results are plotted in Figure 118. Since fracture of ceramic materials generally propagates from surface flaws or cracks [65], the morphologies for both bottom, side and fractured surfaces of any selected materials were captured by an Olympus BX 60 microscope and are presented from Figure 119 to Figure 124.

Table 55:   Flexural Strength for AL-96, AL-99, and Y-TZP Materials

Material	Tested Value, Mpa	Reference Value, Mpa	Difference from the Reference Value (%)	Manufacturer	Website
Alumina wt 96%	159	345	54%	LSP Industrial Ceramics	http://www.lspceramics.com/
Alumina wt 99%	294	379	22%	CoorsTek	www.coorstek.com
Y-TZP	776	793	2%	Superior Technical Ceramics	www.ceramics.net
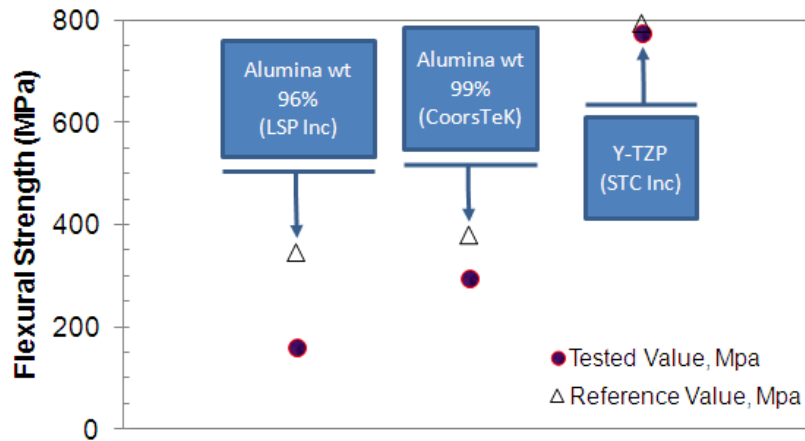
Figure 118:   Flexural Strengths for AL-96, AL-99, and Y-TZP Material at Room Temperature (25°C)

Both AL-99 and Y-TZP show no surface defects or cracks, therefore their observed flexural strength values are more consistent with reference values as compared with AL-96, as shown in Table 55 and Figure 118.

The top surface morphology of alumina 96 wt% (AL-96) shown in Figure 119 (a) is very similar to that of the alumina 99 wt% (AL-99) shown in Figure 120 (a). However, the side surface morphology of AL-96 shown in Figure 119 (b) shows a lot of machining defects and flaws, which could be part of the reason that caused the tested flexural strength values of 159 MPa much lower than the reference value of 345 MPa. Surface morphology for AL-99 is shown in Figure 120 (a) and (b) for the top and side surface, respectively. Surface morphology of the Y-TZP specimen is also shown in Figure 121 (a) and (b).

Optical fractography was also used to study the fracture surface using a stereomicroscope Olympus BX 60. The alumina 96 wt% (Figure 122) fails with larger mirror size, which could be another possible reason for a critical low strength failure [66]. Fracture origins that could be identified on the fracture surface shown in Figure 123 and Figure 124 for alumina 99 wt% and Y-ZTP, respectively.

(a) Alumina 96 wt% (LSP) – As Received Specimen   (b) Alumina 96 wt% (LSP) – As Received Specimen
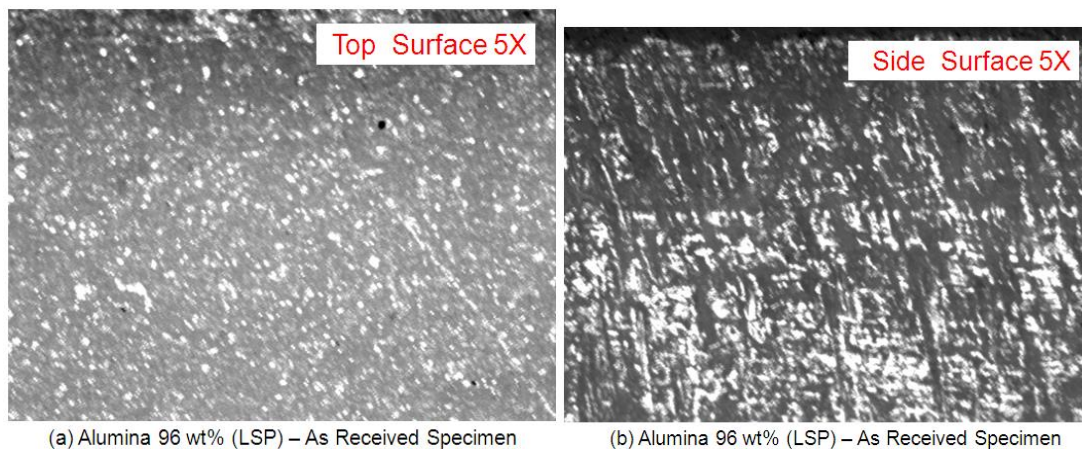
Figure 119:   Optical Observation of Surface Morphology for As-Received AL-96 Sample Bar

(a) Alumina 99 wt% (CoorsTek)   (b) Alumina 99 wt% (CoorsTek)
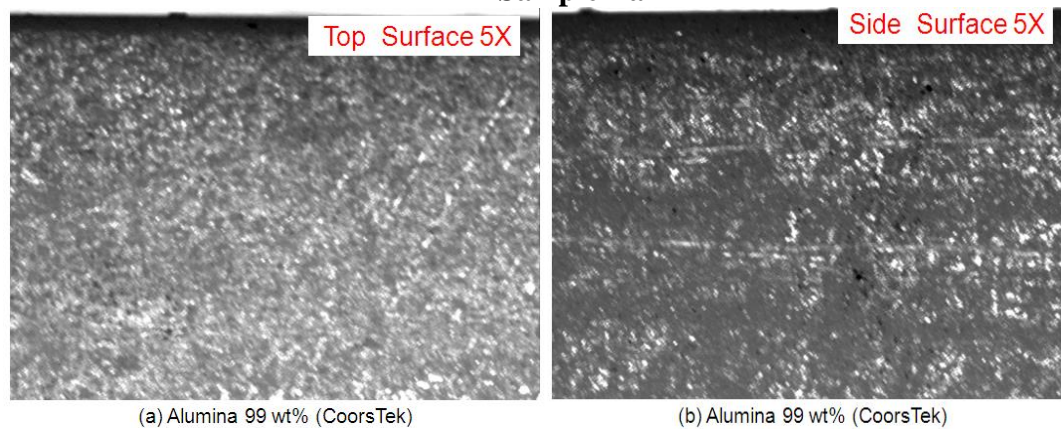
Figure 120:   Optical Observation of Surface Morphology for As-Received AL-99 Sample Bar

(a) Y-TZP (from STC) – As Received Specimen   (b) Y-TZP (from STC) – As Received Specimen
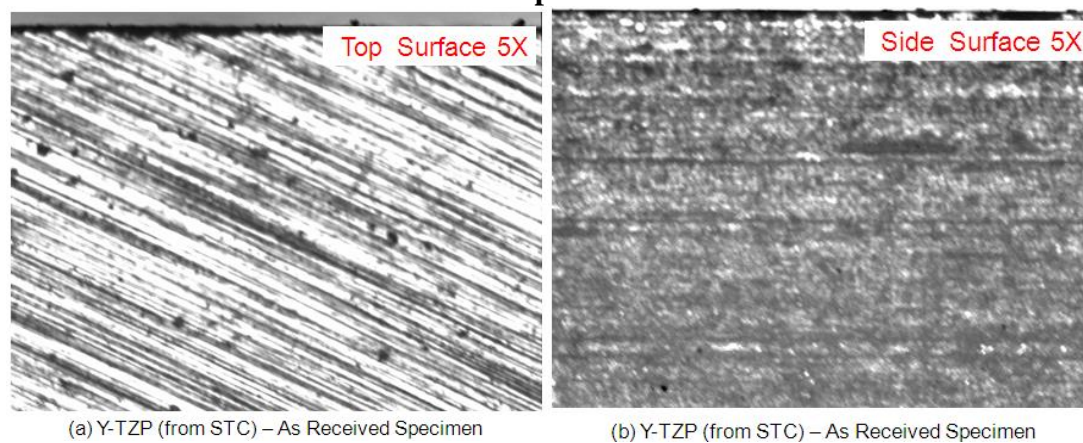
Figure 121:   Optical Observation of Surface Morphology for As-Received Y-TZP Sample Bar
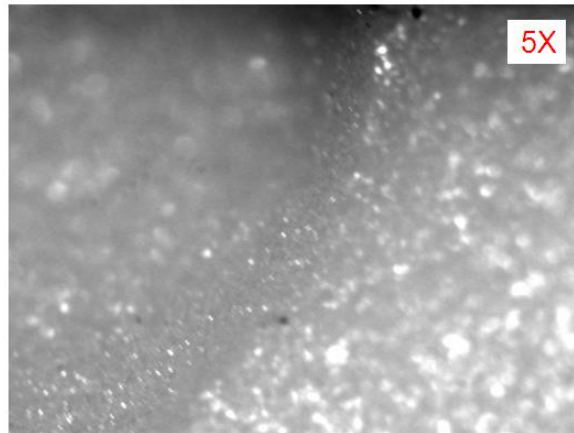
Alumina 96 wt% (LSP) - Fracture Surface

Figure 122: **Optical Observation of Fracture Surfaces for AL-96 after σ_{fs} Test**

Alumina 99 wt% (CoorsTek) - Fracture Surface

Figure 123: **Optical Observation of Fracture Surfaces for AL-99 after σ_{fs} Test**
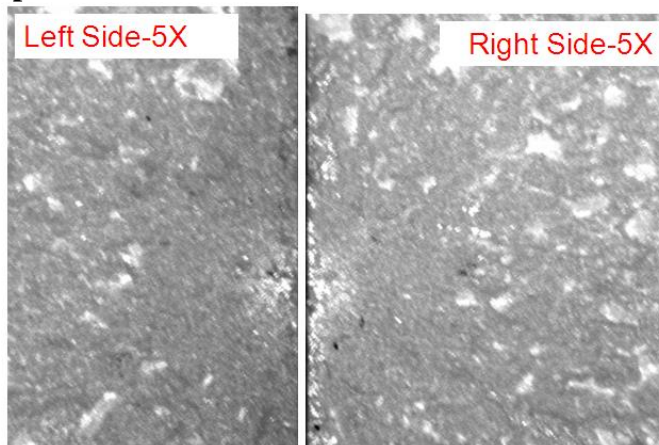
Y-TZP (STC) - Fracture Surface

Figure 124: **Optical Observation of Fracture Surfaces for Y-TZP after σ_{fs} Test**

4.1.5 Subcritical Crack Growth (SCG)

For both dynamic and static SCG fatigue tests, SCG parameters (n-value and D-value) are approximated by the empirical power-law crack-velocity formulation for most ceramics and glasses [67-70]. Alternative crack-velocity formulation takes exponential forms to account for the influence of a corrosive environment [68]. The widely utilized conventional power-law crack velocity is expressed as [68]:

$$v = \frac{da}{dt} = A\left(\frac{K_I}{K_{IC}}\right)^n \qquad\qquad \textit{Equation 48}$$

where, υ – subcritical crack growth rate;

α – crack length;

t – time;

A and n – material/environment-dependent SCG parameters;

K_I – mode I stress intensity factor;

K_{IC} – fracture toughness under mode I loading;

There are two SCG parameters (n-value and D-value) that are determined at each loading rate. For each loading stress rate, a flexural strength-stress rate log diagram is plotted and a linear regression analysis is conducted based on the following equation [67]:

$$log\,\sigma_f = \frac{1}{n+1}log\,\dot{\sigma} + log\,D \qquad\qquad \textit{Equation 49}$$

where,

$$\sigma_f = \frac{3PL}{4db^2} \qquad\qquad \textit{Equation 50}$$
$$\dot{\sigma} = \frac{3\dot{P}L}{4db^2} \qquad\qquad \textit{Equation 51}$$

The equation to calculate the slope of the linear regression is [67]:

172

$$\alpha = \frac{K \sum_{j=1}^{K} (\log \dot{\sigma}_j \, \log \sigma_j) - (\sum_{j=1}^{K} \log \dot{\sigma}_j \sum_{j=1}^{K} \log \sigma_j))}{K \sum_{j=1}^{K} (\log \dot{\sigma}_j)^2 - (\sum_{j=1}^{K} \log \dot{\sigma}_j)^2} \qquad \textit{Equation 52}$$

and

$$n = \frac{1}{\alpha} - 1 \qquad \textit{Equation 53}$$

The equation to calculate the intercept of the linear regression is [67]:

$$\beta = \frac{(\sum_{j=1}^{K} \log \sigma_j) \sum_{j=1}^{K} (\log \dot{\sigma}_j)^2 - (\sum_{j=1}^{K} \log \dot{\sigma}_j \, \log \sigma_j)(\sum_{j=1}^{K} \log \dot{\sigma}_j)}{K \sum_{j=1}^{K} (\log \dot{\sigma}_j)^2 - (\sum_{j=1}^{K} \log \dot{\sigma}_j)^2} \qquad \textit{Equation 54}$$

and

$$D = 10^{\beta} \qquad \textit{Equation 55}$$

The SCG parameters were determined by 3~4 different crosshead speeds varied from 0.00005, 0.0001, 0.001, and 0.01 to 0.1mm/s (3, 6, 60, 600 to 6000 μm/min). The effects of temperature on SCG parameters were evaluated at room temperature and at elevated temperature of 850°C in air. The loading frame and the bending fixture are parts of the in-house design setup.

Subcritical crack growth (SCG) parameters were determined from the modulus of rupture (MOR) or the four-point bending flexural strength test of the selected structural ceramics (alumina 96 wt% (AL-96)) at three different crosshead speeds ranging from 0.0001, to 0.1 mm/s (6, 60, 600 to 6000 μm/m) with a related stress rate varied from 0.1 to 80 MPa/s. The results are summarized in Table 56 and Table 57, respectively. The relationship between flexural strength as a function of stress rate is presented in Figure 125.

The SCG parameters including both the n-value and the D-value calculated from Equations (48) to (55) are summarized in Table 58. The SCG parameters values evaluated from the best fit regression line of the log flexural strength-stress rate at both room temperature and at elevated temperature of 850°C, at displacement rates from 6, and 60 to 600 μm/min are shown in Figure 126 and Figure 127.

Table 56: **Results of Slow Crack Growth (SCG) for AL-96 Material at Room Temperature (25°C) and High Temperature (850°C) by Autoclave System**

Specimens ID	Temperature (°C)	Crosshead Rate (µm/m)	MOR (Mpa)	ở (Mpa/s)	log σ	Log ở
1	25	6000	142.51	81.60	2.15	1.91
2	25	6000	98.50	64.58	1.99	1.81
3	25	600	150.01	9.33	2.18	0.97
4	25	600	137.73	9.04	2.14	0.96
5	25	600	156.09	8.81	2.19	0.95
6	25	600	175.27	9.88	2.24	0.99
7	25	60	146.59	1.25	2.17	0.10
8	25	60	165.47	1.28	2.22	0.11
9	25	60	166.33	1.06	2.22	0.03
10	25	60	140.72	1.15	2.15	0.06
11	25	6	135.00	0.09	2.13	-1.02
12	25	6	123.00	0.07	2.09	-1.17
13	25	6	143.00	0.08	2.16	-1.11
14	25	6	150.00	0.08	2.18	-1.11
15	850	6000	166.33	86.18	2.22	1.94
16	850	6000	138.53	66.15	2.14	1.82
17	850	600	218.93	9.17	2.34	0.96
18	850	600	176.22	9.18	2.25	0.96
19	850	60	167.88	0.85	2.22	-0.07
20	850	60	176.32	0.87	2.25	-0.06
21	850	6	137.54	0.07	2.14	-1.14
22	850	6	108.22	0.10	2.03	-1.01

Table 57: **Results of Slow Crack Growth (SCG) for AL-96 Material at Room Temperature (25°C) and High Temperature (850°C) by MTS System**

Specimens ID	Temperature (°C)	Crosshead Rate (µm/m)	MOR (Mpa)	ở (Mpa/s)	log σ	Log ở
1	25	600	178.82	18.98	1.28	2.25
2	25	600	145.26	13.23	1.12	2.16
3	25	600	117.83	15.45	1.19	2.07
4	25	60	148.67	1.87	0.27	2.17
5	25	60	125.30	1.70	0.23	2.10
6	25	6	144.01	0.30	-0.53	2.16
7	25	6	125.30	0.27	-0.56	2.10

The n-value characterizes resistance of a material to subcritical crack growth [68, 71]. A high n-value is usually interpreted as a low susceptibility to subcritical crack growth. The n-value for AL-96 at room temperature was approximately 38. On the other hand, n-value

was approximately 42 as determined by the MTS testing system. These subcritical crack growth parameters by MTS are consistent with those of the autoclave as illustrated in Figure 127 and shown in Table 58. The n-value was approximately 9 for the AL-96 at elevated temperature of 850°C. A decreasing n-value with increasing temperature up to 850°C indicates that AL-96 is susceptible to SCG. The n-value at elevated temperature for the AL-96 samples is in line with other reported results [68].
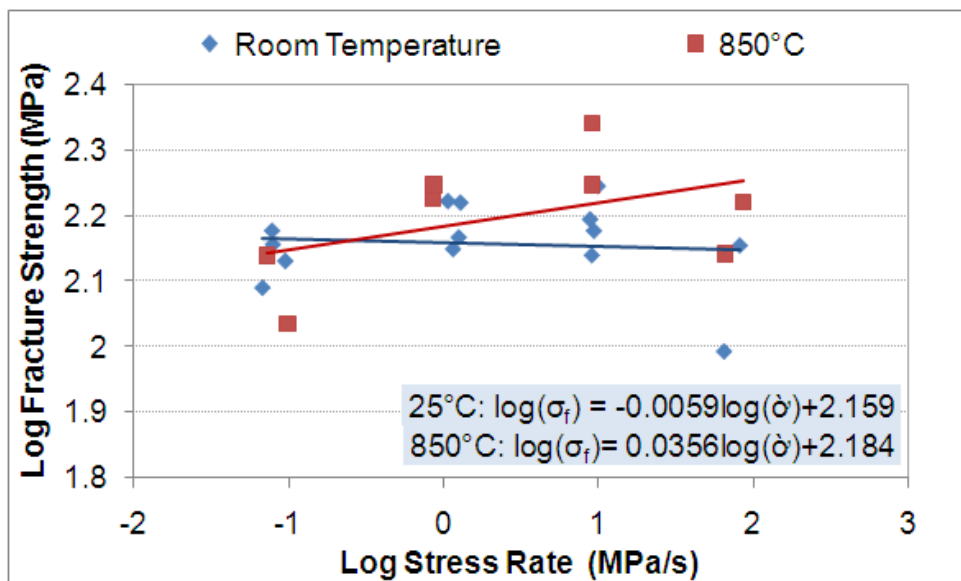
Figure 125:   SCG Schematic of Flexural Strength vs. Stress Rate for AL-96 at Different Crosshead Displacement Controlled Rates: 6, 60, 600 to 6000 µm/min

Table 58:   Results of SCG Parameters (n-value and D-value) for AL-96 Material by Autoclave and MTS Testing Systems

SCG	AutoClave		MTS
Parameters	25°C	850°C	25°C
slop α	0.0256	0.0995	0.023
n	38	9	42
β	2.1721	2.211	2.1448
D	149	163	140

Fracture-mechanics techniques have also been used to show that crack growth in ceramics is a function of temperature [65]. With increasing environment temperature, the

crack propagates faster with a value of K_I. This increase in crack propagation velocity with increasing temperature is consistent with the hypothesis that crack growth in ceramic materials is thermally activated. [65].
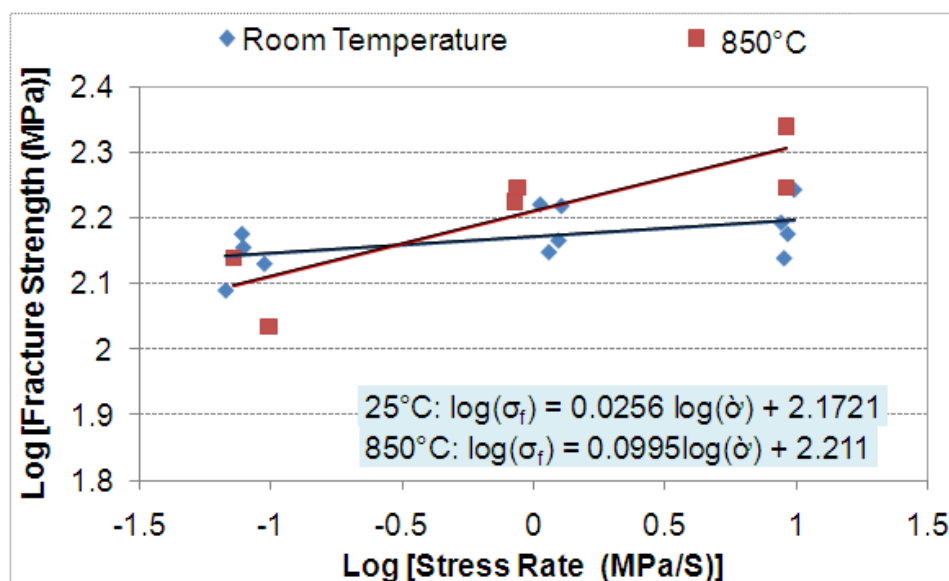
Figure 126: SCG Schematic of Flexural Strength vs. Stress Rate for AL-96 at Different Crosshead Displacement Controlled Rates: 6, 60 and 600 μm/min
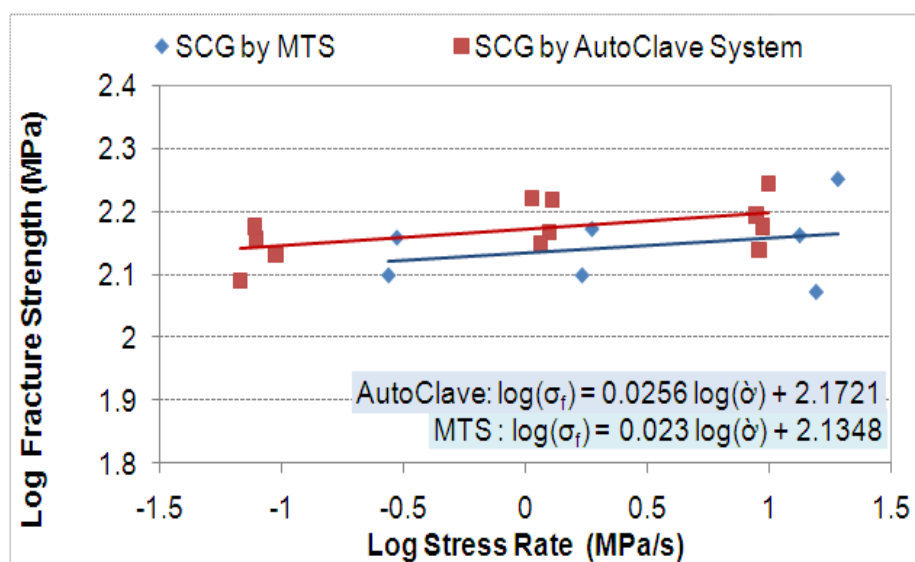
Figure 127: SCG Schematic of Flexural Strength vs. Stress Rate for AL-96 by both MTS and Autoclave Testing Systems

4.1.6 Fractography and Characterization of Fracture Origin by Scanning Electron Microscopy (SEM)

Following the ASTM C1322-05b specifications, fractographic analysis of broken specimens was conducted to characterize types, locations, and fracture origins. Subsequent to the flexural strength test, a SEM study was carried out for various samples at multiple magnifications ranging from 10X to 2500X. Three samples (#2, #6, #16) after the flexural strength test, however, were selected for characterization of fracture types as shown in Figure 128 to 130.

The fracture origin can be seen more clearly at the bottom surface in Figure 128 (a) than at the fracture surface in Figure 128 (b). The intrinsic factor was that could be attributed is the internal pore near the bottom flexural surface (during the flexural strength test) of one of the samples (#2). The fracture surface of sample #6) in Figure 129 shows an irregular angle to the anticipated maximum principal stress, which signifies a misalignment or an error in testing [31]. Another intrinsic type of fracture origin could be observed in sample #16, shown in Figure 130. Additional SEM analyses are needed for better understanding of fracture characterization.
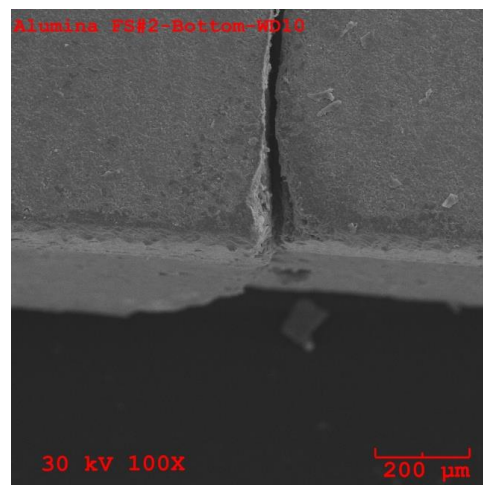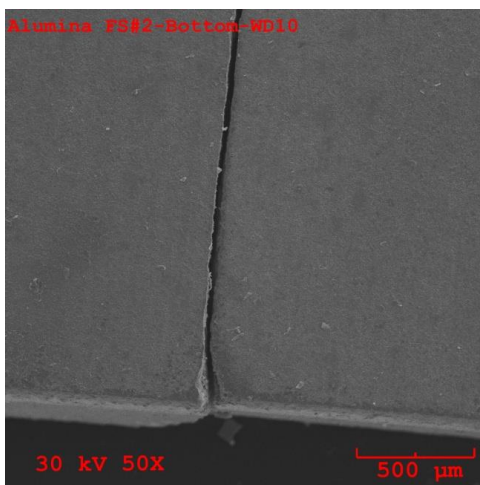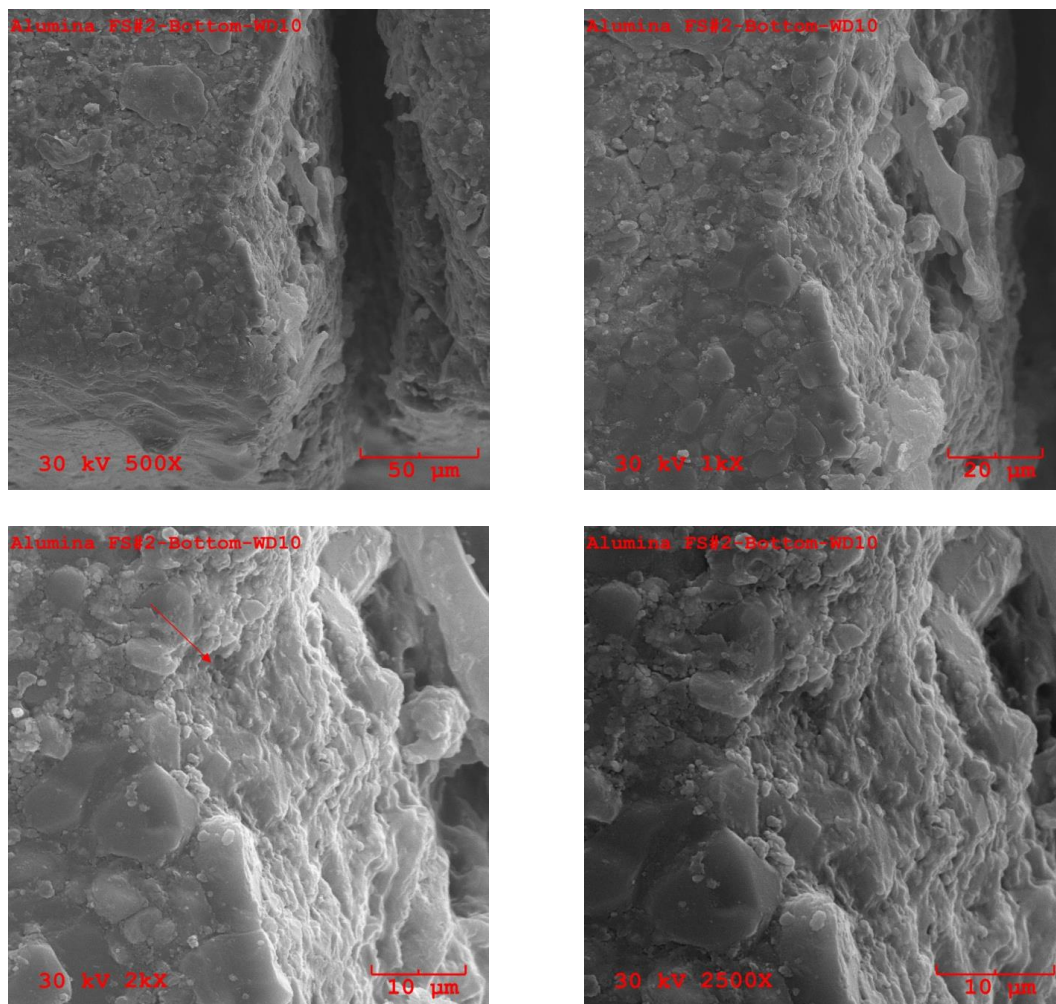
(a)   Bottom Surface of Sample ID #2
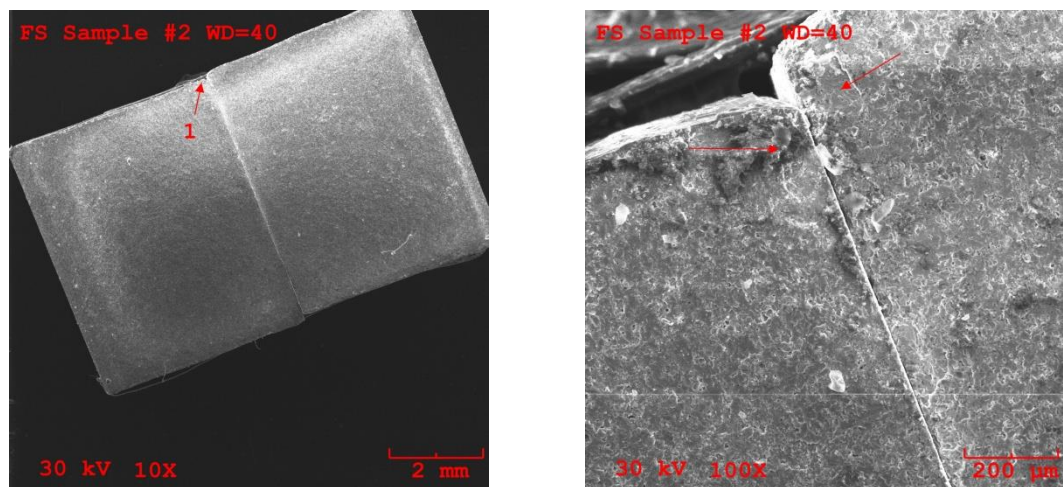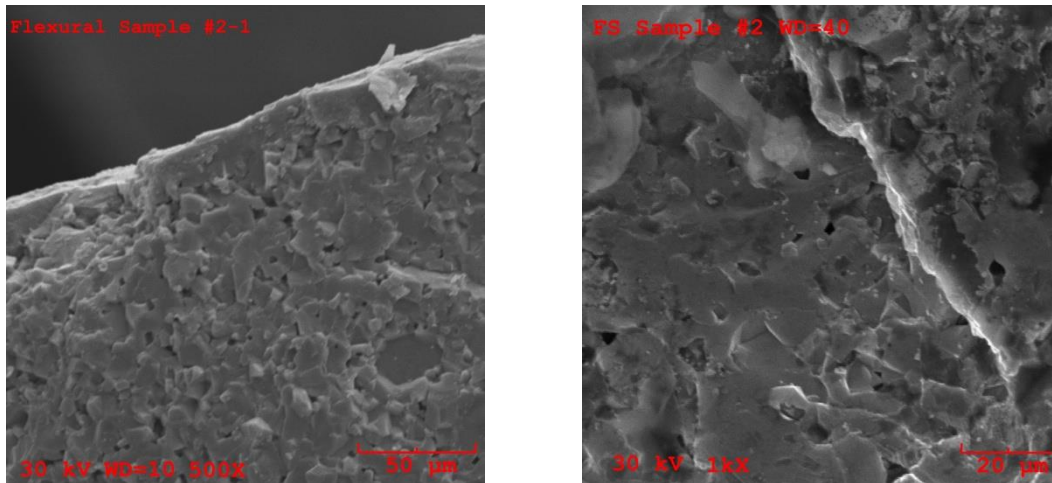
(b)   Fracture Surface of Sample ID #2

Figure 128:   SEM of Fracture Origin for AL-96 Flexural Sample ID #2

The SEM imaging was carried out with 2500x magnification for AL-96, with and without thermal cycling, as shown in Figure 131 (a) to (c). By comparing the grain size and surface morphology, a conclusion was made that grain size increased with increased number of thermal cycles. Generally, the grains in the alumina matrix are subjected to compression and play a major role as a bridge. This corresponds to the grain-bridge model of the R-curve or T-curve properties of ceramic [72]. It has been reported that the slope of R-curve sharply increases from 0.44 to 1.89 as the Al_2O_3 grain size increases from 2.6 to 67.4μm as shown in Table 59 [73]. Residual stress was also reported to increase with grain size due to the thermal expansion anisotropy of Al_2O_3, shown in Table 60 [73]. With increase of grain size of AL-96 after 650 thermal cycles, both R-curve behavior and increased residual stress may have contributed to the increase of hardness, as shown in Figure 116.

High thermal expansion anisotropy also has been known to cause micro-cracks upon cooling [41]. This can be observed in Figure 131 (b) and (c). Many more cracks were also observed with increasing number of thermal cycles. Presence of these cracks contributed to the degradation of E-value (Figure 113).
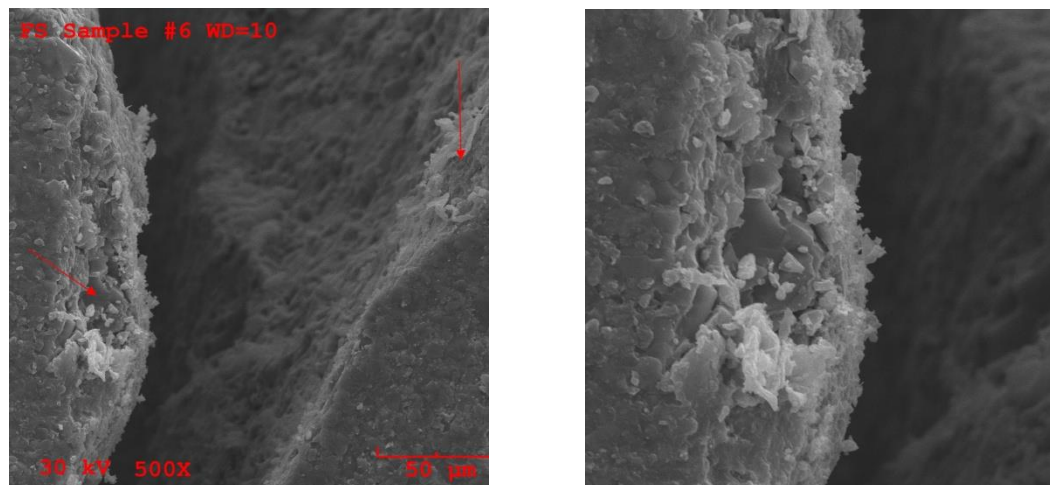
(a)   Bottom Surface of Sample ID #6
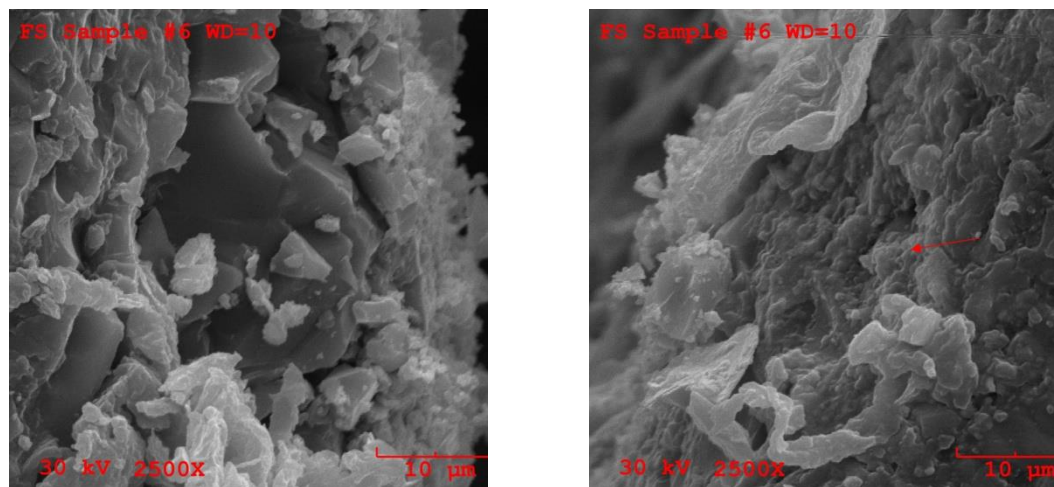
(b) Fracture Surface of Sample ID #6

Figure 129:   SEM Examination of Fracture Origin for AL-96 Flexure Specimen of Sample ID #6

Table 59:   Slope of R-Curve (a) vs. Al$_2$O$_3$ Grain Size [73]

Linear coefficients a and b (from equation $y = ax + b$) as a function of Al$_2$O$_3$ grain size

Al$_2$O$_3$ grain size, μm	2.6±0.8	18.6±8.9	28.4±13.7	39.7±17.2	67.4±29.4
a	0.44±0.19	0.66±0.03	1.02±0.09	1.60±0.03	1.89±0.14
b	3.17±0.45	3.17±0.08	1.94±0.09	0.80±0.28	0.13±0.27

Table 60:   Mean value of Residual Stress vs. Al2O3 Grain Size [73][41]

Mean values of residual stresses measured in alumina ceramics as a function of Al$_2$O$_3$ grain size

Al$_2$O$_3$ grain size, μm	2.6±0.8	18.6±8.9	28.4±13.7	39.7±17.2	67.4±29.4
Mean value of residual stress, MPa	63.1±11.8	78.9±15.8	118.4±27.6	110.5±31.5	126.3±43.4
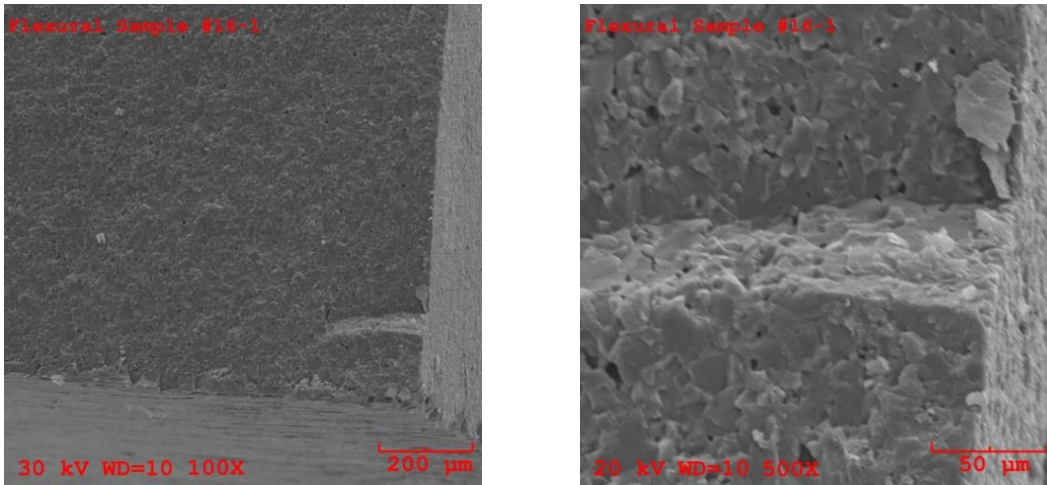
(a) Fracture Surface of Sample ID #16

Figure 130: **SEM Examination of Fracture Origin for AL-96 Flexure Specimen of Sample ID #16**
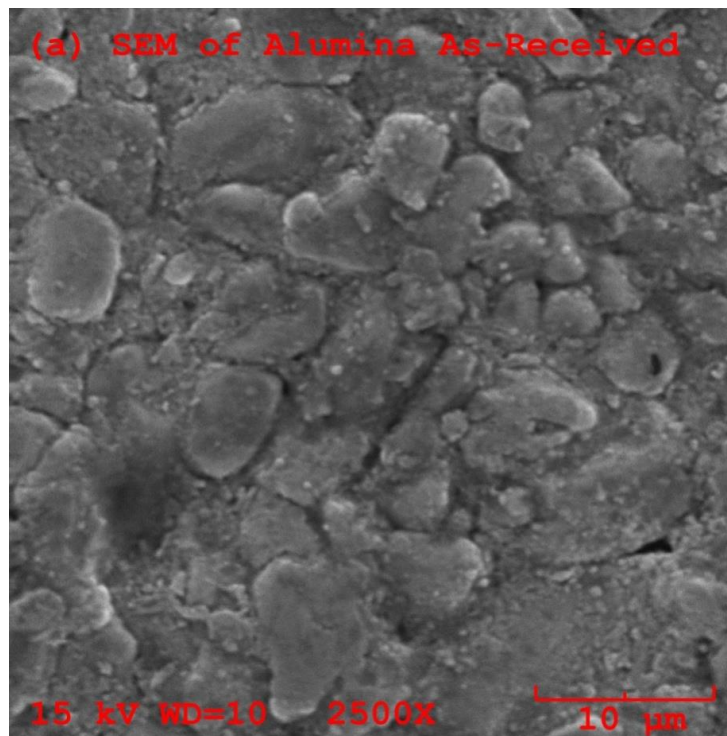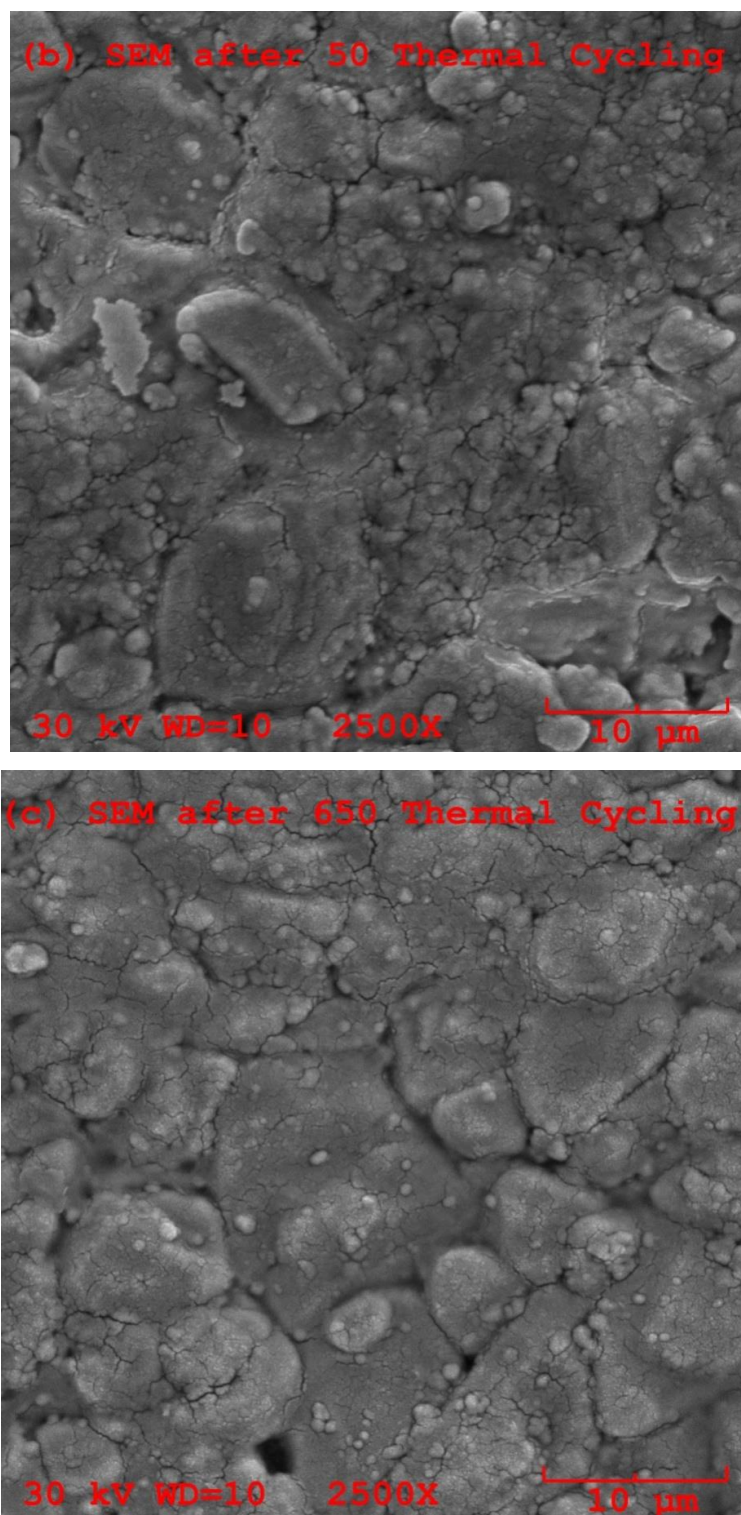
Figure 131: **SEM Images of the Selected Structural Ceramic-Al$_2$O$_3$ (a) As-Received, (b) after 50 Thermal Cycles (c) after 650 Thermal Cycles**

The EDS elemental mapping analysis is shown in Figure 132. It can be seen from this figure that the distribution of the element Al matched the microstructure morphology with SEM imaging for AL-96.
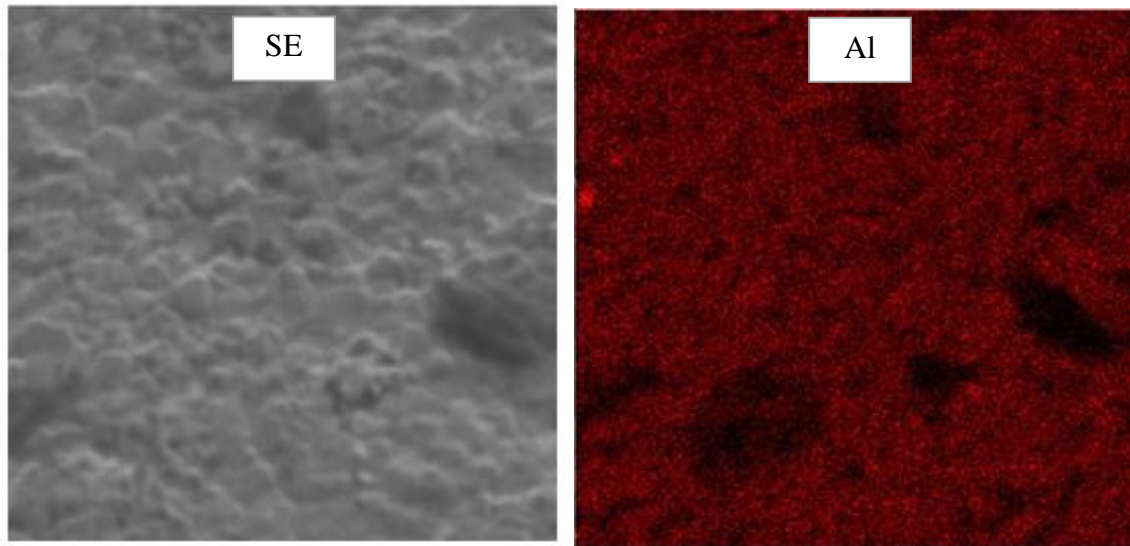
Figure 132:   SEM Imaging (Left) and EDS Elemental Mapping of Al (Right)

4.1.7   Coefficient of Thermal Expansion (CTE)

The instantaneous coefficient of thermal expansion (CTE or α_t) shown in Figure 134 demonstrates a good agreement with the α_t–value of referenced standard Sapphire provided by Netzch's Proteus® software. With the increased testing temperature, the instantaneous CTE increased accordingly because of the asymmetry of the energy well [74], as shown in Figure 133.

It could be noted that the slope of the measured dL/L_0 as a function of temperature in the second axis on the right side of Figure 134 is the same as that of the alpha (α) line vs. temperature in the major axis on the left side. With increase of temperature range, the thermal expansion coefficient also increases, from 6 to 12 x $10^{-6}/°K$. The mean CTE of the selected structural ceramics (AL-96) is estimated to be approximately 8 x $10^{-6}/°K$, in the temperature range of 200–1200°C, which is consistent with data reported in the

literature [75-77].
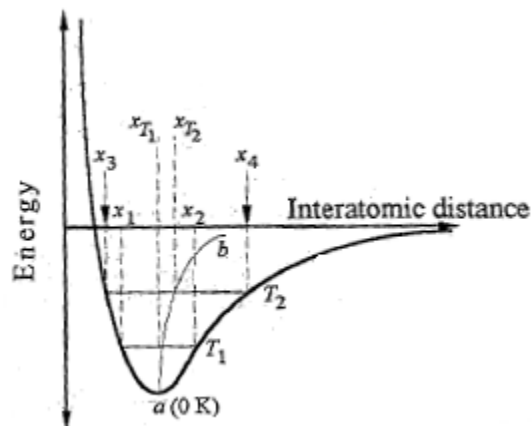
Figure 133: **Effect of Temperature on Interatomic Distance between Atoms and Asymmetry of Well Responsible for Thermal Expansion [74]**
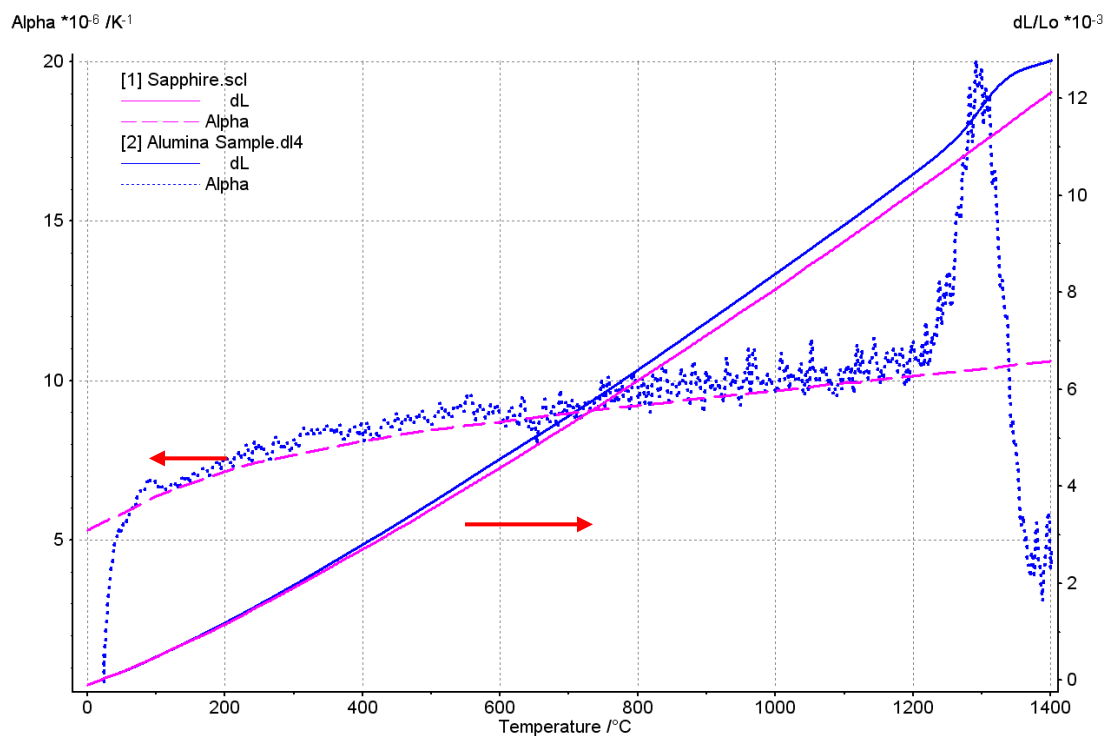
Figure 134: **Coefficient of Thermal Expansion (CTE or α) and dL/L$_0$ vs. Temperature Reference Value of Sapphire (2) Experimental Value of the Selected Structural Ceramic (AL-96)**

4.1.8   X-ray Diffraction (XRD) Phase Analysis and Surface Texture

The phase composition of the selected structural ceramics (AL-96) as α-corundum with a hexagonal crystal structure was verified by XRD powder diffraction method (Figure 135). Pole figures were measured at 2θ values of the peak angles for the four chosen {hkl} planes: {006}, {012}, {113} and {300}, by rotating the sample using the parameters of ψ and φ, as presented in Chapter II of the thesis. The parameter of ψ was set to range from 0° at the center to 90° at the edge, and the parameter of φ was set to range from 0° to 360°.

Based on the hexagonal crystal structure of Al_2O_3 shown in Figure 135, the c-axis pole figure can be defined based on the pole figure of {006} plane which is perpendicular to the c-axis. In Figure 136, with parameter value of α as 0° at the center, the highest intensity along the {006} plane could be observed. At this orientation, the c-axis in the unit cell is normal to the sample's surface.

Similarly, in Figure 136, with parameter value of α as 90° at the edge, the highest intensity of {300} plane pole figure distribution could be observed. At this orientation, the a-axis in the unit cell is parallel to the sample surface. The highest density of other pole figures of {012} and {113} planes was observed at α -value ranging between 30–70°. Therefore, a highly textural polycrystalline alumina can be confirmed by XRD pole figures, and the c-axis in the unit cell is normal to the sample surface.

The texture may have resulted from the grain coarsening at high sintering temperatures, as well as the sintering time [78]. Due to the anisotropy in crystallographic and thermal properties of alumina [72], the texture may induce additional thermal residual stress, which may lead to an increase in the fracture toughness or hardness as the crack grows.
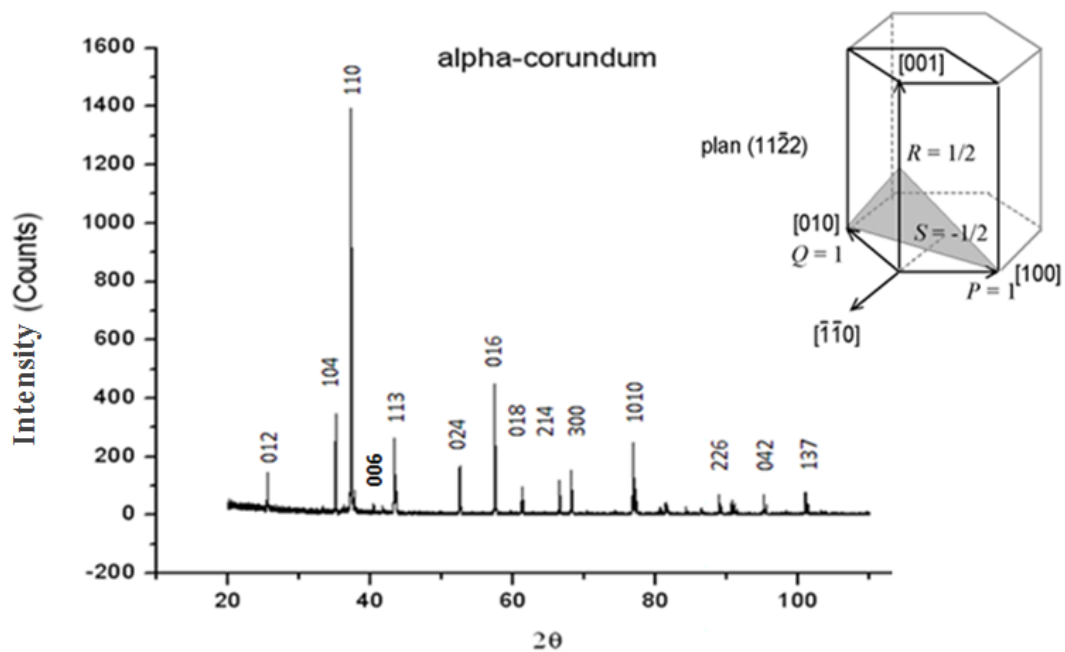
Figure 135:   XRD Phase Analysis of the Selected Structural Al₂O₃, AL-96
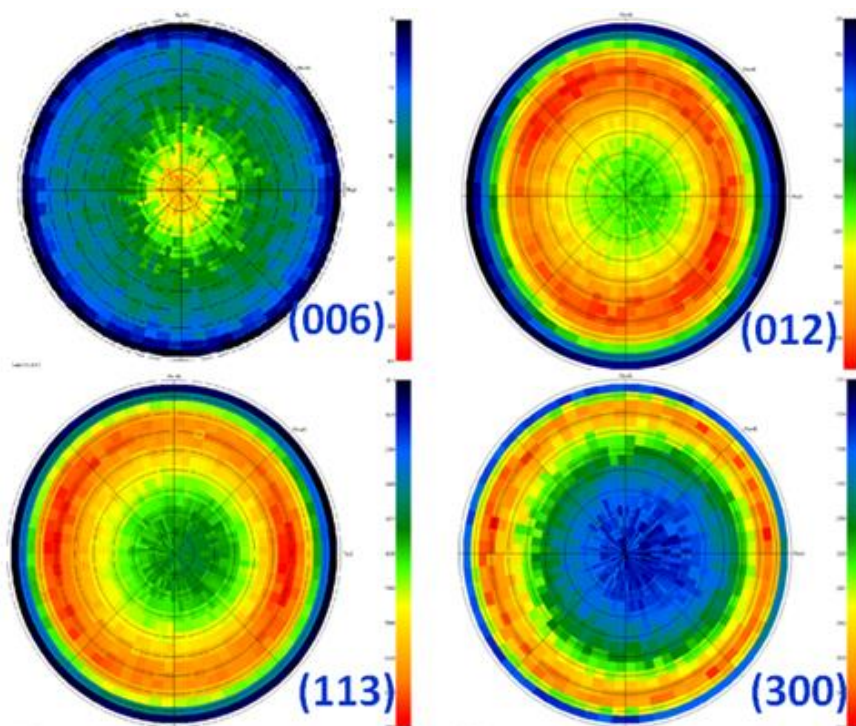
Figure 136:   Pole Figure for Surface Texture Analysis along Several (h k l) Planes:
(006), (012), (113), and (300)

4.1.9   Residual Stress by X-Ray $\sin^2\psi$ Technique

The effects of thermal cycling on residual stress are summarized in Table 61 and plotted in Figure 137. It is generally accepted that the higher the diffraction angle, the greater the precision [34, 79]. A diffraction peak angle of $2\theta \approx 136.170°$ was selected to measure residual stress for the selected structural alumina. The bulk residual stress is the tensile stress and is approximately 96 MPa for as-received specimens. The residual stress increases with thermal cycling from 0 to 650 cycles, and a maximum tensile residual stress of 480 MPa is exhibited after 650 thermal cycles. With the thermal cycling between 650 to 900 cycles, the residual tensile stress decreases to a large extent.

Table 61:   Results of Residual Stress as an Effect of Thermal Cycling for AL-96

Thermal Cycling	$2\theta_{\phi 0}$	Lattice Plane	$d_{\phi 0}$	Elastic Constant E/(1+v) Gpa	Slope of $d_{\phi\psi}$ vs. $\sin^2\psi$	Least Square Regression (R^2)	Residual Stress (MPa)
0	136.0307	(416)	0.8578	274.4	0.0003	0.4827	96
250	136.1700	(416)	0.8578	274.4	0.0010	0.791	320
650	136.0307	(416)	0.8578	274.4	0.0015	0.7726	480
700	136.0307	(416)	0.8578	274.4	0.0009	0.7779	288
900	136.0307	(416)	0.8578	274.4	0.0003	0.4583	96
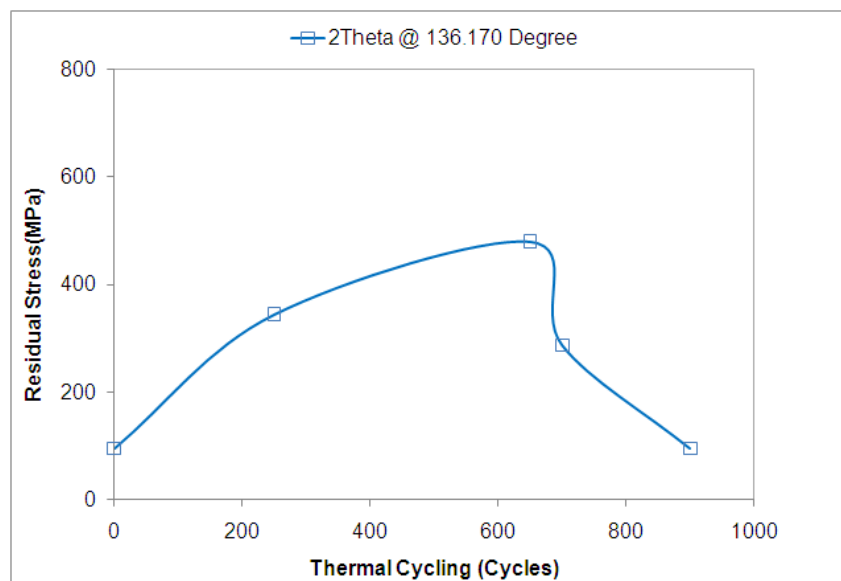
Figure 137:   Diagram of Residual Stress as an Effect of Thermal Cycling for AL-96

4.2 Characterization of Thermo-Mechanical Properties and Microstructure for Selected Structural Ceramic – Yttria-stabilized Tetragonal Zirconia Polycrystalline (Y-TZP)

4.2.1 Bulk Density and Porosity Measurement

The density of the selected dense Y-TZP ceramic was evaluated at ambient temperature based on Archimedes' principle. Results are shown in Table 62. The results are consistent with the reference values published by STC Corp. (www.ceramics.net).

Table 62:   Density of Y-TZP Material

Sample ID	W_d (g)	W_t (g)	W_s (g)	V_s (ml)	ρ (g/cc)
Y-TZP#13	3.16	52.29	3.16	0.61	5.18
Y-TZP#15	3.26	52.39	3.26	0.62	5.25
Average (*g/cc*)			5.21		

4.2.2 Elastic Properties

Dynamic Young's modulus (E) of Y-TZP was evaluated at ambient temperature (25°C) and at high temperature (up to 850°C). The observed Young's modulus of 204 GPa (Table 63) is consistent with the reference value of 206 GPa for this Y-TZP material at room temperature (Table 64).

Effects of temperature on dynamic Young's modulus of Y-TZP are shown in Figure 138. The Young's modulus degrades with increasing temperature. A similar observation was also reported for the selected structural alumina [80]. For the selected alumina AL-96, the dependence of E-value with temperature can be represented by E=A-BT [61, 80]:

The Young's modulus of the as-received Y-TZP material, however, did not follow a linear relationship. In temperatures ranging from 55°C to 88°C, 106°C to 133°C, 254°C

to 298°C, 379°C to 512°C, and 594°C to 818°C, the E-value is fairly constant and independent of temperature (Figure 138). The value of the Young's modulus degrades by 17% from 204 GPa at 25°C to 171 GPa at 400°C; it reduces, however, only 2% from 171 GPa at 400°C to 166 GPa at 800°C.

Table 63:   Elastic Properties for Y-TZP Material at Room Temperature

Elastic Properties	Experimental Results	Reference Value
Young's Modulus (E)	204 GPa	206 GPa
Shear Modulus (G)	/	92 GPa
Poisson Ratio (υ)	/	0.36

Table 64:   Physical and Mechanical Product Specifications for Y-TZP Material Provided by Manufacturer (STC Corp.) [81]

Property	ASTM Method	Units	MSZ-200	Y-TZP
Color	-	-	ivory	ivory
Gas Permeability	-	-	gas tight	gas tight
Density	C 20-97	g/cc	5.72	6.00
Hardness	-	Mohs Scale	8	8
Water Absorption	C 20-97	%	0	0
Flexural Strength	F 417-87	psi	85,000	115,000
Tensile Strength	-	psi	42,000	57,000
Compressive Strength	-	psi	400,000	425,000
Elastic Modulus	C 848	psi x 10^6	30	30
Shear Modulus	C 848	psi x 10^6	12	11
Poisson's Ratio	C 848	none	0.28	0.36
C.T.E., 25 – 100 °C	C 372-96	x10^{-6}/C	8.9	6.9
C.T.E., 25 – 300 °C	-	-	9.7	8.1
C.T.E., 25 – 600 °C	-	-	10.0	8.7

Effect of thermal cycling (up to 1200 cycles) on the E-value is also presented in Figure 138. When compared with the results of Young's modulus for the as-received Y-TZP sample, the E-value decreases slightly for the Y-TZP specimen after 500 thermal cycles, and then increase by a small amount after 1200 thermal cycles. The nature of the

nonlinear relationship of E-value as a function of temperature does not vary for all the tested Y-TZP specimens (i.e., as-received, after 500 thermal cycles and 1200 thermal cycles, respectively).
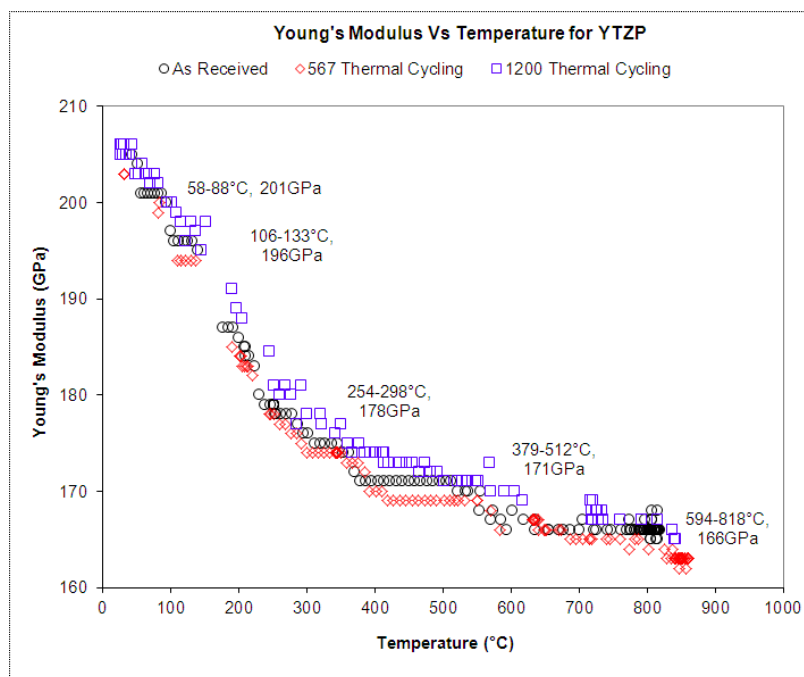
Figure 138: Effects of High Temperature and Thermal Cycling on Young's Modulus (E-Value) for Y-TZP Material

Measured resonant frequencies for the same Y-TZP specimen, both as-received and after 1200 thermal cycles, are shown in Figure 139. The measured resonant frequency for the Young's modulus test follows a trend line similar to that of the Young's modulus for Y-TZP specimens with or without thermal cycling. Repeated tests were conducted in the temperature range of 25°C to 850°C. The results are shown in Figure 140. The measured Young's modulus values and the measured resonant frequencies are consistent. The Y-TZP specimen shrinks in the cross-section after 1200 thermal cycles (Figure 141). This shrinkage in the geometry is related to phase transformation or chemical decomposition as a result of thermal cycling.
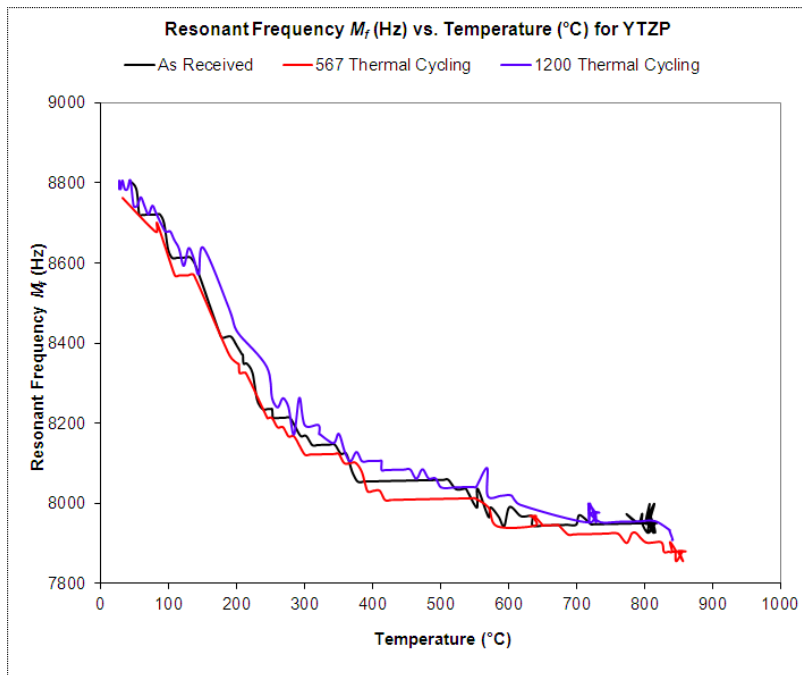
Figure 139: **Effects of High Temperature and Thermal Cycling on Measured Resonant Frequencies during Young's Modulus Test for Y-TZP Material**
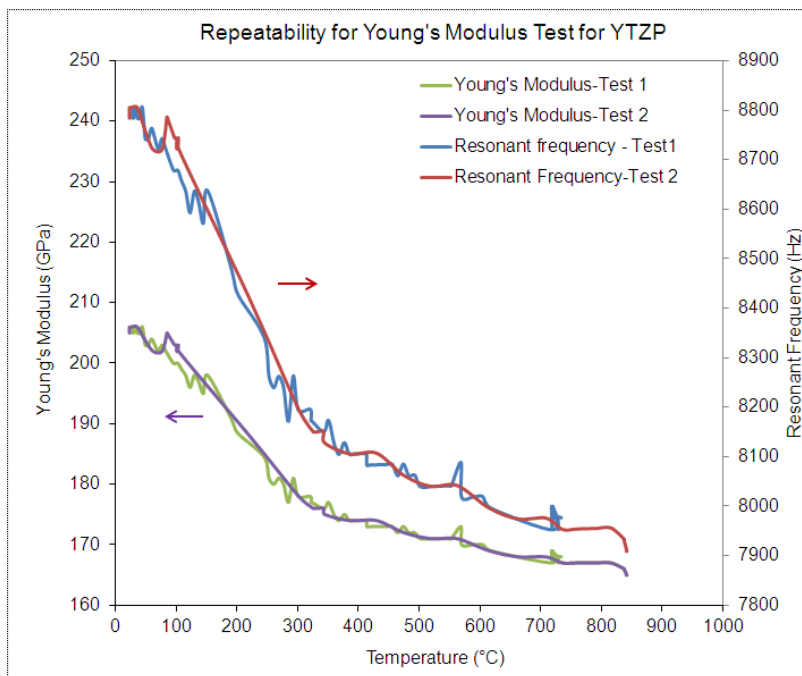
Figure 140: **Results of Young's Modulus Test and Resonant Frequencies Measurement for Y-TZP material**
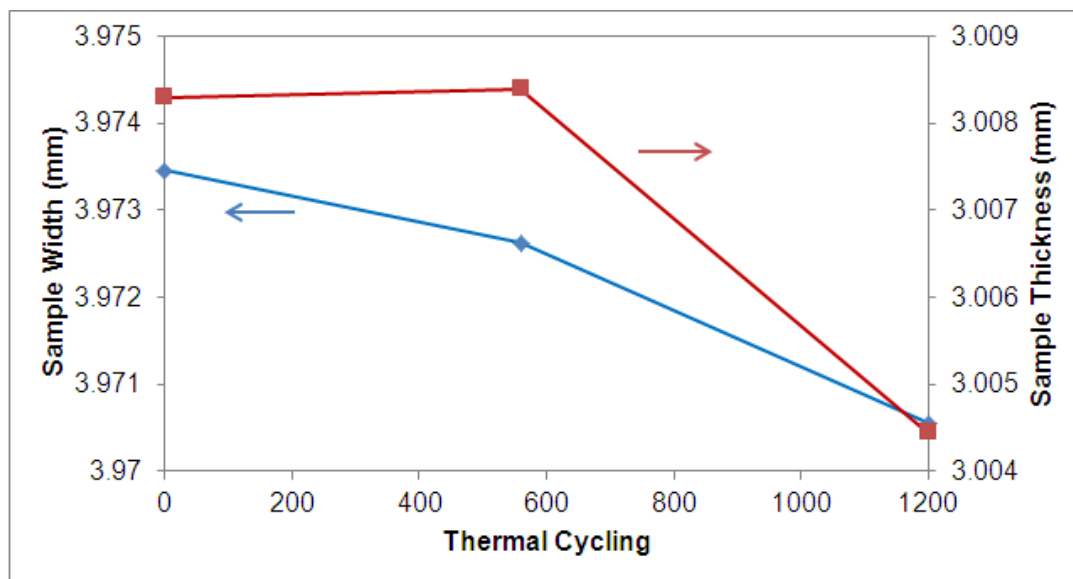
Figure 141: **Effect of Thermal Cycling on the Geometry of Y-TZP Specimen for Young's Modulus Test**

4.2.3 Vickers Hardness Number (HV)

Vickers Hardness (HV) numbers of the Y-TZP sample were evaluated both as-received and after 1200 thermal cycles. The results are shown in Table 65 and the indentation mark is shown in Figure 142. The observed values of hardness are consistent with the values reported in the published literature [82, 83].

Table 65: **Vickers Hardness Number (HV) for Y-TZP at Room Temperature (25°C)**

ID	HV (GPa)	Standard Deviation (GPa)	Difference to the As Received Value (%)
As-Received	13.02	1.05	0
560 Thermal Cycling	12.90	0.81	−0.95%
1200 Thermal Cycling	13.27	0.88	1.91%

Vickers hardness number for the as-received Y-TZP material decreases to a very small extent after 560 thermal cycles and increases approximately 2% after 1200 thermal cycles. This is consistent with the trend of the Young's modulus as previously discussed.
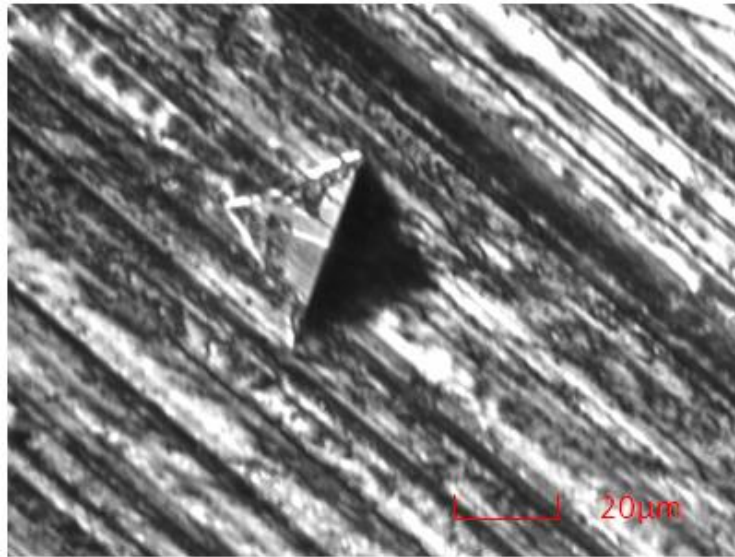
Figure 142:   Optical Observation of the Indentation after Vickers Hardness Test for Y-TZP Material

4.2.4   Microscopic Observation by Scanning Electron Microscopy (SEM)

The SEM imaging was carried out for Y-TZP, as-received and after 1000 thermal cycles, under magnification from 50X to 50000X, (Figure 143). The grain size of the Y-TZP samples is estimated to be in the range of 50–500nm. More tetragonal crystalline grains were observed for Y-TZP material after 1000 thermal cycles than for the as-received sample, which is consistent with the results of XRD analysis presented in the previous section.

4.2.5   Coefficient of Thermal Expansion (CTE)

Results of instantaneous coefficient of thermal expansion (CTE α_t) for Y-TZP material

are presented in Figure 144. The slope of the measured dL/L_0 data shown in the second axis (plotted as a function of testing temperatures) is considered as the CTE instantaneous alpha (α_t) value. Three repeated measurements of the CTE values for the Y-TZP material were conducted on the same CTE sample (Figure 144). The coefficient of thermal expansion increases from 10 x 10^{-6}/°C at room temperature to 14 x 10^{-6}/°C at 1200°C for Y-TZP material. A small peak of the CTE curve occurs at about 850°C, which indicates a possible phase transformation or chemical decomposition.

| (a)   As-Received | (b)   After 1000 Thermal Cycles |
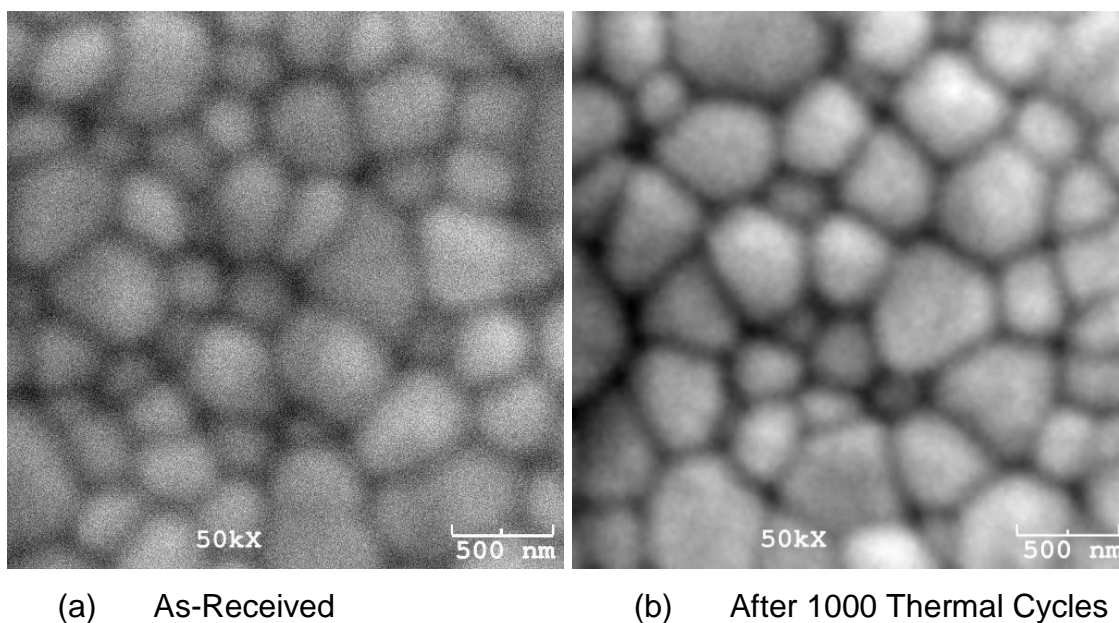
Figure 143:   SEM Observations for YTZP (a) As-Received (b) after 1000 Thermal Cycling between 50-850°C

4.2.6   Thermal Analysis: TG/DTA

The parameters used for TGA and DTA are the weight changes (% or mg) and the endothermic or exothermic microvolt. The TG/DTA for the standard reference material of pure Indium metal is shown in Figure 145. Peak temperature during the heating process is approximately 157.77°C for the melting point and the same for the solidification temperature during the cooling process. The melting point tested is

consistent with the reference value of 156.6°C based on the Perkin Elmer Diamond TG/DTA analyzer manual.
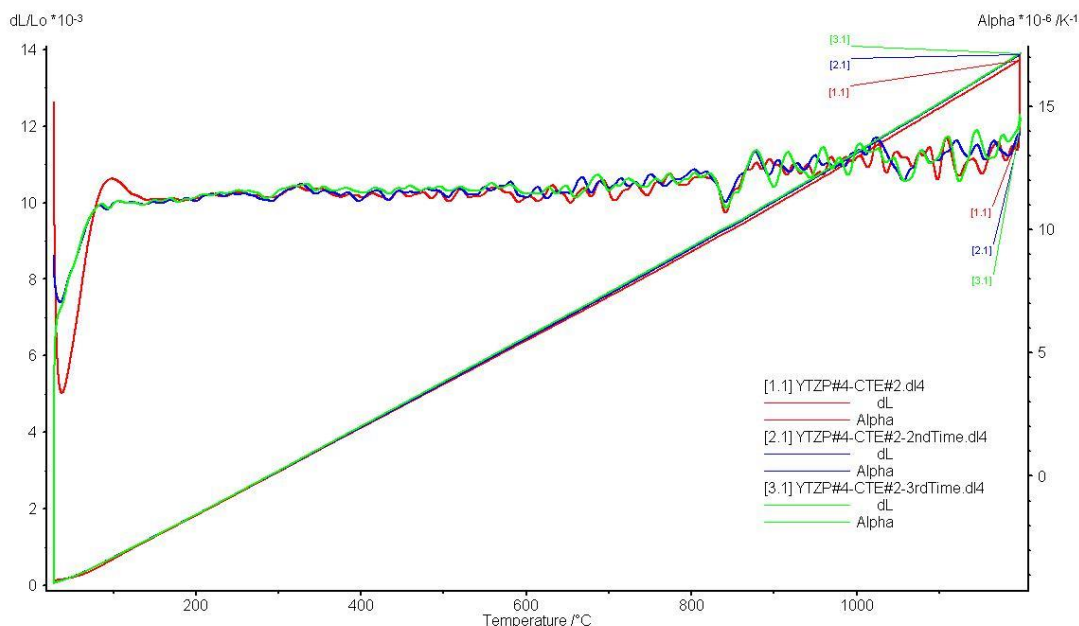
Figure 144: **CTE Instantaneous Physical Alpha (A$_t$) and DL/L$_0$ on Heating Rate at 3k/min in Air for Y-TZP Material**

The solid and crushed samples of Y-TZP material exhibit very little change in weight as a function of temperature (Figure 146). It is generally known that heating rate affects the peak shape in TG/DTA. Two heating rates of 5°C/min and 20°C/min were selected in order to compare the effect of heating rate on DTA curves. Results for solid and crushed samples are shown in Figure 147. The exothermic peak starts approximately at 550°C for both the heating rates; however, the peak for the DTA curve at the heating rate of 20°C/min is, however, more clearly evident than that can be seen at heating rate of 5°C/min.

To study the effect of temperature on DTA results, three different temperature ranges (40°C to 600°C, 40°C to 900°C, and 40°C to 1400°C) were selected for both solid and crushed samples of Y-TZP material. The results are presented in Figure 148 (a) to (c).
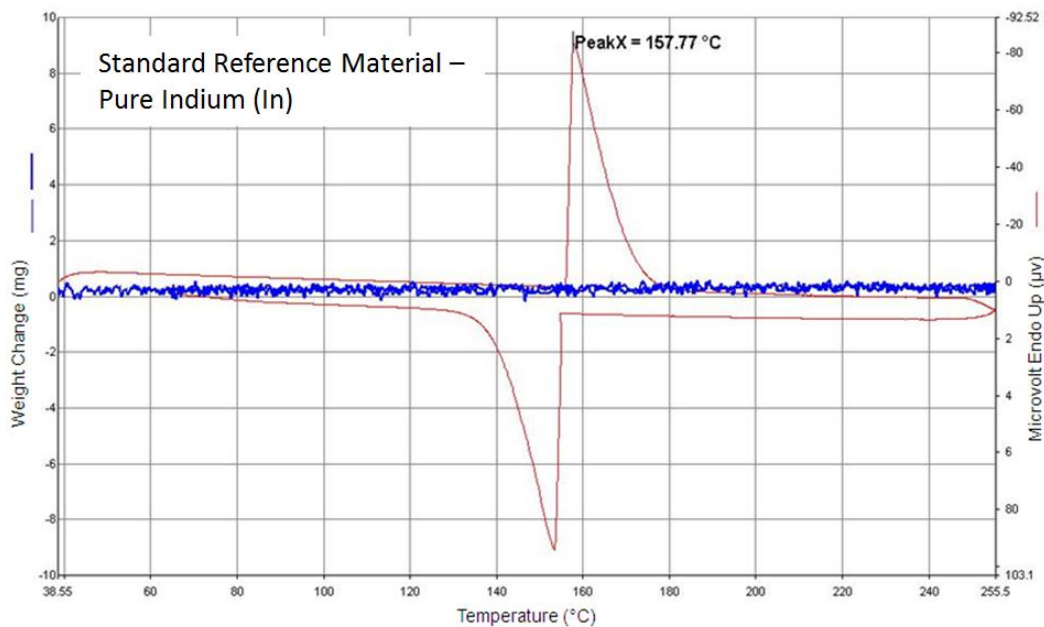
Figure 145:   Thermogravimetry (TG) Result and Differential Thermal Analysis (DTA) Results of Standard Reference Material of Pure Metal Indium at the Heating and Cooling Rate of 20 °C/min
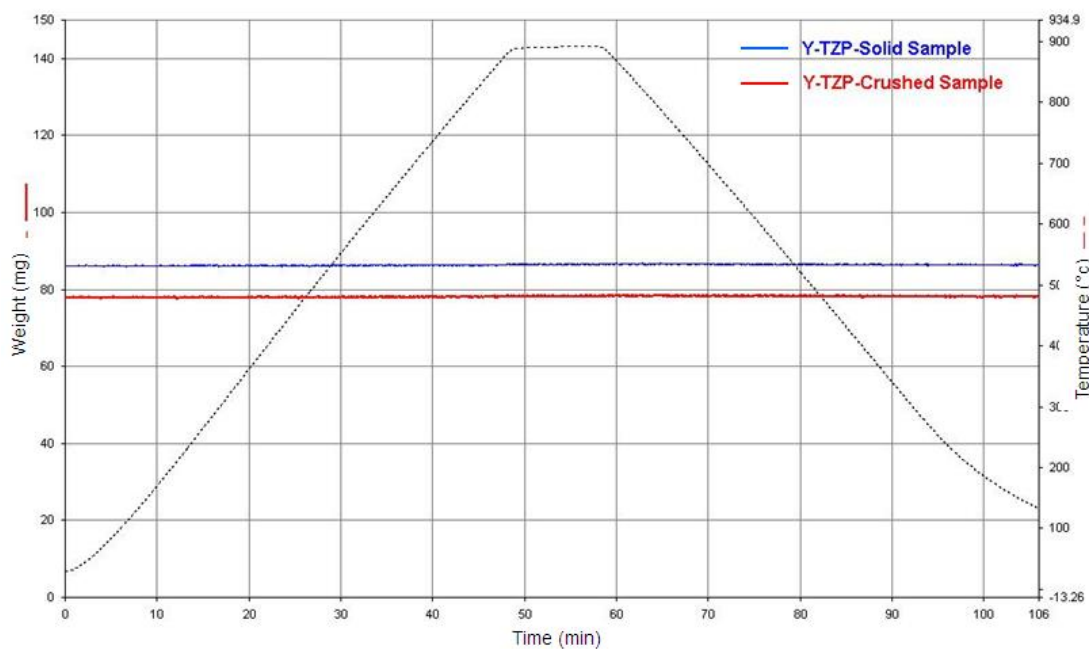
Figure 146:   Thermogravimetry (TG) Result for Y-TZP Material at the Heating and Cooling Rate of 20°C/min
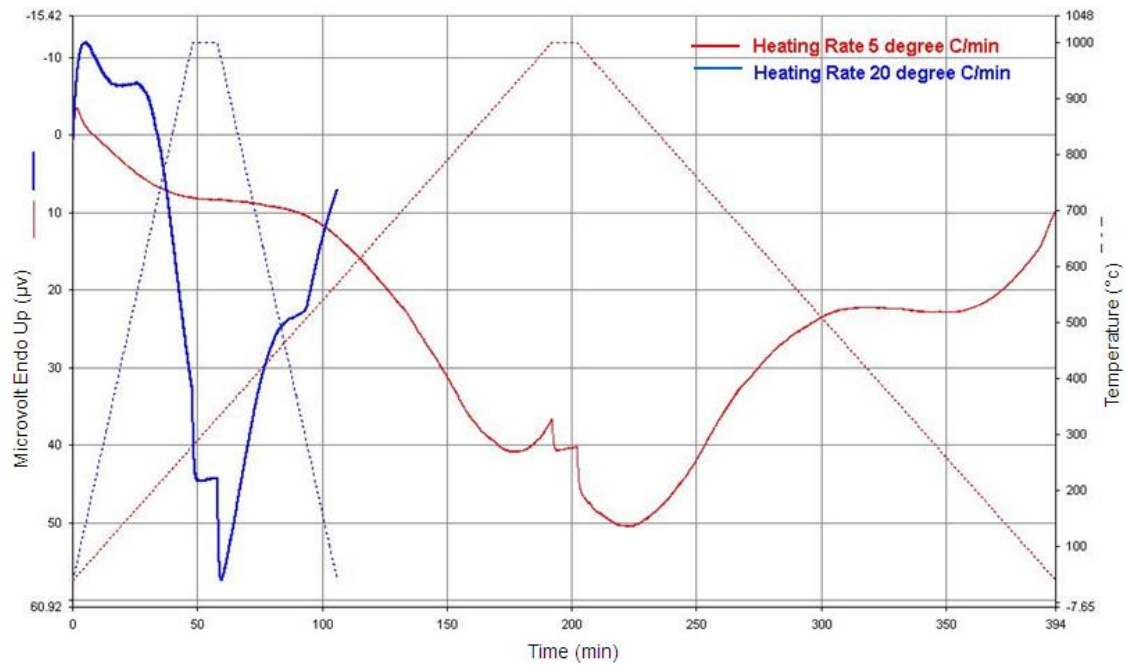
Figure 147:   Differential Thermal Analysis (DTA) Results of Y-TZP Crushed Sample at Different Heating Rates of 5°C/min and 20°C/min
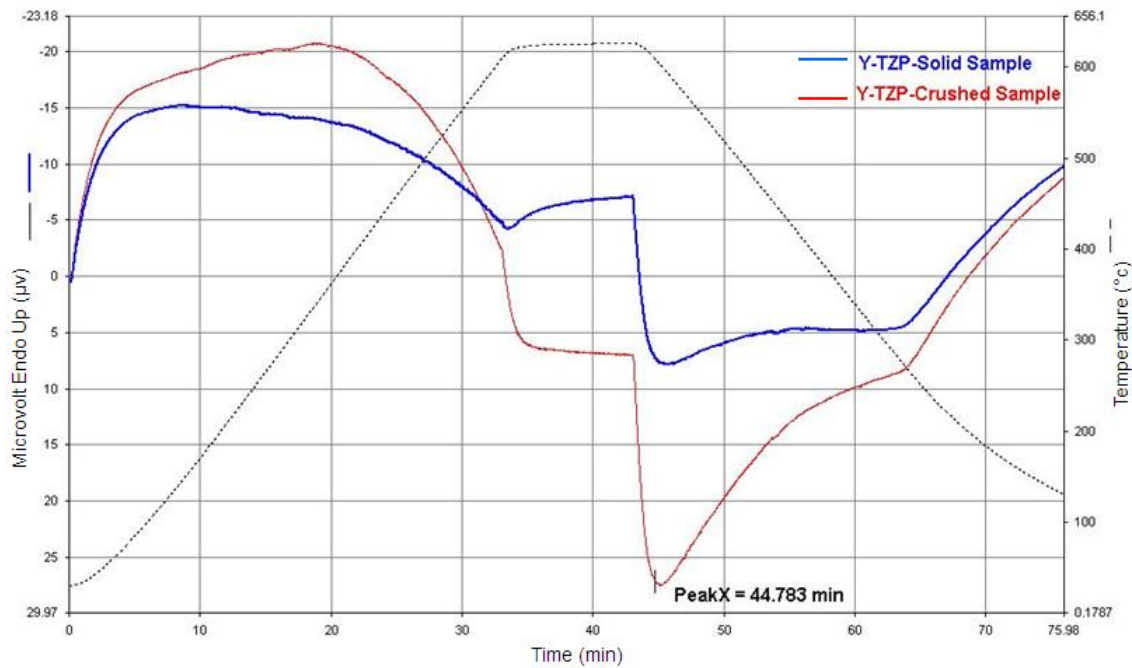
(a) 40–600°C
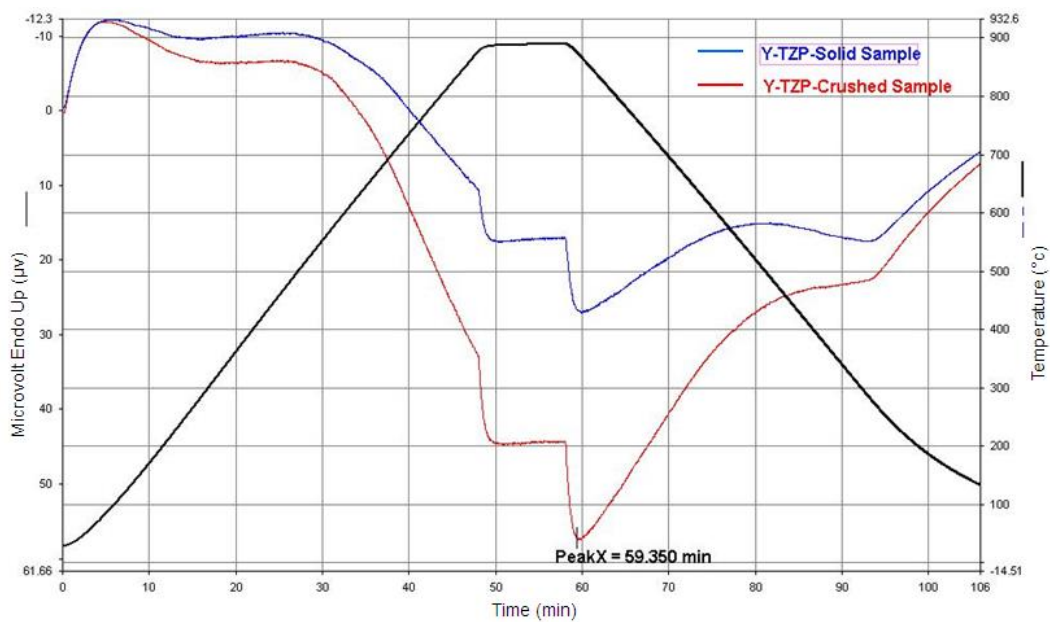
(b) 40–900°C
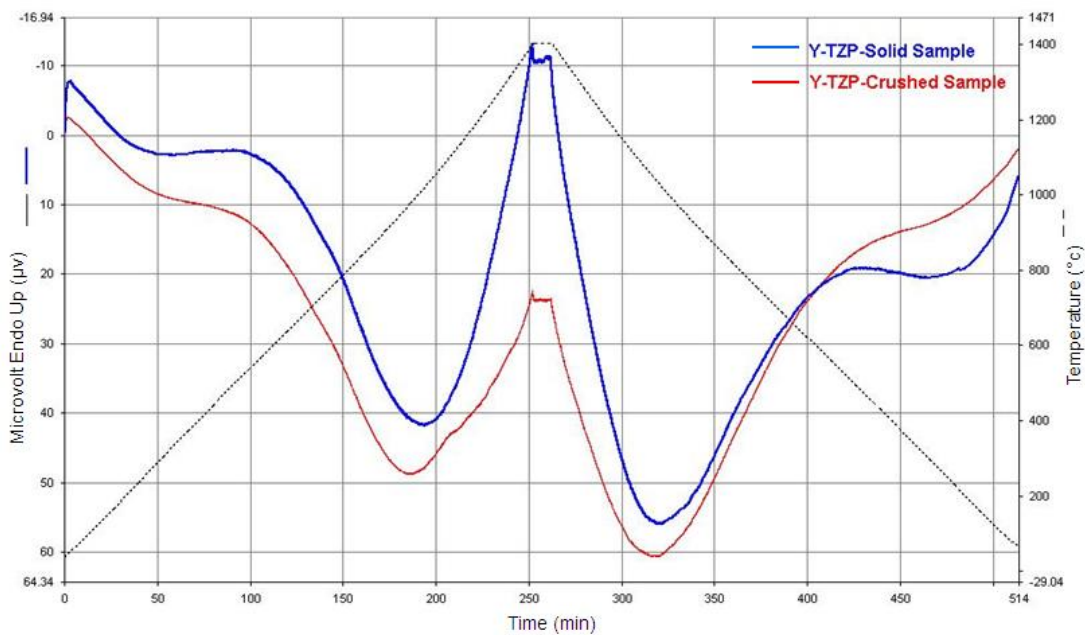
(c) 40–1400°C

Figure 148:   Differential Thermal Analysis (DTA) Results of Y-TZP Material at 3 Different Temperature Ranges

For all the three testing temperature ranges, the crushed sample demonstrated more

exothermic heat loss than the solid sample. From Figure 148 (a) and (b), it can be seen that the exothermic peaks have a wide temperature range from 550°C to 600°C, in both heating and cooling processes. At a temperature around 500°C, it seems that the phase changes from amorphous or low crystalline phases to high crystalline phase. The exothermic peaks can be observed in Figure 148 (c) in the heating and the cooling process. This suggests that the phase transformation may not be reversible.

4.2.7   X-Ray Diffraction (XRD) Phase Analysis

Shown in Figure 149 are reference diffraction patterns for the three common zirconia phases: monoclinic (M), tetragonal (T), and cubic (C). The standard diffraction pattern for 3 mol% yttria- stabilized tetragonal zirconia polycrystalline (3Y-TZ) is also shown in Figure 150. The atomic structures of these reference diffraction patterns are shown in the 3D diagrams in Figure 151.

The diffraction pattern of the selected and as-received Y-TZP sample is indexed within the angle $25° < 2\theta < 85°$ (Figure 152) through which most Bragg reflection peaks coincide with the strong peaks of 3Y-TZP material, and the other phases are presented in Figure 149. The Y-TZP sample is considered to be the polymorph of monoclinic (M-phase) zirconia and tetragonal 3Y-TZP phase. The strongest peak occurs at $2\theta \approx 36.5°$ with Miller indices $(110)_T$ plane for T-Phase and $(102)_M$ for M-Phase. Comparing the observed patterns with the reference powder diffraction database, a significant discrepancy can be identified for the relative intensities between the experimental and the database entries for the Miller indices $(101)_T$, $(110)_T$, and $(112)_T$ crystallographic planes. The deviation may be due to the sample alignment or to the existence of preferred orientations [84].

A series of XRD tests were conducted to evaluate the effects of the sample alignment and surface morphology. Diffraction patterns for the Y-TZP sample after 500 and 1200 thermal cycles and for the as-received sample are shown in Figure 152.
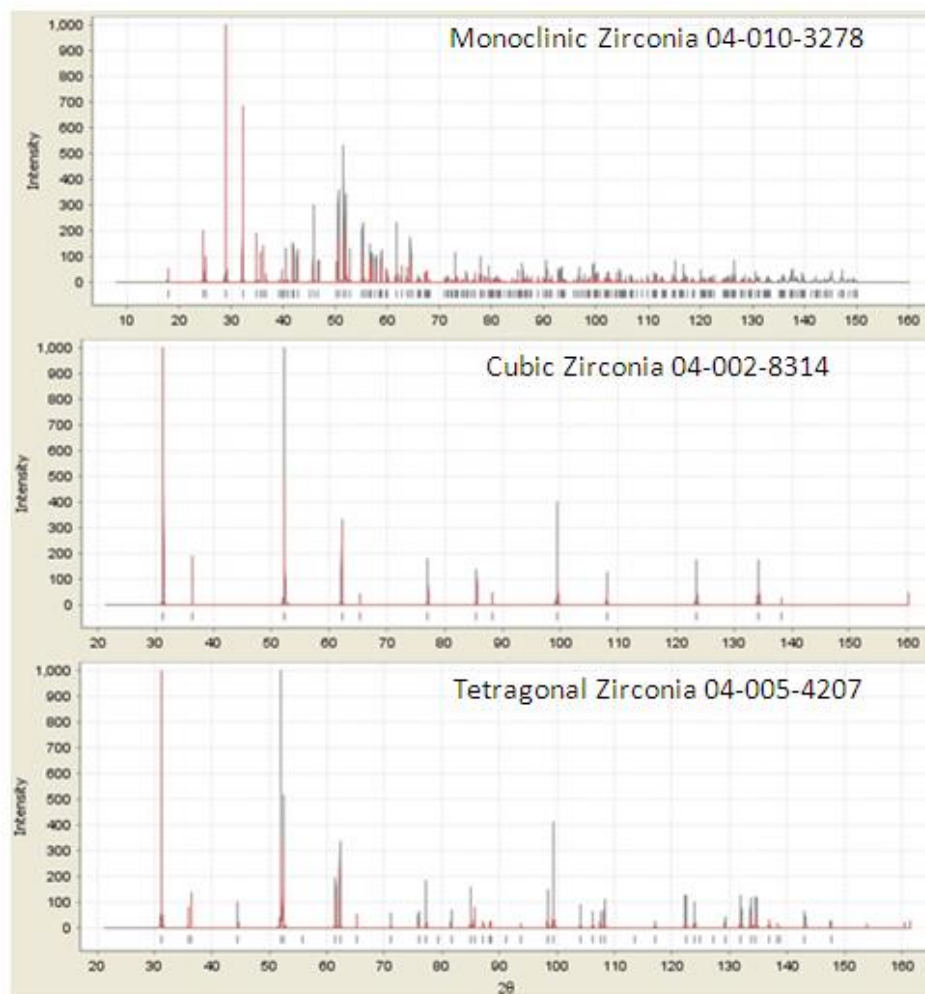
Figure 149:   Reference Powder Diffraction Patterns for Three Common Crystalline Zirconia (ZrO₂) Materials: Monoclinic Zirconia (M-ZrO₂), Tetragonal Zirconia (T-ZrO₂), and Cubic Zirconia (C-ZrO₂) [62]
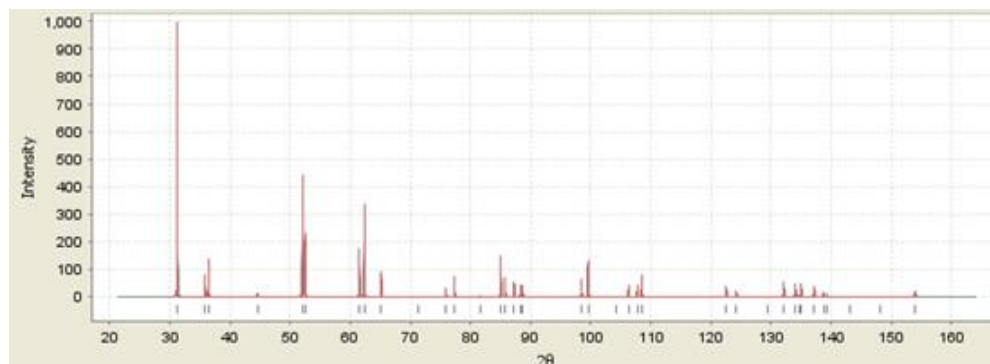
Figure 150:   Reference Powder Diffraction Pattern for 3Y-TZP [62]

(a)   Monoclinic Crystal Structure

(b)   Cubic Crystal Structure

(c)   Tetragonal Crystal Structure

(d) Y-TZP Tetragonal Structure
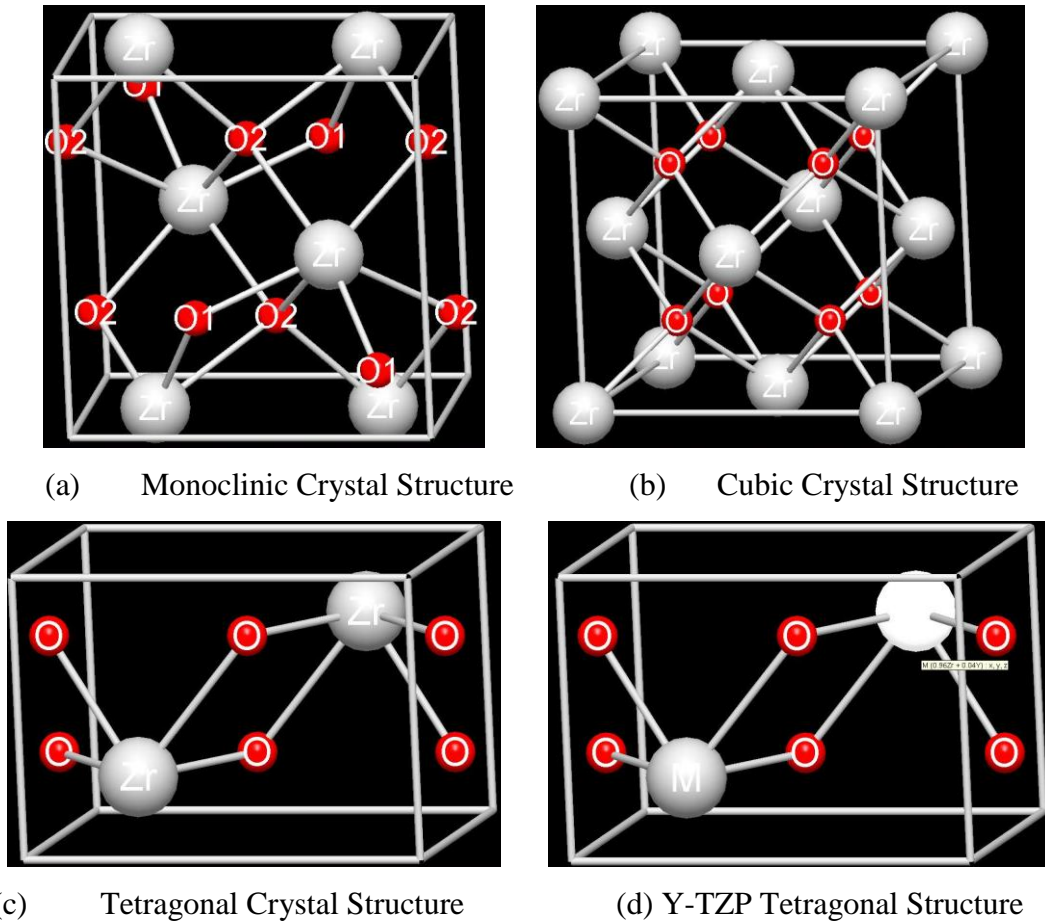
Figure 151:   3D Unit Cell Structure for Crystalline Zirconia and Y-TZP [62]

Because of the presence of a very intense Bragg peak for the Miller plane (110), and since all others are quite weak, the intensity was plotted as the dependent variable (y-axis) versus the Bragg angle (2θ), shown in Figure 152 (a), and also calibrated as its square root versus 2θ, as shown in Figure 152 (b) for a better visualization of the low-intensity features.

In a powder diffraction pattern, the peak position normally is a function of the unit cell parameters (a, b, c, α, β, γ), the peak intensity is related to the atomic parameters that determine the preferred orientation of a specimen, and the peak shape is related to grain size or strain and stress. These relationship are shown in Table 66 [59].
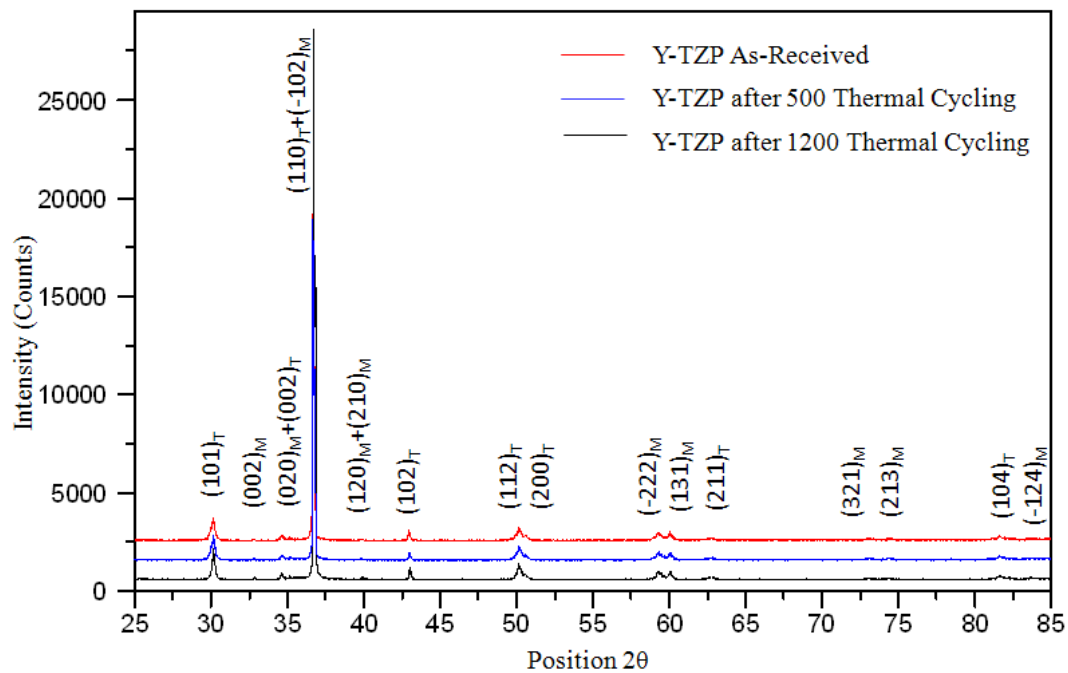
(a)   **Y-Scale in Intensity (counts)**
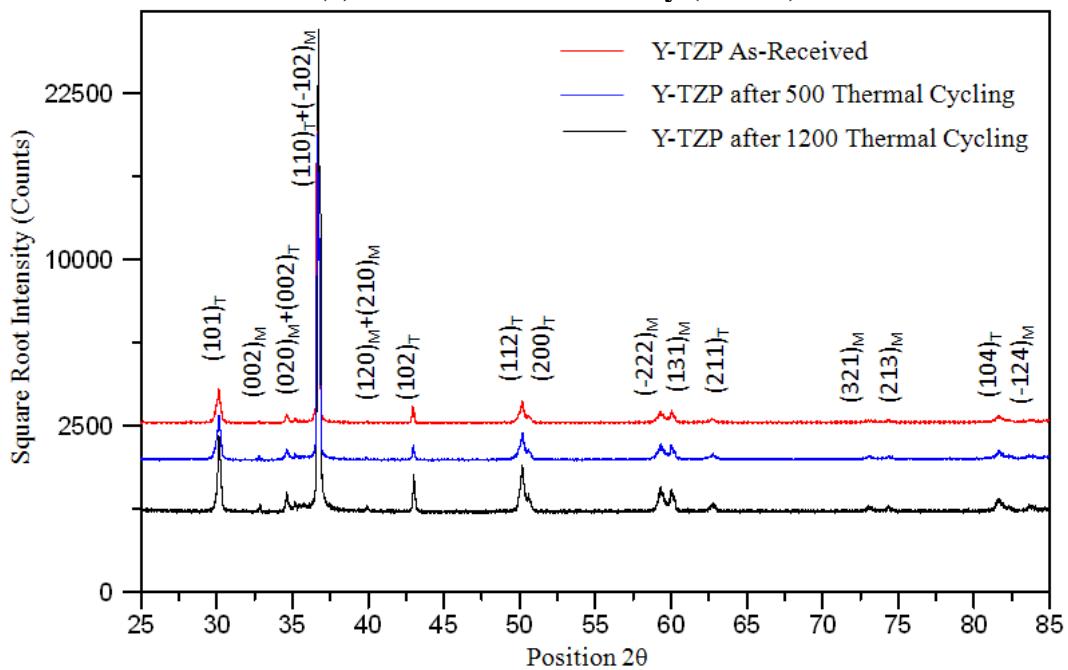
(b)   **Y-Scale in square root intensity (counts)**

Figure 152:   XRD Powder Diffraction Pattern and Phase Analysis at 25°<2θ<85° for Y-TZP materials, As-Received, and after 500 and 1200 Thermal Cycles (M-Monoclinic phase; T-Tetragonal phase)
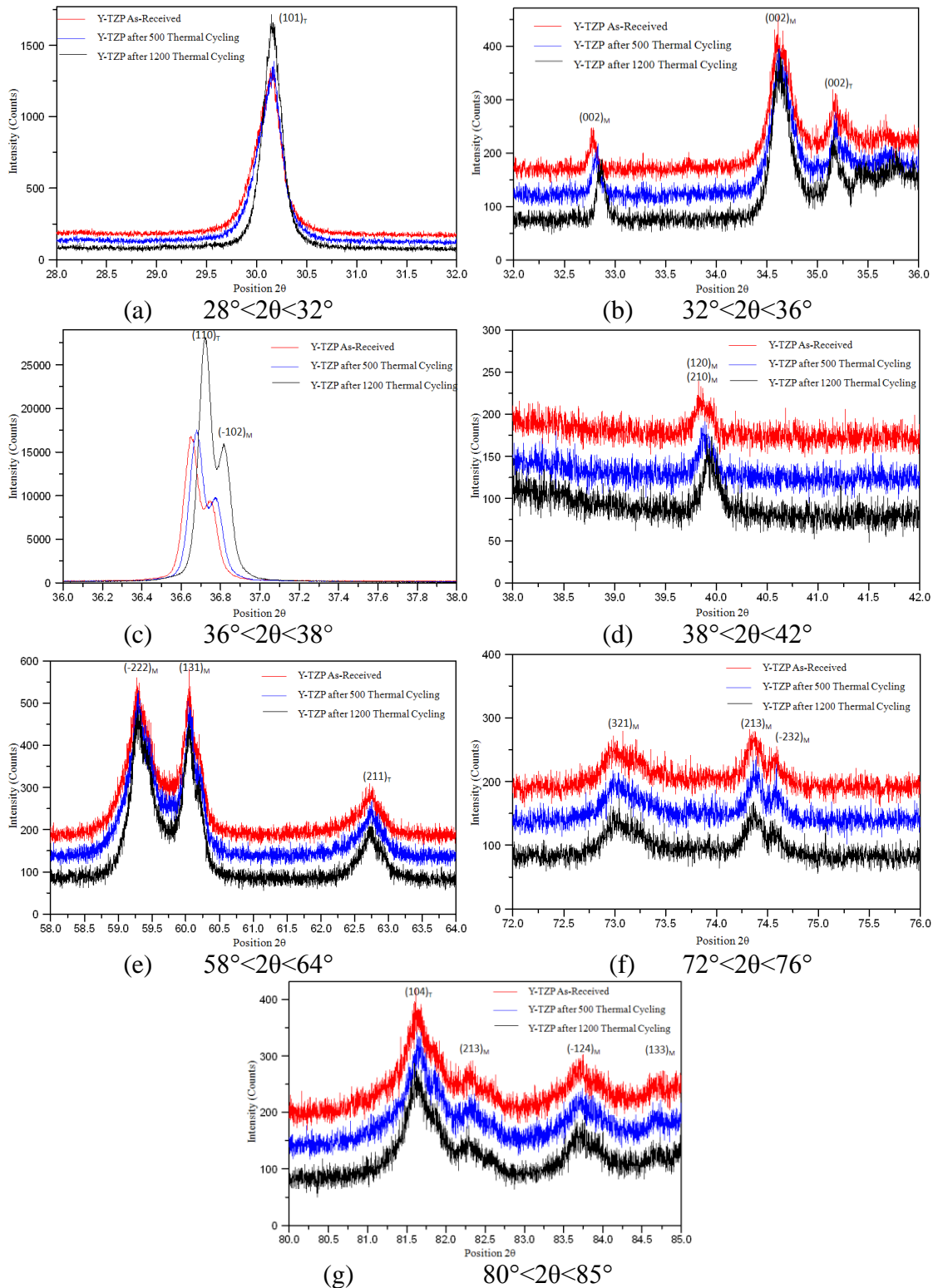
Figure 153: **XRD for Y-TZP materials at Smaller and Different 2θ Scales**

Table 66:   Powder Diffraction Pattern as A Function of Various Crystal Structures, Specimen Properties, and Instrumental Parameters [59]

Pattern component	Crystal structure	Specimen property	Instrumental parameter
Peak position	Unit cell parameters: (a,b,c,α,β,γ)	Absorption; porosity	Radiation (wavelength) Instrument/sample alignment; Axial divergence of the beam;
Peak Intensity	Atomic parameters: (x, y, z, B, etc.)	Preferred orientation; Absorption; Porosity	Geometry and configuration Radiation (Lorentz polarization)
Peak shape	Crystallinity Disorder Defects	Grain size Strain Stress	Radiation (spectral purity) Geometry Beam conditioning

In general, polycrystalline samples contain amorphous or low crystallinity phases in both crystalline and amorphous forms [85]. Diffraction from low crystallinity and amorphous solid is normally characterized by broadening peaks, but it tends to resemble the original crystalline material [86]. Though the peak position of the Y-TZP material doesn't shift after 500 and 1200 thermal cycles, the higher peak intensity and the narrower shape of the peak can be observed on the powder diffraction patterns with increased thermal cycles. This suggests a transition of amorphous material to crystalline material for both m-phase and t-phase during thermal cycling. The increased content of the crystalline phase may be the reason for changes in physical properties such as Young's modulus and Vickers hardness after 1200 thermal cycles. The peak shape and intensity do not vary to a large extent for other weaker peaks of the polymorphic zirconia system, as shown in Figure 153 (b) and (d) to (g).

The effect of stress induced by the hardness test on the diffraction patterns of Y-TZP is presented in Figure 154. The possible phase changes influence the Bragg peaks at $2\theta \approx 34.8°$, $36.7°$ and $44.5°$, which correspond to the Miller planes of $(002)_M$, $(110)_T$, and $(102)_T$. These reflection peaks shift obviously on the diffraction pattern of the Y-TZP samples after the Vickers hardness test as compared to peaks of specimens without it. The thermodynamic and associated kinetic of the stress-induced transformation can be used to explain the above observation [87]. The stress incurred by the Vickers hardness test may have induced transformation of the tetragonal phase to the monoclinic phase [87, 88]. The peak intensities of the monoclinic phase are much higher for Y-TZP specimens

after the Vickers hardness test as compared to the specimens those were not subjected to the hardness test.
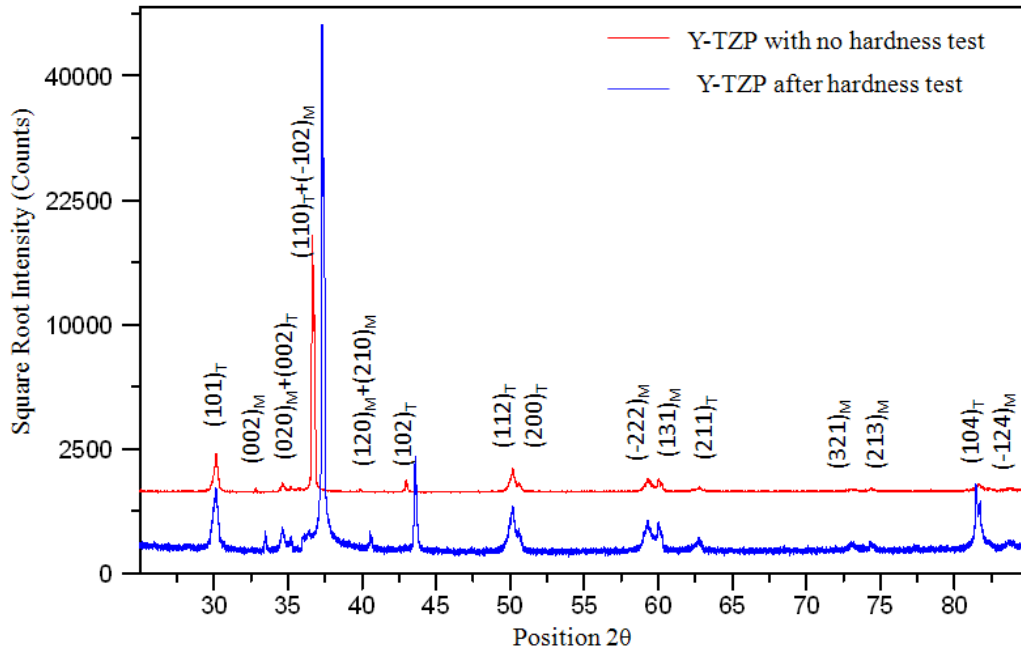
Figure 154:   Effects of Induced Stress after Hardness Test on XRD Diffraction Pattern and Phase Analysis for Y-TZP Material

The effect of sample morphology on the powder diffraction pattern was also compared between the top surface and side surface of the same Y-TZP specimen. The surface setup for the sample tested is illustrated in Figure 155. The micrographic and the surface morphology observed with an optical microscope are shown in Figure 156.

The effects of surface morphology on the diffraction pattern are plotted in Figure 157. The monoclinic peaks at Miller indices planes $(002)_M$ and $(020)_M$ are more evident on the top surface than on the side surface Figure 158. During sample preparation, polishing the sample surface with a diamond grinder may have induced a phase change from tetragonal to monoclinic [89]. The higher reflection intensity and the symmetric peak shape for the tetragonal phase can be observed more clearly on the side surface than the top surface, as shown in Figure 157.

(a) Top surface (b) Side surface
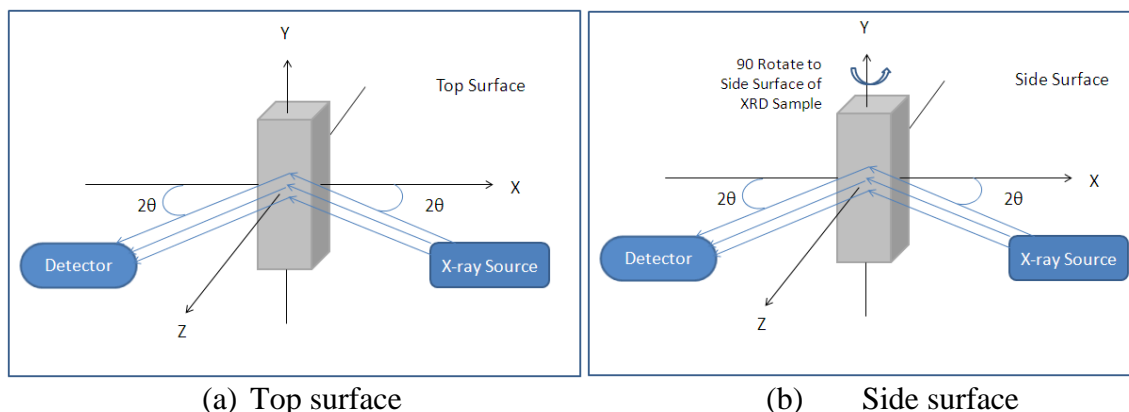
Figure 155:   Diagram of Specimen Surface Setup for Y-TZP Sample Bar in X-Ray Powder Diffraction Tests
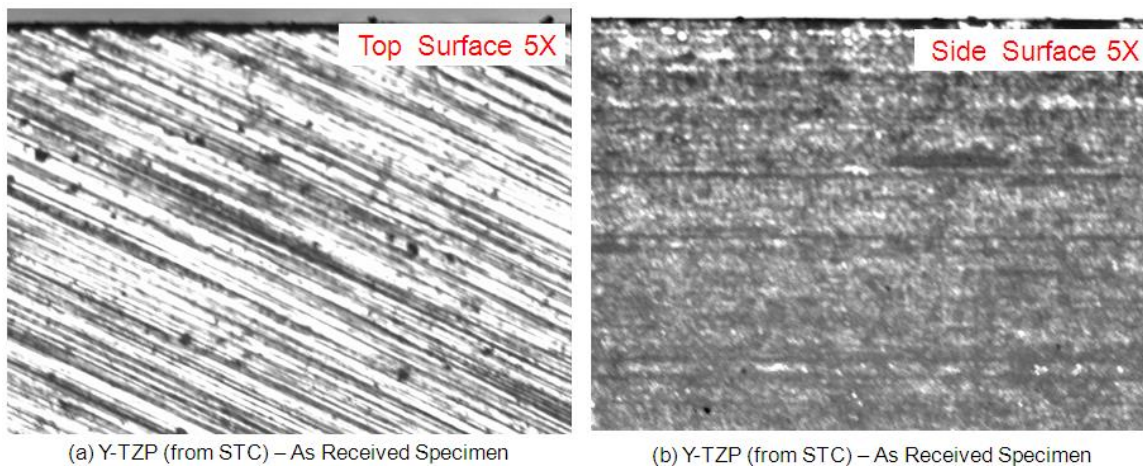
(a) Y-TZP (from STC) – As Received Specimen   (b) Y-TZP (from STC) – As Received Specimen

Figure 156:   Micrographic Observations of Surface Morphology for Y-TZP Material on Different Specimen Surfaces, i.e. Top and Side Surfaces

The effect of sample alignment on the powder diffraction pattern was also studied by setting the XRD instrument parameter $\Phi = 0°$ and $90°$. Figure 158 shows the sample alignment diagram for the sample bar tested, and the effects of sample alignment on the diffraction pattern are plotted in Figure 159. No peak shift or change of peak shape is evident for these two different sample alignments.

However, relative peak intensity of Miller indices $I_{(101)}/I_{(110)}$ for the sample aligned at $\Phi = 90°$ tends to be much higher than that of the ratio of $I_{(101)}/I_{(110)}$ for the sample aligned at $\Phi = 0°$. This phenomenon suggests a crystallographic orientation or texture for the Y-TZP

solid bar during the fabrication process.
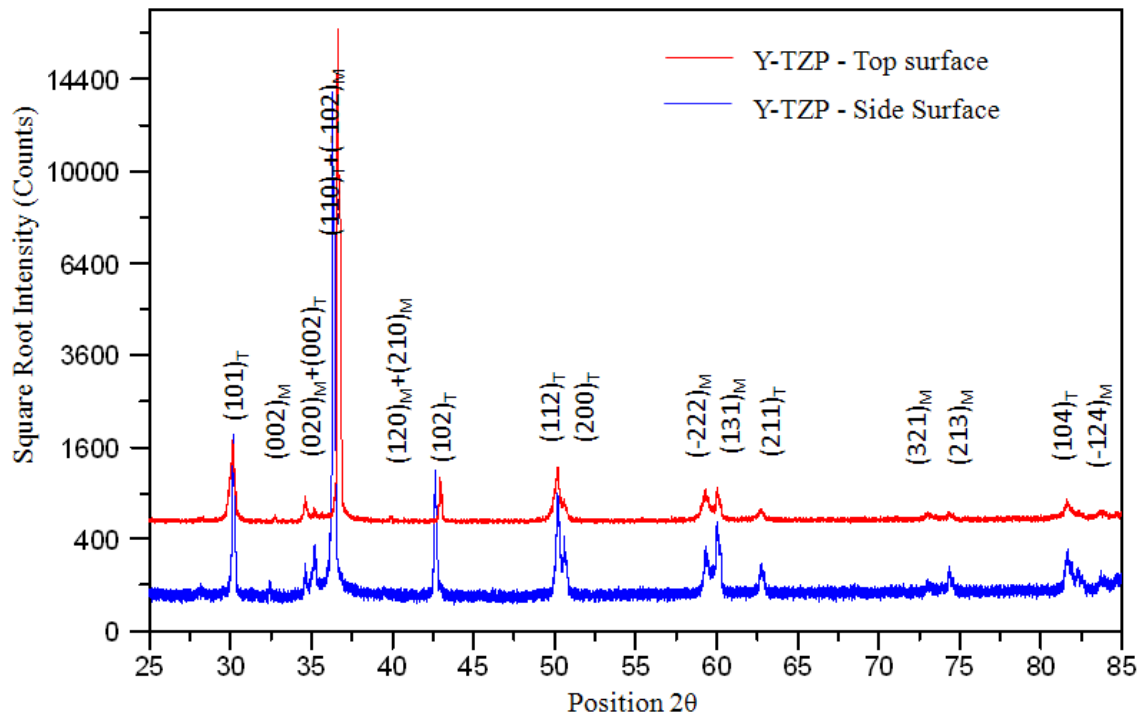
Figure 157: **Effects of Surface Morphology on Experimental Powder Diffraction Pattern and Phase Analysis for Y-TZP Material**

(a)   Sample alignment φ=0°   (b)   Sample alignment φ=90°
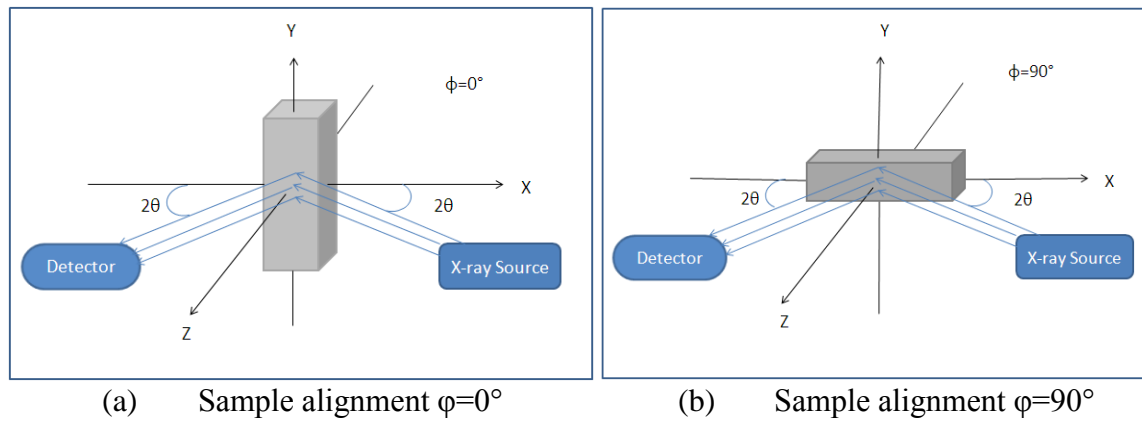
Figure 158: **Diagram of Sample Alignment for Y-TZP Sample Bar for X-ray Powder Diffraction (XRD)**
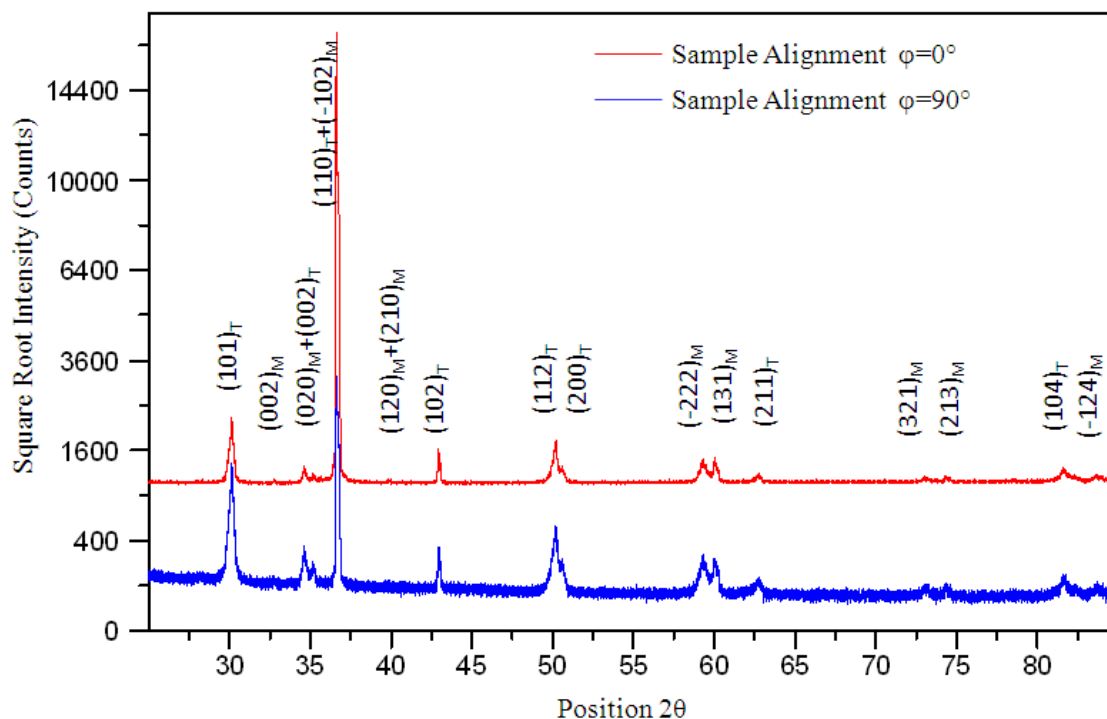
Figure 159: **Effects of Sample Alignment on Experimental Powder Diffraction Pattern and Phase Analysis for Y-TZP Material**

4.3 Characterization of Thermo-Mechanical Properties and Microstructure for Selected Structural Ceramic – Ceria-Stabilized Tetragonal Zirconia Polycrystalline (Ce-TZP)

4.3.1 Bulk Density and Porosity Measurement

The density of the two porous substrate materials, 25% toughened zirconia and 50% toughened zirconia (25%OTM and 50%OTM), were evaluated at ambient temperature based on Archimedes' principle. Results presented in Table 67 and Table 68, respectively. The density of the porous 50% toughened zirconia is approximately 3.42g/cc, almost 2 times the density of the 25% toughened zirconia material. Estimated porosity of the 50% toughened zirconia is approximately 6.41% as compared to porosity of 23.63% for the 25% toughened zirconia.

Table 67:   Density of 25% Toughened Zirconia

Sample ID	W_d (g)	W_t (g)	W_s (g)	V_s (ml)	ρ (g/cc)	Porosity (%)
25%OTM#2	0.98	50.08	1.03	0.56	1.73	10.30
25%OTM#6	0.99	50.27	1.20	0.55	1.81	38.89
25%OTM#7	1.03	50.11	1.12	0.62	1.68	13.02
25%OTM#8	0.93	50.22	1.10	0.50	1.87	34.38
25%OTM#9	0.95	50.14	1.06	0.53	1.78	21.55
Average (g/cc)			**1.78**			**23.63**

Table 68:   Density of 50% Toughened Zirconia

Sample ID	W_d (g)	W_t (g)	W_s (g)	V_s (ml)	ρ (g/cc)	Porosity (%)
50%OTM#2	2.03	51.13	2.08	0.57	3.54	10.24
50%OTM#3	2.07	51.10	2.11	0.62	3.34	6.32
50%OTM#4	1.88	51.03	1.92	0.50	3.77	7.56
50%OTM#5	1.90	50.95	1.93	0.60	3.19	4.03
50%OTM#6	20.3	51.05	2.05	0.62	3.27	3.89
Average (g/cc)			**3.42**			**6.41**

4.3.2 Elastic Properties

Dynamic Young's modulus (E-Value) values for 25% toughened zirconia and 50% toughened zirconia material (25% OTM and 50% OTM) at room temperature are approximately 5.72 and 29.91 GPa, as shown in Table 69. These values are much lower than the E-value of 204 GPa for the dense Y-TZP material from STC, as shown in Table 70 [90].

The dynamic Young's modulus is empirically related to porosity by an exponential relationship [91, 92] :

$$E = E_0 e^{-bP}$$ *Equation 56*

where,   E = Young's or shear modulus at some porosity *p*

E_0 = Young's or shear modulus at zero porosity

b = constant

P = porosity

Table 69:   E-value of 25% and 50% Toughened Zirconia

Thermal Cycles	Sample ID	Length (mm)	Width (mm)	Thickness (mm)	Mass (g)	Resonant frequency (Hz)	Calculate E-Value (GPa)	Mean E-Value (GPa)
0	25%OTM #2	50.0900	4.0764	3.1670	0.9769	2522	5.87	5.72
	25%OTM #6	50.0167	4.0743	3.2234	0.9874	2578	5.87	
	25%OTM #7	49.9900	4.0515	3.3751	1.0379	2581	5.42	
	50%OTM #2	50.2200	4.1130	3.4659	2.0720	4433	28.84	29.91
	50%OTM#3	50.1900	4.1128	3.5258	2.0669	4447	28.08	
	50%OTM#6	50.2175	4.1876	3.2624	2.0271	4364	32.79	
Thermal Cycles	Sample ID	Length (mm)	Width (mm)	Thickness (mm)	Mass (g)	Resonant frequency (Hz)	Calculate E-Value (Gpa)	Mean E-Value (Gpa)
50	25%OTM #2	50.1380	4.0738	3.1630	0.9761	2531	6.00	6.00
	25%OTM #6	50.0300	4.0709	3.2171	0.9871	/	/	
	25%OTM #7	49.9540	4.0494	3.3443	1.0366	/	/	
	50%OTM #2	50.1740	4.1113	3.4559	2.0272	4435	29.00	30.00
	50%OTM#3	50.1560	4.1109	3.5212	2.0672	4447	28.20	
	50%OTM#6	50.2380	4.1866	3.2610	2.0271	4360	32.80	

Table 70:   E-value for Y-TZP, 25% and 50% Toughened Zirconia

Material	E (or E_0)	B (constant)	P (Porosity)
Y-TZP	204	b	0
25%OTM	5.72	b	$P_{25\%OTM}$
50%OTM	29.91	b	$P_{50\%OTM}$

The elastic modulus of tetragonal zirconia polycrystalline doped with cerium (Ce-TZP) ceramics with a range of 5–35% of porosity was also measured at room temperature by dynamic mechanical analysis (DMA) [91]. A linear decrease of the elastic modulus with increasing porosity can be observed in Figure 160. The elastic modulus varied from 17.5 to 144 GPa in the porosity range of the study [91].
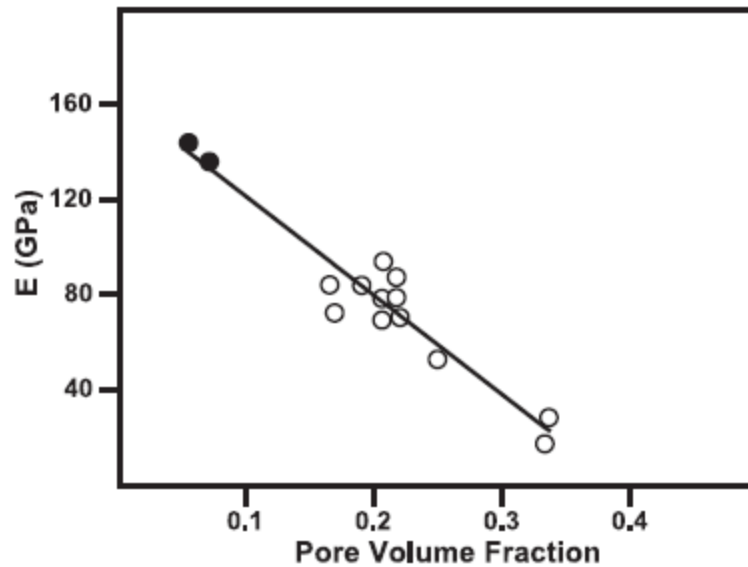
Figure 160: Variation of Elastic Modulus with Porosity Measured at Room Temperature by DMA at Frequency Of 1 Hz. Sintered Bars Prepared from Mixed (●) and Miller (○) Powders [91]

Equation 56 could also take the form:

$$ln\,E = ln\,E_0 - bP \qquad \qquad \textit{Equation 57}$$

Therefore, fractional porosity of 25% toughened zirconia (25% OTM) P_1 to that of 50% toughened zirconia (50% OTM) P_2 could be estimated, using values from Table 70:

$$\frac{P_1}{P_2} = \frac{ln\,E_0 - ln\,E_{25OTM}}{ln\,E_0 - ln\,E_{50OTM}} = \frac{ln\,204 - ln\,5.72}{ln\,204 - ln\,29.91} = 1.86 \qquad \textit{Equation 58}$$

The empirically estimated porosity of 25% toughened zirconia is more porous than the 50% toughened zirconia, which is consistent with the porosity results based on Archimedes' principle.

The E-value showed no significant difference after 50 thermal cycles for both 25% OTM and 50% OTM as compared to the as-received samples (Table 69). Elastic properties of

the 25% OTM and 50% OTM were evaluated by BuzzMac International (www.buzzmac.com) based on pulse excitation techniques. For comparison, the results are shown in Table 71 with those from UAF. Results from both laboratories for dynamic Young's modulus (E-Value) for 25% OTM and 50% OTM are found to be consistent. The Poisson ratios for these two porous materials are similar, and approximately 0.25.

Because of the weak structural property of the 25% Ce-TZP, only the 50% Ce-TZP was selected to be evaluated further for thermomechanical properties. The thermal cycling effect on Young's modulus (E-value) is also shown in Table 72; no significant change of E-value was found for 50% Ce-TZP.

Table 71:   Elastic Properties for 25% and 50% Ce-TZP

Sample ID	Thermal Cycles	Laboratoy	Out-of Plane Resonant Frequency (Hz)	In Plane Resonant Frequency (Hz)	Longitudina l Resonant Frequency (Hz)	Torsion Resonant Frequency (Hz)	Calculate Young's Modulus (GPa)	Calculate Shear Modulus (GPa)	Calculate Poisson Ration (v)
50%OTM#6	500	BuzzMac	4366	5760	34790	19326	34.78	14.02	0.24
	500	UAF CMRL	4365	/	/	/	33.00	/	/
25% OTM#7	0	BuzzMac	2571	3242	20246	11246	6.00	2.40	0.26
	0	UAF CMRL	2582	/	/	/	5.50	/	/

Table 72:   E-value for 50% Ce-TZP as a Result of Thermal Cycling

Sample ID	Thermal Cycles	Length (mm)	Width (mm)	Thickness (mm)	Mass (g)	Resonant frequency (Hz)	Calculate E-Value (GPa)
50%OTM#6	0	50.22	4.19	3.26	2.03	4365	32.90
	50	50.24	4.19	3.26	2.03	4365	32.90
	500	50.28	4.19	3.26	2.03	4365	33.00

4.3.3   Coefficient of Thermal Expansion (CTE)

Instantaneous coefficients of thermal expansion (CTE or Alpha (α_t)) were measured for the Y-TZP, 25% toughened zirconia (25%OTM) and 50% toughened zirconia (50%OTM) in the temperature ranges of 40–1200°C and 40–1500°C at a constant heating rate of 3°C/min. All results for the selected dense and porous toughened zirconia material are plotted in Figure 161 and Figure 162. No obvious shrinkage of the α_t could be seen in the temperature range below 1200°C (Figure 161). However, an obvious shrinkage of the α_t

for the porous zirconia material could be observed in the temperature range of 1100–1200°C for 25% toughened zirconia (25% OTM) and 1200–1300°C for 50% toughened zirconia (50% OTM) shown in Figure 162. This shrinkage is related to the transition from monoclinic to tetragonal phase as temperature increases [93]. The transition temperature for the 25% OTM is lower than that for the 50%OTM (Figure 162), therefore it could be concluded that their porosity difference is a factor affecting the transition temperature value for the porous, toughened zirconia material.
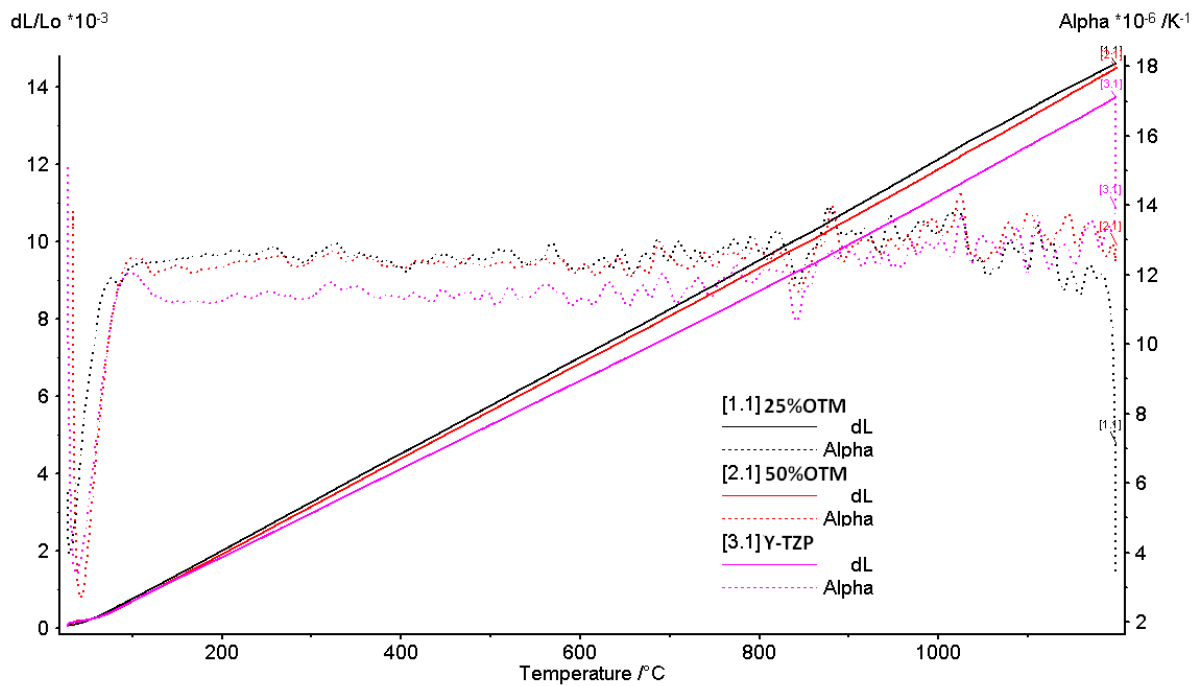
Figure 161:   CTE Instantaneous Physical Alpha (α_t) and dl/l$_0$ on Heating in Air at 3°k/min for Y-TZP, 25% Ceria Toughened Zirconia (25%Ce-TZP) and 50% Ceria Toughened Zirconia (50%Ce-TZP) in the Temperature Range of 40–1200°C

4.3.4   X-ray Diffraction (XRD) Phase Analysis

The XRD powder diffractions for the polished Y-TZP, 25% toughened zirconia (25% OTM) and 50% toughened zirconia (50% OTM) samples are presented in Figure 163.
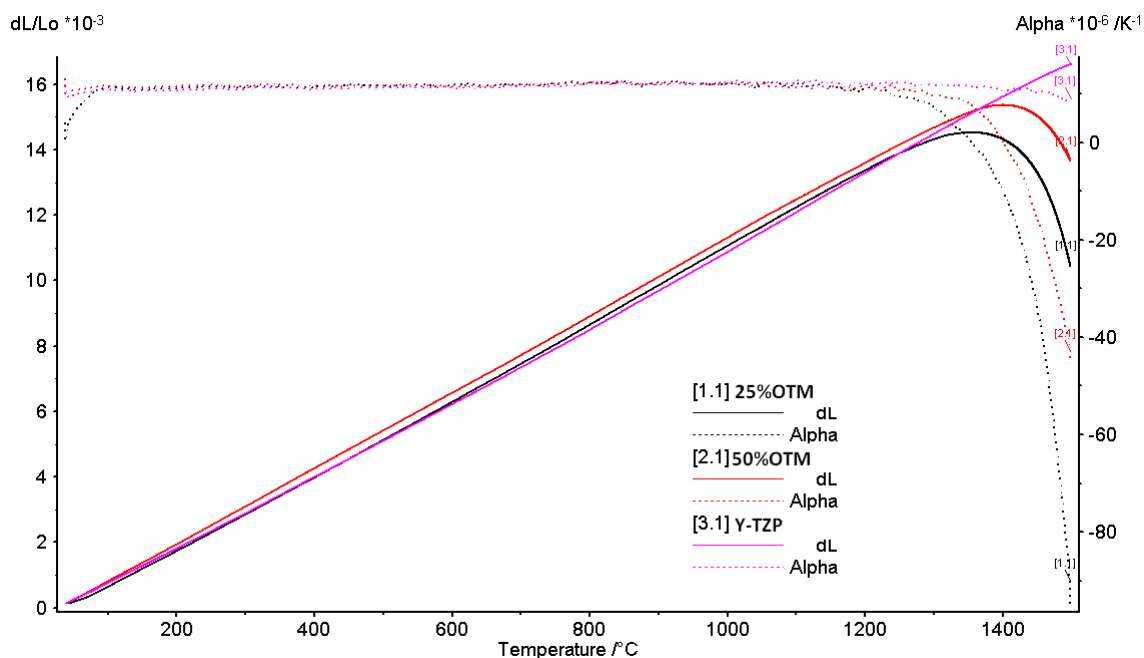
Figure 162: **CTE Instantaneous Physical Alpha (α_t) and dl/l$_0$ on Heating in Air at 3°k/min for Y-TZP, 25% Ceria Toughened Zirconia (25%Ce-TZP) and 50% Ceria Toughened Zirconia (50%Ce-TZP) in the Temperature Range of 40–1500°C**

The peak positions as well as the corresponding peak intensities for both the 25%-OTM and 50%-OTM are identical in the 2-theta ranged from 25–150°, as shown in Figure 163. Though powder diffraction for the polished Y-TZP sample displays a pattern similar to that of the porous substrates, there is a constant shifting of the diffraction peak positions as compared to the corresponding peaks of the above porous substrate. The chemical composition (from the auto-search engine) provided by the XRD instrumental High-Score software suggests a high possibility that the 25%-OTM and 50%-OTM could be porous Cerium-stabilized tetragonal zirconia polycrystalline (Ce-TZP) [94]. This material has been widely used for oxygen transport membrane (OTM) in solid oxide fuel cell. Powder diffraction for the Y-TZP corresponds to the crystallographic structure of tetragonal yttrium zirconium oxide [95]. The existence of a $(-111)_M$ peak for the monoclinic zirconia phase could be observed in the diffraction patterns for the porous substrate, Figure 164(a). This is consistent with the TG/DTA result, and there is phase transition from monoclinic to tetragonal.
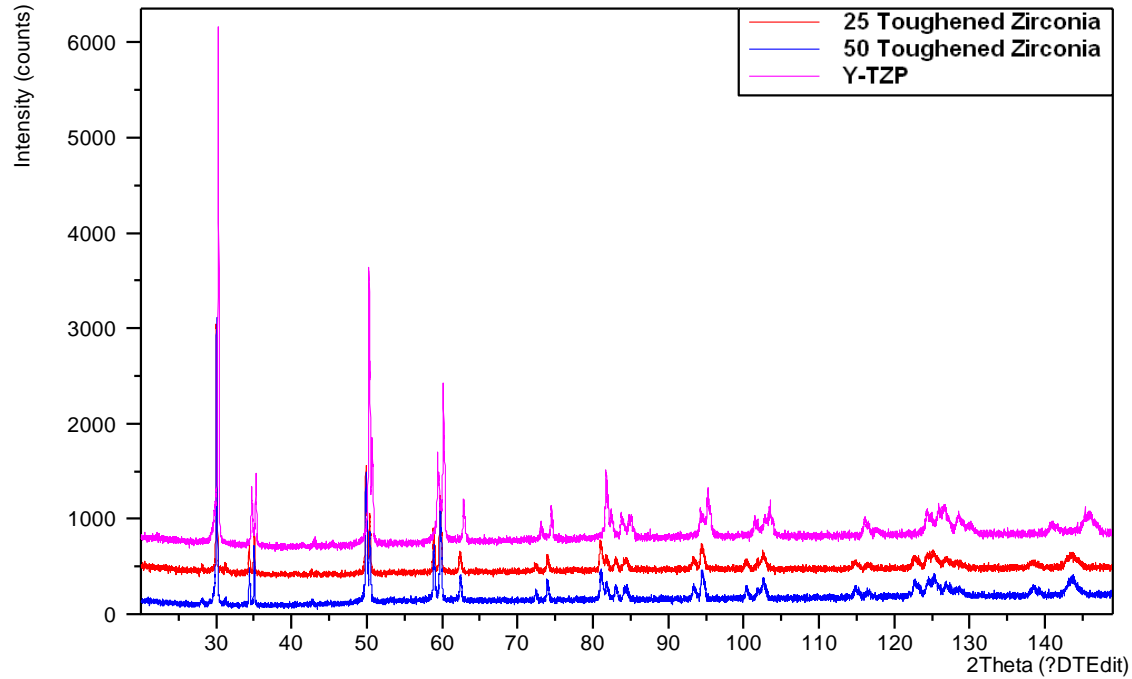
Figure 163:   Experimental Powder Diffraction Pattern and Phase Analysis for As-Received Y-TZP, 25% Toughened Zirconia, and 50% Toughened Zirconia at 20°<2θ<150°

(a) 25°<2θ<37°

(b) 45°<2θ<55°

(c) 55°<2θ<65°

(d) 70°<2θ<80°

(e) 80°<2θ<90°

(f) 97°<2θ<107°

(g) 110°<2θ<120°

(h) 120°<2θ<130°

(i) 135°<2θ<149°
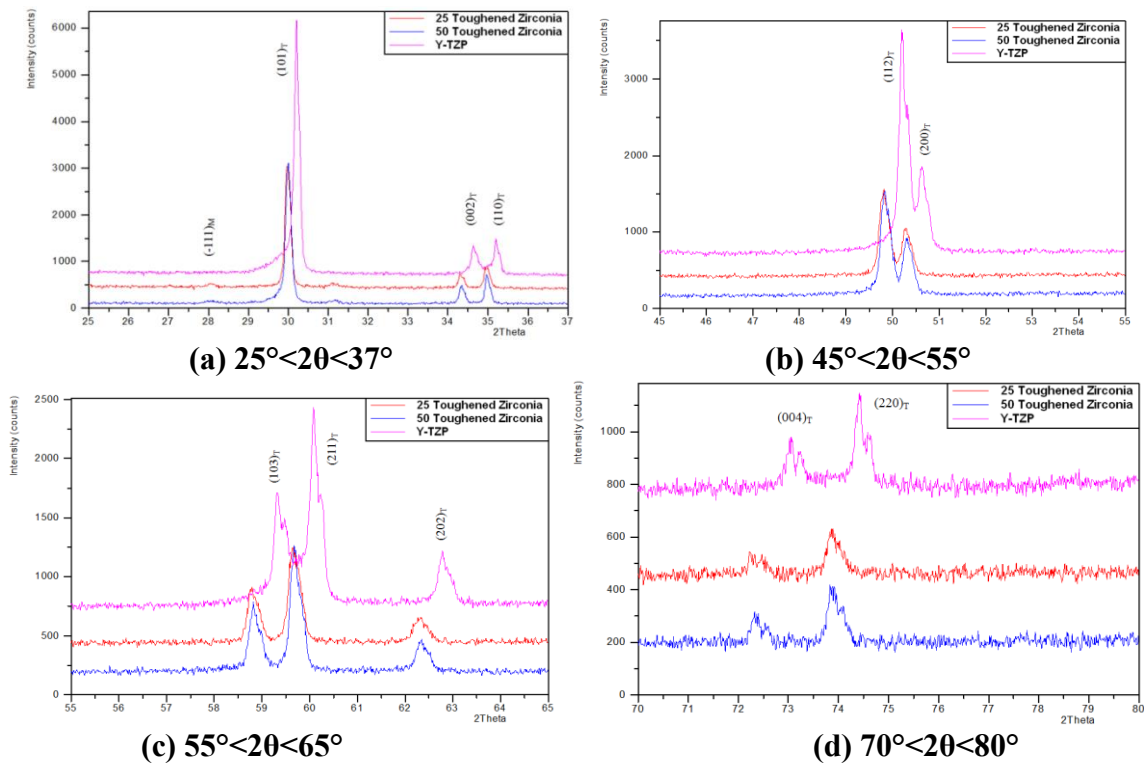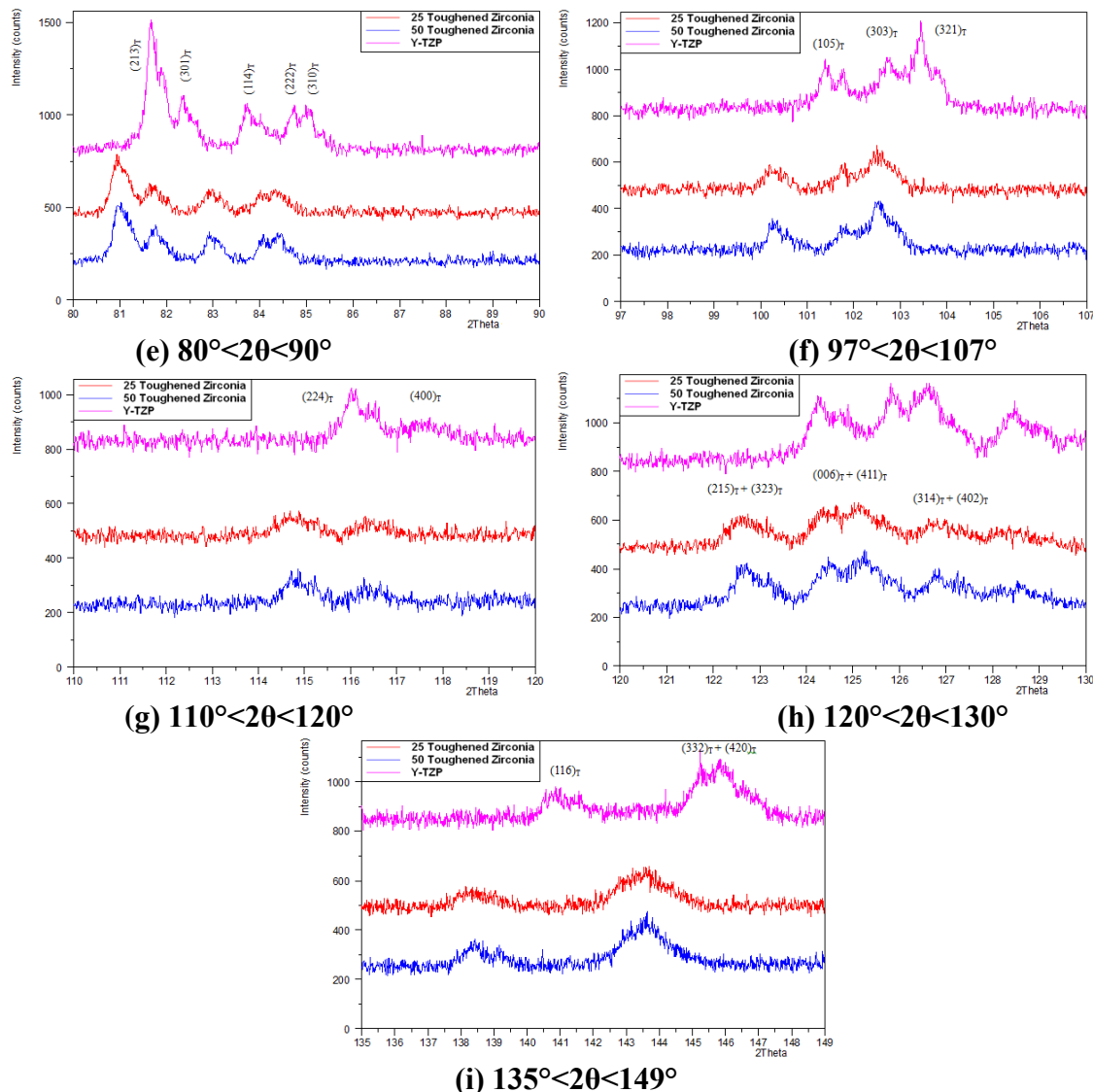
Figure 164:   Experimental Powder Diffraction Patterns and Phase Analyses for As-Received Y-TZP, 25% And 50% Ce-TZP

4.3.5   Residual Stress by XRD $\sin^2\psi$ Technique

XRD $\sin^2\psi$ technique was used to measure residual stress for the polished Y-TZP, 25% and 50% Ce-TZP samples before and after thermal annealing. The (h k l) plane selected on the XRD patterns in the measurement of residual stress is $(116)_T$, shown in Figure 164(i) for both the Y-TZP and Ce-TZP material, considering its higher angles (over 120°) and noninterference with other Bragg peaks [34, 36].

Measurements were carried out at various ψ angles defined from 0~30°. The measured d values vs. $\sin^2\psi$ are plotted in Figure 165 to Figure 168 for 25%-Ce-TZP, 50%-Ce-TZP, and Y-TZP side surface and top surface, respectively. The residual stress of the polished Y-TZP, 25%Ce-TZP and 50%Ce-TZP samples before and after thermal annealing are presented in Table 38 and Table 39. Results show that the residual stress is mainly compressive; thermal annealing of the polished samples did not have any influence. Therefore, the manual polishing process did not induce any residual stress for these selected materials. Residual stress for the side and top surfaces of the selected dense Y-TZP sample is fairly consistent. The residual stress is higher for the dense Y-TZP than for the porous substrates, and it is mainly attributed to its higher elastic constant and higher slope of differential d value to $\sin^2\psi$. Residual stress for the porous substrate is lower than the dense substrate as a result of relaxation of the stress from the porosity.
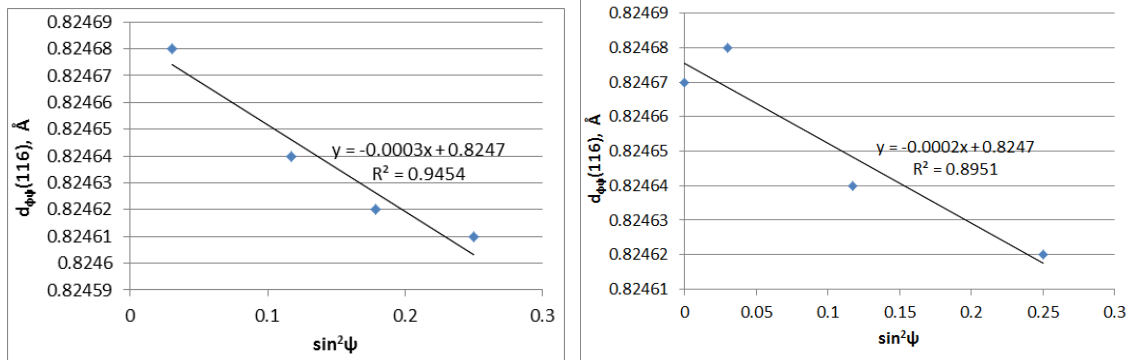
(a) Polished sample before annealing   (b) Polished sample after annealing

Figure 165:   Plot of d-Value of (116)$_T$ vs. $\sin^2\psi$ for 25% Ce-TZP

Table 73:   Residual Stress Values of the Examined Polished Zirconia Material (before Annealing) Determined by XRD $\sin^2\psi$ Method

Residual Stress (MPa) of Polished Sample before Annealing							
0≤ψ≤40							
Material	$2\theta_{\phi 0}$	Lattice Plane	$d_{\phi 0}$	Elastic Constant E/(1+v) GPa	Slope of $d_{\phi\psi}$ vs. $\sin^2\psi$	Least Square Regression (R^2)	Residual Stress (MPa)	Figures
25% Toughened Zirconia	137.965	(116)	0.8252	4.62	-0.0003	0.9454	-1.68	Figure 13 (a)
50% Toughened Zirconia	137.965	(116)	0.8252	23.08	-0.0002	0.7965	-5.59	Figure 14 (a)
Y-TZP-Side Surface	140.791	(116)	0.8177	170.00	-0.0004	0.9199	-83.16	Figure 15 (a)
Y-TZP-Top Surface	140.791	(116)	0.8177	170.00	-0.0004	0.9678	-83.16	Figure 16 (a)
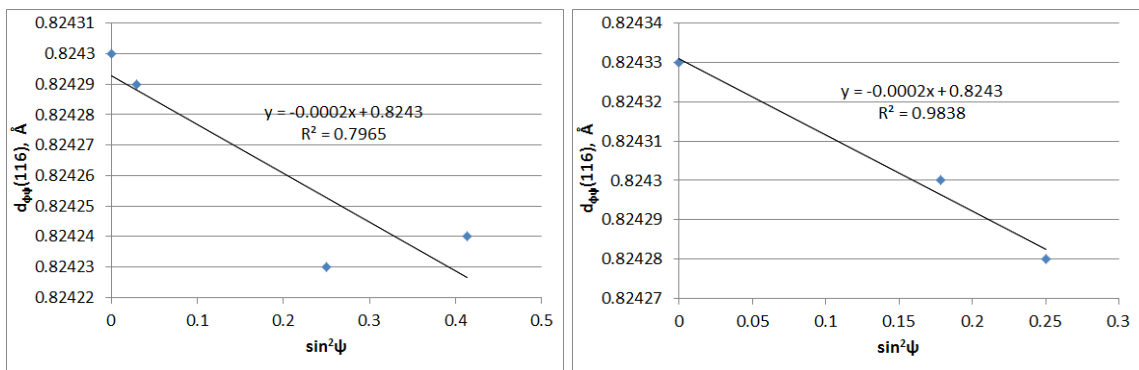
(a) Polished sample before annealing (b) Polished sample after annealing

Figure 166: Plot of d-Value of $(116)_T$ vs. $\sin^2\psi$ for 50% Ce-TZP
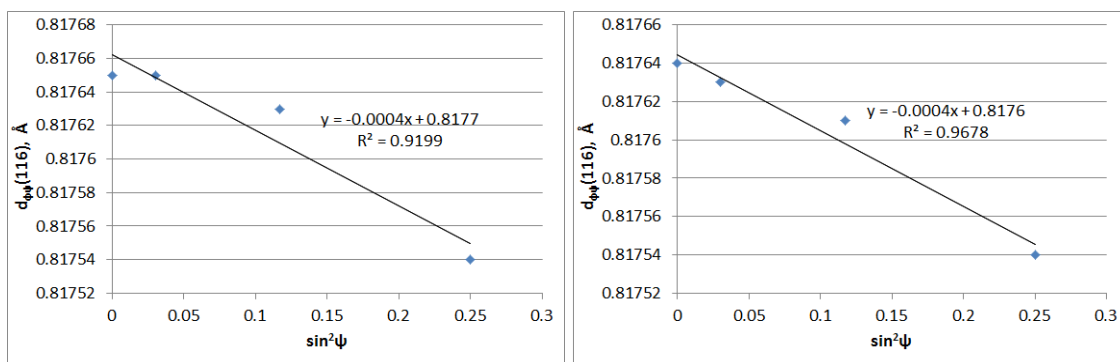
(a) Polished sample before annealing (b) Polished sample after annealing

Figure 167: Plot of d-Value of $(116)_T$ vs. $\sin^2\psi$ for Y-TZP (Side Surface)
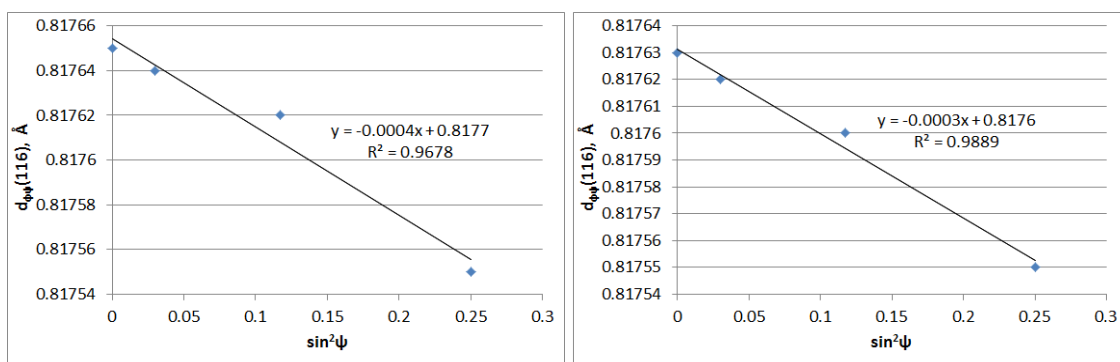
(a) Polished sample before annealing (b) Polished sample after annealing

Figure 168: Plot of d-Value of $(116)_T$ vs. $\sin^2\psi$ for Y-TZP (Top Surface)

Table 74: **Residual Stress Values of the Examined Polished Zirconia Material (after Annealing) Determined by XRD $\sin^2\psi$ Method**

Residual Stress (MPa) of Polished Sample after Annealing							
$0 \leq \psi \leq 40$							
Material	$2\theta_{\phi 0}$	Lattice Plane	$d_{\phi 0}$	Elastic Constant E/(1+v) Gpa	Slope of $d_{\phi\psi}$ vs. $\mathrm{Sin}^2\psi$	Least Square Regression (R^2)	Residual Stress (MPa)	Figures
25% Toughened Zirconia	137.965	(116)	0.8252	4.62	-0.0001	0.8951	-0.56	Figure 13 (b)
50% Toughened Zirconia	137.965	(116)	0.8252	23.08	-0.0002	0.9838	-5.59	Figure 14 (b)
Y-TZP-Side Surface	140.791	(116)	0.8177	170.00	-0.0004	0.9678	-83.16	Figure 15 (b)
Y-TZP-Top Surface	140.791	(116)	0.8177	170.00	-0.0003	0.9889	-62.37	Figure 16 (b)

4.3.6   Thermal Analysis: TG/DTA

Generally three different types of thermodynamic processes can be revealed by TG/DTA results for zirconia-based ceramics:

1) The endothermic peak centered at 220°C, which is attributed to a loss of the physically adsorbed water [96].

2) The exothermic peak appearing at 480–800°C, which is associated with the enthalpy of the transformation of amorphous zirconia into crystalline zirconia [96, 97].

3) The endothermic peak centered at 1450°C, which is observed during the monoclinic to tetragonal phase transition in the heating direction, the exothermic peak at 1300°C during the reversible phase transition from tetragonal to monoclinic phase in the cooling direction [98].

The TG and DTA tests were simultaneously performed for Y-TZP, 25% toughened zirconia, and 50% toughened zirconia solid samples in an inert (nitrogen) environment at a constant heating or cooling rate of 20°C/min. The DTA and TG curves for these selected materials are presented in Figure 169 to Figure 171. Two repetitive tests were conducted on two different weighted samples. The endothermic peaks appeared on the DTA heating/cooling curves for both 25% and 50% Ce-TZP, while the exothermic peaks appeared on the DTA results for Y-TZP material. The endothermic peak occurred at

about 1100°C for 25% Ce-TZP during both heating and cooling processes (Figure 170), while it occurred at approximately 1200°C for 50% Ce-TZP (Figure 171). These endothermic peaks center around 1100–1200°C, which is consistent with the observation of the CTE tests and is associated with the transition from monoclinic to tetragonal phase in both the heating and cooling processes.

The exothermic peak for YTZP material occurred at 850°C. The exothermic peak is closely associated with the enthalpy of the transformation of the amorphous phase into crystalline zirconia in the temperature range above 450°C [96, 97]. This observation is supported by the results of the XRD phase analysis and SEM observation for Y-TZP material, as presented earlier.
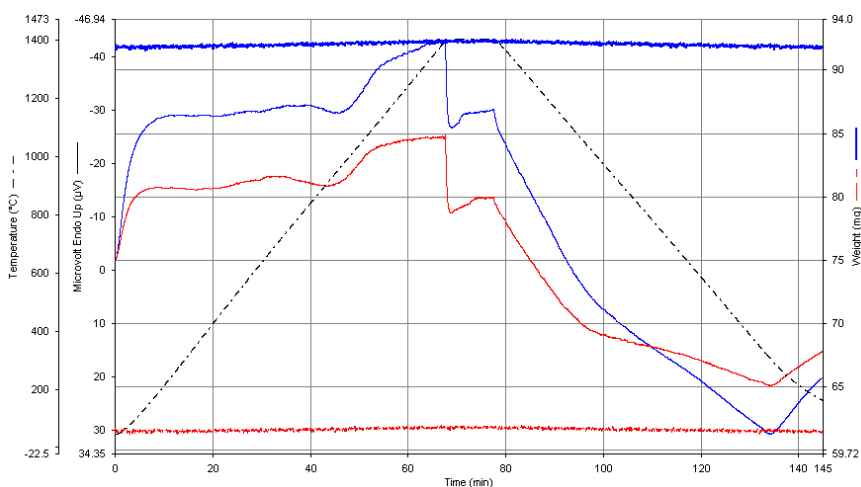
Figure 169:   Thermogravimetry/Differential Thermal Analysis (TG/DTA) Results for Y-TZP Material at the Heating (Cooling) Rate of 20°C/min between 40–1400°C

4.3.7   X-Ray Spectrometry Microanalysis

Figure 172 shows the XRF spectra acquired from irradiation of the 50% toughened zirconia material excited at different photon energies. The identified peaks reveal the presence of major elements of cerium (Ce) and zirconium (Zr). This observation confirms that the crystallographic structure of the 50% toughened zirconia is ceria-stabilized

tetragonal zirconia polycrystalline (Ce-TZP), as which was previously ascertained by x-ray diffraction powder diffraction. A Semi-quantitative analysis for the 50% toughened zirconia is presented in Table 75. The Ce-TZP material is approximately composed of 78 wt% of ZrO_2 and 18 wt% of Ce_2O_3.
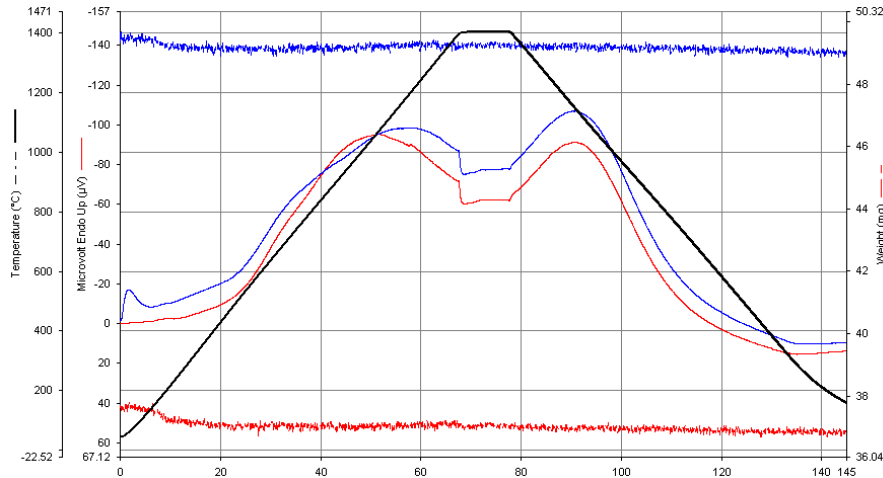
Figure 170: **Thermogravimetry/Differential Thermal Analysis (TG/DTA) Results for 25% Toughened Zirconia (25%Ce-TZP) at the Heating (Cooling) Rate of 20°C/min between 40–1400°C**
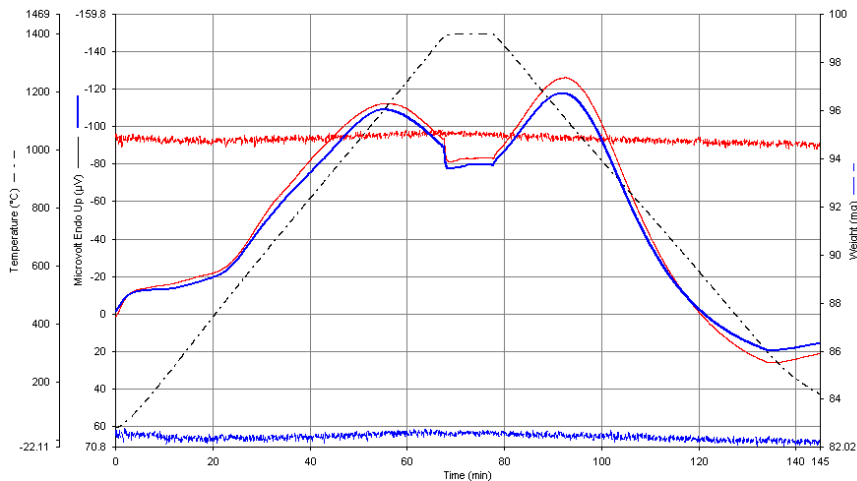
Figure 171: **Thermogravimetry/Differential Thermal Analysis (TG/DTA) Results for 50% Toughened Zirconia (50%Ce-TZP) at the Heating (Cooling) Rate of 20°C/min between 40–1400°C**

[LILY-50YSZ-POLISHED]

Axios XRF spectrometer
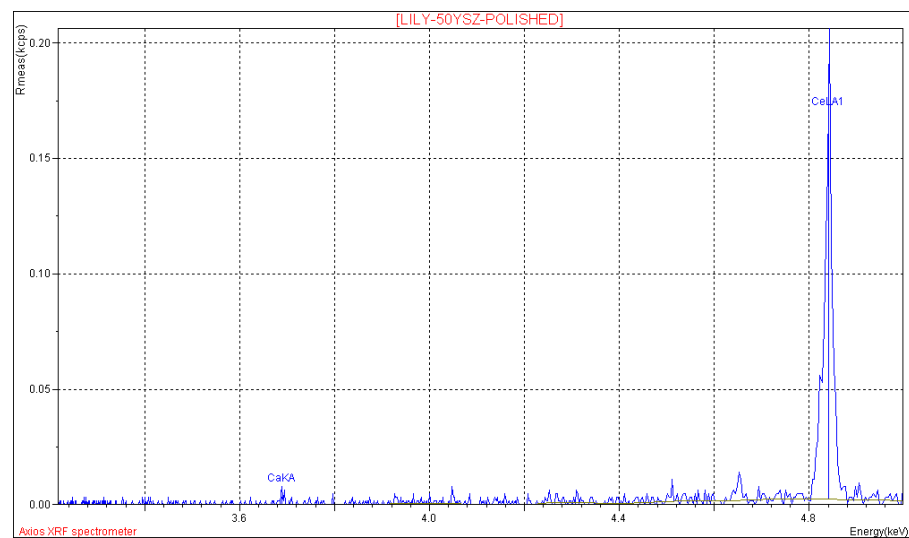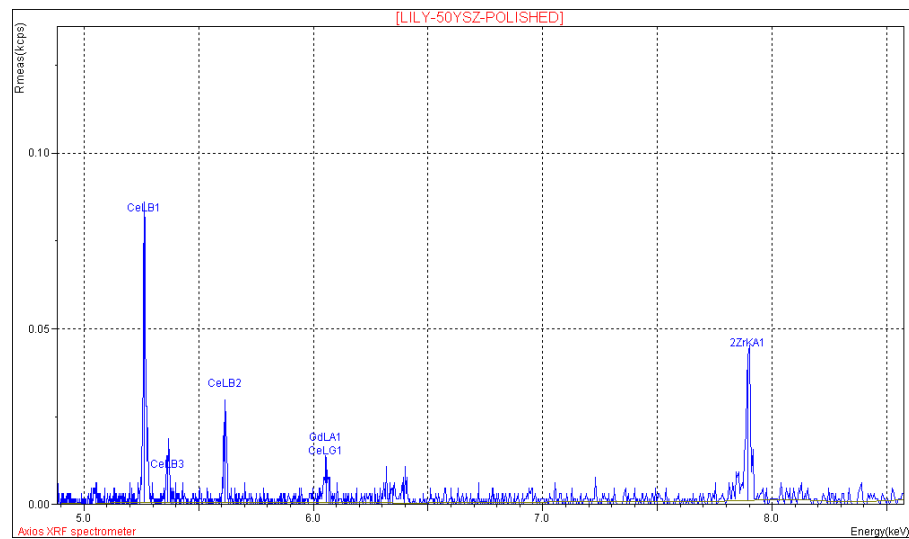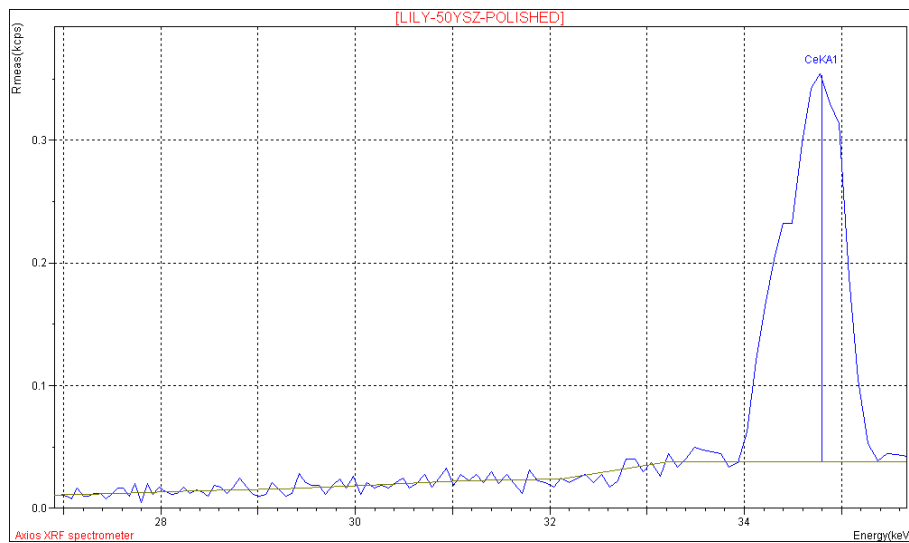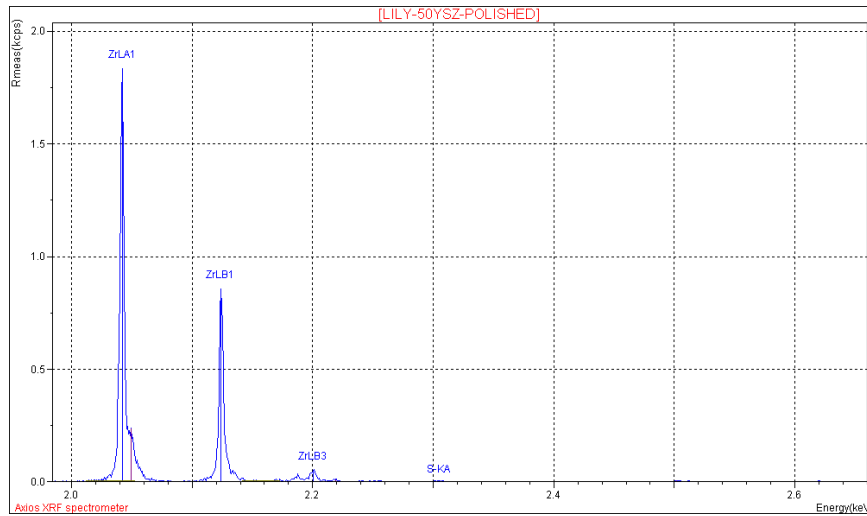
Figure 172:   XRF Spectra of 50% Toughened Zirconia Excited at Different Photon Energies

Table 75:   Semi-Quantitative Analysis of 50% Toughened Zirconia by XRF

No.	Compound Name	Concentration (%)
1	Ce_2O_3	18.85
2	ZrO_2	78.24
3	Other components	2.91

CHAPTER V: CORRELATION OF MICROSTRUCTURE AND THERMO-MECHANICAL PROPERTY FOR HTM SYSTEM

It is recognized that none of these hydrogen membranes will be used without a porous support. Therefore, a good porous support is essential on which a functional membrane can be deposited. A clear understanding of the correlation between the microstructural and the thermo-mechanical properties of a porous substrate is, therefore, required to define the complete HTM system, which consists of a functional HTM membrane and a porous substrate. Thermomechanical and microstructural properties of selected structural ceramics and porous ceramic substrates and the HTM cermet are discussed in Chapters III and IV. In this chapter, correlations of microstructure and thermomechanical properties are presented.

5.1   Physical Properties

Table 76 summarizes the physical properties for all selected reference, porous substrate, and HTM cermet. Young's modulus (E-value) versus porosity is presented in Figure 173 for the three toughened zirconia materials: dense Y-TZP, porous 25%, and 50% Ceria toughened zirconia, which could be a potential substrate material for the HTM system in the future. E-value is assumed to have an exponential relationship with porosity for all the toughened zirconia materials, (either Yttria (Y_2O_3) or Ceria (Ce_2O_3), which were characterized by similar tetragonal crystallographic structure by XRD powder diffraction.

Young's modulus (E-value), shear modulus (G-value), and density values are plotted in Figure 174 for the three selected dense ceramic materials, i.e. AL-96, Y-TZP, and HTM. The lowest E and G values were found to have the highest density for HTM cermet (Palladium is a very heavy metal), shown in Figure 174. The highest E and G values were found to have the lowest density for AL-96. Both the Young's Modulus (E) and Shear

224

Modulus (G) increased by about 18% with the dual-phase HTM membrane (HTM-50CeTZP) as compared to those the porous substrate (50Ce-TZP), as shown in Table 76. From above results it can be stated that, material with similar crystallographic structure generally follows a trend for their Young's modulus and other properties such as porosity. On the contrary, Young's modulus for materials with a different crystallographic structure does not correlate with either density or porosity of the material.

Table 76:   Summarization of Physical Properties for Selected Structural Ceramic Materials

Material	Density (g/cc)	Porosity (%)	Young's Modulus (GPa)	Shear Modulus (GPa)	Poisson Ratio (υ)
AL-96	3.20	0.00	334.70	136.50	0.23
Y-TZP	5.21	0.00	204.00	96.00	0.36
50Ce-TZP	3.42	6.41	34.78	14.02	0.24
25Ce-TZP	1.78	23.63	6.00	2.40	0.26
HTM Cermet	11.30	0.00	150.62	56.40	0.34
HTM-50CeTZP	TBA	TBA	41.25	16.5	0.25
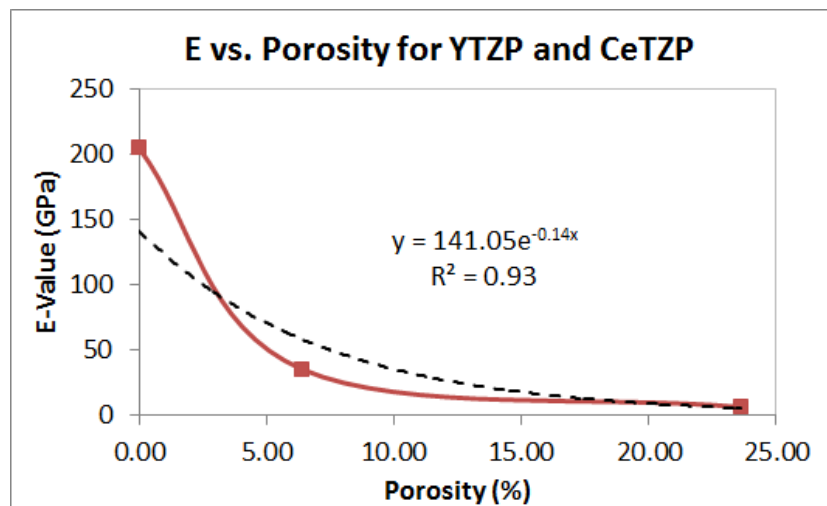
Figure 173:   Relationship of Young's Modulus (E-value) to Porosity for Toughened Tetragonal Zirconia Materials
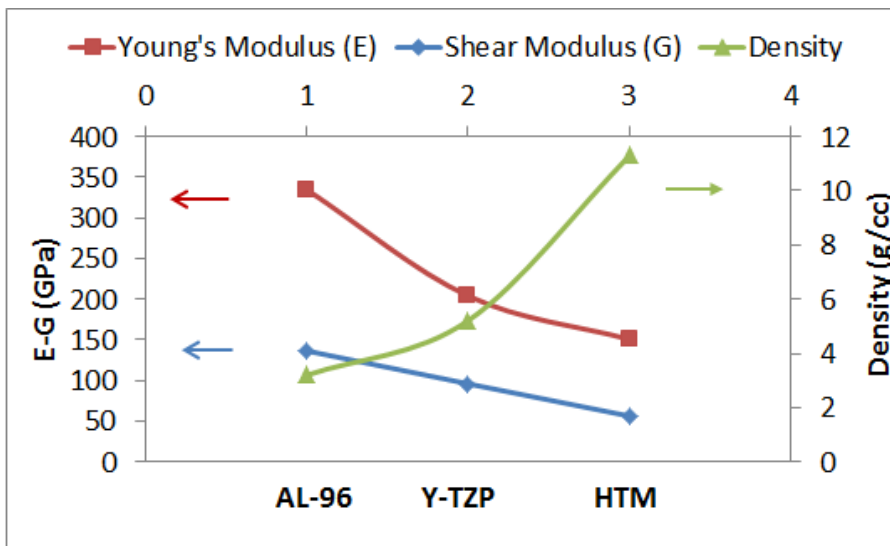
Figure 174:   Relationship of Young's Modulus (E-Value), Shear Modulus (G-Value), And Density for Three Different Crystallographic Structured Materials: AL-96, Y-TZP, And HTM Cermet Solid (HTM)

5.2   Mechanical Properties at Room Temperature

Mechanical properties for all selected reference, porous substrate and HTM cermet at room temperature are summarized in Table 77. Flexural strength (σ_{fs}) results are plotted in Figure 175 as a function of porosity for all three toughened zirconia materials: dense Y-TZP and porous 25% and 50% Ce-TZP. From Figure 175, it could be seen that the σ_{fs} could be has an exponential relationship with the porosity. Since flexural strength (σ_{fs}) and Young's modulus are exponentially related to porosity, σ_{fs} is correlated to have a linear relationship with E-value for these toughened zirconia materials (Figure 176).

Young's modulus (E-value), flexural strength (σ_{fs}) and density values are plotted in Figure 177 for the selected dense ceramic materials: AL-96, Y-TZP, and HTM. No clear relationship between E-value and σ_{fs} could be identified for these three different crystallographic ceramics (Figure 177). The flexural strength (σ_{fs}) and Vickers hardness number are presented in Figure 178. A higher σ_{fs} is also associated with a higher VH number for the Y-TZP and the HTM material. However, with highest VH number, (AL-

96) has smallest value of σ_{fs} (Figure 177). Optical microscopic observation of the fractured surface reveals that AL-96 failed with the largest mirror size, as shown in Figure 179 (a), while the HTM failed in a medium stress concentration area, as shown Figure 179 (b), whereas, the Y-TZP failed mainly by a stress concentration point as shown in Figure 179 (c). The mode of failure, therefore, can be attributed to one of the reasons that induced a critical low strength failure for AL-96 [66]. Fractography analysis by SEM for the fractured surfaces is also shown in Figure 180. Average grain size for Y-TZP is found to be smallest in the nanometer (nm) ranges, while AL-96 has the largest grain size in micrometer range.

SEM and Microprobe with EDS were also conducted for their morphology and elemental composition for the HTM surfaces (Figure 181 and Figure 182). Generally, with increasing atomic number, the color of the phase gets brighter for both SEM and microprobe analysis. Therefore, a dark grey color is generally the phase of YSZ, phase PdO is the medium grey, and phase Pd is brightest of all the three phases. Cracks were found to grow between the phase boundary of Pd and YSZ. Most of the crack origins are, however, attributed to originate from the YSZ phase. From Figure 183, it can be seen that flexural strength (σ_{fs}) increases slightly for the dual-phase HTM membrane (HTM-50CeTZP) as compared to the porous substrate (50Ce-TZP), and the E-value has a positively linear correlation with σ_{fs} (Figure 184).

Table 77:   Mechanical Properties at Room Temperature

Material	Density (g/cc)	Porosity (%)	Young's Modulus (GPa)	Flexural Strength (MPa)	Vickers Hardness (Gpa)
AL-96	3.20	0.00	334.70	158.87	13.54
Y-TZP	5.21	0.00	204.00	776.00	13.02
50Ce-TZP	3.42	6.41	34.78	77.00	TBA
25Ce-TZP	1.78	23.63	6.00	20.00	TBA
HTM Cermet	11.30	0.00	150.62	356.56	2.11
HTM-50CeTZP	TBA	TBA	41.25	83.10	TBA
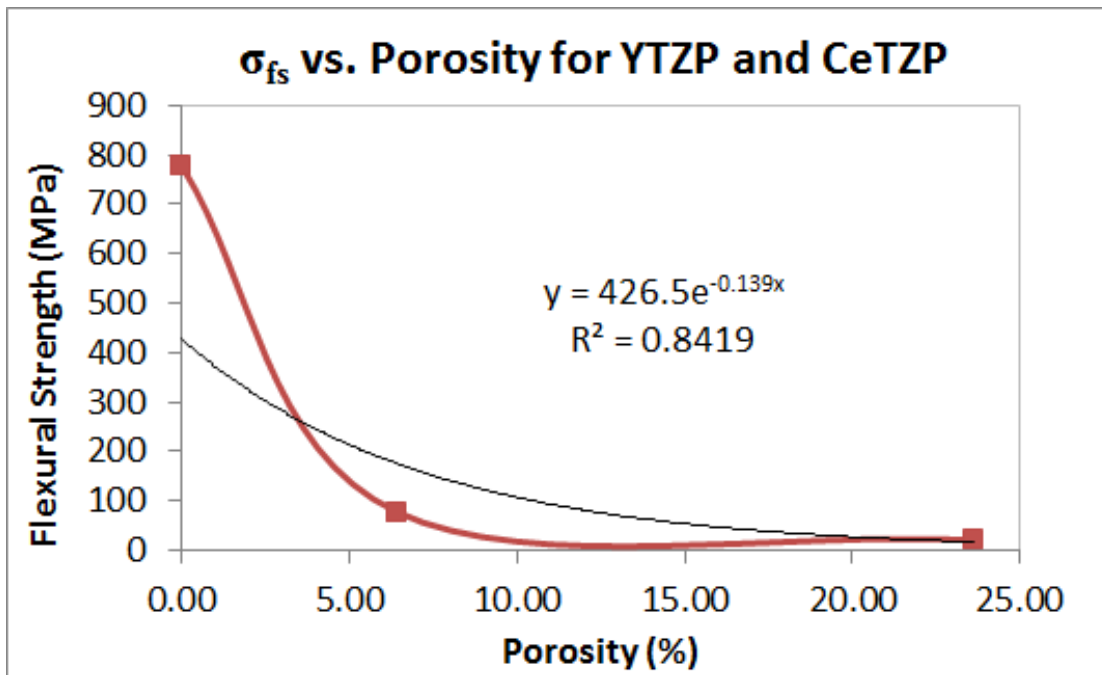
Figure 175: Relationship of Flexural Strength (σ_{fs}) vs. Porosity for Toughened Tetragonal Zirconia Materials: Y-TZP, 25% and 50% Ce-TZP
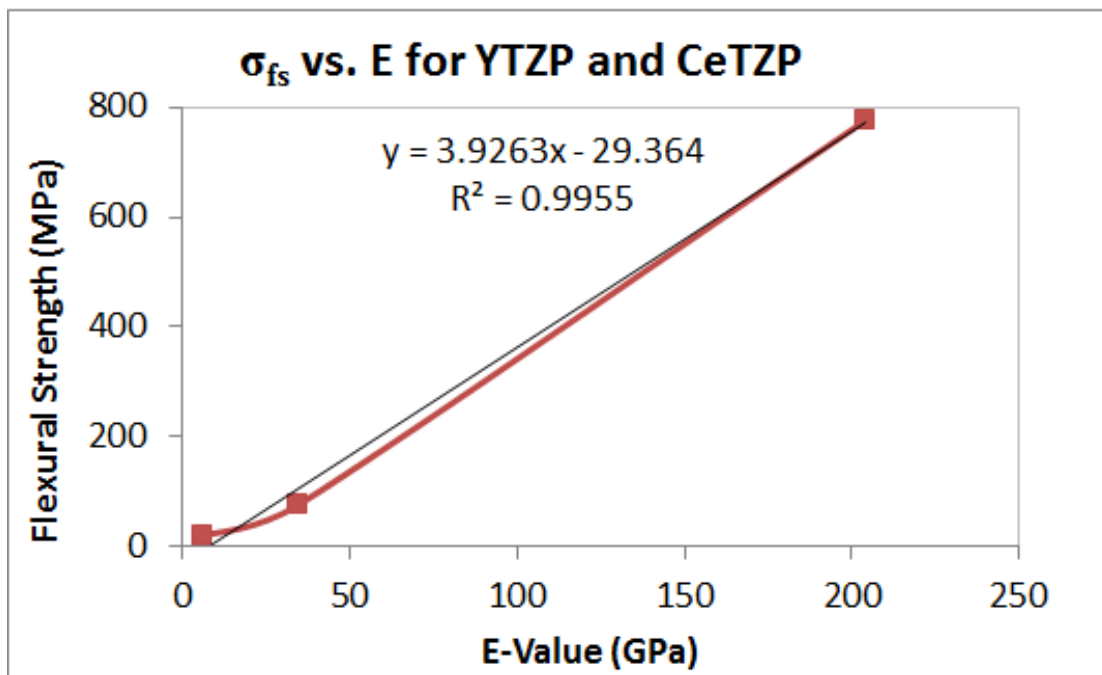
Figure 176: Relationship of Young's Modulus (E-value) and Flexural Strength (σ_{fs}) for Toughened Tetragonal Zirconia Materials: Y-TZP, 25% and 50% Ce-TZP
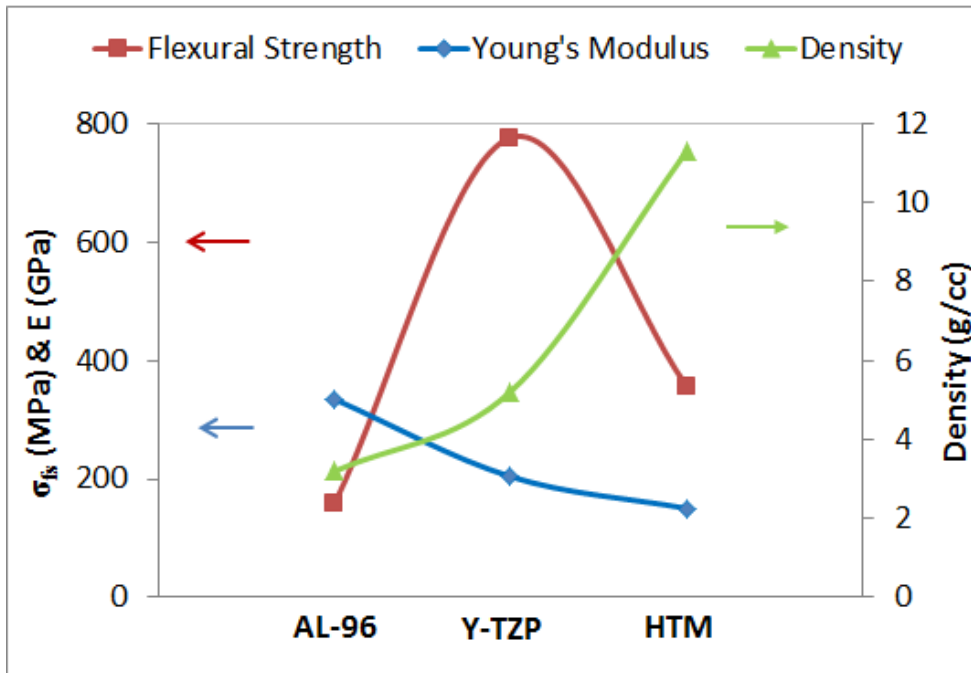
Figure 177: Flexural Strength (σ_{fs}), Young's Modulus (E-value), and Density for Different Crystallographic Materials: AL-96, Y-TZP, and HTM Cermet
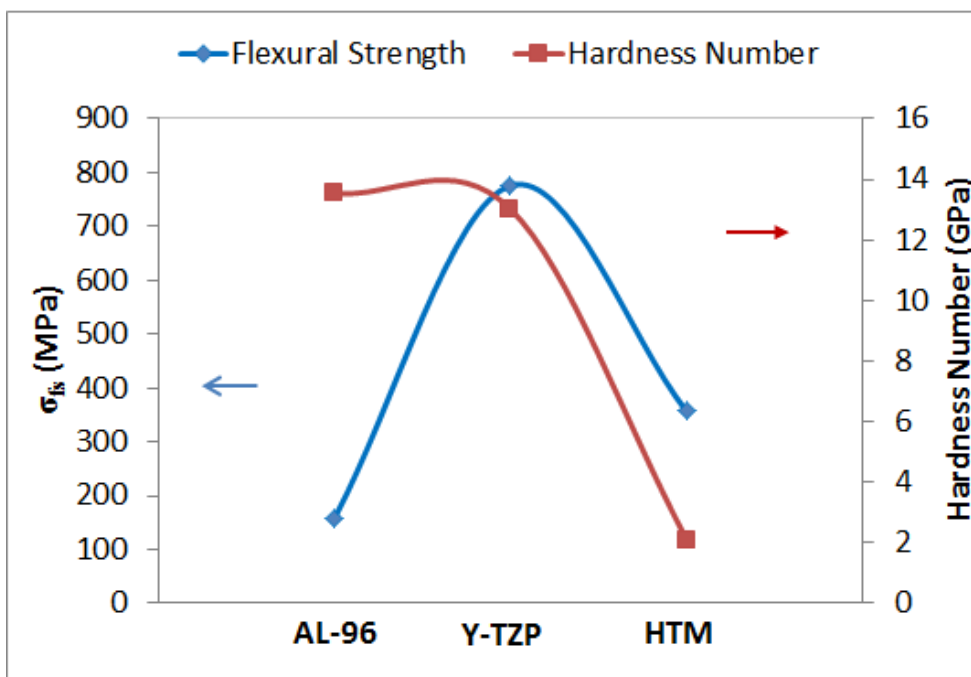
Figure 178: Flexural Strength (σ_{fs}) and Vickers Hardness Number for Three Crystallographic Materials: AL-96, Y-TZP, and HTM Cermet Solid (HTM)
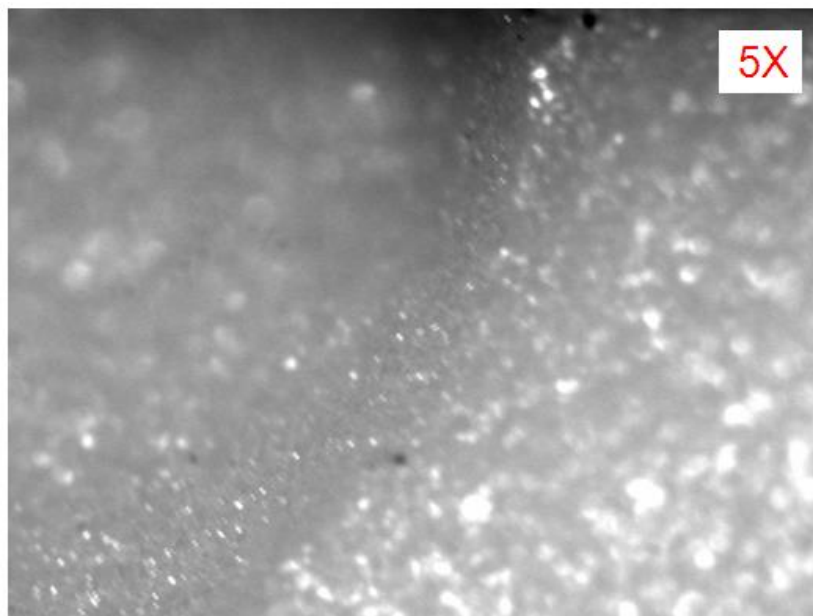
Alumina 96 wt% (LSP) - Fracture Surface

Y-TZP (STC) - Fracture Surface

230
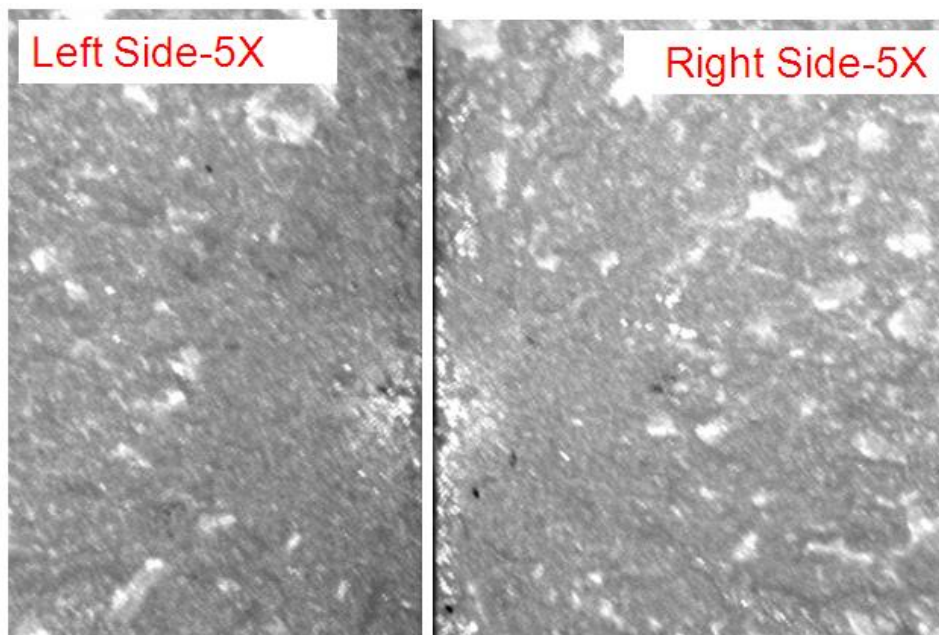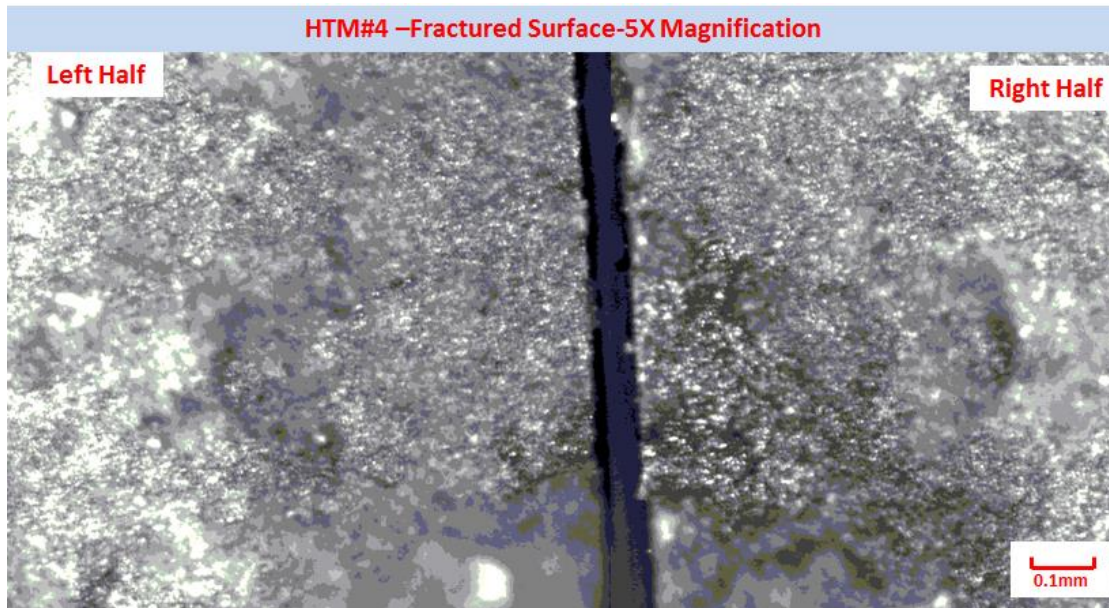
Figure 179: Optical Microscopic Observation of the Fractured Surface for AL-96, YTZP, and HTM Cermet Sample Bars after Flexural Strength Tests
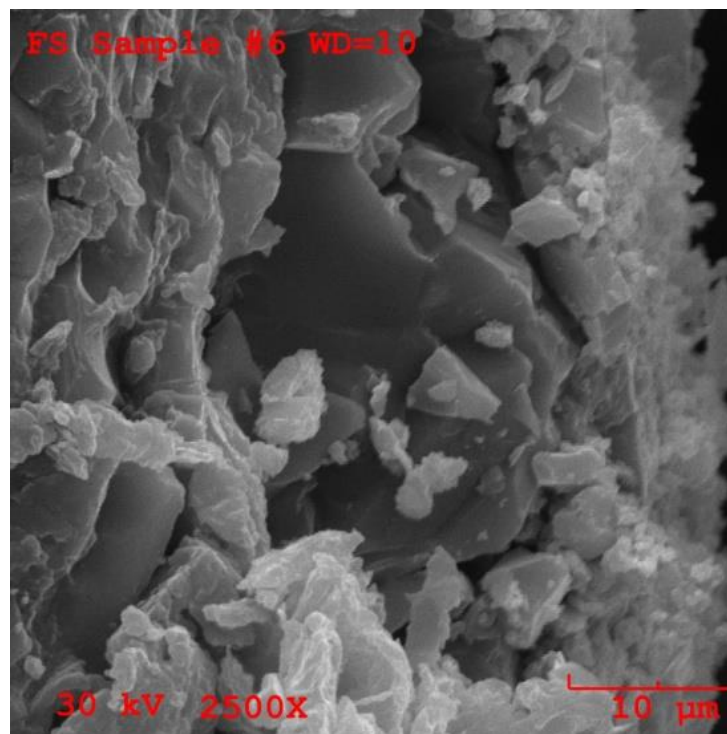
(a) AL-96
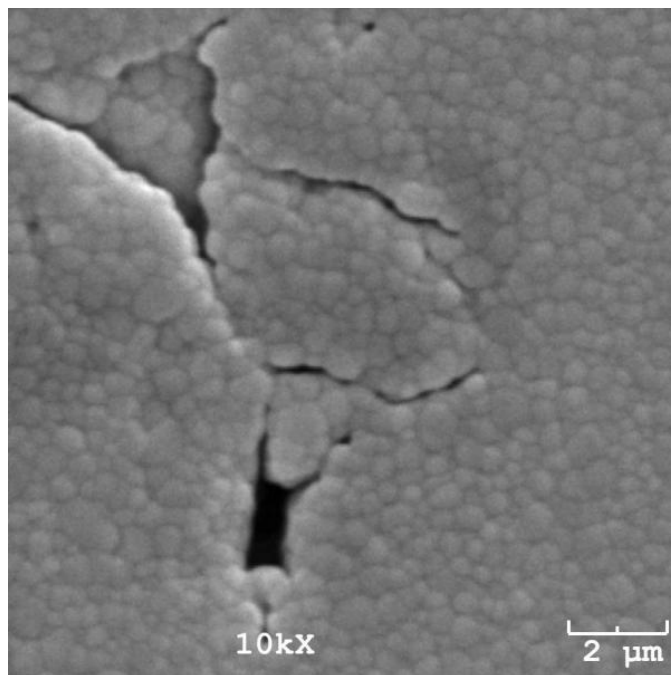
(b) Y-TZP
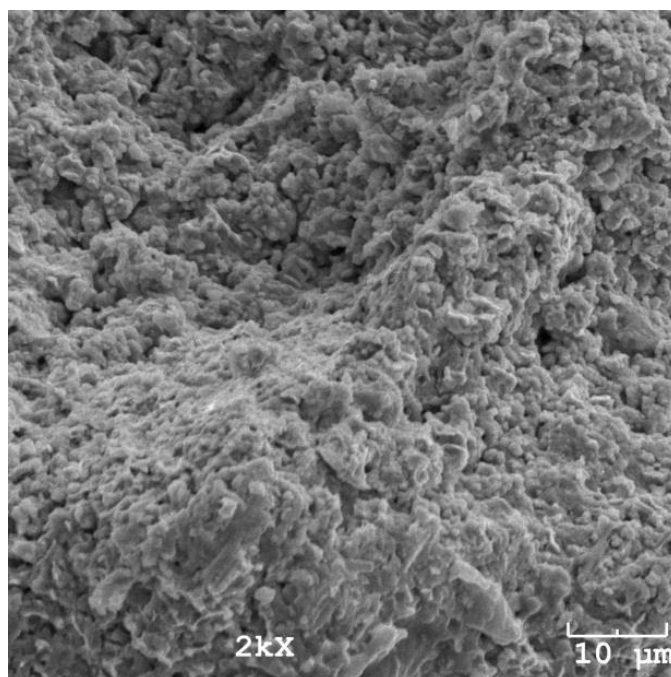
(c) HTM

**Figure 180:   SEM Microscopic Observation of the Fractured Surface for AL-96,
YTZP and HTM Cermet Sample Bars after Flexural Strength Tests**
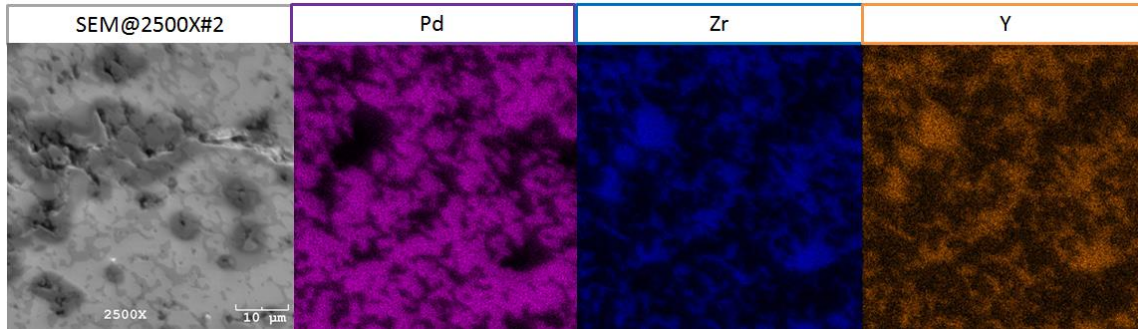
Figure 181: **SEM with EDS Microscopic Observation of Top Surface of HTM Cermet Sample Bars after Flexural Strength Tests**
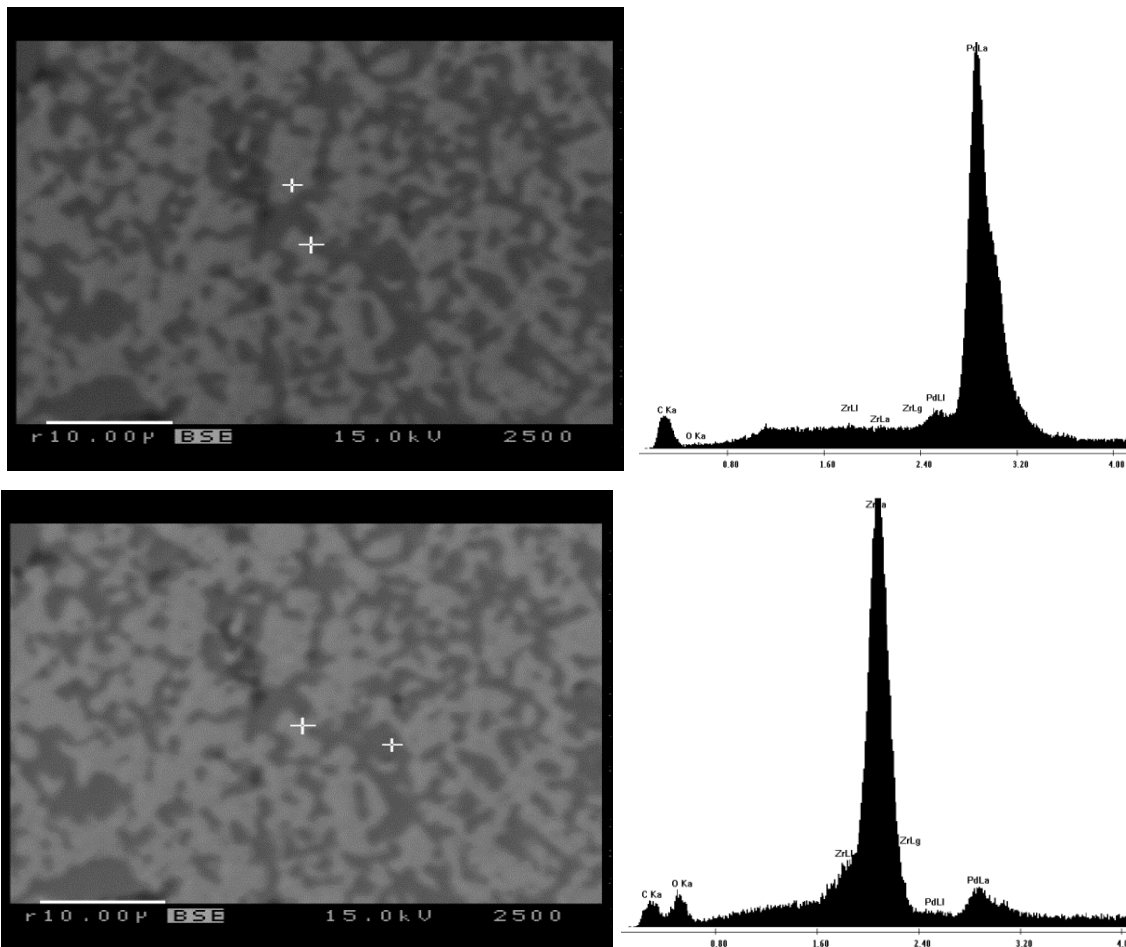
Figure 182: **Microprobe EDS of Top Surface of HTM Cermet Sample Bar**
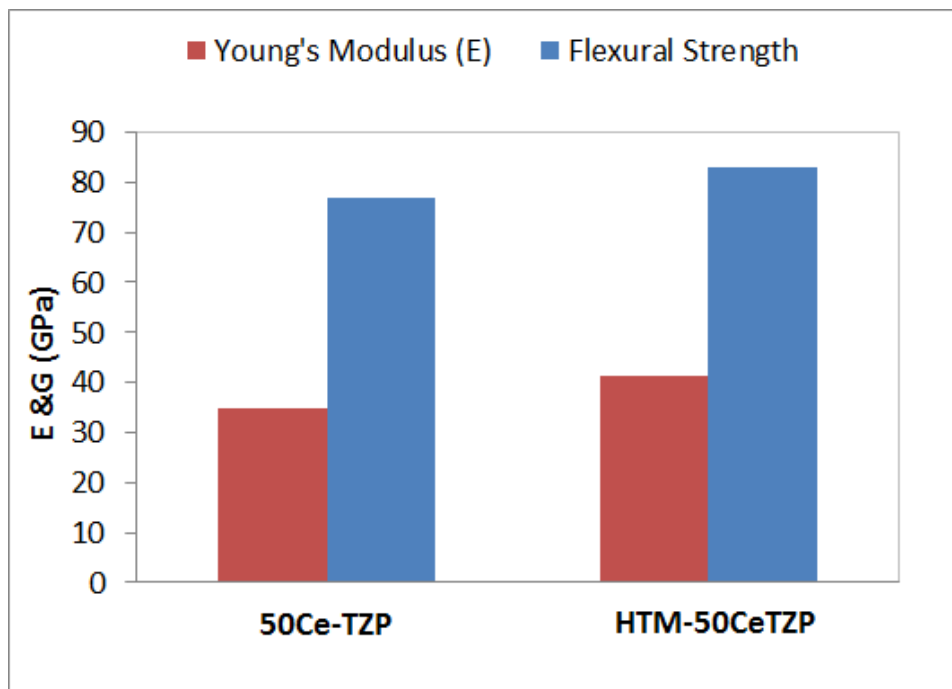
Figure 183: Results of Young's Modulus (E-value) and Flexural Strength (σ_{fs}) for Porous Substrate (50Ce-TZP) and HTM Dual-Phase Membrane (HTM-50CeTZP)
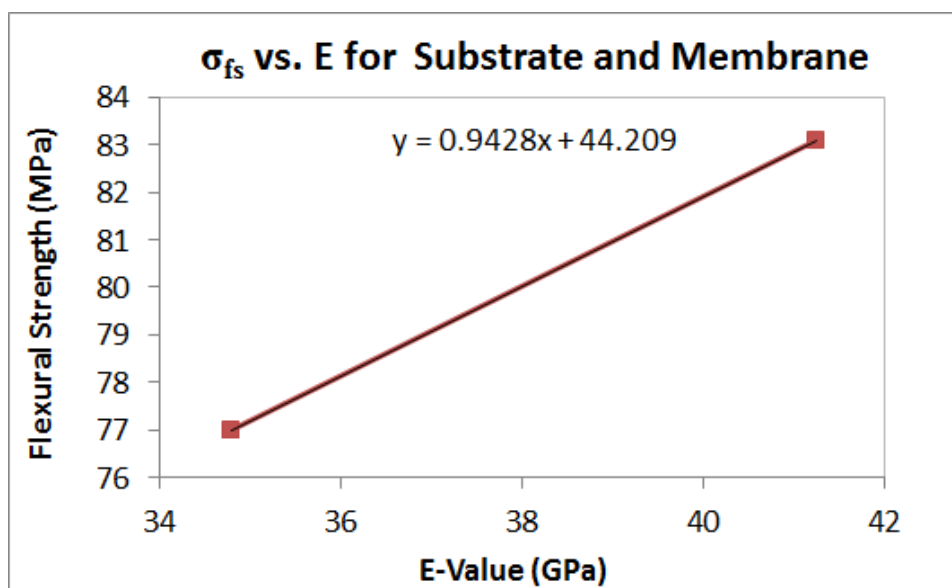
Figure 184: Correlations of Young's Modulus and Flexural Strength (σ_{fs}) for Porous Substrate (50Ce-TZP) and HTM Dual-Phase Membrane (HTM-50CeTZP)

234

5.3 Effect of Temperature on Both Physical and Mechanical Properties

Temperature is one of the major environmental factors that affect the physical and the mechanical properties, such Young's Modulus and strength. Effects of temperature and thermal cycling on dynamic Young's modulus (E) for the selected structural AL-96 material (can be represented by an interpolation equation as E= A-BT. On the other hand, the effects of temperature on the dynamic Young's modulus for Y-TZP material did not follow similar relationship. This could be explained by the DTA curve shown in Figure 148. The exothermic peaks occurred at a wide temperature range starting from 550°C to 600°C, in both heating and cooling processes, which could be related to phase changes from amorphous, or low crystalline phases to high crystalline phase.

Table 78 summarizes the mechanical properties for the structural ceramic (AL-96) and HTM cermet at both room temperatures (25°C) as well as at the elevated temperature (850°C). The effects of temperature on these two materials are plotted in Figure 184. Treating the sample at a high temperature testing environment of 850°C for 1 hour in air, however, increased the flexural strength of AL-96, which is attributed to the healing function of the surface and the inherent cracks for alumina material [64]. With other materials such as HTM cermet, however, with increase in temperature, the dislocation of the HTM cermet become more obvious and the HTM sample shows plasticity as compared to the HTM sample at room temperature.

Table 78:   Mechanical Properties at Both Room Temperature and Elevated Temperature for AL-96 and HTM Cermet

Material	Temperature (°C)	Flexural Strength (GPa)	Weibull Modulus (m-Value)	SCG Number (n-Value)
AL-96	25	158.87	6.70	38.00
	850	174.03	6.00	9.00
HTM Cermet	25	356.56	TBA	TBA
	850	284.5	TBA	TBA
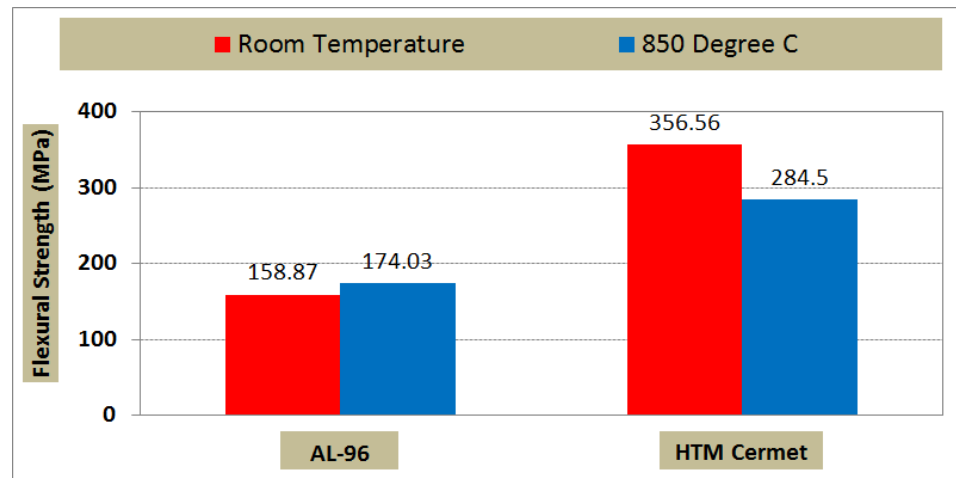
Figure 185: **Results of Flexural Strength (σ_{fs}) for Two Selected Different Crystallographic Structured Materials, i.e. AL-96 and HTM, at 25°C and 850°C**

5.4 Effect of Thermal Cycling on E-Value and Mechanical Properties

Table 79 summarizes the effect of thermal cycling on E-value and mechanical properties for the structural AL-96 and HTM cermet. Thermal cycling has insignificant effect on the E-values of both AL-96 and HTM cermet. Flexural strength (σ_{fs}) results for these two materials as a function of thermal cycling are plotted in Figure 186. The mean σ_{fs} value for AL-96 decreases with thermal cycling, although the hardness number increases. The SEM imaging was done in 2500x magnification for AL-96, both with and without thermal cycling, and results are shown in Figure 187 (a) to (b).

By comparing the grain size and the surface morphologies, it could be concluded that the grain size increases with increased number of thermal cycles. Generally, some grains in the alumina matrix are subjected to compression and play a major role as a bridge, which corresponds to the grain-bridge model of R-curve or T-curve properties of ceramic [72], resulting in the increased hardness. Meanwhile, several thermally induced cracks occur, resulting in the decrease of flexural strength of AL-96 sample.

A microprobe with EDS was also used for morphology and elemental composition of the

236

HTM surfaces, shown in Figure 188 (a) and (b). The PdO phase was found to enclose Pd phase at the cross-section of the HTM cermet sample, and the reaction product of a new strong PdO phase might be the reason for the improvement of σ_{fs} value after 500 thermal cycles as compared to the as-received sample.

Table 79:   Summary of E-value and Mechanical Properties as Effect of Thermal Cycling Treatment

Material	Thermal Cycling	E-Value (GPa)	Flexural Strength (MPa)	Weibull Modulus (m-Value)	Hardness Number (GPa)
AL-96	0	334.70	158.87	6.70	13.54
	650	338.4	115.46	5.90	17.96
	1150	335.2			
HTM Cermet	0	150.62	356.56		2.11
	120	148.95			
	500	149.75	422.09		
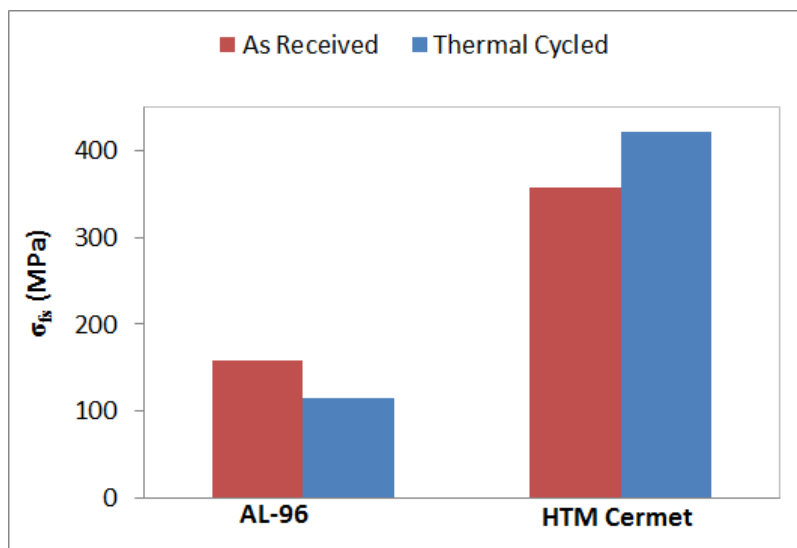
Figure 186:   Effect of Thermal Cycling on Flexural Strength for AL-96 and HTM
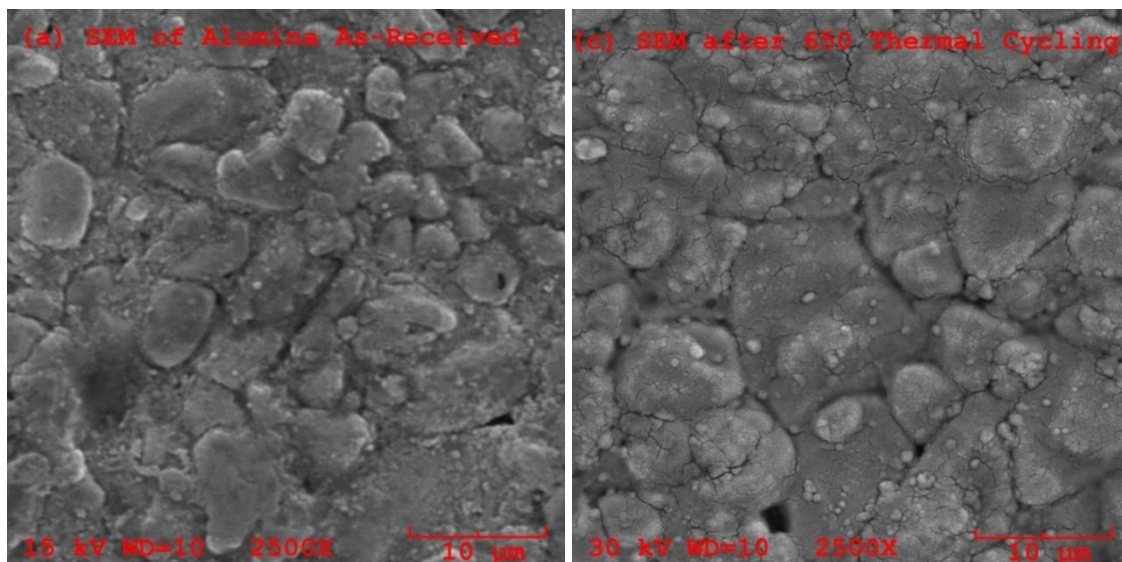
Figure 187: SEM Microscopic Observation of Surface for AL-96 both As-Received and after Thermal Cycling Treatment
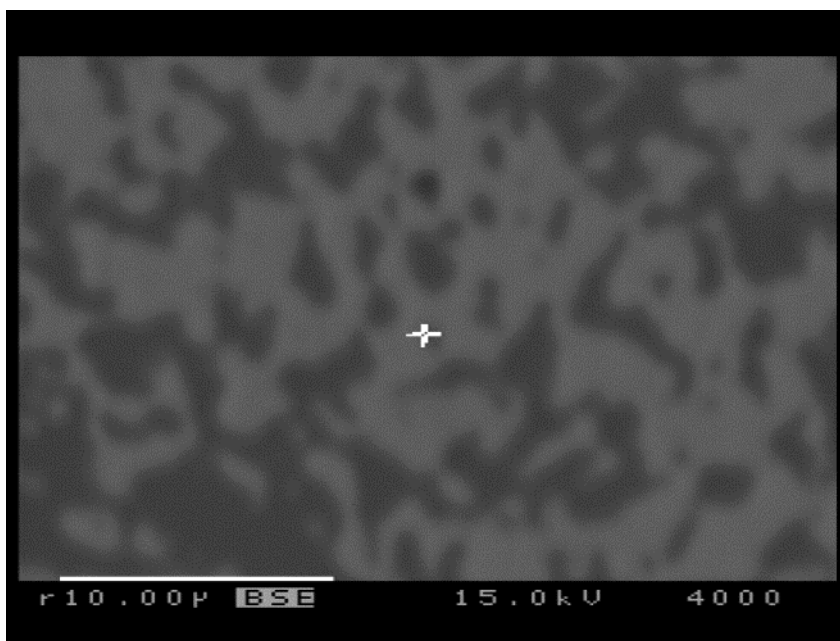
(a)   As-Received
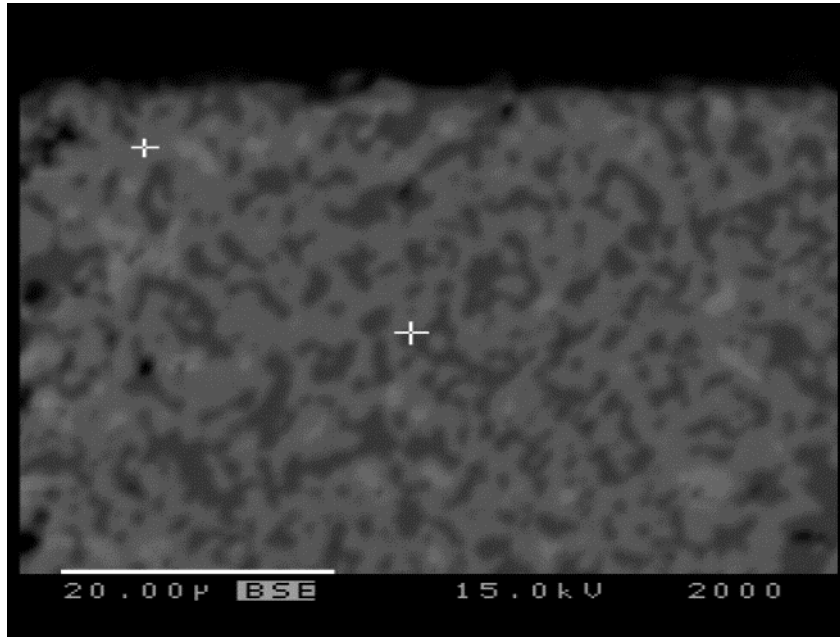
(b)   500 Thermal Cycles

Figure 188:   Microprobe Microscopic Observation of the Surface for HTM As-Received and after 500 Thermal Cycles

5.5   Effect of Thermal Cycling on Residual Stress

Table 80 summarizes the effect of thermal cycling on residual stress for the structural ceramic AL-96, HTM cermet, and HTM dual-phase membrane. Residual stress results are plotted in Figure 190 as a function of thermal cycling for AL-96. The bulk residual stress is the tensile stress and is approximately 96 MPa for the as-received specimens. The residual stress increases with thermal cycling increasing from 0 to 650 cycles, and a maximum tensile residual stress of 480 MPa is exhibited after 650 thermal cycles. With thermal cycling between 650 to 900 cycles, however, there is a large decrease in the residual tensile stress.

Mohr's circles in Figure 191 are based on the residual stress as a function of thermal cycling for the HTM cermet. The residual stress is first appears mainly as compressive residual stress with an insignificant amount of shear stress.
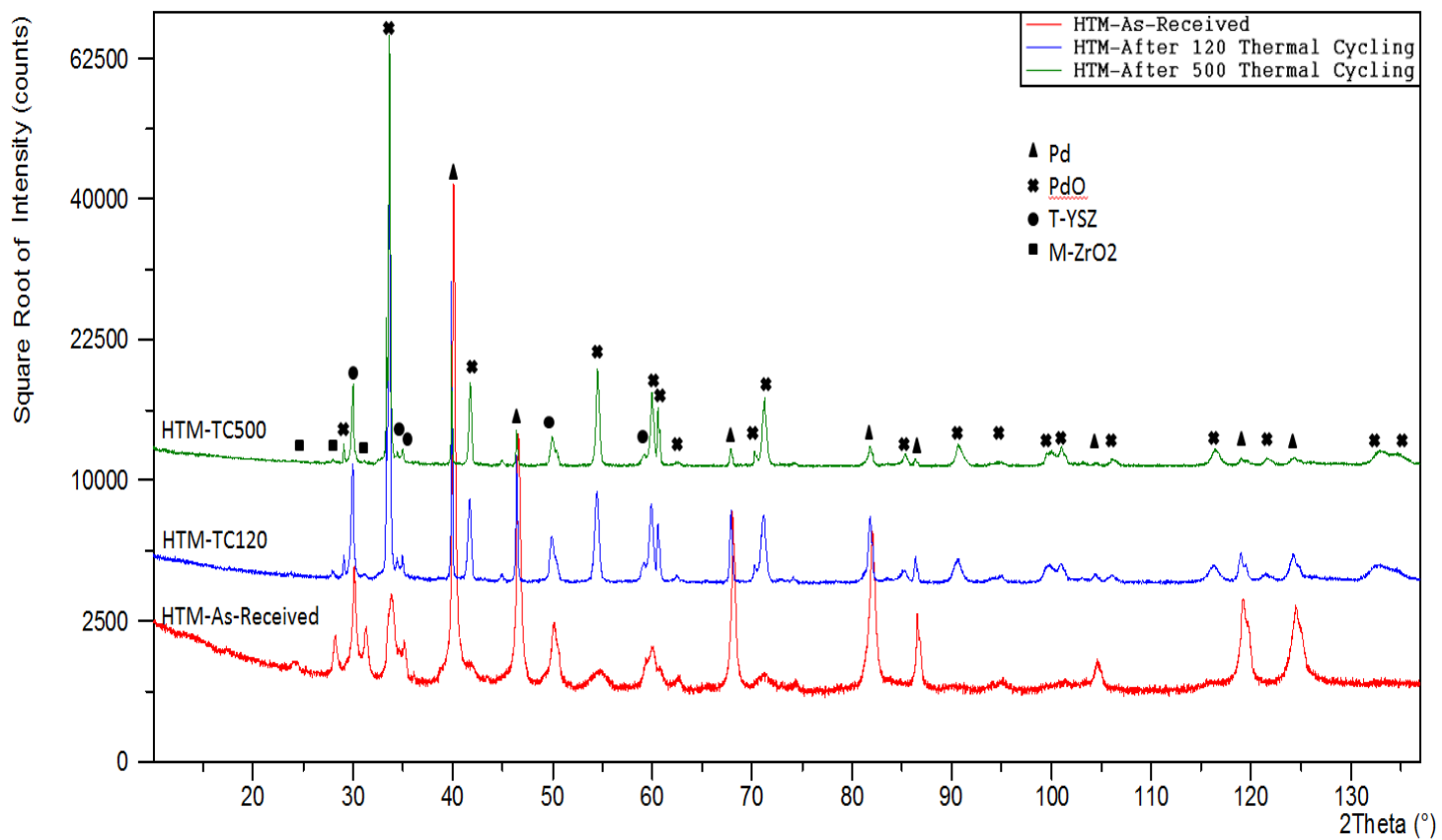
Figure 189:   XRD phase analysis for HTM cermet as an effect of thermal cycling treatment
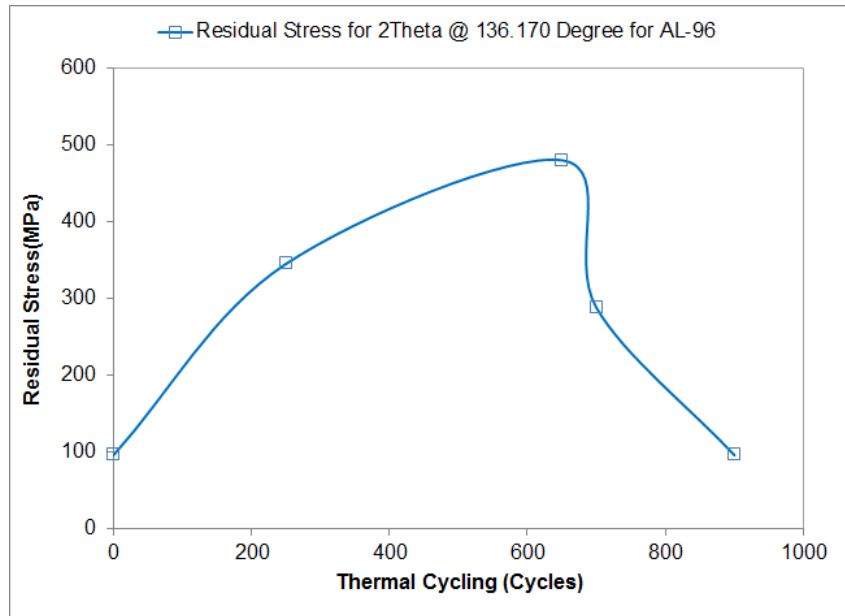
Figure 190:   Effect of Thermal Cycling on Residual Stress for AL-96

Table 80:   Summary of E-value and Mechanical Properties as an Effect of Thermal Cycling Treatment

Material	Thermal Cycling	Residual Stress (Mpa)
AL-96	0	96
	250	320
	650	480
	700	288
	900	96
HTM Cermet	0	-139
	120	-137
	500	13
50Ce-TZP	0	-1.12
	500	-0.56

With thermal cycling up to 120 cycles, there are changes in the Pd phase for the residual stress as can be seen from Table 80 and Figure 191. With the thermal cycling increased up to 500 cycles, the residual stress is found to be mainly as the tensile residual stress and a more obvious shear residual stress (Figure 191).

The relationship between residual stress and mechanical properties is presented in Table 81. Increase in the residual stress is found to be beneficial to the hardness value for AL-96 and leads to the increase of Vickers hardness number. Though a tensile residual stress is not beneficial to the flexural strength of HTM, the new phase layer of PdO seems to have a much greater effect for the increase of flexural strength for HTM after 500 thermal cycling.
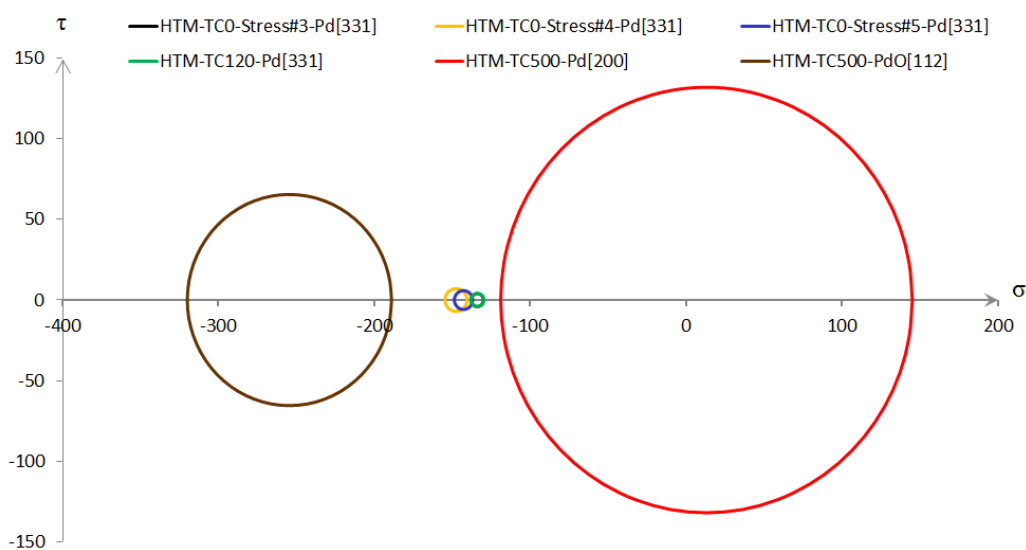
Figure 191:   Effect of Thermal Cycling on Residual Stress for HTM Cermet

Table 81: Summary of E-value and Mechanical Properties as an Effect of Thermal Cycling Treatment

Material	Thermal Cycling	Flexural Strength (MPa)	Hardness Number (GPa)	Residual Stress (MPa)
AL-96	0	158.87	13.54	96
	650	115.46	17.96	480
HTM Cermet	0	356.56	2.11	-139
	500	422.09		13

CHAPTER VI: **CONCLUSIONS AND RECOMMENDATIONS**

6.1 **Conclusions for Thermo-Mechanical and Microstructural Properties for HTM Cermet Bulk and HTM Powder**

1. The density of HTM cermet is approximately 11.3g/cc at the ambient temperature based on Archimedes' principle. Young's modulus is approximately 145.5MPa for HTM cermet as-received. Poisson ratio (ν) is consistently about 0.34 despite of the difference in geometry of the tested sample. The Vickers' hardness numbers of the as-received HTM cermet are constant in the range of 2.0 ~ 2.2 GPa with the change of loading force from 200-1000 grams.

2. The mean flexural strength (σ_{fs}) of the HTM cermet is about 356 MPa at room temperature and decreases to 284 MPa at the the elevated temperature 850ºC. Difference of testing atmosphere (air or N_2) has insignificant effect on the load-displacement curves during the flexural strength test at an elevated temperature of 850°C for HTM cermet. The total displacement for HTM subjected to the strength test at 850°C is about 3 times to that at room temperature. With the testing temperature increased to 850°C, the load-displacement curves for HTM initially result in an elastic deformation, and then are followed by some obvious plastic deformation. From the load vs. displacement curves, HTM cermet behaves much more like elastic material at room temperature; with the temperature increased to 850°C, the HTM cermet behaves much more like a metallic material with fractures preceded by plastic deformation.

3. The crack propagation and the direction of the fracture surface based on the optical observation after flexural strength provides some basic information about the mode of the failure and characteristic of material such as brittle or ductile. For the HTM MOR bar tested at room temperature, the type of fracture is appears to be intergranular fracture, where the phases in the grain boundary is weak and brittle. Fracture originated from existing pores and micro-cracks and crack modes can be

characterized as crack Mode I or the crack opening mode. For HTM MOR bars tested at the elevated temperature of 850°C, the cracks also originated from existing pores and micro-cracks. The cracks are growing in combination of both transgradual and intergradual. The crack failed in combination Modes I and II, or tearing and opening modes.

4. With the assumption that residual stress (σ_{φ}) is constant for any crystallographic plane of a selected phase (Pd) in a homogeneous polycrystalline materials such as the HTM cermet, the elastic constant for any crystallographic plane (h k l), being proposed for the first time, could be calculated with no expensive and complicated experimental work. This assumption had been approved by a duplicate of running residual stress tests for all Pd crystallographic planes by having constant results for the residual stress.

5. All crystallographic planes of Pd phase from lower diffraction angles to higher diffraction angles could also be used to precisely evaluate the residual stress, if the XRD powder diffraction pattern provides a diffraction peak of suitable intensity and free of interference from neighboring peaks.

6. Because HTM cermet is homogeneous in terms of its microstructure and mechanical properties in all direction, the size of selected diffraction areas (2-64 mm^2) does not influence the results of the residual stress. The other selected instruments parameters, such as step size and stepping time, played insignificant roles in getting the residual compressive stress in the HTM cermet with the values somewhere in between -130 to -150 MPa.

7. Maximum and minimum principle stress and the maximum shear stress were calculated from Mohr's circle calculated from the selected σ_{φ} at three different selected φ angles. Maximum and minimum principle stresses are found to be in the magnitude between -135 and -155 MPa, whereas, the maximum shear stress is only 10 MPa for HTM cermet as-receive. The theoretical values of residual stress based on Mohr's circle are found to be consistent with the experimental values for HTM as-received.

8. As a result of thermal cycling up to 120 thermal cycles, different phases in the HTM cermet have substantial differences in residual stresses. PdO phase has an average of about 700 MPa in compressive stress as compared to 120 Mpa for the Pd phase. The Tetragonal Yttria-Stabilized Zirconia (T-YSZ) phase has about 530 MPa in compressive stress as compared to 160 MPa for the monoclinic zirconia phase (M-ZrO2). The difference of residual stress in different phases in the HTM cermet is due to the disparities in the coefficient of thermal expansion between the various phases during thermal cycling.

9. The residual stress of HTM cermet after 500 thermal cycling. Phases of PdO and Pd in HTM cermet after 500 thermal cycles are found to have decreased compressive residual stress as compared to HTM as-received and after 120 thermal cycles. At some φ angle, the residual stress is found to be as tensile stress based on both experimental results and Mohr's circle. Macroscopic cracks can be observed by naked eyes as well as by a microscope because of the residual tensile stress that. The PdO phase in HTM cermet is found as -120 MPa compressive residual stresses after 500 thermal cycles, but the value had been greatly decreased as compared to -700 MPa after 120 thermal cycles.

10. Based on all the selected peaks of both Pd and YSZ phases of the HTM cermet sample, the residual compressive stresses for the HTM as-received are found to be greatly reduced after the HTM is soaked or annealed in N_2 at 900°C for 48 hours. There is also no peak shift for the residual-stress-free powder sample. Both tests above approve the validity and precision of the employed technique and equipment setup.

11. The average CTE, α_{avg}, of HTM cermet in air is approximately 10×10^{-6}/K. There is an instantaneous thermal expansion from 650°C to 750°C and another instantaneous thermal shrinkage around 825°C-875°C in air. The expansion of HTM cermet during the heating process in air is related to the oxidation of palladium (Pd) metal. The shrinkage of HTM cermet could be related to the softening of the palladium phase at high temperature in both nitrogen and air environment, as well as the dissociation of

palladium oxide (PdO) back to Pd. No sharp expansion occurs for HTM cermet in the testing environment of N_2, although there was an obvious decrease of the instantaneous coefficient of thermal expansion α_t for HTM cermet in temperature from 675 to 825°C in N_2 because the sample might have a change of its phase status for Pd in HTM.

12. Thermal analysis by TG/DTA proved that both the heating/cooling rates and the total numbers of thermal cycling affected he amount of PdO that was permanently transformed from Pd phase.

13. XRD powder diffraction patterns for the HTM cermet are found to conform with the reference ICDD patterns of pure palladium (Pd), palladium oxide (PdO), tetragonal zirconia ($T\text{-}ZrO_2$), and monoclinic zirconia ($M\text{-}ZrO_2$). Microanalysis of the elemental composition by both XRF and EDS detected a minor amount of yttrium (Y) in addition to Pd and Zr. Therefore, the phase of tetragonal ZrO_2 ceramic is yttria-stabilized zirconia (YSZ) phase, in which the tetragonal crystal structure of zirconium oxide is made stable at room temperature by an addition of yttrium oxide. In terms of quantitative analysis, both XRF and EDS software gave a consistent result of 70–80 wt% of Pd and 20–30 wt% of YSZ.

14. The novel HTM was approved to have no surface texture by XRD pole figure. Surface morphology is found to affect the pole figure significantly, such that the polished surface was found to approve a consistent pole figure.

15. With the thermal cycling up to 120 cycles between 50–850°C, HTM cermet started to have some micro-cracks that could be observed only by Microscope in the magnification 50. There are some macro-cracks which could be seen by naked eyes on the surface of the HTM cermet after 500 thermal cycles.

16. As discussed in the XRD powder diffraction phase analysis and TG/DTA, the top and bottom layers could be composed mainly of Palladium oxide (PdO), the unreactive Pd or dissociated Pd phase, and the YSZ phases. The middle layer of the HTM Disc sample is therefore estimated unreactive after 500 thermal cycles and is mainly composed of the same Pd and YSZ phases as the raw material.

17. Both SEM and Microprobe analysis show that the temperature gradient during thermal cycling produced more micro-cracks inside the HTM Disc, whereas the chemical reaction between Pd and Oxygen to form PdO disturbed the continuity of Pd-YSZ dual interconnection system from surface down.

18. A semi-quantitative analysis is conducted based on the scale factor and the RIR values. As the treatment of thermal cycling increased from 0 to 500 cycles, the mass fraction of Pd is greatly reduced from 74% to 12%, whereas, increased amount of PdO is produced by the oxidation of Pd with O_2. The other zirconia phases, including both $M-ZrO_2$ and YSZ, did not change significantly with the treatment of up to 500 thermal cycling between 50 to 850°C.

6.2 Conclusion for the Correlation between Microstructural Properties and Mechanical Properties for HTM and Other Selected Structural Ceramic Materials

1. For the selected toughened zirconia materials, such as Y-TZP or Ce-TZP, physical and mechanical properties are mainly affected by porosity and microstructural characterizations, such as grain size and inherited pores. Especially, E-value is positively propositional to mechanical properties, such as flexural strength.

2. For different crystallographic materials, physical properties such as E and density are independent of mechanical properties. Microstructural properties, especially grain size and crystallographic structure, and thermodynamic properties are the main factors affecting the mechanical properties at both room and high temperature.

3. Mechanical properties of Al_2O_3 are found to be correlated to the grain size, porosity and texture etc.. Mechanical properties of ZrO2 group are found to be mainly correlated to the phase transformation. The oxidation of Pd and plasticity at high temperature mainly affect the mechanical properties of HTM cermet subjected to high temperature or to thermal cycling treatment.

248

4. Change of residual stress and microstructure is found to be the main reason affecting the mechanical properties of HTM at high temperature or under thermal cycling treatment.

6.3 Future Work

Residual stress for HTM induced by thermo cycles shows a very critical role in defining the thermo-mechanical properties. Therefore, significant efforts should be focused on characterization of the residual stresses by employing XRD $\sin^2\psi$ methods and should be verified an alternative experimental technique, such as hardness measurement. A simulation FEM model should be focused on the residual stress development and verified by the real experimental data. The structure-property-performance of thin cermet membranes on porous support structures should also be addressed for the future research work.

REFERENCES

1.   Stocker, J., M. Whysall, and G. Miller, *30 Years of PSA Technology for Hydrogen Purification.* UOP LLC; 1998, 1998.

2.   S., S. and G. T.C., *Purification of hydrogen by Pressure Swing Adsorption.* Sep., Sci. Technol, 2000. 35: p. 11.

3.   Adhikari, S. and S. Fernando, *Hydrogen Membrane Separation Techniques.* Industrial & Engineering Chemistry Research, 2006. 45(3): p. 7.

4.   Balachandran, T.H.L. U., and S.E. Dorris, *Hydrogen production by water dissociation using mixed conducting dense ceramic membranes.* International Journal of Hydrogen Energy, 2007. 32(4).

5.   Iwahara, H., *Hydrogen pumps using proton-conducting ceramics and their applications.* Solid State Ionics, 1999. 125(1-4): p. 8.

6.   Dorris.S.E., Lee.T.H., and B. U., *U.S. Patent, 6,569,226, May 27, 2003.* 2003.

7.   Y.S., C., et al., *Performance of alumina, zeolite, palladium, Pd-Ag alloy membranes for hydrogen separation from town gas mixture.* J. Membr. Sci, 2002. 204: p. 12.

8.   Balachandran, U., et al.,, *Dense Membranes for Hydrogen Separation From Mixed Gas Streams.* 23rd Annual International Pittsburgh Coal Conference, Pittsburgh, PA, 2006.

9.   Stanislowski, J. and J. Laumb, *Gasification of Lignites to Produce Liquid Fuels, Hydrogen, and Power.* Presented at the Pittsburgh Coal Conference, Sept 2009, 2009.

10.   Kluiters, S.C.A., *Status review on membrane systems for hydrogen separation* Energy Center of The Netherlands: Petten, The Netherlands, 2004.

11.   *Standard Test Method for Flexural Strength of Advanced Ceramics at Ambient Temperature.* ASTM C1161–02c.

12.   Ockwig, N. and T. Nenoff, *Membranes for Hydrogen Separation.* ACS Publications Chemical Review, 2007.

13.   Coker, D.T., R. Prabhakar, and B.D. Freeman, *Tools for teaching gas separation using polymers.* Chem. Eng. Educ. , 1995. 31: p. 8.

250

14.   Ritter, J.A. and A.D. Ebner, *DOE/ITP/ Chemicals & Chemicals Industry Vision 2020 Technology Partnership (December 2005); J.A. Ritter and A.D. Ebner, Sep. Sci. Technol (2006) submitted.* 2006.

15.   T.M., N. and S. R.J., *Membranes for Hydrogen Purification: An Important Step toward a Hydrogen-Based Economy.* MRS Bulletin, 2006. 31(October 2006).

16.   Bhandari, R. and Y.H. Ma, *Pd–Ag membrane synthesis: The electroless and electro-plating conditions and their effect on the deposits morphology.* Journal of Membrane Science 2009. 334: p. 14.

17.   Gadea, S.K., et al., *palladium–ruthenium membranes for hydrogen separation fabricated by electroless co-deposition.* international journal of hydrogen energy, 2009. 34: p. 8.

18.   Gadea, S.K., et al., *The effects of fabrication and annealing on the structure and hydrogen permeation of Pd–Au binary alloy membranes.* Journal of Membrane Science 2009. 340: p. 7.

19.   Ryia, S.K., et al., *Low temperature diffusion bonding of Pd-based composite membranes with metallic module for hydrogen separation.* Journal of Membrane Science 2009. 326: p. 6.

20.   Wee, S.L., C.T. Tye, and S. Bhatia, *Membrane separation process— Pervaporation through zeolite membrane.* Separation and Purification Technology 2008. 63: p. 17.

21.   Tsuru, T., et al., *Membrane reactor performance of steam reforming of methane using hydrogen-permselective catalytic SiO2 membranes.* Journal of Membrane Science, 2008. 316: p. 10.

22.   Xiao, W., et al., *A novel method to synthesize high performance silicalite-1 membrane.* Separation and Purification Technology 2009. 67: p. 6.

23.   Prabhu, A.K. and S.T. Oyama, *Highly hydrogen selective ceramic membranes: application to the transformation of greenhouse gases.* Journal of Membrane Science, 2000. 176(2): p. 233-248.

24.   Sebastián, V., et al., *Improved Ti-silicate umbite membranes for the separation of H2.* Journal of Membrane Science, 2008. 323(1): p. 207-212.

25.   Balachandran, U., et al., *Project Meeting for Novel Dense Membranes for Hydrogen Separation for Energy Applications (DOE#DE-FG02-09ER46628).* 2010.

26.   Balachandran, U., et al.,, *Hydrogen separation by dense cermet membranes.* Fuel, 2006. 85(2).

27.   Rhodes, J. and E.D. Wachsman, *Mixed Protonic Electronic Barium Cerates for Hydrogen Separation.* Solid State Ionic Devices II - Ceramic Sensors. 2001: Electrochem. Soc, 2001.

28.   S.Bandopadhyay, et al., *Final Report for Oxygen Transport Cearmic Membranes, DOE Award#DE-FC26-99FT40054.* 2009.

29.   *Standard Test Method for Dynamic Young's Modulus, Shear Modulus, and Poisson's Ratio for Advanced Ceramics by Impulse Excitation of Vibration.* ASTM C1259-08.

30.   *Standard Test Method for Vickers Indentation Hardness of Advanced Ceramics.* ASTM C1327-08.

31.   *Standard Practice for Fractography and Chracterization of Fracture Origins in Advanced Ceramics.* ASTM C1322-05b.

32.   Barsoum, M.W., *Fundamentals of Ceramics.* Institute of Physics Publishing, Bristol and Philadelphia, 2003, ISBN 0 7503 0902 4 2003: p. 387-389.

33.   Wikipedia, *Texture (crystalline), May, 2014.*
http://en.wikipedia.org/wiki/Texture_%28crystalline%29.

34.   Prevey, P.S., *X-RAY DIFFRACTION RESIDUAL STRESS TECHNIQUES.* American Society for Metals, 1986: p. 380-392.

35.   Zheng, X., J. Li, and Y. Zhou, *X-ray diffraction measurement of residual stress in PZT thin films prepared by pulsed laser deposition.* Acta Materialia, 2004. 52(11): p. 3313-3322.

36.   Prevey, P.S., *A Method Of Determining The Elastic Properties Of Alloys In Selected Crystallographic Directions For X-Ray Diffraction Residual Stress Measurement.* Advances in X-Ray Analysis, Vol. 20, Plenum Press,New York, NY, 1977: p. 345-354.

37.   Pecharsky, V.K. and P.Y. Zavalij, *Fundamentals of Powder Diffraction and Structural Characterization of Materials (2nd Version).* 2009: p. 172.

38.   *Standard Test Method for Linear Thermal Expansion of Solid Material with a Push-Rod Dilabometer.* ASTM E228-06.

252

39.   Wikipedia, *Palladium, May, 2014.* **http://en.wikipedia.org/wiki/Palladium**.

40.   Ozga, P., *Pole Figures: Registration and Plot Conventions.* 2007.

41.   Barsoum, M.W., *Fundamentals of Ceramics.* Institute of Physics Publishing, Bristol and Philadelphia, 2003, ISBN 0 7503 0902 4 2003: p. 453-454.

42.   Kandil, H.M., J.D. Greiner, and J.F. Smith, *Single-Crystal Elastic Constants of Yttria-Stabilized Zirconia in the Range 20° to 700°C.* Journal of the American Ceramic Society, 1984. 67(5): p. 341-346.

43.   Adams, J.W., R. Ruh, and K.S. Mazdiyasni, *Young's Modulus, Flexural Strength, and Fracture of Yttria-Stabilized Zirconia versus Temperature.* Journal of the American Ceramic Society, 1997. 80(4): p. 903-908.

44.   Wikipedia, *Thermochromism, May, 2014.* **http://en.wikipedia.org/wiki/Thermochromism**.

45.   Wikipedia, *Thermochromism, Inorganic materials, May, 2014.* **http://en.wikipedia.org/wiki/Thermochromism#Inorganic_materials**.

46.   Serrano, J.L., *Metallomesogens.* 1997.

47.   Wikipedia,   *Third   Law   of   Thermodynamics,   May,   2014.* **http://en.wikipedia.org/wiki/Third_law_of_thermodynamics**.

48.   Bayer, G. and H.G. Wiedemann, *Formation, dissociation and expansion behavior of platinum group metal oxides (PdO, RuO2, IrO2).* Thermochimica Acta, 1975. 11(1): p. 79-88.

49.   Barsoum, M.W., *Fundamentals of Ceramics.* Institute of Physics Publishing, Bristol and Philadelphia, 2003, ISBN 0 7503 0902 4 2003: p. 111-121.

50.   Lyubovsky, M. and L. Pfefferle, *Complete methane oxidation over Pd catalyst supported on α-alumina. Influence of temperature and oxygen pressure on the catalyst activity.* Catalysis Today, 1999. 47(1–4): p. 29-44.

51.   Wikipedia, *First Law of Thermodynamics, May, 2014.* **http://en.wikipedia.org/wiki/First_law_of_thermodynamics**.

52.   Ushakov, S.V. and A. Navrotsky, *Experimental Approaches to the Thermodynamics of Ceramics Above 1500°C.* Journal of the American Ceramic Society, 2012. 95(5): p. 1463-1482.

53.   Chen, J.J. and E. Ruckenstein, *Role of interfacial phenomena in the behavior of alumina-supported palladium crystallites in oxygen.* The Journal of Physical Chemistry, 1981. 85(11): p. 1606-1612.

54.   Zhang, H., et al., *PdO/Pd system equilibrium phase diagram under a gas mixture of oxygen and nitrogen.* Journal of Phase Equilibria, 2002. 23(3): p. 246-248.

55.   Wachtman, J.B., W.R. Cannon, and M.J. Matthewson, *Mechanical properties of ceramics*2009, Hoboken, N.J.: Wiley. 317-331.

56.   *Reference code: 04-015-0492; PDF Index name: Palladium.* 2011.

57.   *Reference code: 01-075-9648; PDF Index name: Zirconium Oxide (Tetrogonal).* 2011.

58.   *Reference code: 01-080-0966; PDF Index name: Zirconium Oxide (Monoclinic).* 2011.

59.   Pecharsky, V.K. and P.Y. Zavalij, *Fundamentals of Powder Diffraction and Structural Characterization of Materials (2nd Version).* 2009: p. 160-161.

60.   Liebowitz, H., *Francture: An Advanced Treatise. Vol I: Microscopic and Macroscopic Fundamentals* 1968: p. 408-409.

61.   Munro, M., *Evaluated Material Properties for a Sintered alpha-Alumina.* Journal of the American Ceramic Society, 1997. 80(8): p. 1919-1928.

62.   Ullner, C., et al., *Hardness testing on advanced technical ceramics.* Journal of the European Ceramic Society, 2001. 21(4): p. 439-451.

63.   Krell, A. and S. Schädlich, *Nanoindentation hardness of submicrometer alumina ceramics.* Materials Science and Engineering A, 2001. 307(1-2): p. 172-181.

64.   Chou, I.A., H.M. Chan, and M.P. Harmer, *Effect of Annealing Environment on the Crack Healing and Mechanical Behavior of Silicon Carbide-Reinforced Alumina Nanocomposites.* Journal of the American Ceramic Society, 1998. 81(5): p. 1203-1208.

65.   Wiederhorn, S.M., *Mechanics of Subcritical Crack Growth in Brittle Materials.* Encyclopedia of materials : science and technology, 2001: p. 5307-5311.

66.   Bansal, G.K. and W.H. Duckworth, *Fracture Stress as Related to Flaw and Fracture Mirror Sizes.* Journal of the American Ceramic Society, 1977. 60(7-8): p. 304-310.

67.   *Standard Test Method for Determination of Slow Crack Growth Parameters of Advanced Ceramics by Constant Stress-Rate Flexural Testing at Ambient Temperature.* ASTM C1368-10.

68.   Choi, S.R., N.N. Nemeth, and J.P. Gyekenyesi, *Exponential slow crack growth of glass and advanced ceramics—dynamic fatigue.* Fatigue & Fracture of Engineering Materials & Structures, 2005. 28(5): p. 489-497.

69.   *Standard Test Method for Determination of Slow Crack Growth Parameters of Advanced Ceramics by Constant Stress-Rate Flexural Testing at High Temperature.* ASTM C1465-10.

70.   *Standard Test Method for Determination of Slow Crack Growth Parameters of Advanced Ceramics by Constant Stress Flexural Testing (Stress Rupture) at Ambient Temperature.* ASTM C1576-05(2010).

71.   Choi, S.R., N.N. Nemeth, and J.P. Gyekenyesi, *Slow crack growth of brittle materials with exponential crack velocity under cyclic fatigue loading.* International Journal of Fatigue, 2006. 28(2): p. 164-172.

72.   Bennison, S.J. and B.R. Lawn, *Role of interfacial grain-bridging sliding friction in the crack-resistance and strength properties of nontransforming ceramics.* Acta Metallurgica, 1989. 37(10): p. 2659-2671.

73.   Tomaszewski, H., M. Boniecki, and H. Weglarz, *Effect of grain size on R-curve behaviour of alumina ceramics.* Journal of the European Ceramic Society, 2000. 20(14-15): p. 2569-2574.

74.   Barsoum, M.W., *Fundamentals of Ceramics.* Institute of Physics Publishing, Bristol and Philadelphia, 2003, ISBN 0 7503 0902 4 2003: p. 94-95.

75.   Hayashi, H., M. Watanabe, and H. Inaba, *Measurement of thermal expansion coefficient of LaCrO3.* Thermochimica Acta, 2000. 359(1): p. 77-85.

76.   Echsler, H., et al., *Residual stresses in alumina scales grown on different types of Fe-Cr-Al alloys: effect of specimen geometry and cooling rate.* Materials Science and Engineering A, 2004. 384(1-2): p. 1-11.

77.   Huntz, A.M., et al., *Thermal expansion coefficient of alumina films developed by oxidation of a FeCrAl alloy determined by a deflection technique.* Applied Surface Science, 2006. 252(22): p. 7781-7787.

78.   Böcker, A., et al., *Texture formation in Al2O3 substrates.* Journal of the European Ceramic Society, 1994. 14(4): p. 283-293.

79.   Bobet, J.L., et al., *Thermal residual stresses in ceramic matrix composites--II. Experimental results for model materials.* Acta Metallurgica et Materialia, 1995. 43(6): p. 2255-2268.

80.   Zhang, J. and S. Bandopadhyay, *Annual Report of Novel Dense Membranes for Hydrogen Separation for Energy Application.* 2010.

81.   *Property Chart for Yttria Stablized Zirconia and Other Standard Materials from Superios Technical Ceramics Corp.* 2011.

82.   Motohashi, Y., T. Sekigami, and N. Sugeno, *Variation in some mechanical properties of Y-TZP caused by superplastic compressive deformation.* Journal of Materials Processing Technology, 1997. 68(3): p. 229-235.

83.   Tanaka, K., et al., *Phase stability after aging and its influence on pin-on-disk wear properties of Ce-TZP/Al2O3 nanocomposite and conventional Y-TZP.* Journal of Biomedical Materials Research Part A, 2003. 67A(1): p. 200-207.

84.   Pecharsky, V.K. and P.Y. Zavalij, *Fundamentals of Powder Diffraction and Structural Characterization of Materials.* 2009: p. 380.

85.   Pecharsky, V.K. and P.Y. Zavalij, *Fundamentals of Powder Diffraction and Structural Characterization of Materials-2nd Edition.* 2009: p. 395.

86.   Pecharsky, V.K. and P.Y. Zavalij, *Fundamentals of Powder Diffraction and Structural Characterization of Materials 2nd Edition.* 2009: p. 257.

87.   Evans, A.G. and R.M. Cannon, *Overview no. 48: Toughening of brittle solids by martensitic transformations.* Acta Metallurgica, 1986. 34(5): p. 761-800.

88.   Hannink, R.H.J., P.M. Kelly, and B.C. Muddle, *Transformation Toughening in Zirconia-Containing Ceramics.* Journal of the American Ceramic Society, 2000. 83(3): p. 461-487.

89.   Karakoca, S. and H. Yılmaz, *Influence of surface treatments on surface roughness, phase transformation, and biaxial flexural strength of Y-TZP ceramics.* Journal of Biomedical Materials Research Part B: Applied Biomaterials, 2009. 91B(2): p. 930-937.

90.   Zhang, J. and S. Bandopadhyay, *Annual Report of Novel Dense Membranes for Hydrogen Separation for Energy Application.* 2011.

91.   Lima, L.F.C.P., A.L.E. Godoy, and E.N.S. Muccillo, *Elastic modulus of porous Ce-TZP ceramics.* Materials Letters, 2004. 58(1-2): p. 172-175.

256

92.   Smith, C.F. and W.B. Crandall, *Calculated High-Temperature Elastic Constants for Zero Porosity Monoclinic Zirconia.* Journal of the American Ceramic Society, 1964. 47(12): p. 624-627.

93.   Ochrombel, R., et al., *Thermal expansion of EB-PVD yttria stabilized zirconia.* Journal of the European Ceramic Society, 2010. 30(12): p. 2491-2496.

94.   *Reference code: 04-013-4346; PDF index name: Cerium Zirconium Oxide.* 2011.

95.   *Reference code: 04-008-7255; PDF Index name: Yttrium Zirconium Oxide.* 2011.

96.   Manivasakan, P., et al., *Synthesis of Monoclinic and Cubic ZrO2 Nanoparticles from Zircon.* Journal of the American Ceramic Society, 2011. 94(5): p. 1410-1420.

97.   Upadhyaya, D.D., M.R. Gonal, and R. Prasad, *Studies on crystallization behaviour of 3Y-TZP/Al2O3 composite powders.* Materials Science and Engineering A, 1999. 270(2): p. 133-136.

98.   Moriya, Y. and A. Navrotsky, *High-temperature calorimetry of zirconia: Heat capacity and thermodynamics of the monoclinic-tetragonal phase transition.* The Journal of Chemical Thermodynamics, 2006. 38(3): p. 211-223.